Development and characterisation of novel silicon pixel detectors for tracking and timing



Martin Gaži
Magdalen College
University of Oxford

A thesis submitted for the degree of
Doctor of Philosophy

Michaelmas Term 2024

This thesis is dedicated to
the memory of a dear friend,
Peťa Petrášová.
Thank you for opening
the world to me.

Abstract

To achieve a total integrated luminosity of 3,000 fb^{-1} collected after the High-Luminosity LHC upgrade, the ATLAS Inner Detector will be replaced by the Inner Tracker (ITk) with an increased demand for sensor radiation hardness. Based on the Low Gain Avalanche Detector (LGAD) technology, the High-Granularity Timing Detector (HGTD) will be installed to mitigate against the effect of increased pile-up and enhance vertex separation with a 30 ps timing resolution per track.

This thesis presents the electrical characterisation of wafers from the first LGAD batch manufactured by Teledyne e2v, featuring samples with a range of gain layer implant energy and dose. Multiple 1×1 mm^2 LGAD devices were tested in a test beam at the CERN North Area. The results demonstrate excellent hit efficiency (>99%), charge collection (>15 fC), and timing resolution below 20 ps.

Electrical measurements of the LGAD sensors after neutron irradiation give acceptor removal coefficients of 7-8$\times10^{16}$ cm^2, comparable to other non-carbon enriched LGAD productions. Post-irradiation laser injection tests demonstrated jitter better than 10 ps up to 5×10^{14} 1 MeV $n_{eq}cm^{-2}$, with some devices maintaining charge gain of $\sim$15 and jitter <25 ps at fluences up to 2×10^{15} 1 MeV $n_{eq}cm^{-2}$. This thesis also includes measurements of the inter-pad distance for multi-pad LGAD devices.

The MALTA2 sensor, developed as a monolithic candidate for the outermost layer of the ATLAS ITk, was extensively tested in a test beam with 180 GeV hadrons. The investigation characterised samples up to neutron fluence of 5×10^{15} 1 MeV $n_{eq}cm^{-2}$. Samples produced on the Czochralski (Cz) substrate demonstrated better radiation hardness than those on the epitaxial substrate, particularly with backside metallisation. At 3×10^{15} 1 MeV $n_{eq}cm^{-2}$, MALTA2 Cz samples achieved superior performance with 98% efficiency and 6.3 ns RMS timing resolution.

Furthermore, this thesis outlines a preliminary investigation of improved clustering methods that use Time-of-Arrival information to enhance the spatial resolution of the MALTA2 sample by $\sim$20% and improve the timing resolution by $\sim$7%. Further steps for generalisation of the method are also discussed.

Acknowledgements

This journey has been shaped by the support and guidance of many individuals. If I have inadvertently forgotten to mention anyone, please accept my sincere apologies and know that I appreciate your support, no matter how big or small.

I would like to thank my supervisors, Daniela Bortoletto and Steve McMahon, for their invaluable guidance and insightful discussions.

The countless days (and the occasional late nights) spent at the OPMD laboratory were integral to my DPhil experience. I would like to say thank you to Daniela and Ian for setting up a state-of-the-art laboratory in the heart of Oxford, and to Richard Plackett and Daniel Hynds for ensuring the lab ran smoothly (and for keeping the coffee machine well-stocked), to Alex Knight and Morgan Larner-Smith for their professional opinions, to Maryam Akhtar, Dennis Yborne, and Gale Lockwood for not complaining about bonding one wire over and over again, to Giulio Villani, Dan Weatherill, Dan Wood, and Sultan for their patience and willingness to teach me how detectors work, and to Umberto Molinatti, Ashley McDougall, Simon Koch, Anabelle Brookes, and Nina Dimova for making the lab a fun place to work. My job here is done.

I must also mention Daniel and Giulio again, as a single thank you does not suffice. Giulio, thank you for giving me the opportunity to work alongside you and learn from you. Daniel, thank you for caring, our chats, the Friday lab cakes, pub trips, and for helping me find the right path when I felt lost.

To my colleagues from the LGAD-Te2v collaboration - Jonathan, Laura, Phil, Doug, Kev, and everyone else who contributed over the years. Thank you for your valuable thoughts and feedback. I wish you all the best in your future endeavours.

One of the highlights of my DPhil was working with the MALTA group at CERN. Thank you, Carlos, Valerio, Milou, Florian H., Florian D., Ignacio, Giuliano, and others, for making my months in Geneva both productive and enjoyable. A special thank you to Milou for always making me feel welcome – I truly enjoyed working with you.

I would also like to thank Sue Geddes and Kim Proudfoot, the particle physics administration team at Oxford, for their help and kindness.

My research was made possible through financial support from the Science and Technology Facilities Council, the AIDAinnova project, and the Magdalen College Student Support Fund. Ultimately, none of this would have been possible without the Secondary School Scholarships Program, the Head's Conference (HMC) and the generosity of Whitgift School. I hope to one day repay the kindness and support you gave me.

To all my friends from Slovakia, thank you for lifting my spirits and staying in touch despite the difficulties of long-distance friendship.

Všetkým mojím priateľom zo Slovenska ďakujem, že mi vždy viete zdvihnúť náladu a že sme ostali v kontakte aj napriek veľkej vzdialenosti.

I want to say a huge thank you to my parents, Karina and Ivan, my brother, Michal, and my whole family for their unwavering support on this journey.

Chcem povedať jedno veľké ďakujem mojim rodičom, Karin a Ivanovi, môjmu bratovi Michalovi a celej mojej rodine za ich podporu na tejto ceste.

Last but not least - thank you, Em, for always being there for me. Whether we were working in the same flat or halfway across Europe, you never failed to put a smile on my face. Thank you for always believing in me.

Preface

The measurements, data processing, and result analysis presented in this thesis have been carried out at the Oxford Physics Microstructure Detector (OMPD) laboratory in Oxford, and within the MALTA group as part of the ATLAS Pixel group at CERN in Geneva. The primary focus of the material presented here is on my own contributions. Figures taken from external sources are marked with a reference to their origin. All other figures are either my own or a result of collaboration with colleagues within the research groups. Below, I provide a brief summary of the different projects I worked on during my DPhil research, highlighting my specific contributions.

Electrical characterisation of LGAD sensors
Using a probe station setup at the OPMD laboratory, I have performed measurements of the leakage current and capacitance of unirradiated and neutron-irradiated Low Gain Avalanche Detector (LGAD) sensors. This work is discussed in Section 3.2 for the unirradiated LGAD sensors and Section 3.4 for those exposed to neutron irradiation. I analysed the data, compared the different manufactured splits, and established the performance trend as a function of neutron irradiation. As the primary author, I prepared a publication of a subset of the results for the unirradiated sensors in [1]. In December 2022, I presented the measurements of the irradiated LGAD sensor and other results at the 41st RD50 workshop in Seville, Spain [2].

Development of LGAD readout board
With colleagues from the OPMD laboratory, I developed the custom readout boards for the LGAD sensors referred to as COLA. In particular, I designed the layout and debugged the multi-channel board COLA v2.1. The COLA boards are used throughout Chapter 3, with data acquired with the multi-channel version presented in Section 3.6.

Test beam measurements of LGAD sensors
I carried out the pre-measurement characterisation and subsequent analysis of the sensors for the test beam measurements at the CERN North Area. This work is discussed in Section 3.3. With the technical support of colleagues from the MALTA group, I set up and debugged the LGAD data acquisition system in the test beam area. I analysed the acquired data to establish the efficiency and timing resolution and quantify the charge collected by the sensor.

Laser injection measurement of LGAD sensors

I significantly upgraded and calibrated the pre-existing fast laser setup at the OPMD laboratory, implementing a new fast laser, oscilloscope, and vortex cooler. I wrote custom Python libraries for the new hardware and developed scripts for automated data acquisition. The results for irradiated single LGAD devices are presented in Section 3.5. I analysed the acquired LGAD signals and produced the figures reporting device behaviour with increasing radiation fluence. The results for the LGAD arrays are included in Section 3.6. These focus on the extraction of the inter-pad distance. I acquired and analysed all laser injection data presented in this thesis using my own scripts.

Test beam measurements of irradiated MALTA2 sensors

With several collaborators, I was part of the test beam campaign focused on characterising MALTA2 samples using the MALTA telescope at the North Area at CERN. This work is discussed in Section 4.2. In particular, I was responsible for characterising the performance of the irradiated MALTA2 samples on an epitaxial substrate conducted in November 2022. I developed a framework to analyse the signal time delay within the MALTA2 pixel and quantify the evolution of sensor performance with received fluence. The results were published in [3], where I was one of the primary authors. Most notably, I analysed data, produced the plots, and wrote part of the publication on detector timing performance. In March 2023, I presented these and other results at the TREDI 2023 workshop in Trento, Italy [4].

Analysis of MALTA2 hit clusters

I studied the timing distributions of the MALTA2 hits within the pixel clusters. This work is discussed in Section 4.3. Based on my understanding of the MALTA2 clusters, I proposed a modified clustering method that improves the sensor's position resolution. I developed an extension to the data analysis algorithms that validated the new method and compared its performance to the standard binary clustering used previously. Following my investigation, I introduced the improved clustering method into the standard MALTA2 analysis framework.

Contents

1 Introduction **1**
- 1.1 The Large Hadron Collider . . . 2
  - 1.1.1 The High Luminosity LHC . . . 5
- 1.2 The ATLAS Detector . . . 6
  - 1.2.1 The ITk and HGTD upgrades . . . 7

2 Silicon Pixel Detectors **9**
- 2.1 Interaction of particles with matter . . . 9
  - 2.1.1 Charged particles . . . 9
  - 2.1.2 Photons . . . 11
- 2.2 Silicon detectors . . . 12
  - 2.2.1 The p-n junction . . . 14
  - 2.2.2 Carrier transport and signal generation . . . 15
- 2.3 Silicon pixel sensor types . . . 17
  - 2.3.1 Hybrid pixel detectors . . . 17
  - 2.3.2 Monolithic pixel detectors . . . 18
- 2.4 Radiation damage . . . 18
  - 2.4.1 TID damage . . . 19
  - 2.4.2 Bulk damage . . . 20
  - 2.4.3 Annealing . . . 23

3 Development and Characterisation of Low Gain Avalanche Detectors **24**
- 3.1 Introduction . . . 24
  - 3.1.1 Improved timing via internal gain . . . 26
  - 3.1.2 Low Gain Avalanche Detectors (LGADs) . . . 26
  - 3.1.3 Optimising the LGAD design for timing . . . 30
  - 3.1.4 The High Granularity Timing Detector . . . 32
  - 3.1.5 LGAD fabrication by Te2v . . . 33
  - 3.1.6 Compact OPMD LGAD Amplifier (COLA) readout board . . . 36
- 3.2 Static characterisation of non-irradiated LGADs . . . 39
  - 3.2.1 Measurement procedure . . . 39
  - 3.2.2 Capacitance measurements . . . 41
  - 3.2.3 Leakage current characterisation . . . 48
  - 3.2.4 Summary . . . 52

3.3 Hadron beam measurements of Te2v-LGADs at the SPS . . . 53
3.3.1 Experimental setup . . . 53
3.3.2 Data analysis . . . 57
3.3.3 Results . . . 64
3.3.4 Summary . . . 67
3.4 Characterisation of neutron-irradiated LGAD sensors . . . 68
3.4.1 Neutron irradiation of LGAD samples . . . 68
3.4.2 Active gain fraction after irradiation . . . 70
3.4.3 Acceptor removal coefficient calculation . . . 77
3.4.4 Summary . . . 79
3.5 Laser injection measurements of irradiated LGAD devices . . . 80
3.5.1 Principle of operation . . . 81
3.5.2 Data acquisition and processing . . . 87
3.5.3 Performance before irradiation . . . 96
3.5.4 Results for irradiated samples . . . 98
3.5.5 Summary . . . 100
3.6 Characterisation of LGAD pixel arrays . . . 103
3.6.1 LGAD array description . . . 103
3.6.2 IV measurements of LGAD arrays . . . 105
3.6.3 Inter-pad distance . . . 108
3.6.4 Summary . . . 114

4 The MALTA2 Monolithic Active Pixel Sensor 115
4.1 Introduction . . . 116
4.1.1 The MALTA family . . . 116
4.1.2 MALTA2 . . . 120
4.1.3 Sensor characterisation with the MALTA telescope . . . 122
4.2 Radiation hardness of MALTA2 . . . 126
4.2.1 Test beam set-up and sample characterisation . . . 126
4.2.2 Irradiated MALTA2 on Czochralski substrate . . . 130
4.2.3 Timing performance of the irradiated MALTA2-Cz samples . . . 136
4.2.4 Irradiated MALTA2 on epitaxial substrate . . . 142
4.2.5 Summary . . . 144
4.3 Improving position and timing resolution with clusters . . . 145
4.3.1 Introduction of timing . . . 149
4.3.2 Exponential clustering . . . 152
4.3.3 Improving timing with position information . . . 154
4.3.4 Summary . . . 156

5 Conclusions and Outlook 157

Bibliography 161

1 Introduction

High-energy physics (HEP) experiments at the Large Hadron Collider at CERN continue in their successful period of data-taking and scientific discovery. Throughout its lifetime, the ATLAS experiment reached and exceeded its physics goals and is still pushing our understanding of the Standard Model, discovering the Higgs boson in 2012. Towards the end of this decade, the LHC is due to be upgraded to High Luminosity LHC (HL-LHC), with instantaneous luminosity increasing up to 7.5×10^{34} cm^{-2}s^{-1} and aiming to collect a total integrated luminosity of up to 3,000 fb^{-1}. This change would represent almost a four times increase in instantaneous luminosity (from the current LHC peak value of 2×10^{34} cm^{-2}s^{-1}) and results in multiple events in the same region of the detector occurring very close in time [5] (for instantaneous luminosity, see Section 1.1).

With an order of magnitude more data than what would be collected before the HL-LHC, the upgrade creates a unique opportunity to explore physics beyond the Standard Model and detect rare particle interactions. Well-separated collision vertices are necessary for the success of the ATLAS experiment during the HL-LHC era. An all-silicon ATLAS inner tracker (ITk) is needed to cope with higher particle fluxes per bunch crossing and increased radiation levels. However, using only the ATLAS ITk, the spatial separation on the vertex is insufficient in the forward region at pseudorapidity $|\eta| > 2.4$ for low energy tracks [6] (for pseudorapidity, see Section 1.2). A High Granularity Timing Detector (HGTD) based on Low Gain Avalanche Detector (LGAD) technology will provide timing information with 30 ps resolution per track to improve vertex separation.

The structure of this thesis is as follows. The rest of Chapter 1 is dedicated to setting the thesis framework and exploring the Large Hardon Collider and its future upgrades. Chapter 2 provides an overview of silicon pixel detectors, their operating principles, types, and the effect of radiation-induced damage. Chapter 3 focuses on the development and characterisation of Low Gain Avalanche Detectors (LGADs) for the High Granularity Timing Detector (HGTD), summarising the results obtained with LGADs before and after neutron irradiation. Chapter 4 discusses the MALTA2 monolithic CMOS sensor developed with the aim of exploring its suitability in ATLAS ITk and other HEP experiments. The chapter presents test-beam results for highly irradiated samples and outlines a new pixel clustering method developed to improve the spatial and timing resolution of the sensor. Finally, Chapter 5 summarises the conclusions of the thesis.

1.1 The Large Hadron Collider

The Large Hadron Collider (LHC) at The European Organization for Nuclear Research (CERN) in France and Switzerland is the world's largest particle accelerator [7]. Operational since 2008, it is a synchrotron with a 27 km circumference located about 100 m underground. It is primarily used as a proton-proton collider but can also accelerate heavy ions such as lead ions. The LHC is the last element in a chain of accelerators, each injecting the particle beam into the next, as shown in Figure 1.1. Negative hydrogen ions are accelerated to energies of 160 MeV using a linear accelerator Linac4. The beam is injected into the Proton Synchrotron Booster (PSB), which strips the electrons from the ions, boosts the particle energy to 2.0 GeV, and passes the remaining proton beam into the Proton Synchrotron (PS). In the PS, the energy is increased to 25 GeV, followed by Super Proton Synchrotron (SPS), increasing it further to 450 GeV. The proton beam from the SPS can be injected into the LHC or directed to a dedicated area for smaller experiments and detector testing called the North Area.

In the LHC, the protons travel along two opposite beamlines in 2800 bunches of about 10^{11} protons per bunch. They are accelerated using radio-frequency (RF) cavities to the energy of 6.8 TeV per beam and are kept in a circular path along the beamline

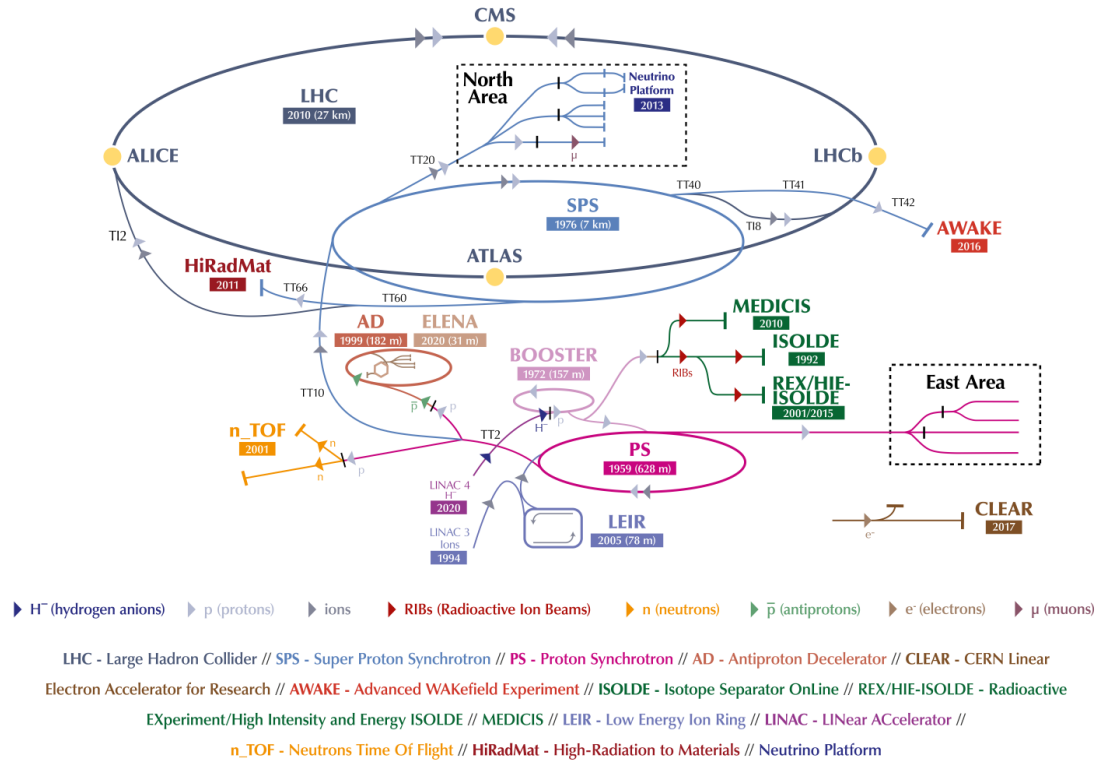


Figure 1.1: The CERN accelerator complex layout from 2022. Figure from [8].

by superconducting dipole magnets producing a magnetic field of 8 T. The counter-circulating beams with proton bunches spaced by 25 ns are focused and set to collide at four locations around the ring, corresponding to the position of the four main LHC experiments: ATLAS [9], CMS [10], LHCb [11], and ALICE [12].

The main parameters of the LHC experiment are summaries in Table 1.1. Three important quantities in collider physics – centre-of-mass energy, luminosity, and the number of interactions per event – are discussed in more detail below.

Centre-of-mass energy

As the two circulating proton beams collide head-on, each of energy 6.8 TeV, the maximum available energy for producing new particles is 13.6 TeV. This quantity is known as the *centre-of-mass energy* $\sqrt{s}$. During 2011 and 2012 (LHC Run 1), proton-proton collision data was collected at $\sqrt{s}$ = 7 TeV and 8 TeV. The centre-of-mass energy was increased to 13 TeV for LHC Run 2 (2015-2018) and then again to the current value $\sqrt{s}$ = 13.6 TeV for LHC Run 3 (from 2022).

Table 1.1: The main parameters of the LHC.

Parameter	**Value**
Collision bream energy	6.8 TeV
Injection beam energy	450 GeV
Peak luminosity (protons)	2×10^{34} cm^{-2}s^{-1}
Interactions per bunch crossing	average 47.7 (LHC Run 3)
Dipole magnetic field	8.3 T
Circulating current/beam	0.53 A
Time between bunches	24.95 ns
Protons per bunch	1.05×10^{11}
Stored beam energy	334 MJ
Beam lifetime	22 h

Luminosity

The instantaneous luminosity $\mathcal{L}$ can be expressed in terms of the collider parameters

$$\mathcal{L} = \frac{N_1 N_2 f N_b}{4\pi\sigma_x\sigma_y}, \tag{1.1}$$

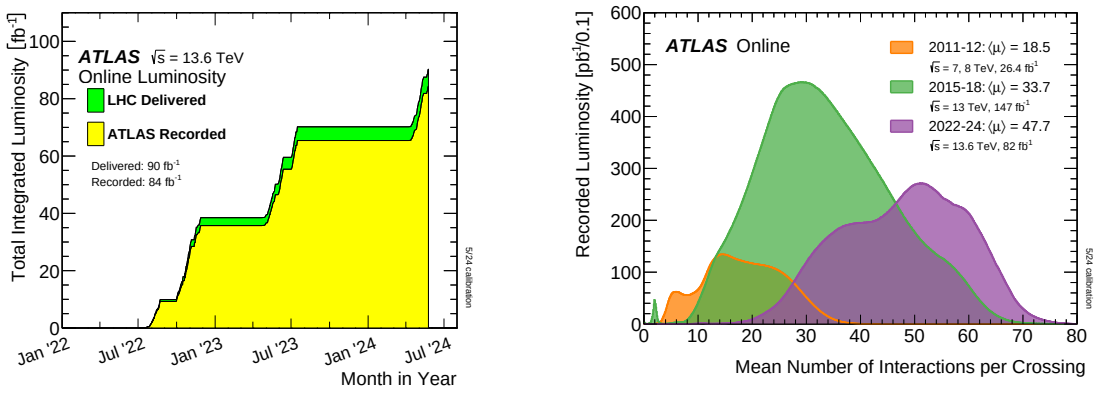
where N_1 and N_2 are number of protons in each bunch, f is the frequency of the collider, N_b is the number of bunches, and $\sigma_{x/y}$ is the width of the beam density distribution in the x/y-direction (with the beam along the z-axis). The rate at which a particular physics process occurs dN/dt is the product of the instantaneous luminosity and the process cross-section σ

$$\frac{dN}{dt} = \mathcal{L} \times \sigma. \tag{1.2}$$

By integrating the interaction rate over time, the total number of events produced for the given process can be written as

$$N = \mathcal{L}_{int} \times \sigma, \tag{1.3}$$

where $\mathcal{L}_{int} = \int \mathcal{L}\, dt$ is a quantity known as the *integrated luminosity*. The ongoing LHC Run 3 (2022-2025) aims to increase the total integrated luminosity of the LHC from the initial target of about 300 fb^{-1} to the current goal of 350 fb^{-1}. Figure 1.2a shows that the integrated luminosity recorded by ATLAS in LHC Run 3 between 2022 and May 2024 reached $\mathcal{L}_{int}$ = 84 fb^{-1} [13], which gives an indication for the size of the obtained dataset over this time period.



(a) **(b)**

Figure 1.2: (a) Time evolution of the cumulative luminosity delivered (green) and recorded by ATLAS (yellow) during stable beams for p-p collisions at $\sqrt{s}$ = 13.6 TeV in LHC Run 3 (2022-2024). (b) The distribution of the mean number of interactions per crossing for p-p collisions for LHC Runs 1-3. Figures from [13].

Number of interactions

Whereas in general, it is true that the more interactions, the better; too many interactions can make the event reconstruction process more difficult. The additional interactions, often from soft proton-proton events, are known as *pile-up*. The mean number of interactions per bunch crossing at the ATLAS detector is shown in Figure 1.2b. For Run 3, there are 47.7 interactions on average every 25 ns.

1.1.1 The High Luminosity LHC

To fully harness the physics potential of the LHC, CERN plans an ambitious upgrade of the current collider to the High-Luminosity LHC (HL-LHC). As the name may suggest, one of the key targets of the project is to increase the peak luminosity of the LHC to 7.5×10^{34} cm^{-2}s^{-1} with a goal to reach an integrated luminosity of 3,000 fb^{-1} over the course of approximately 12 years of operation. Implementation of the upgrade is proceeded by several years of research and development efforts on a global scale. The operation of the HL-LHC is expected to start in 2029 after the Long Shutdown 3 (LS3). The different phases of LHC and HL-LHC implementation and operation are shown in Figure 1.3.

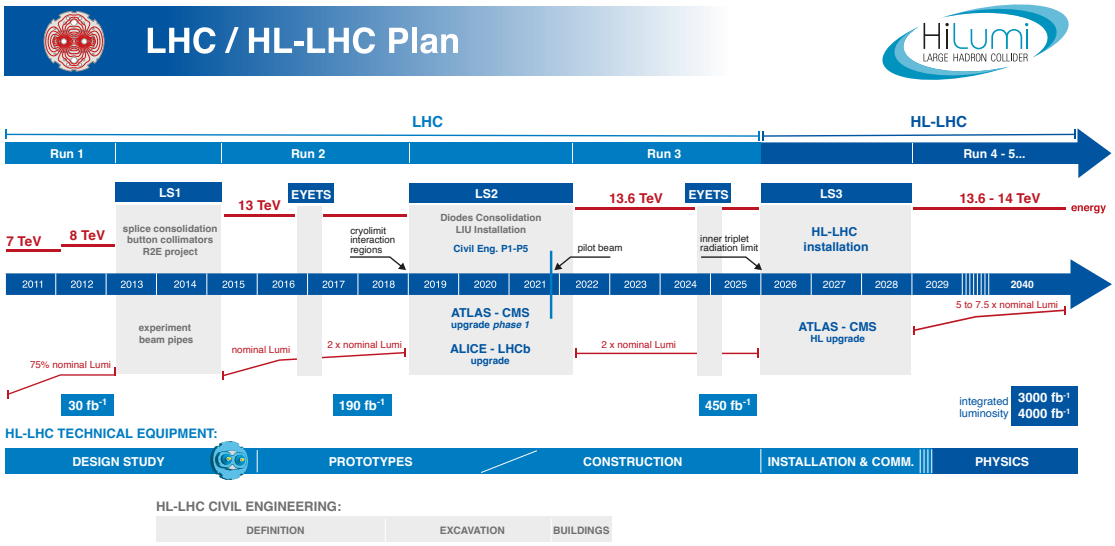


Figure 1.3: Stages of the LHC and HL-LHC projects. Figure from [14].

1.2 The ATLAS Detector

The ATLAS detector is one of the two general-purpose particle detectors at the LHC. It has a total length of 44 m, a height of 25 m, and a weight of 7000 tonnes [9]. The two particle beams collide at the centre of the ATLAS detector and produce new particles travelling from the interaction point in all directions. The detector covers almost the whole solid angle, recording tracks, momenta, and the energies of the particles and their decay products as they traverse the different detecting subsystems arranged in layers. The experiment consists of four detector subsystems: The Inner Detector (tracking), the Electromagnetic and Hadronic Calorimeters, and the Muon Spectrometer. Additionally, it also contains the Toroid Magnets and the Solenoidal Magnet.

In the coordinate system used for the ATLAS detector, the z-axis is defined as the direction along the counterclockwise particle beam, the x-axis points towards the centre of the LHC ring, and the y-axis points upwards from the interaction point. Due to the cylindrical shape of the detectors, it is helpful to use polar coordinates, with the azimuthal angle ϕ in the x-y plane and the angle θ relative to the beam axis. For ultra-relativistic particles, the direction of a particle can be approximately parametrised using the pseudorapidity $\eta = -\ln(\tan(\theta/2))$. For ultra-relativistic particles, pseudorapidity intervals $\Delta\eta$ are Lorentz invariant under boosts along the longitudinal axis.

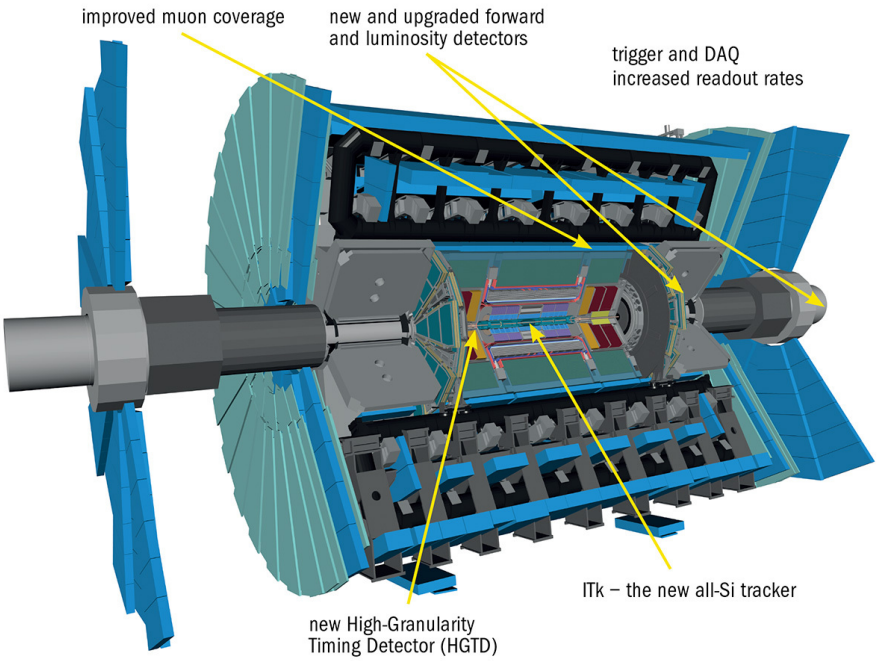


Figure 1.4: Schematic of the major upgrades to the ATLAS detector for the HL-LHC era. Figure from [15].

1.2.1 The ITk and HGTD upgrades

During Long Shutdown 3, the ATLAS experiment will undergo several upgrades to prepare the detector for the challenging conditions of the HL-LHC operation. Figure 1.4 shows some of these upgrades.

The Inner Detector (ID) [16] will be replaced by a new all-silicon Inner Tracker (ITk) [17, 18]. Similarly to the current ID, the ITk will consist of pixel detectors in the region close to the interaction point and strip detectors located at larger radii. Figure 1.5 shows the schematic layout of the two types of silicon sensors in the ITk. The pixel system contains five barrel layers and endcap rings. Due to their proximity to the interaction point, the two innermost pixel layers will receive the highest amount of radiation damage and, therefore, will be replaced after reaching a total luminosity of around 2000 fb^{-1}. The strip detectors are arranged into four barrel layers and six endcap disks, positioned up to 1 m radially from the interaction point.

Compared to the ID, the ITk detector is significantly larger, with a sixty-fold increase in the number of pixel channels and a ten-fold increase in strip channels. The new design also benefits from improved hermeticity, higher granularity, and an increased

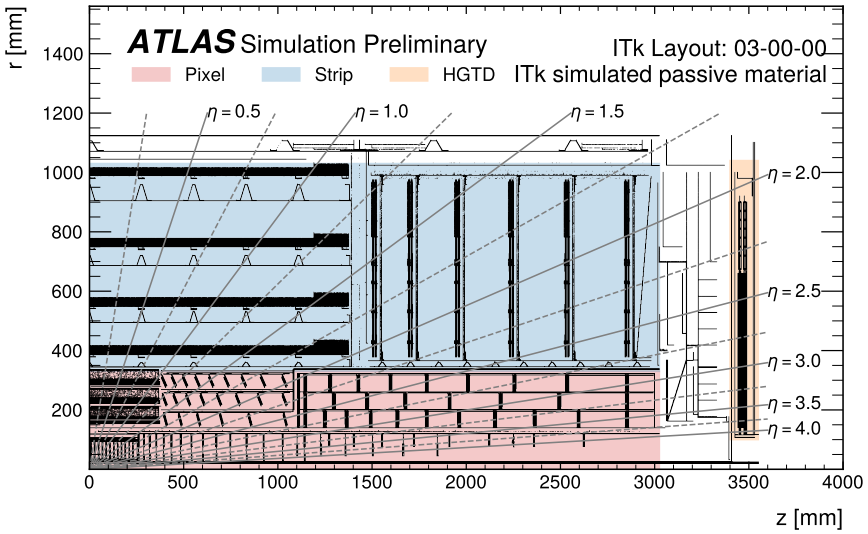


Figure 1.5: Layout of the ITk Pixel and Strip detectors, alongside the High-Granularity Timing Detector. Only one quadrant of the detector is visible. Paths of simulated particles at various pseudorapidities are shown. Figure from [19].

number of expected hits-on-track. As mentioned above, one of the significant challenges is the intense radiation environment, which puts strict requirements on the radiation hardness of the detector. The MALTA sensor discussed in Chapter 4 was developed as an option for the outermost layer of the ATLAS ITk. For this layer, it is required that the modules achieve detector efficiency >97% and timing resolution better than 25 ns up to NIEL (non-ionising energy loss) fluence of 10^{15} 1 MeV $n_{eq}cm^{-2}$ [17] (for NIEL, see Section 2.4.2).

During the upgrade, a new silicon detector will be installed outside the endcaps of the ITk known as the High Granularity Timing Detector (HGTD) [6] – see Figure 1.5. It will cover a pseudorapidity range of $2.4 < |\eta| < 4$ and provide a 30 to 50 ps timing resolution for charged particles by exploiting the Low Gain Avalanche Detector (LGADs) technology. The new detector allows for the reduction of pile-up by resolving spatially overlapping tracks using precise timing information. More information on the HGTD can be found in Section 3.1.4. The entire silicon ITk and HGTD detectors will use a CO_2 cooling system to achieve a temperature around -35°C. The low temperatures allow for reduced sensor power consumption by lowering the leakage current and prevent detrimental reverse annealing effects after prolonged exposure to the radiation environment [6, 17].

2 Silicon Pixel Detectors

This chapter introduces silicon detectors and their operating principles. The aim is to provide the essential background for the measurements presented in Chapters 3 and 4.

2.1 Interaction of particles with matter

2.1.1 Charged particles

As the massive particles produced in HEP experiments pass through a material, they interact with it, depositing some of their kinetic energy. The detection of particles is achieved by measuring these interactions. In the case of charged particles passing through a semiconductor detector, the particles interact via the Coulomb interaction. The mean energy loss per unit distance can be described by the Bethe-Bloch formula

$$-\left\langle \frac{dE}{dX} \right\rangle = 2\pi N_a r_e^2 m_e c^2 \rho \frac{Z}{A} \frac{z^2}{\beta^2} \left\{ \ln\left(\frac{2m_e c^2 \beta^2 \gamma^2 T_{max}}{I^2} \right) - 2\beta^2 - \delta - 2\frac{C}{Z} \right\}, \tag{2.1}$$

where N_a is the Avogadro's number, r_e is the classical electron radius, m_e is the electron mass, c is the speed of light, ρ is the density of absorbing material, Z is the atomic number of absorbing material, A is the atomic weight of absorbing material, z is the charge of the incident particle, β is v/c of the incident particle with speed v, $\gamma = 1/\sqrt{1-\beta^2}$, T_{max} is the maximum energy transfer in a single collision, I is the mean excitation potential, δ is the density correction, and C is the shell correction [20]. The density correction arises due to the tendency of the atoms in the material to be polarised by the electric field of the incident particle, which is particularly relevant

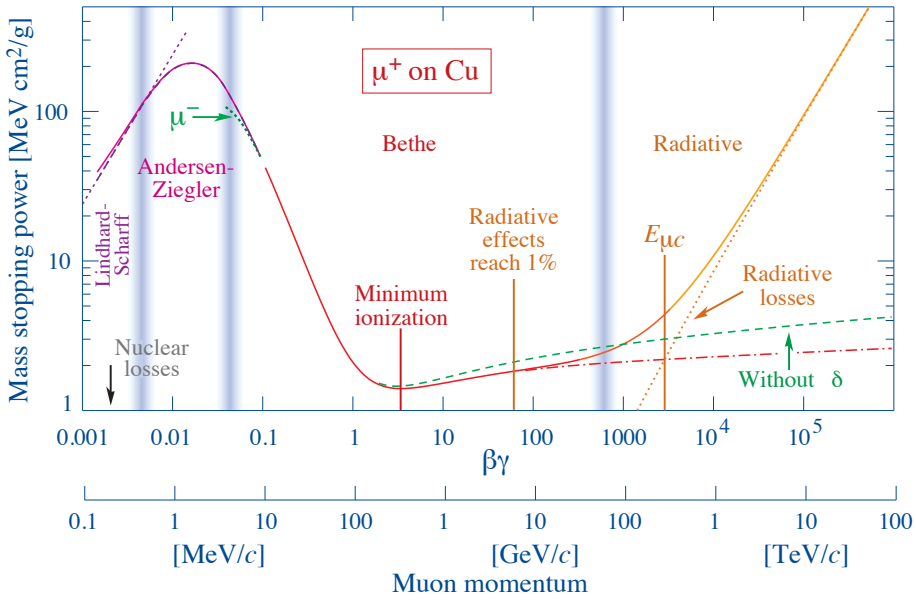


Figure 2.1: Mean energy loss for a muon passing through a copper medium approximated by the Bethe-Bloch formula. Figure from [21].

at high energies. On the other hand, the shell correction is relevant at low energies when the velocity of the incident particle is comparable to or smaller than the orbital velocity of the bound electrons [20]. The average muon energy loss in a copper material approximated by the Bethe-Bloch formula is shown in Figure 2.1.

The Bethe-Bloch equation has a minimum at around $\beta\gamma = 3.5$. The average energy loss per unit distance (also known as the *stopping power*) of a particle with such $\beta\gamma$ is 1.664 MeV cm^{2}g^{-1} for materials with atomic number $10 \leq Z \leq 30$. For silicon, this would correspond to 3.88 MeV/cm [21]. As this is the minimum amount of kinetic energy the particles can lose when traversing the material, such particles are referred to as the minimum ionising particles (MIP). Since the stopping power is relatively flat in the range $1 \leq \beta\gamma \leq 10$, the MIP properties are relevant to particles in this range, such as the typical hadrons and muons in the LHC [22]. In the case of electrons, the energy deposition is more complicated due to their small mass, with radiative losses (Bremsstrahlung) becoming significant at energies of a few tens of MeV. [20].

The amount of energy deposited by a MIP is not always equal to the mean because the number of collisions and the amount of energy transferred are affected by statistical fluctuations. The energy loss distribution for thin sensors can be described using the Landau distribution. The probability distribution shown in Figure 2.2 is asymmetric,

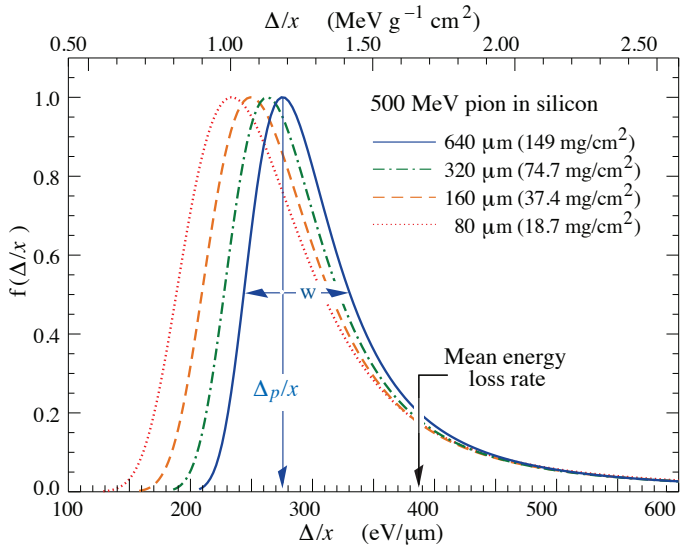


Figure 2.2: Peak-normalised Landau distribution for a 500 MeV pion passing through a silicon material of various thicknesses. The width w is the full width at half maximum. Figure from [21].

with a long tail due to rare but non-negligible large energy transfers in a single collision. The mean energy loss no longer equals the peak value, referred to as the *most probable value* or MPV. As the mean is not a well-defined parameter (due to the long tail), the MPV is often used to parametrise the Landau distribution together with its width (full width at half maximum), which depends on the thickness of the detector.

2.1.2 Photons

As photons do not have mass, a different description of their interactions with matter is needed. They interact via three main processes, with the relative probability of each process determined by the photon energy and the atomic number of the absorbing material Z. The dominant regions of the three processes – photo-electric effect, Compton scattering, and pair production are shown in Figure 2.3.

Photo-electric effect

Photons can interact with matter and be absorbed entirely by depositing all of their energy. The photon's energy is transferred to an atomic electron, which is subsequently ejected from the atom. The ejected electron can produce further ionisation along its track. This process dominates for low-energy photons between 50-500 MeV.

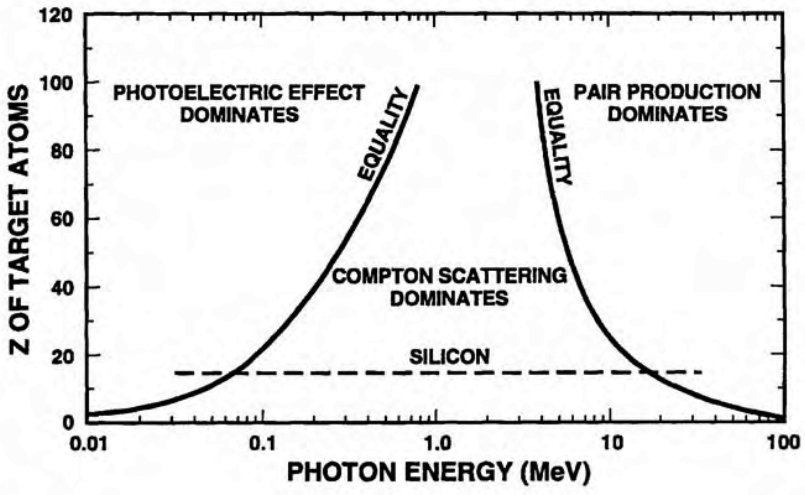


Figure 2.3: The dominant energy loss process for photons of various energies interacting with a medium with atomic number Z. The dashed line represents silicon. Figure from [23].

Compton scattering

Photons can be deflected. In this process, the photons scatter inelastically on outer-shell electrons. A part of the photon's energy is transferred to the electron, which is ejected from the atom. Compton scattering is the most dominant process for photons between roughly 50 keV and 5 MeV.

Pair production

Photons that have more energy than twice the rest mass of an electron (1.02 MeV) can produce an electron-positron pair. For photon energies >5 MeV, this process dominates.

2.2 Silicon detectors

In crystalline materials with a closely packed periodic arrangement of atoms, the electron wavefunctions start to overlap and form *energy bands*, which can be considered as a continuum of allowed electron energy states. The electrons in the *valence* bands are bound to the atoms, but those in the *conduction* bands can move freely through the lattice. The energy gap between the highest valence and lowest conduction bands is known as the *band gap*. The size of the band gap determines the properties of the material. Figure 2.4 schematically illustrates these concepts for an insulator (large >3 eV band gap), a semiconductor (<3 eV band gap), and a metal (no band gap).

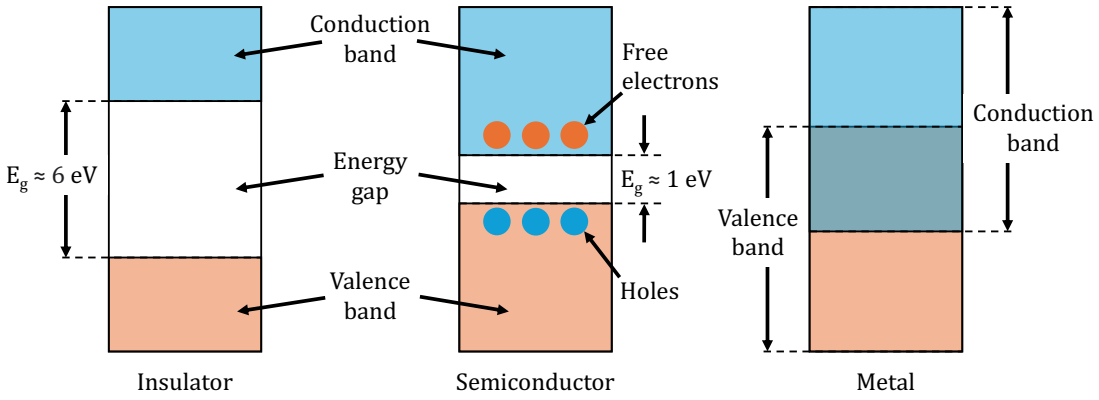


Figure 2.4: Energy band structure of insulators, semiconductors, and conductors (metals).

In a semiconductor, a pair of charge carriers is generated by exciting a valence electron into a conduction band – a free electron in the conduction band and a positive hole left in its place. Electrical signals arise in semiconductors from the movement of the charge carriers. In pure undoped semiconductor, the number of electrons in the conduction band equals the number of holes and is referred to as the *intrinsic carrier concentration*. The intrinsic concentration n_i can be expressed as

$$n_i = AT^{\frac{3}{2}} \exp\left(\frac{-E_g}{2k_B T}\right), \tag{2.2}$$

where A is a material-dependent constant, T is the absolute temperature, E_g is the energy gap at 0 K, and k_B is the Boltzmann constant.

Introducing atoms with a higher number of valence electrons into semiconductor lattice (donors) creates a region with excess negative charge carriers - electrons. Semiconductor with such impurities is referred to as n-type. Conversely, doping semiconductor with atoms with fewer valence electrons (acceptors) creates a p-type region. P-type semiconductor has an excess of positive charge carriers, referred to as holes. Donor elements such as arsenic, phosphorus, and antimony are used to create n-type semiconductor, while boron, gallium, and indium often take the place of the acceptor impurities to form p-type semiconductor [20].

While a range of materials are being used to manufacture HEP particle detectors, such as diamond [24], germanium [25] or gallium arsenide [26], silicon is the most widely used semiconductor material for charged particle detection [20]. Compared

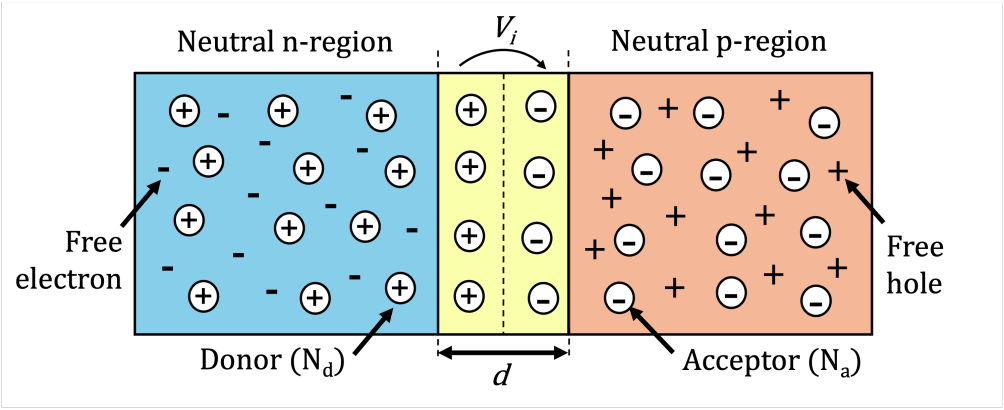


Figure 2.5: Schematic of a p-n junction. Contact region of width d is depleted of free charge carriers with intrinsic potential difference V_i preventing further diffusion of free charge carriers between p-doped and n-doped neutral regions.

to silicon, diamond detectors require less power due to lower leakage current and demonstrate lower radiation length, which is advantageous for tracking detectors. However, the larger ionisation energy of diamond detectors can reduce the collected charge. In silicon, the band gap is 1.12 eV, allowing for room temperature detector operation, which is not possible with germanium with a smaller 0.66 eV band gap.

2.2.1 The p-n junction

The majority of silicon detectors are built on the concept of a p-n junction. As shown in Figure 2.5, when the p- and n-doped regions are brought into contact, a fraction of the excess holes from the p-type silicon recombine with the excess electrons from the n-type silicon. As a result, a region free of charge carriers is created, known as the *depletion region*. The maximum extent of the depletion region is reached when there is a sufficient potential difference V_i from the charge imbalance to stop any further diffusion of charge carriers from one region into the other.

The extent of the depletion region can be modified by applying an external voltage across the junction - referred to as *bias voltage* V_{bias}. When a positive voltage is applied to the p-type silicon, such that the intrinsic potential due to the charge carrier imbalance is exceeded, charges can flow through the junction. This arrangement is known as *forward bias*. Conversely, if the positive bias voltage is applied to the n-type silicon in *reverse bias*, charge carriers are pushed away from the depletion

region, allowing the depletion region to grow. In the reverse bias mode, a small current flows through the junction primarily due to thermal excitations, referred to as the *leakage current*.

The depth of the depletion region d, known as the *depletion depth*, is given by

$$d = \begin{cases} \sqrt{\frac{(V_{bias}+V_i)2\epsilon}{e}\left(\frac{1}{N_d}+\frac{1}{N_a}\right)} & \text{if } V_{bias} + V_i > 0 \\ 0 & \text{if } V_{bias} + V_i \leq 0 \end{cases}, \tag{2.3}$$

where ϵ is the permittivity of the material, N_d and N_a are the donors and acceptors densities. Usually, the junction is formed such that the doping of one side is much larger than the other. In the case of $N_d >> N_a$, the depletion extends primarily into the p-doped region with resistivity $\rho_p = (e\mu_h N_a)^{-1}$, such that for $V_{bias} + V_i > 0$, the expression for the depletion depth becomes

$$d = \sqrt{(V_{bias} + V_i)2\epsilon\mu_h\rho_p}, \tag{2.4}$$

where μ_h is the hole mobility. For the other case ($N_a >> N_d$), the depletion depth is defined analogously with n-doped region resistivity ρ_n and electron mobility μ_e.

For a p-n junction that can be modelled as a parallel plate capacitor with area A, the capacitance is given as

$$C = \frac{A\epsilon}{d} = A\sqrt{\frac{\epsilon}{2(V_{bias} + V_i)\mu\rho}}, \tag{2.5}$$

where the expression on the right-hand side uses Equation 2.4. Notably, the capacitance depends on the applied bias voltage V_{bias}.

2.2.2 Carrier transport and signal generation

If the charges are generated within a volume containing free charge carriers, the changes can recombine and prevent signal formation. On the other hand, when electron-hole pairs are created within the depleted volume, the probability of recombination is much lower. Due to the potential difference (either intrinsic V_i or the applied reverse bias V_{bias}), the charge carriers are swept in opposite directions - holes towards the negative p-type electrode and electrons towards the positive n-type electrode. This

movement is known as *drift*. The drift velocity can be expressed as a function of the applied electric field E as

$$v_{drift} = \mu E. \tag{2.6}$$

As the mobility of the carriers is different for the electrons and holes, μ_e and μ_h are used to distinguish the two. For fields below 100 kV/cm, the mobilities can be assumed to be constant. For intrinsic silicon, the electron mobility at room temperature is μ_e = 1450 $cm^2V^{-1}s^{-1}$ and the hole mobility is μ_h = 450 $cm^2V^{-1}s^{-1}$. Hole mobilities are generally lower than electron mobilities. The mobilities decrease as the doping concentration increases due to the scattering from the dopants [27].

If an external field is not applied, the charge carriers do not drift. Rather, they diffuse, scattering from silicon lattice and impurities. As this is a random process, the mean distance travelled by a charge carrier is zero. However, if a gradient in the concentration of carriers is created, such as when a MIP traverses the volume, the random movements of the free charges create an electron diffusion current density

$$J_{diff} = -qD_n\Delta n, \tag{2.7}$$

where q is the amount of charge, D_n is the electron diffusion constant, and Δn gives the electron concentration gradient. The concentration gradient determined the direction of the drift current. An equivalent expression for holes can be obtained by substituting n with p.

Current induction

The movement of the charge carriers induces a current on the electrodes, according to Ramo's theorem [28]. The amount of induced current is proportional to the generated charge within the junction and can be written as

$$i(t) = q\vec{v} \cdot \vec{E_w}, \tag{2.8}$$

where v is the velocity and E_w is the weighting field. The weighting field can be found by applying a unit potential to the electrode under consideration and zero potential to all other electrodes [29]. The current starts when the charge begins to move and stops when the charge has reached the electrode or has recombined.

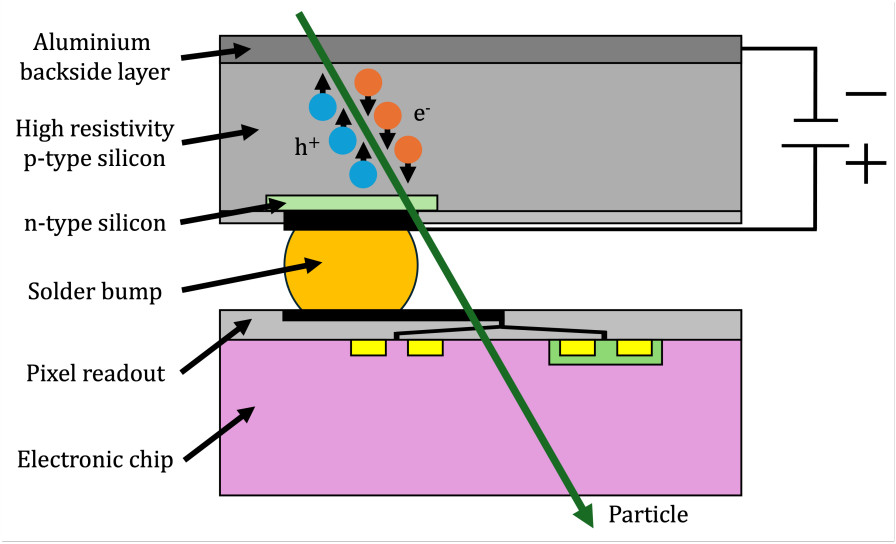


Figure 2.6: Schematic representation of a hybrid sensor with a particle passing through. The active high-resistivity silicon sensor is connected to the pixel readout on a separate electronic chip via a bump bond.

2.3 Silicon pixel sensor types

A silicon pixel detector is formed when a large number of p-n junctions are put next to each other into a two-dimensional grid. The collection of individual pixels is referred to as an *array* or a *matrix*. For particle physics applications, it is common for the signal to be read from each pixel separately. The two most common approaches for silicon pixel detector types are *hybrid sensors* with readout on a separate piece of silicon and *monolithic detectors* where the active detector area and the readout electronics are located on the same piece of silicon. As this thesis is concerned with hybrid and monolithic detectors, both types are briefly discussed here, and further information is included in the relevant chapters.

2.3.1 Hybrid pixel detectors

Hybrid pixel detectors consist of a *sensor* with an depletion region and the *front-end chip* (or ASIC, an application-specific integrated circuit) where the electronic signal is processed. The schematic of a hybrid sensor is shown in Figure 2.6. The two parts are fabricated on separate silicon wafers and then conductively connected pixel-by-pixel using *bump bonds*, typically with a diameter of a few tens of µm. The under-bump

metallisation (UBM) is applied to both silicon parts to achieve a better contact with the bump bond. The charge generated by the particle is moved through the bump bond into the ASIC, where the signal is shaped, compared to a threshold, and digitised. Wire bonds are usually used to transfer the digital signal from the readout chip to a printed circuit board.

The most significant disadvantage of the hybrid design is the high cost of the bump-bonding process. On the other hand, the technology copes well with high data rates and can withstand high radiation levels. Hybrid detectors are currently the basis of most tracking technologies in high-energy physics experiments such as those at the LHC [30, 31]. The LGAD devices presented in Chapter 3 are designed such that they can be assembled into a hybrid pixel detector.

2.3.2 Monolithic pixel detectors

The monolithic pixel detectors merge the active sensor part and the readout electronics into one piece of silicon. As the electrical connection between the two can be achieved easily, the expensive bump-bonding step is removed. The detectors are also known as *monolithic active pixel sensors* (MAPS) or CMOS (Complementary Metal-Oxide Semiconductor) sensors due to the type of fabrication technology.

Figure 2.7 shows a typical MAPS sensor with a small collection electrode. It consists of the n-well collection electrode within the p-type epitaxial layer surrounded by circuitry inside the p-well. A small depletion area is formed around the collection electrode where the generated charge is collected by drift. The charge from the undepleted region is collected by diffusion. The main advantage of the small electrode is a low sensor capacitance (a few femtofarads), which helps reduce noise and sensor power consumption [32]. Further discussion of monolithic pixel detectors is presented in Chapter 4, which focuses on the MALTA family of CMOS sensors.

2.4 Radiation damage

The silicon detectors often operate in an intense radiation environment, which degrades their performance over time. It is therefore imperative to understand the evolution

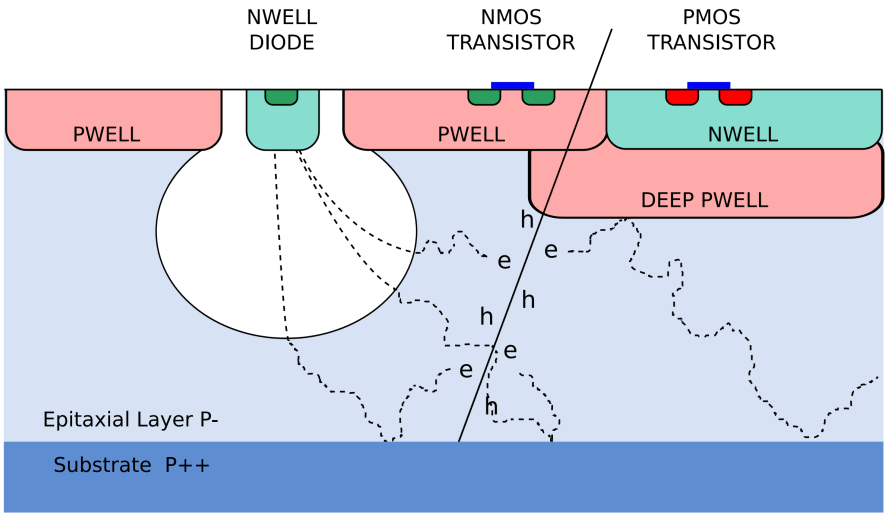


Figure 2.7: Schematic cross-section of a MAPS pixel in the imaging CMOS technology. The charge carriers generated by the crossing particle move slowly by diffusion in the undepleted region, but move faster via drift in the depleted region surrounding the the NWELL diode before being collected. Figure from [33].

of the sensor behaviour as it is exposed to radiation. The effect of radiation depends on the radiation type, the rate of exposure, and the detectors themselves. In general, however, the radiation damage can be divided into two types: TID (total ionising dose) and bulk damage.

2.4.1 TID damage

The TID damage affects primarily the front-end electronics and sensor surface, leading to component degradation or failure. The sensor's surface contains metal layers and a silicon dioxide dielectric layer between the metal and the silicon. Ionising radiation creates electron-hole pairs in the silicon dioxide (SiO_2). A fraction of the charge carriers that do not recombine can travel in the material. The electrons are collected quickly due to their high mobility, but the holes are more likely to get trapped along the boundary between the Si and SiO_2. As the holes accumulate, the total charge in the dielectric increases. This can impact the behaviour of the transistors used in the readout logic and increase the electronic noise. To reduce the effect of TID damage, several electronics design techniques can be applied [34]. For example, p+ guard rings can be used to isolate different silicon areas.

2.4.2 Bulk damage

The bulk damage encompasses different defects caused by particles traversing the material via non-ionising energy loss (NIEL). Interactions with the lattice may lead to permanent changes that can alter the performance of the device. In the path of the particle, individual atoms can be displaced, generating *point defects* (interaction energy >25 eV). The particle can displace an atom from its place in the lattice, creating an empty lattice position (*vacancy*) and a displaced atom (*interstitial*). Further interactions of the vacancies and interstitial can occur, such as when an atom of a different kind moves to a vacancy (*substitution*). At the end of the particle's path, where most of its energy is deposited, *cluster defects* are formed (interaction energy 2-12 keV).

The type of defects depends on the energy, dose, and type of radiation. However, an approximate NIEL scaling hypothesis can be used to convert the damage to that caused by 1 MeV neutrons per unit area (expressed in the units of 1 MeV $n_{eq}cm^{-2}$). The hardness factor κ is used such that the displacement damage of a particle fluence Φ can be expressed as the equivalent 1 MeV fluence Φ_{eq} as

$$\Phi_{eq} = \kappa\Phi. \tag{2.9}$$

The NIEL cross-section, also known as the displacement damage function D, has been fixed as 95 MeV mb for 1 MeV neutron equivalent. Using the NIEL scaling and the hardness factor, the displacement damage function can be calculated for various particles, as shown in Figure 2.8. The radiation-induced defects with energy levels in the silicon band gap impact the performance, causing three main effects – leakage current increase, effective doping changes, and charge trapping [35]. Figure 2.9 shows diagrams for the mechanisms behind the mentioned effects.

Leakage current

The leakage current increase is mostly caused by defect level states near the middle of the band gap. The increase has a detrimental effect on the detector performance as higher leakage current leads to an increase of noise and power consumption. The defect levels produce leakage current by transferring electrons from the valence to the

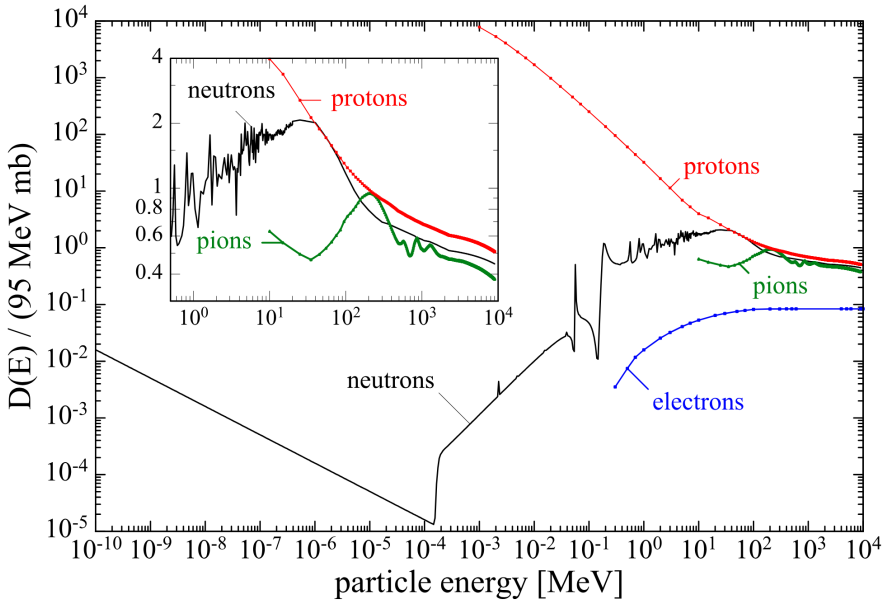


Figure 2.8: NIEL cross-section for different types of particles normalised to 95 MeV mb [35].

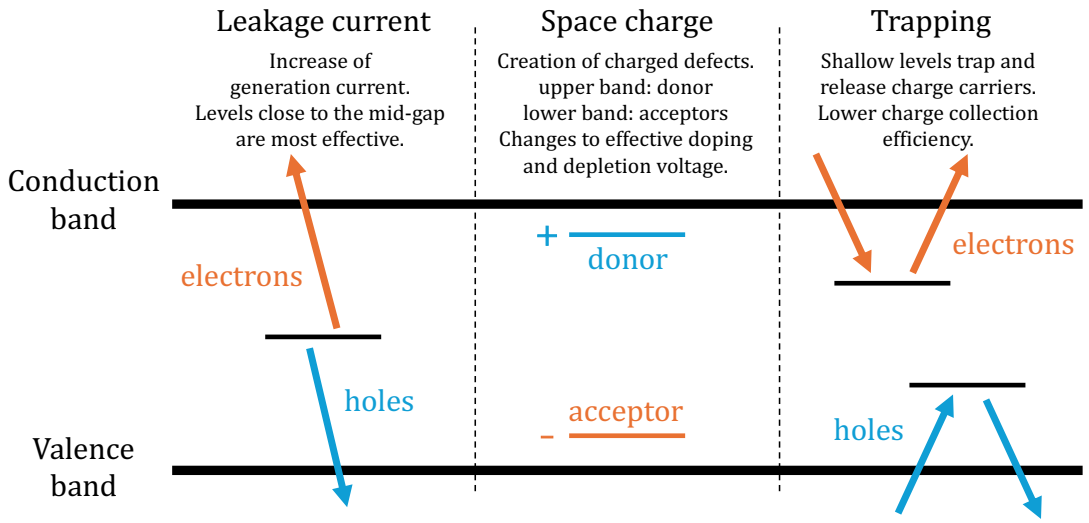


Figure 2.9: The device performance effects of the defect energy state creation.

conduction band. Experimentally, it has been observed that the increase in leakage current ΔI after radiation fluence Φ follows

$$\Delta I = \alpha \Phi V, \tag{2.10}$$

where V is the active volume of the detector and α is the proportionality factor known as the *current related damage factor* [36].

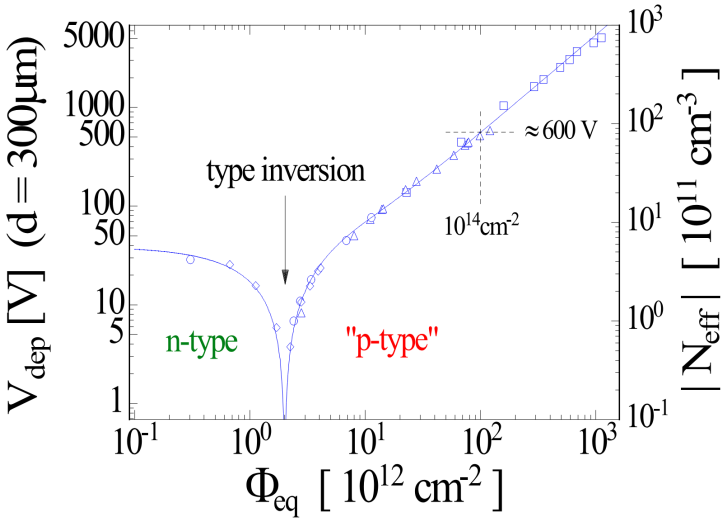


Figure 2.10: The depletion voltage as a function of received particle fluence for an n-type silicon detector. Figure from [35] with data from [38].

Effective doping

The radiation defects can act as donors, acceptors, or be neutral. Their behaviour affects the effective doping concentration of the silicon material, causing a shift in the depletion voltage - the amount of applied bias voltage required to achieve depletion through the whole of the semiconductor bulk. Higher operation voltages may have to be applied to avoid under-depletion and loss of active volume. As shown in Figure 2.10, after irradiation, previously n-type silicon can undergo type inversion and effectively become “p-type” [35]. Note that this does not imply that the n-dopants are removed from the silicon. Instead, the n-type dopants become inactive due to displacement, and additionally, new effectively p-type defect states are formed [37].

Trapping

Defects with energy levels close to either the conduction or the valence bands can capture the charge carriers via a process known as *trapping*. If the time after which the charges are released is longer than the signal acquisition time, the charge is lost, and the overall signal of the sensor is reduced. The reduction of the charge collection efficiency (CCE) due to trapping becomes the limiting factor for high-fluence applications [35]. To mitigate this issue, collecting electrons at the sensing electrodes can be advantageous due to their higher mobility compared to holes.

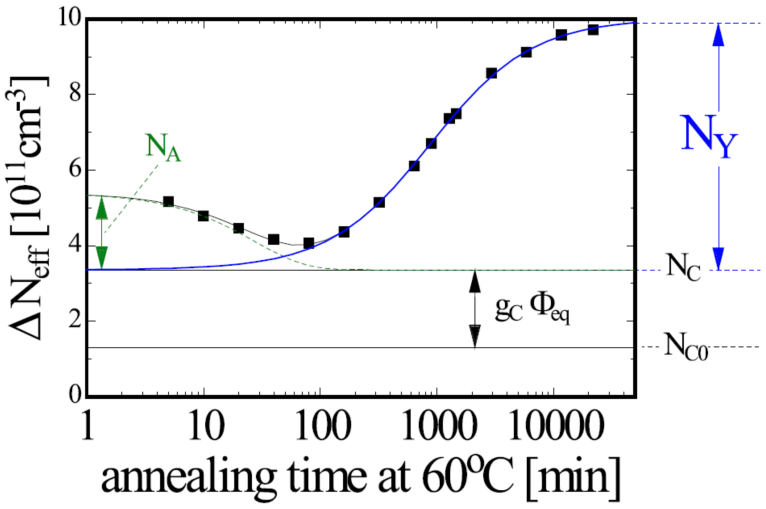


Figure 2.11: The change of the effective doping concentration as a function of annealing time at 60°C. The symbol g_C represents the introduction rate for the stable damage component. The investigated device is a PiN diode irradiated with a fluence of 1.4×10^{13} cm^{-2}. Figure from [35].

2.4.3 Annealing

The properties of irradiated silicon samples tend to evolve over time. A given defect can transform into a different kind of defect, or a lattice vacancy can recombine with an interstitial. This process is known as *annealing* [39]. As annealing is a thermal process, its rate can be accelerated at elevated temperatures and decelerated when going to lower temperatures [35]. Figure 2.11 shows an example of a typical annealing behaviour after irradiation. This measurement's annealing temperature is fixed at 60°C. Over a short period of time, the change of the effective doping concentration due to irradiation ΔN_{eff} decreases as defects can recombine. This effect is called *short-term* or *beneficial annealing* and may improve the detector performance. However, after a prolonged annealing period, previously inactive defects can interact and become active, causing a *reverse annealing* effect. The annealing time dependence of ΔN_{eff} can be parametrised as

$$\Delta N_{eff} = N_C + N_A(t) + N_Y(t), \tag{2.11}$$

where $N_C = g_C \Phi_{eq}$ is the stable damage component which does not change over time, N_A is the short-term annealing component, and N_Y is the reverse annealing component [35].

3 Development and Characterisation of Low Gain Avalanche Detectors

This chapter discusses the development and testing of the Low Gain Avalanche Detectors (LGADs). Section 3.1 introduces the LGAD technology and the ATLAS High Granularity Timing Detector project. Static characterisation results are outlined in Section 3.2, followed by hadron test beam results in Section 3.3. Sections 3.4 and 3.5 focus on testing the performance of neutron-irradiated LGAD devices with a probe station and a fast infra-red laser. Finally, inter-pad distance measurements for LGAD arrays are presented in Section 3.6.

3.1 Introduction

After the upgrade of the LHC to the High-Luminosity LHC, the average number of interactions per bunch crossing will increase from 47.7 (observed at the LHC during Run 3) to 150-200 when the HL-LHC is fully operational [13, 40]. The density of the primary proton-proton collisions will be such that the events will overlap in the interaction region at scales smaller than the spatial resolution of the current detectors [40]. While the ATLAS ITk vertex separation resolution along the beam direction remains relatively constant and small (<300 μm) for pseudorapidities $\eta < 1.5$, it increases rapidly with η, reaching several millimetres for $\eta > 2.5$ [41]. For low-momentum particles, in particular,

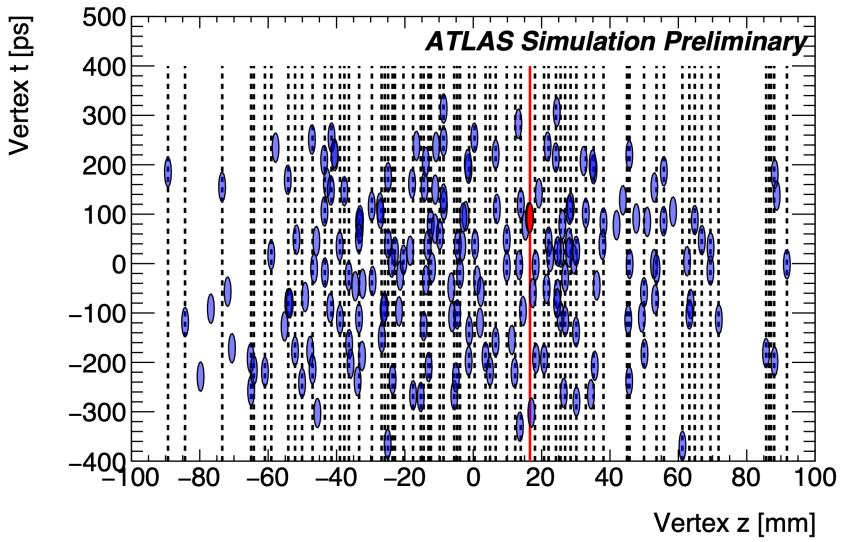


Figure 3.1: Visualisation of an event with a hard scatter (red ellipse) with 200 interactions (blue ellipses) superimposed in the z–t plane. The extent of each ellipse is 30 ps in time and 1 mm in z. The dashed vertical lines represent the positions of reconstructed vertices. From [41].

the precision of path reconstruction degrades in quality to the point where individual interactions may not be resolved.

A way of addressing this challenge is to use high-precision timing information to exploit the time spread of the collisions within each bunch crossing. An example illustrating the effect of timing is shown in Figure 3.1. The plot shows a single event with 200 interactions in the z–t plane [41]. The z plane is defined as in Section 1.2 and t represents time. The vertical dotted lines indicate the z position of the reconstructed primary vertices in the event. The red ellipse corresponds to the hard-scatter vertex. The tracker sees the event as a one-dimensional projection on the z axis, where a large number of tracks from vertices occurring at different times but very close in space leads to ambiguities in the track-to-vertex association. With the addition of the precise timing information with 30 ps resolution (the extent of each ellipse in t), ATLAS can view the event in two dimensions, making it possible to resolve the ambiguities of tracks belonging to different interactions [42, 43].

One of the ways a particle sensor can improve its timing performance is by increasing the signal-to-noise ratio while keeping the signal rise time short, hence minimising the effect of jitter and time walk. For these purposes, dedicated ultra-fast timing detectors with an intrinsic signal gain are under active development.

3.1.1 Improved timing via internal gain

In the presence of an electric field, free electrons gain kinetic energy as they are accelerated by the field. When an electron in the conduction band possesses enough kinetic energy to excite electron-hole pairs, it can pass some of its energy to the silicon lattice and create additional charge carriers. The process is referred to as the *impact ionisation*. The minimum necessary electric field to initiate the mechanism in silicon is approximately 300 kV/cm [44]. The newly generated charge carriers are accelerated by the electric field as well, and their collisions with the lattice produce more electron-hole pairs. As the process repeats itself, a large number of free charge carriers is generated. The ratio of the total number of collected charges to the initially generated charges (before charge multiplication via impact ionisation) is called *charge gain*.

Various designs of silicon detectors with internal multiplication are used in high-energy physics, including silicon photon multipliers (SiPM) with charge gain of the order 10^6 [45], avalanche photodiodes (APD) [46] with gain of few 100s and Low Gain Avalanche Detectors (LGADs) with gain of 10-30 [47].

3.1.2 Low Gain Avalanche Detectors (LGADs)

LGADs were developed and first manufactured at Centro Nacional de Microelectrónica (CNM) in Barcelona, Spain [47] with a number of groups producing them worldwide in the following years, including Hamamatsu Photonics (HPK), Fondazione Bruno Kessler (FBK), Brookhaven National Laboratory (BNL), Micron Semiconductor, and Teledyne e2v (Te2v). Introducing some modifications to the original design, LGADs found potential applications in various fields outside high-energy physics, including synchrotron applications [48] and proton therapy [49].

The LGAD design is based on a modified pn-junction featuring an additional highly doped p-type implant (p^+ gain layer) as shown in Figure 3.2. The high doping concentration near the junction creates a large electric field in a very localised region as a reverse bias is applied. The gain implant needs to be closely controlled to allow sensor operation at a high bias voltage without breakdown.

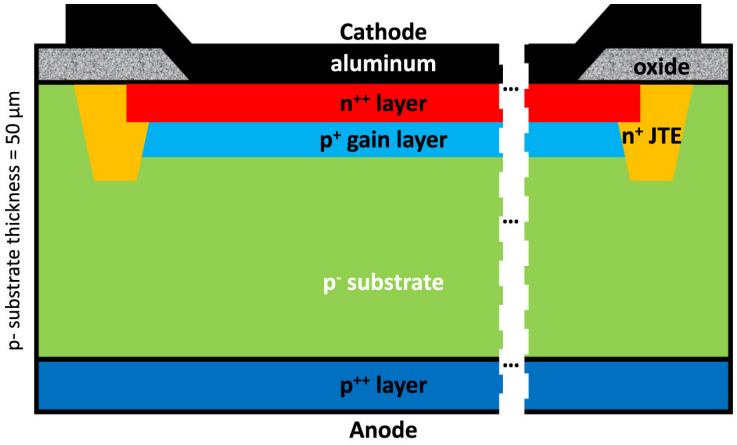


Figure 3.2: Diagram of a Low Gain Avalanche Detector. A highly p-doped gain layer (p^+) implanted near the junction creates a large electric field providing charge multiplication via impact ionisation. The superscript + sign denotes a higher concentration of doping atoms compared to the p-type substrate p^-. Analogously, the superscript ++ is used when referring to a higher doping level than the one present in p^- or p^+ layers. Figure from [50].

The addition of dopants into the silicon is an essential step during the manufacture of any semiconductor device. Doping is achieved by the process of ion implantation when atoms are introduced into the silicon lattice using a high-energy ion beam. Compared to diffusion, ion implantation exhibits far greater control of the doping profile within silicon. Most commonly, boron and phosphorus are used as p-type and n-type dopants, respectively. During the formation of the gain layer, its doping concentration and depth (the value at which the dopant concentration is greatest) are closely controlled. While the concentration is regulated by the implantation dose (ion beam current and total implantation time), the depth of the implant is controlled by the ion beam energy. Any small changes to the implant parameters can have large consequences for the device's performance. For LGADs, this can manifest as variations in the gain or the electrical properties, such as capacitance or leakage current.

The p^+ gain layer is implanted deeply into the bulk ($\sim$4 µm, depending on the dopant implantation energy) and has a peak doping concentration in the region of 1×10^{16} cm^{-3}. The charge gain of the device is strongly dependent on the doping profile of the gain layer [51]. For a peak doping concentration of the p-doped gain layer of 1×10^{16} cm^{-3}, a peak electric field in the range of 400 kV/cm can be expected at 300-400 V bias, enough to initiate impact ionisation [52]. The electric field increases

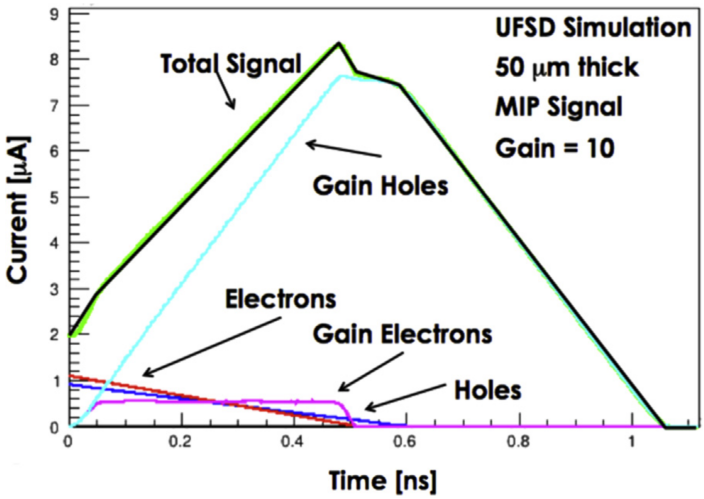


Figure 3.3: Simulated current signal from a minimum-ionising particle (MIP) passing through a 50 μm thick Ultra-Fast Silicon Detector (UFSD) with an n-in-p LGAD design. The charge gain of the device is close to 10. The total signal (black solid line) is broken down into the components due to the electrons and hole, both primary and gain (created via charge multiplication) [53].

further as a function of the boron implant dose. The n-type electrode n^{++} on top of the gain layer has a peak doping concentration in the region of 1×10^{19} cm^{-3} and has a shallow profile of $\sim$1 μm into the bulk. The bulk material p^{-} is high resistivity p-type silicon (5-10 kΩcm), corresponding to a doping concentration around 2×10^{12} cm^{-3}, with p^{++} anode contact on the backside.

In the presence of an external bias voltage, a depletion region is formed within the device, extending laterally from the junction as the reverse voltage is increased in magnitude. When a charged particle crosses the sensor, charge carriers are excited along its trajectory. In an n-in-p LGAD (with a p-type bulk and an n-type electrode on top as described above), the electrons are accelerated from the bulk towards the n^{++} cathode. A high electric field region is present at the boundary between the n^{++} and p implants, which causes impact ionisation as the primary electrons cross the region, generating gain electrons and gain holes. Since the multiplication only occurs near the n^{++} cathode, the gain electrons are collected quickly. As shown in Figure 3.3, the current increases as the electrons drift towards the cathode, hence the rise time of an LGAD is given by the electron's drift time. The gain holes then drift across the bulk before being collected by the anode. In an n-in-p LGAD, the gain hole current has the greatest contribution to the total current.

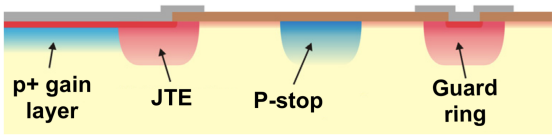


Figure 3.4: Diagram of the periphery structures of an n-in-p LGAD sensor. Figure from [54].

In the multiplication region, when the electric field surpasses a critical value, the junction breaks down. At the bias voltage when a breakdown occurs (breakdown voltage V_{bd}), the amount of current flowing through the junction rises exponentially, preventing the normal operation of the sensor. The breakdown voltage V_{bd} decreases with increasing active doping due to higher fields in the device at lower bias voltages. To prevent early breakdown, it is therefore important to control the field strength through an accurate doping profile and additional structures included in the detector design such as guard rings.

Periphery structures

Guard rings are placed at the edge of the LGAD sensors to reduce edge leakage currents, as shown in Figure 3.4. These structures, either left floating or at ground potential, grade the voltage from the sensor edge to the device cathode held at a virtual ground by the connected read-out electronics. Devices can also feature a multi-guard-ring layout. If the inner guard ring is left floating, the neighbouring devices will exhibit a higher leakage current.

Any edge effects can strongly influence the performance of the LGADs, leading to a high leakage current and a device breakdown. The gain layer edge region is particularly critical due to the increase of the electric field caused by the cylindrical curvature of the junction [52]. At the edges of the gain region, an additional n-doped region is introduced, known as the Junction Termination Extension (JTE) [55]. The JTE features an n-type implant which is diffused deeper into the bulk compared to the p-type multiplication layer. The structure decreases the maximum electric field in the edge regions, preventing early breakdown, as shown with the simulated IV curves in Figure 3.5. The simulation shows the breakdown voltage more than doubling with the introduction of the JTE structure.

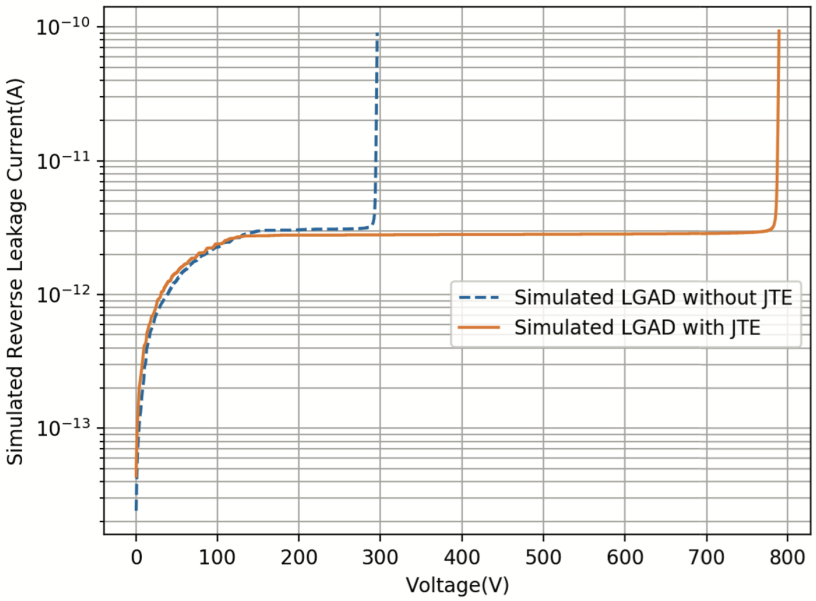


Figure 3.5: Simulated Reverse Leakage Current for LGAD devices with (solid orange) and without (dashed blue) the Junction Termination Extension (JTE) structure. The data shows a lower breakdown voltage if JTE is not included. Figure from [56].

When p-type bulk is present (such as in the case of n-in-p LGAD), a P-stop is used to isolate the cathodes of neighbouring devices, with peak doping concentration in the range 1×10^{15} to 10^{17} cm^{-3} and up to 4 µm deep. Without the structure, the inversion layer created by the positive charges at the Si-SiO_2 boundary would create a conductive path between n^{++} implants. Alternatively, a P-spray approach can be implemented by implanting a low-dose and low-energy boron blanket at the surface, avoiding the creation of the inversion layer. However, small variations in the P-spray implantation process can cause abnormal capacitance behaviour as reported by [54]. The P-stop implant is therefore the most effective solution for eliminating the surface current path.

3.1.3 Optimising the LGAD design for timing

While high-gain silicon devices such as SiPMs and APDs achieve much greater charge gain and can detect single/few photon events, high internal gain increases the dark count noise and leads to difficulties in sensor segmentation (producing pixelated sensors) [40]. To minimise noise and allow for thin sensors, the underlying idea of LGAD development for high energy physics is centred around producing sensors that have the lowest gain sufficient to perform accurate particle time measurements.

The thickness of the LGAD is strongly interlinked with the signal rise time, which should be minimised to achieve a better timing resolution. The current generated by the gain mechanism can be estimated from the number of electrons that enter the multiplication layer in a given time interval *dt*. If the electrons are drifting with velocity v_{sat}, the amount of generated gain charge carriers within *dt* is equal to

$$dN_{gain} \propto G\, n_{eh}\, v_{sat}\, dt, \tag{3.1}$$

where n_{eh} gives the number of e-h pairs per unit length (assuming uniform ionisation along the particle's path) for a device with gain G. Assuming a device with thickness d and a parallel plate geometry, Ramo's theorem (Equation 2.8) gives the current induced by the gain charge carriers as

$$\begin{aligned} dI_{gain} &= q v_{sat} \frac{1}{d} \times dN_{gain} \\ &\propto \frac{G}{d} dt \end{aligned}, \tag{3.2}$$

where q is the electron charge and other quantities are defined as before [28]. From Equation 3.2, the rate at which the current signal rises is then given by

$$\frac{dI_{gain}}{dt} \propto \frac{G}{d}. \tag{3.3}$$

Therefore, thin sensors produce signals with a faster rising edge, which improves their timing resolution by minimising jitter. On the other hand, if the sensors are too thin, not enough charge is generated by passing particles and the sensor has a large capacitance, which increases the noise. Experimental results and simulation suggest that an LGAD gain of about 20 and sensor thickness of around 50 µm provide optimum performance [40].

This thesis is mainly concerned with n-in-p LGADs. While p-in-n LGADs are also possible, in their case the multiplication process is initiated by the holes drifting towards the p++ electrode as the bulk and the gain implants are n-doped. As the impact ionisation coefficient is smaller for holes compared to electrons, the multiplication mechanism for holes requires a higher value of the electric field [57]. Due to higher fields, the p-in-n design is less stable and prone to earlier breakdown. Additionally, since the holes' drift velocity is lower, the signal rise time is longer, degrading the timing performance of the devices.

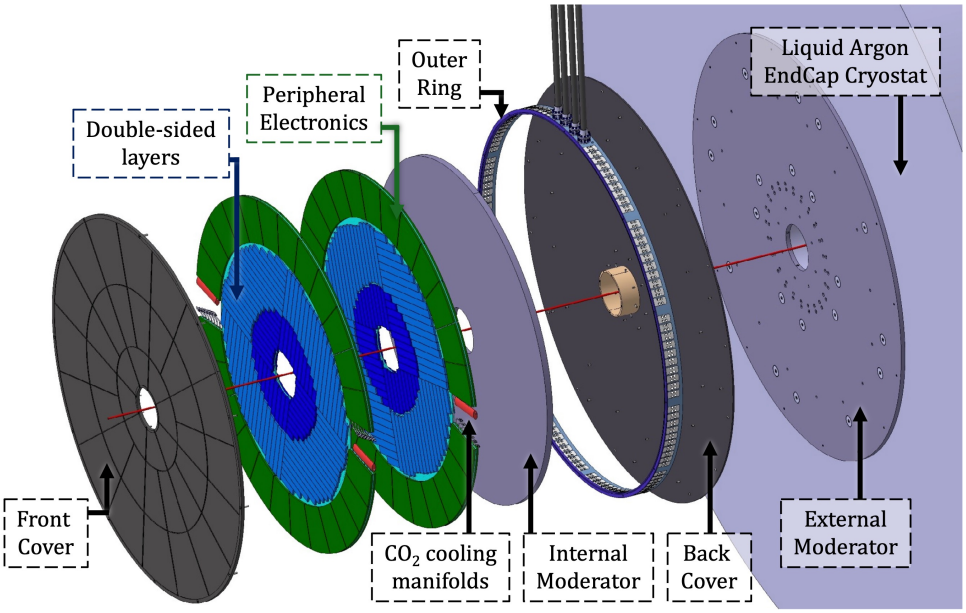


Figure 3.6: Global view of the HGTD to be installed on each of two end-cap calorimeters. The various components are shown: hermetic vessel (front and back covers), two instrumented double-sided layers (mounted in two cooling disks with sensors on the front and back of each disk), two moderator pieces placed inside and outside the hermetic vessel. Figure from [58].

3.1.4 The High Granularity Timing Detector

Based on the LGAD sensor technology, the ATLAS collaboration is building the High Granularity Timing Detector (HGTD), consisting of two hermetic vessels, each one with two double-sided layers of LGAD sensors mounted on two support disks that also provide cooling. Figure 3.6 shows a diagram of one of the vessels of the detector with its components. Given that each layer is double-sided, there are four layers of LGADs per vessel. The HGTD will be located just outside the ITk, in front of the liquid argon end-cap calorimeters, covering the pseudorapidity region between 2.4 and 4.0, with a distance of approximately 3.5 metres from the nominal interaction point along the beam axis [41]. The detector will measure the times of arrival of particles with an average timing resolution of approximately 30 ps per track (45 ps per hit) at the beginning of operation. Towards the end of the operation, the resolution degrades to 50 ps per track (65 ps per hit) due to radiation damage to the detector.

The design uses LGAD sensors segmented into 15×15 pad (electrode) arrays with an active thickness of 50 μm, with a total active area per sensor of 19.5×19.5 mm^2. Two LGAD sensors will form one module read out by two separate ASICs. The modules

Table 3.1: Specifications of the LGAD sensors by HGTD

Parameter	**Value**
Pad size	1.3×1.3 mm^2
Pad array	15×15
Substrate	p-type
Thickness (D) active/total	50±5 µm / 300±30 µm
Timing resolution	∼35 ps
Charge collection	>15 fC
Passivation thickness	between 0.8 µm and 5 µm
Target pad capacitance	<4.5 pF
Gain layer depletion (V_{gl})	24 V < V_{gl} < 55 V
Full depletion (V_{fd})	<70 V
Breakdown voltage (V_{bd})	(V_{bd}-V_{gl})/D > 0.7/µm (-30°C)
Breakdown condition	>200 nA/pad (-30°C)
Device leakage current	< 2 µA/cm^2
Pad leakage current	< 200 nA/cm^2
Inter-pad gap (IP)	40 µm < IP < 100 µm

are arranged into three rings (inner, middle, and outer), with each ring exposed to a different radiation level based on their distance from the nominal interaction point [41].

As the HGTD consists of a total of 8032 modules, with those close to the beamline due to be replaced during the lifetime of the detector, CERN has invited several device manufacturers to bid to supply the sensors to facilitate their manufacture and delivery. A Market Survey published by the HGTD collaboration ensures that all manufacturers who want to bid to supply devices for the detector meet electrical and performance requirements [59]. The specifications are listed in Table 3.1.

3.1.5 LGAD fabrication by Te2v

Teledyne e2v (Te2v) [60] in collaboration with the University of Oxford, the University of Birmingham, the Open University, and the Rutherford Appleton Laboratory manufactured LGAD sensors targeting sensor specifications for the ATLAS High Granularity Timing Detector. As part of the first production of LGADs by Te2v - referred to as *Batch 1*, 21 6-inch wafers were produced on high resistivity silicon substrate (>1500 Ωcm), with an active epitaxial thickness of 50 µm. In order to test a variety of gain layer implants, 8 different combinations of gain layer (GL) implant dose and energy were used during the production (a particular combination referred to as a *split*), with

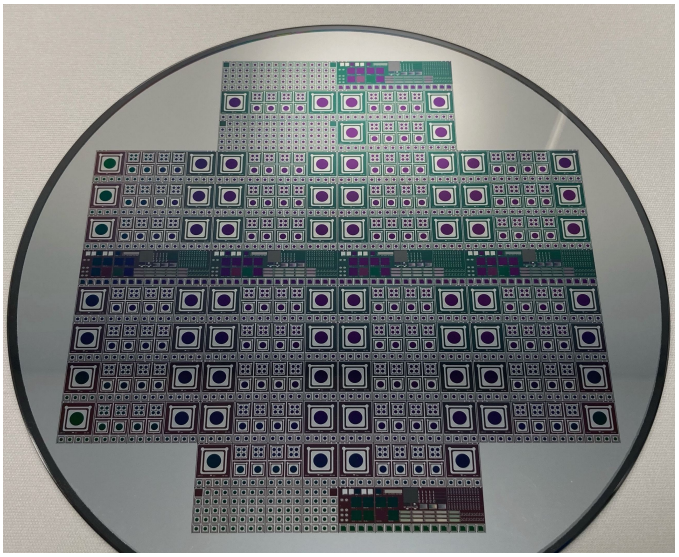


Figure 3.7: Layout of LGAD wafer from production *Batch 1*. The devices are manufactured on a 6-inch silicon wafer.

two or three wafers produced using the same split. The layout of the LGAD wafer from *Batch 1* is shown in Figure 3.7.

The exact doping parameters for the gain layer energy and dose are part of a proprietary process and kept secret by the manufacturer. Hence, all values presented in this thesis are quoted in relation to the reference wafer W21, designated as GL doping *Low* and GL energy *Low*. A full list of produced wafers within the split with corresponding GL doping and GL energy normalised to the reference wafer is shown in Table 3.2.

Apart from a small number of fields for test structures, each wafer from *Batch 1* contains 33 fields with LGAD and PiN devices. Each field is separated in two halves, with LGADs on the left-hand side and PiNs on the right, as shown in Figure 3.8. The PiN diodes are manufactured to be identical to the LGADs but lack the gain layer for charge multiplication, allowing for a direct comparison between the two device types. A lowercase 'i' is used in 'PiN' to distinguish it from a 'PIN' diode, which also features an intrinsic semiconductor region.

Each field contains LGADs of cathode size 4×4 mm^2, 2×2 mm^2 (of two variants - A and B), 1×1 mm^2 (of four variants - A, B, C, and D - two devices per variant) and two 2×2 arrays of 1×1 mm^2 devices (of two variants - A and B). The variants only differ in terms of the distance between the guard ring and the cathode, which does not affect

Table 3.2: Wafers manufactured as part of Batch 1 of LGAD production sorted into eight splits. Each split features a unique combination of gain layer (GL) implant energy and dose. Values are normalised to that of the reference wafer W21. GL implant energies are grouped into *Low*, *Medium*, and *High*. GL implant doses are grouped into *Very Low*, *Low*, *High*, and *Very High*. Reference wafer W21 has attribute *Low* for both GL implant properties.

Split	Wafers	GL implant energy	GL implant dose
F	W19, W20, W21	1.00 / *Low*	1.00 / *Low*
C	W17, W18	1.00 / *Low*	1.07 / *High*
D	W15, W16	1.05 / *Medium*	0.92 / *Very Low*
G	W12, W13, W14	1.05 / *Medium*	1.00 / *Low*
B	W09, W10, W11	1.05 / *Medium*	1.07 / *High*
E	W07, W08	1.05 / *Medium*	1.15 / *Very High*
H	W04, W05, W06	1.11 / *High*	1.00 / *Low*
A	W02, W03, W24	1.11 / *High*	1.07 / *High*

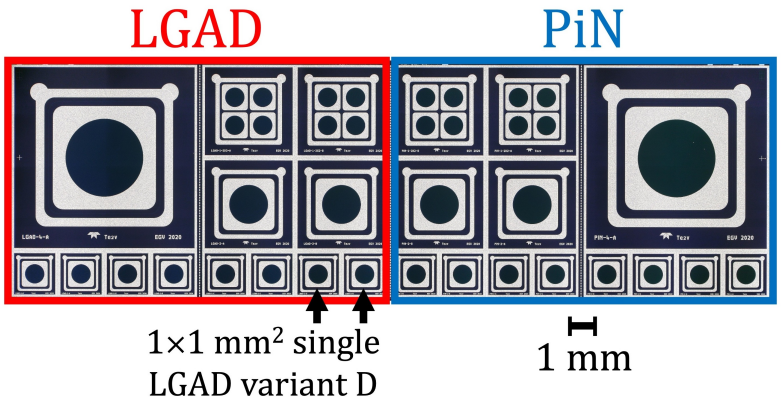


Figure 3.8: Detail of devices within one field of LGAD wafer from *Batch 1*.

the avalanche process. The quoted cathode size is measured from the outer edge of the JTE structure on one side to the outer edge of the JTE structure on the other side of the device. The thickness of the JTE for devices from *Batch 1* is 15 µm.

Individual devices feature a metal aperture with a diameter of roughly 75% of the cathode size, centred at the middle of the device. For the 1×1 mm^2 device, the metal aperture has a diameter of 755 µm. The aperture allows for the injection of laser light, as otherwise, photons would be reflected by the metal layer and hence would not reach the active silicon volume. Often, LGAD devices are fully metallised to allow for faster signal propagation. In the absence of a metal layer, the signal propagates to the readout electronics through the n^{++} electrode, introducing a non-zero delay due to its resistivity. The introduced delay (approx. 0.5 ps/µm) can spoil the timing resolution of the device [57].

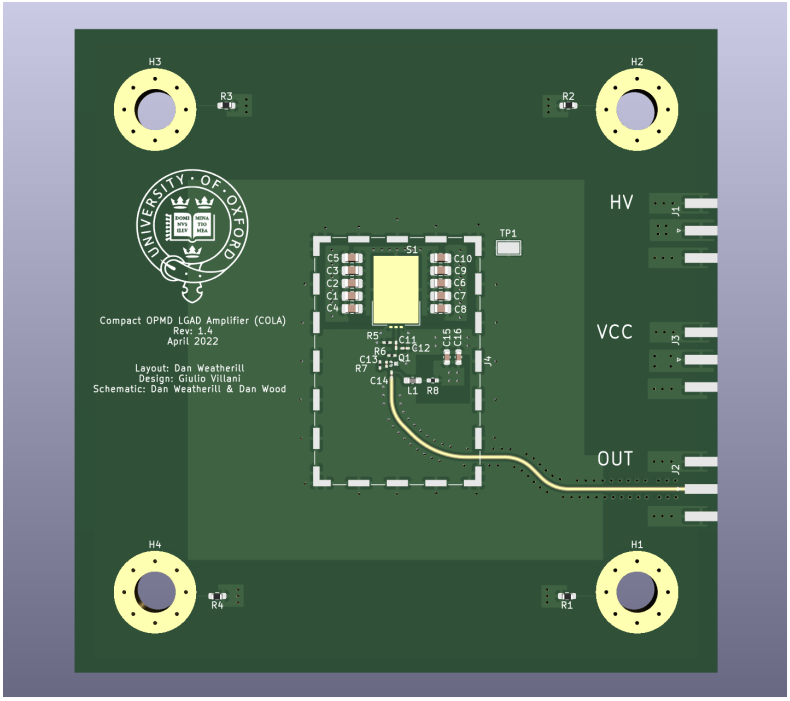


Figure 3.9: 3D models of the COLA readout board - version 1.4.

3.1.6 Compact OPMD LGAD Amplifier (COLA) readout board

The accurate matching of the LGAD sensor to the read-out electronics is essential to obtain a good timing resolution. Therefore, minimising the jitter contribution of the electronics is one of the key objectives for the LGAD readout systems. Driven by the advances of the LGAD technology, a dedicated ASIC ALTIROC is in development for the HGTD, reaching jitter lower than 30 ps for pad capacitance in the range of 2-6 pF [61]. As the ALTIROC is optimised for arrays of 1.3×1.3 mm^2 LGAD devices bump bonded to the ASIC, several simpler read-out boards for device testing purposes have been developed by the University of California in Santa Cruz (UCSC) [62], the High Energy Accelerator Research Organization in Japan (KEK) [63], the Fermi National Accelerator Laboratory (Fermilab) [64], and the University of Oxford, amongst others. These boards offer a fully analogue readout from a single wire-bonded device (single-channel) or an array of a few devices (multi-channel) – nominally up to 16 channels.

The Oxford Physics Microstructure Detector (OPMD) laboratory at the University of Oxford developed the Compact OPMD LGAD Amplifier (COLA) family to provide high-bandwidth analogue readout for LGAD devices. The results presented in this

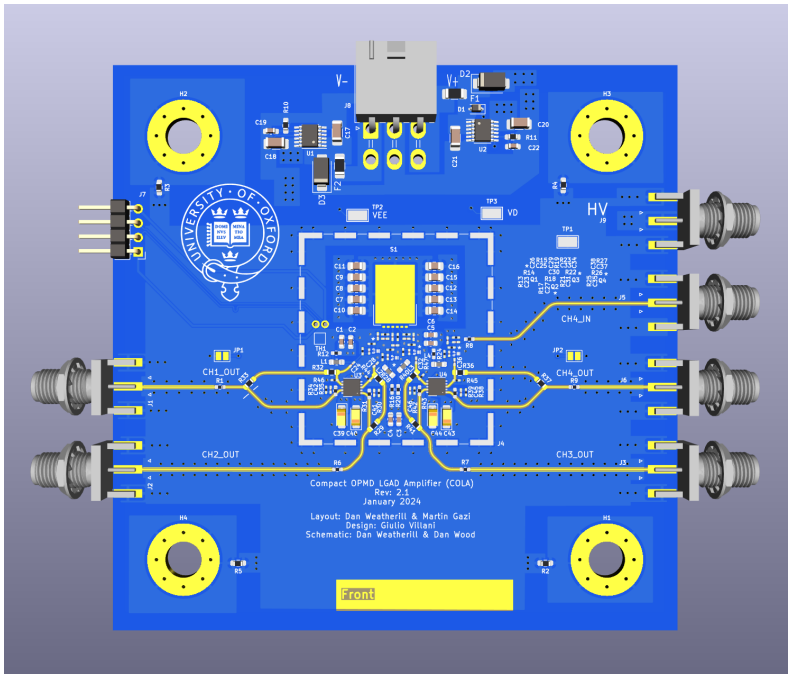


Figure 3.10: 3D models of the COLA readout board - version 2.1.

thesis are primarily obtained using the COLA family of readout boards. The COLA v1.4 (shown in Figure 3.9), utilising a bipolar transistor BFR840L3 by Infineon [65], provides a transimpedance gain of 316 V/A with a 1.5 GHz bandwidth. The board can accommodate a single LGAD device, which is wire-bonded to the electronics. While performing measurements, the signal output of the readout board is often further amplified with an external voltage amplifier before being processed by an oscilloscope. Further amplification is discussed later in the relevant sections of the thesis.

Building on top of the COLA v1.4 single-stage amplification, the COLA v2.1 (shown in Figure 3.10) was developed, allowing for a readout of up to three LGAD devices. The new design couples the standard transimpedance amplification stage from v1.4 with a second stage 30 dB voltage amplifier based on an LTC6269 operational amplifier by Analog Devices [66]. Figure 3.11 shows the schematics for the transimpedance amplification stage common to both COLA v1.4 and v2.1, and Figure 3.12 shows the second-stage voltage amplifier featured on COLA v2.1. In addition to allowing for a simultaneous readout from a few LGAD devices, the v2.1 design eliminated the need for additional amplification, allowing for the signal from the readout board to be directly recorded by an oscilloscope.

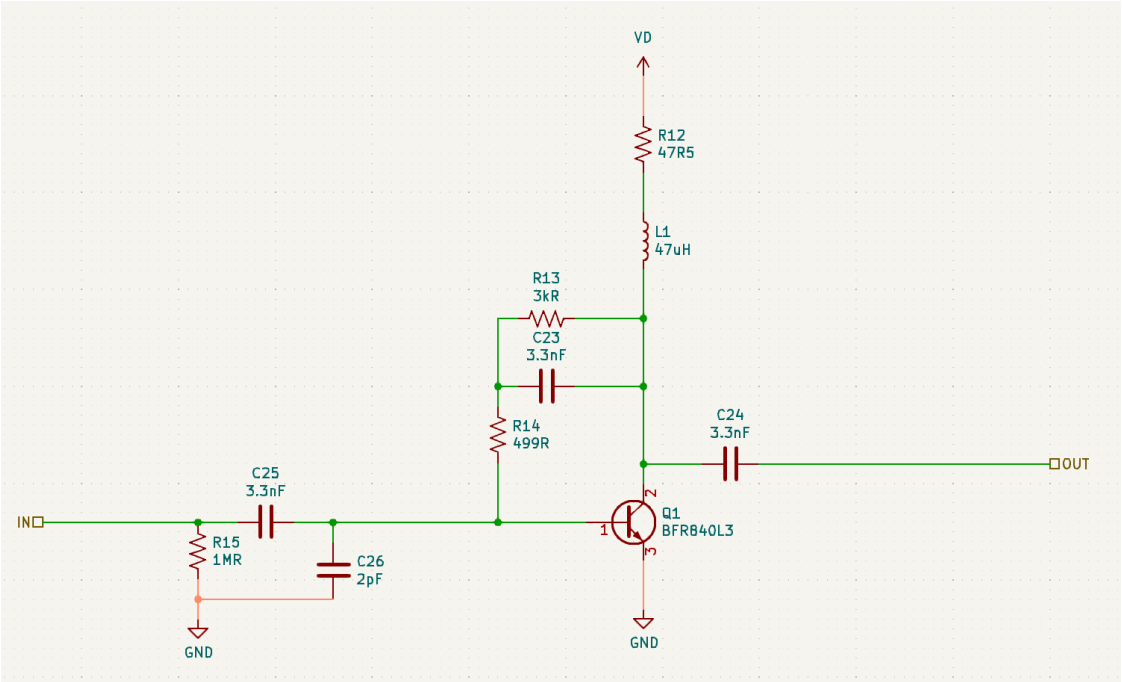


Figure 3.11: Schematics of the transimpendance amplifier used by the COLA readout board family. This stage is used by both COLA v1.4 and COLA v2.1. The input is directly connected to the cathode of the LGAD device.

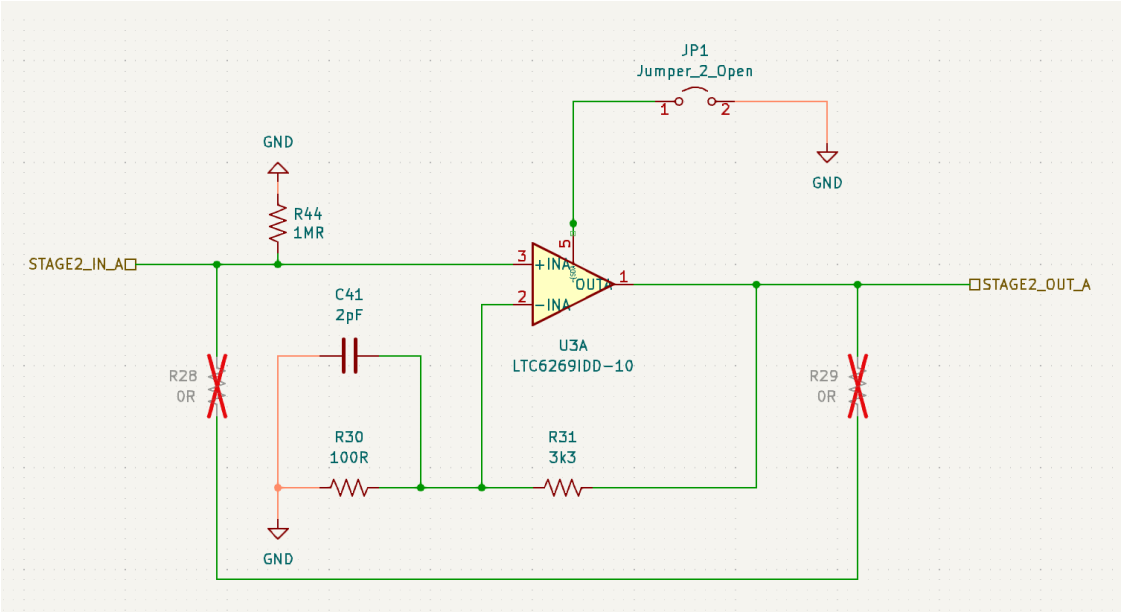


Figure 3.12: Schematics of the voltage amplifier implemented on COLA v2.1 readout board. The output from the transimpedance amplifier is used as the input for the voltage amplifier. The 0 Ω resistors R28 and R29 are not placed by default and are only used to bypass the voltage amplification stage if desired. By closing the jumper JP1 connection, the operational amplifier can be shut down if signal bypass via 0 Ω resistors is implemented.

3.2 Static characterisation of non-irradiated LGADs

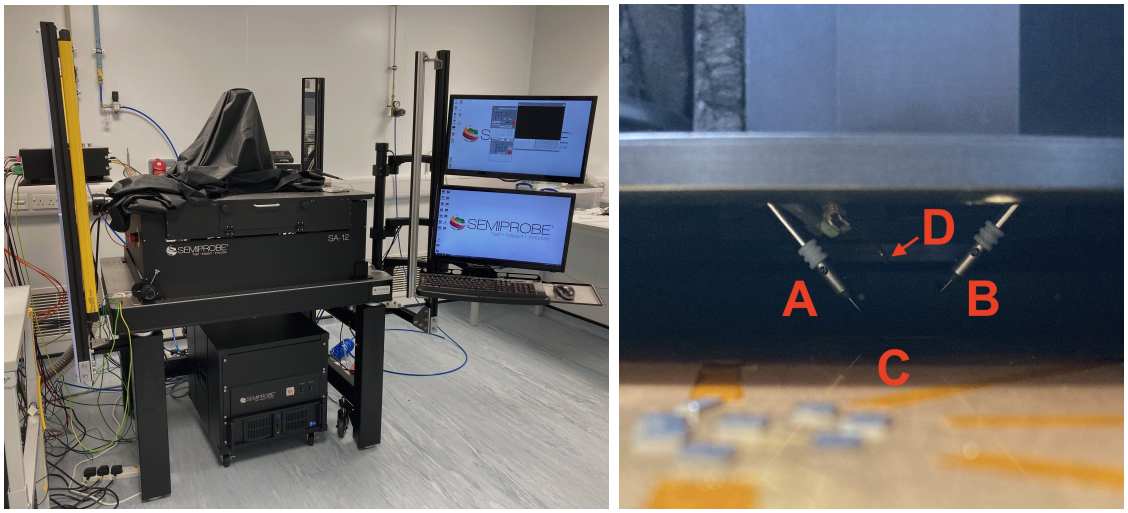
In order to understand the behaviour of silicon detectors, it is crucial to perform an accurate electronic characterisation of the devices [57]. The two essential measurements are capacitance as a function of applied bias voltage (CV) and monitoring current flowing through the device as a function of applied bias (IV). These measurements determine the leakage current, the breakdown voltage, the gain layer depletion voltage, and the full depletion voltage of the device under test. If the tested device is not exposed to any particles while under investigation, these measurements are considered to be *static*.

The presented characterisation of LGADs was undertaken within the framework of comparing their performance with the requirements for the supply of LGADs for the High Granularity Timing Detectors (HGTD). References to specific performance and design requirements as outlined in the HGTD Technical Specification [58] are given throughout this chapter when relevant.

3.2.1 Measurement procedure

The static characterisation of non-irradiated devices described in this chapter was carried out at the OPMD laboratory using a Keithley SCS 4200 parameter analyser [67] integrated with a probe station SemiProbe SA-12 [68] as shown in Figure 3.13a. The probe station is located in an ISO 5 Class cleanroom with well-controlled temperature and humidity conditions (nominally 20°C and ∼40% RH). The probe station has an enclosure with a dry-air supply, such that the humidity around the detector volume can be lowered below the room air humidity. The device's temperature can be controlled by cooling or heating the chuck using an external heater-chiller.

The device under test (DUT) is placed on a gold conductive chuck, which provides electrical contact with the backside of the DUT. The chuck can freely move in all dimensions to position the device in the desired location. Contact with the pad (electrode) metallisation is established using a probe needle connected to a High-Voltage Source Monitor Unit (HV-SMU) as depicted in Figure 3.13b.



(a) **(b)**

Figure 3.13: (a) Probe station SemiProbe SA-12 in an ISO 5 Class cleanroom in the OPMD laboratory used for static electrical characterisation of devices. (b) Electrical contacts and monitoring inside the probe station - **A** and **B** are probe needles, **C** is the chuck, and **D** is the temperature and humidity sensor.

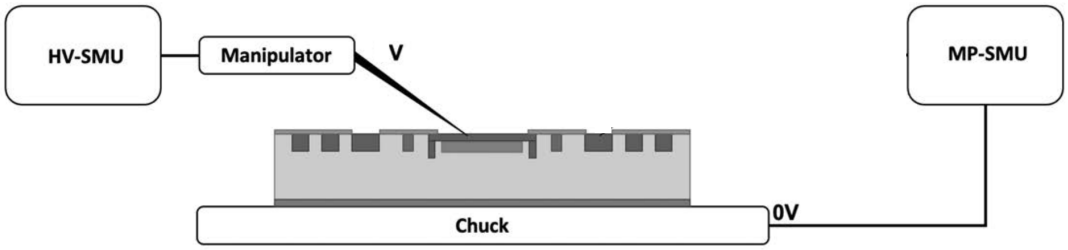


Figure 3.14: Schematic representation of a probe station configured for current-voltage measurements in the Needle-Bias configuration. The probe needle in contact with the device's top side is biased to a positive bias voltage, while the chuck in the electrical contact with the backside of the device is held at 0 V. The guard ring is left unbiased (floating). Figure from [57], modified.

A schematic representation of the setup is shown in Figure 3.14 for the Needle-Bias configuration, where the chuck is held at 0 V (ground potential) via the Medium-Power Source Monitor Unit (MP-SMU), while the metallisation layer of the device is biased using a HV-SMU. In the setup, a Keithley SMU 2650 unit [69] acts as both SMUs, simultaneously providing biasing and current measurement. In this configuration, the guard ring of the device (GR) is left floating.

3.2.2 Capacitance measurements

Investigating the device capacitance is a vital part of the characterisation and qualification of semiconductor structures. In the case of LGADs, changes in capacitance as a function of applied bias voltage (CV) provide information regarding the gain layer implant. The CV measurement uses a probe AC-signal at a fixed frequency f superimposed with the DC voltage providing sensor biasing. The frequency f used in this investigation is fixed at 100 kHz. For non-irradiated LGADs, frequencies $f >$ 100 kHz are not recommended due to observations of capacitance decrease due to the shunting of the AC signal frequency to the ground before the full sensor volume can be explored [57]. For irradiated devices, the decrease of capacitance is already observed at frequencies of a few kHz.

In order to study electrical devices, an equivalent circuit is often considered to simplify calculations while capturing the essential aspects of the given device. A silicon sensor with parallel plate geometry, such as the LGADs under investigation, can be modelled as a parallel capacitor-resistor C_p-R_p system. In this case, the capacitance C_p can be obtained from the imaginary part of the sensor admittance Y (the inverse of impedance Z)

$$Y = \frac{1}{Z} = \frac{1}{R_p} + j2\pi f C_p, \tag{3.4}$$

where f denotes the frequency of the probe AC-signal [57]. Alternatively, a capacitor and a resistor are modelled in series C_s-R_s. The capacitance is obtained from the imaginary part of the impedance Z as

$$Z = R_s + j\frac{1}{2\pi f C_s}. \tag{3.5}$$

Both parallel and series models are suitable for non-irradiated sensors, as the leakage current of the devices is low. This condition ensures that the conductivity of the device is low, such that the admittance Y in Equation 3.4 and impedance Z in Equation 3.5 are given predominantly by the capacitance term. However, given that the effect of the leakage current cannot be neglected after irradiation, the C_s-R_s model is only suitable for non-irradiated devices [57]. In this investigation, the C_p-R_p model is used.

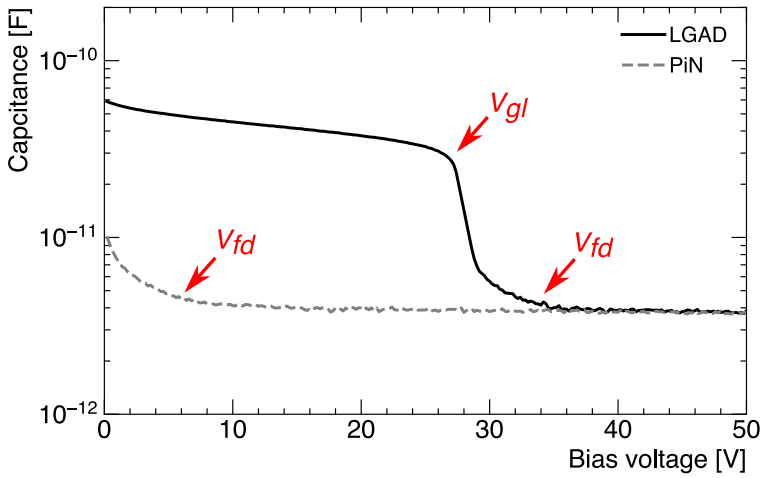


Figure 3.15: An example comparison between the capacitance-voltage curves of a 1×1 mm^2 LGAD device and a PiN device, both produced by Te2v. The approximate positions of the gain layer depletion voltage V_{gl} and full depletion voltage V_{fd} are marked. Measurements were performed at AC signal frequency of 100 kHz.

3.2.2.1 Gain layer depletion and full depletion voltage extraction

The typical capacitance of 1×1 mm^2 LGAD and PiN devices is shown in Figure 3.15. The capacitance of an LGAD decreases substantially after the *gain layer depletion voltage* V_{gl} is reached. V_{gl} is an important quantity for LGADs, as it relates to three device parameters: the amount of dopant N_A, the gain layer implant width w, and gain implant depth d via [57]

$$V_{gl} \propto \left(1 + 2\frac{d}{w}\right) N_A w^2. \tag{3.6}$$

After the capacitance drop, when applied bias voltage V_{fd} is sufficient to fully deplete the sensor, a low capacitance value is reached. The value of capacitance then does not change with a further increase of bias voltage - the capacitance becomes constant. V_{fd} is known as the *full depletion voltage*.

Fitting procedure

The V_{gl} and V_{fd} values are extracted from a $1/C^2$–V curve. An example fit for an LGAD from wafer W07 is shown in Figure 3.16. The value of V_{gl} is defined as the crossing point of the flat initial part and the linear rise of the $1/C^2$ curve (corresponding to a decrease

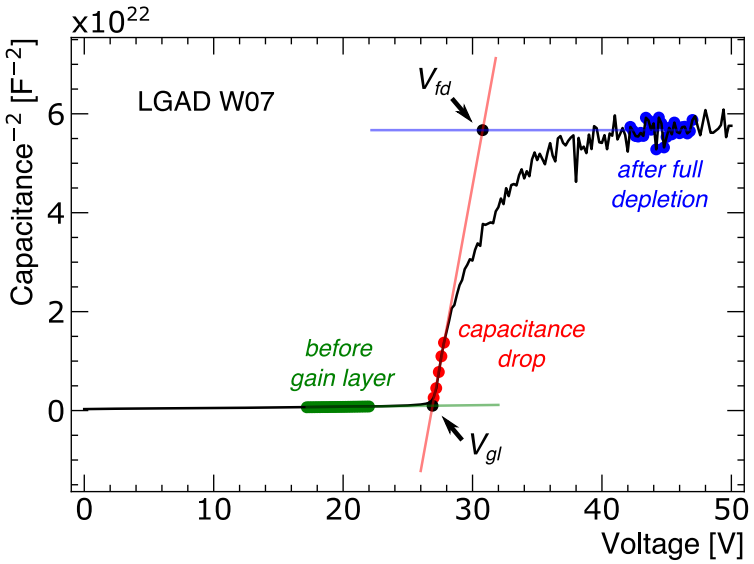


Figure 3.16: $1/C^2$ curve of a 1×1 mm^2 LGAD from wafer W07 as a function of applied bias voltage V measured at 100 kHz. Red points show the capacitance drop region with the red line as the linear fit. Green and blue points denote the regions before gain layer depletion and after full depletion, respectively. The intersections of the linear fit lines mark the points of the extracted gain layer depletion voltage V_{gl} and full depletion voltage V_{fd}.

Table 3.3: Extent of regions of interest for CV curve analysis. V_{guess} is defined as the voltage at which the slope of the capacitance-voltage curve is most negative.

Region	**starts from**	**ends at**
before gain layer	$V_{guess} - 10$ V	$V_{guess} - 5$ V
capacitance drop region	$V_{guess} - 0.2$ V	$V_{guess} + 0.8$ V
after full depletion	$V_{guess} + 15$ V	$V_{guess} + 20$ V

of capacitance). Similarly, the value of V_{fd} is defined as the crossing point of the linear rise of $1/C^2$ and the saturated value for voltages above full depletion.

The fitting algorithm identifies the voltage at which the numerical derivative of the capacitance-voltage relationship (dC/dV) is most negative, corresponding to the sharpest drop of capacitance with respect to the voltage change, referred to as V_{guess}. Using the initial guess V_{guess}, the ranges [$V_{guess} - 10$ V, $V_{guess} - 5$ V] and [$V_{guess} + 15$ V, $V_{guess} + 20$ V] are used to define the regions before gain layer depletion and after full depletion, respectively. Linear fits for $1/C^2$ are performed within each region. For the purpose of the analysis, the capacitance drop region is defined as [$V_{guess} - 0.2$ V, $V_{guess} + 0.8$ V]. The extents of the regions of interest are summarised in Table 3.3.

3.2.2.2 Wafer comparison results

According to the HGTD Technical Specifications [58], non-irradiated LGADs are required to demonstrate a gain layer depletion voltage within the range 24 V < V_{gl} < 55 V. Additionally, the full depletion voltage must not exceed 70 V. To ensure consistency between manufactured devices, the specifications also limit acceptable variation in electrical properties between different sensors - gain layer depletion voltage within $\pm$1% from the average $< V_{gl} >$, and full depletion within $\pm$10% from the average $< V_{fd} >$.

To assess the uniformity across a given wafer and the differences between wafers, CV measurements were performed on LGAD devices from 5 fields per wafer. Within each field, two 1×1 mm^2 single devices of variant D (as described in Section 3.1.5) were measured for wafers W05, W07, W12, W14, and W17, resulting in 10 measurements per wafer. For wafers W02 and W10, only measurements from one LGAD device of variant D per field are available, with a total of 5 measurements per wafer.

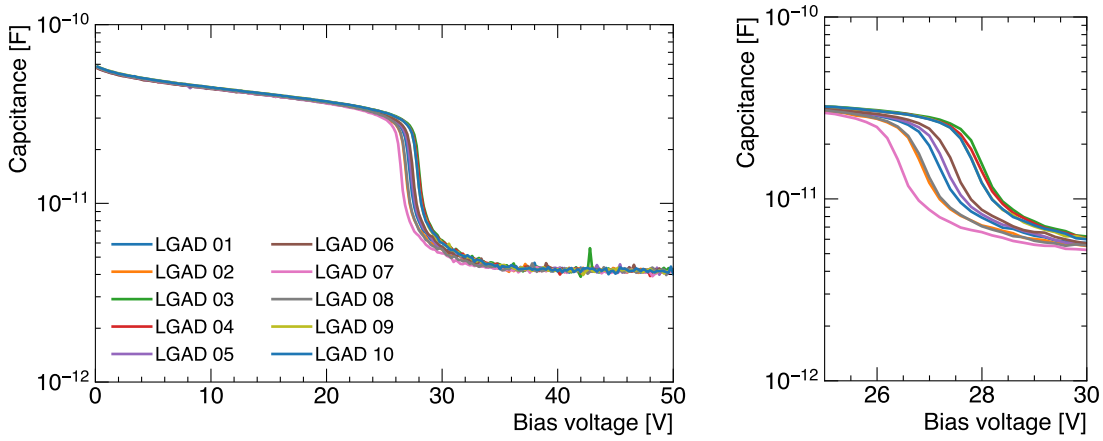
CV uniformity across a wafer

To illustrate the uniformity across a wafer, CV curves obtained for wafer W07 are shown in Figure 3.17. For wafer W07, the extraction of V_{gl} yielded an average value of 27.1 V with a standard deviation of 0.5 V. All extracted values are within 3.5% of the mean V_{gl} for wafer W07. This variation is larger than the maximum tolerable difference of $\pm$1%. The V_{fd} has a mean of 31.0 V with a standard deviation of 0.5 V. The maximum variation of a V_{fd} measurement was 2.6% from the mean W07 value - within the accepted $\pm$10% range.

CV variation between wafers

The V_{gl} and V_{fd} results across all wafers are reported in Table 3.4. The average V_{gl} as a function of implant dose and implant energy is visualised in Figure 3.18. The variation from the wafer mean for individual devices is shown in Figure 3.19, both as the absolute and percentage deviations. Similarly, the average V_{fd} and its variation across the samples are shown in Figures 3.20 and Figures 3.21, respectively.

Only wafers W07, W02, and W10 have average V_{gl} above the required 24 V. Hence, gain layer implant energy above 1.06 and gain layer implant dose above 1.07 (both



(a) Full measured range **(b)** Zoom

Figure 3.17: Capacitance as a function of bias voltage for ten 1×1 mm^2 LGAD devices from five different fields on wafer W07. (a) Full measured range. (b) Zoomed range between 25-30 V. The capacitance is measured at a frequency of 100 kHz with a 0.2 V step between measurements.

Table 3.4: Average gain layer depletion voltage V_{gl} and full depletion V_{fd} per given LGAD wafer. The table shows the calculated standard deviation of the tested sample (st dev) and the maximum percentage deviation of a device from the mean wafer value (max dev).

Wafer	$< V_{gl} >$	**st dev**	**max dev**	$< V_{fd} >$	**st dev**	**max dev**
W21	20.8 V	0.1 V	0.8%	22.8 V	0.3 V	1.5%
W17	22.6 V	0.5 V	2.9%	26.5 V	0.8 V	5.4%
W14	22.1 V	0.6 V	3.8%	26.0 V	0.6 V	3.3%
W12	21.6 V	0.5 V	3.1%	25.1 V	0.6 V	2.8%
W10	24.5 V	0.6 V	3.6%	28.7 V	0.5 V	3.0%
W07	27.1 V	0.5 V	3.5%	31.0 V	0.5 V	2.6%
W05	23.9 V	0.6 V	4.1%	27.7 V	0.6 V	2.9%
W02	27.4 V	0.8 V	4.0%	31.8 V	0.7 V	3.4%

relative to W21) are needed in order to meet the V_{gl} criterion. It should be noted, however, that some individual LGADs from W10 have gain layer depletion voltage less than 24 V. As the average V_{gl} rises with both gain layer implant dose and implant energy, combining the implant dose of W07 (*Very High*, 1.15 a.u.) and implant energy of W02 (*High*, 1.11 a.u.) should yield devices with average V_{gl} close to 30 V.

The variation of V_{gl} of individual devices from the wafer mean, as shown in Figure 3.19, indicates that out of the studied wafers, only those from wafer W21 are within the required ±1% from the wafer mean. The other wafers from the batch do not satisfy these conditions. With regards to the allowed variation of full depletion voltage in Figure 3.21, all tested wafers are within the required ±10% from the mean wafer value.

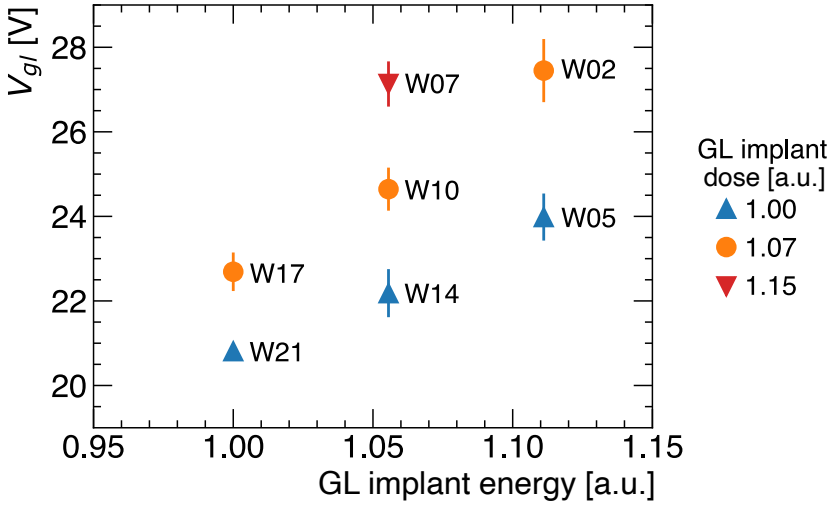


Figure 3.18: The average gain layer depletion voltage V_{gl} for a given wafer as a function of the gain layer (GL) implant energy. Different markers are used for wafers with different gain layer (GL) implant dose. Both the GL implant energy and dose are normalised to wafer W21. The error bars represent the standard deviation of the wafer V_{gl} distribution.

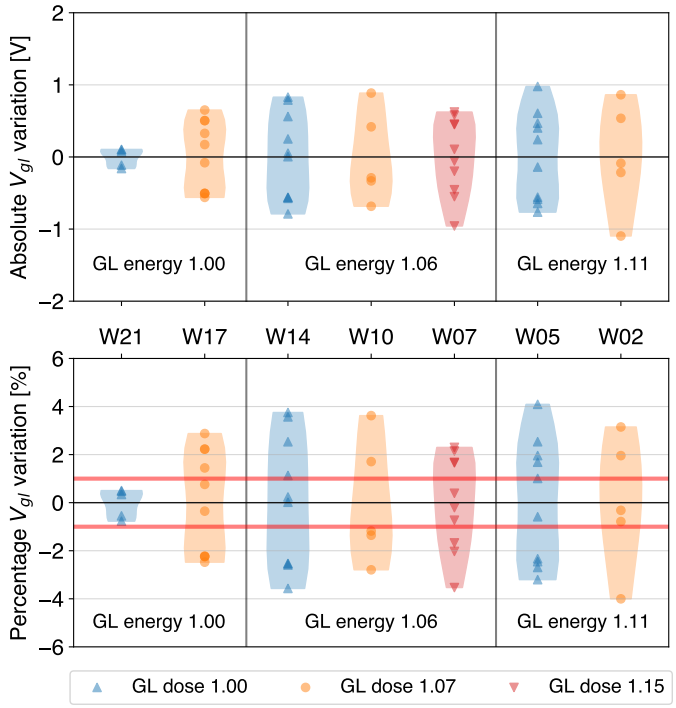


Figure 3.19: Absolute (top) and percentage (bottom) variation of extracted gain layer depletion voltage V_{gl} for individual LGAD devices compared to the mean value for a given wafer. Wafers are grouped by gain layer implant energy into three groups - energy 1.00 (*Low*), 1.06 (*Medium*), 1.11 (*High*) - with the GL implant energy values normalised to that of W21. Colours represent the GL implant dose grouping of the wafers. The horizontal red lines shown in the bottom plot correspond to the maximum allowed variation of sensor V_{gl} ($\pm$1%) from the wafer average.

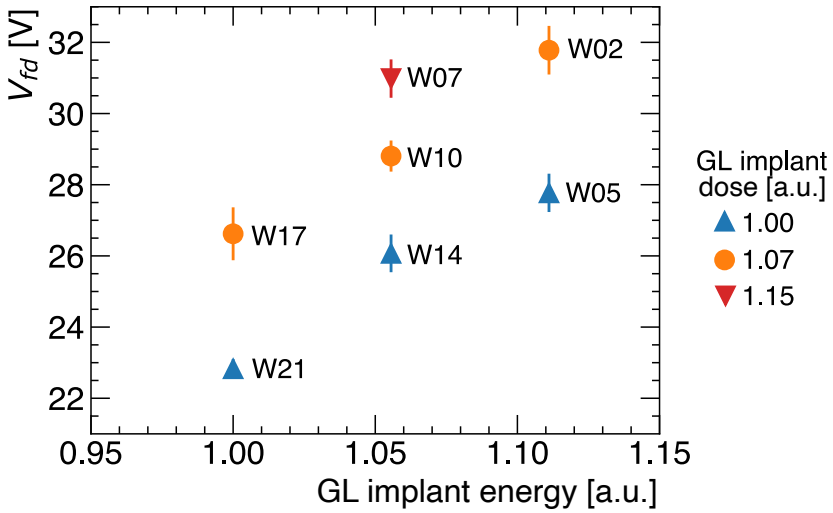


Figure 3.20: The average full depletion voltage V_{fd} for a given wafer as a function of the gain layer (GL) implant energy. Different markers are used for wafers with different gain layer (GL) implant dose. Both the GL implant energy and dose are normalised to wafer W21. The error bars represent the standard deviation of the wafer V_{fd} distribution.

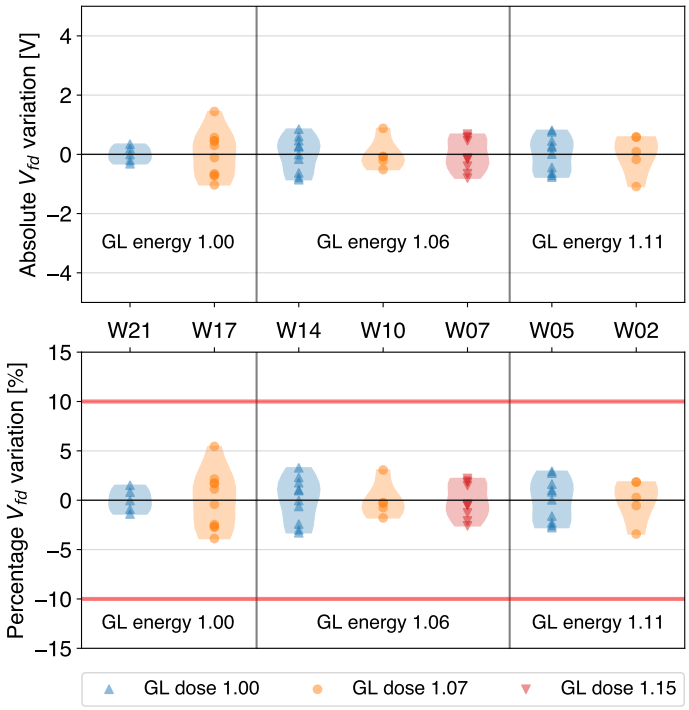


Figure 3.21: Absolute (top) and percentage (bottom) variation of extracted full depletion voltage V_{fd} for individual LGAD devices compared to the mean value for a given wafer. Wafers are grouped by gain layer implant energy into three groups - energy 1.00 (*Low*), 1.06 (*Medium*), 1.11 (*High*) - with the GL implant energy values normalised to that of W21. Colours represent the GL implant dose grouping of the wafers. The horizontal red lines shown in the bottom plot correspond to the maximum allowed variation of sensor V_{fd} ($\pm$10%) from the wafer average.

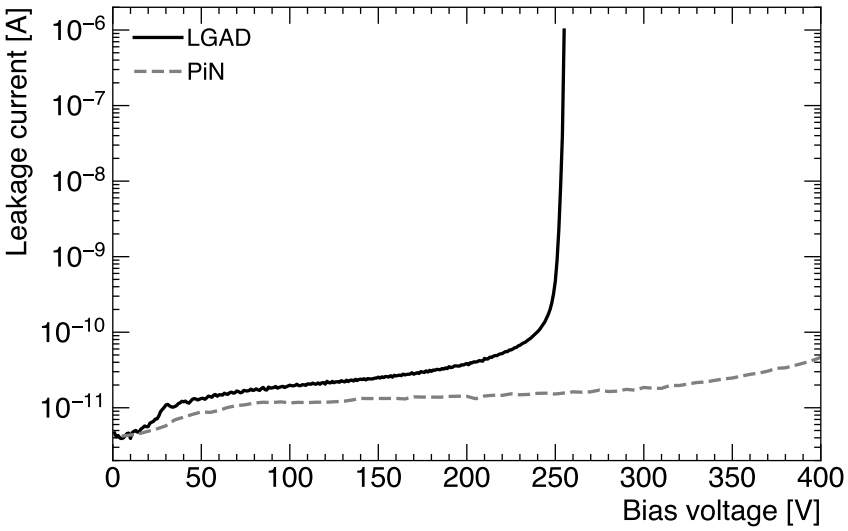


Figure 3.22: Typical IV curves for LGAD (black solid line) and PiN diode (grey dashed line) of 1×1 mm^2 pad size.

3.2.3 Leakage current characterisation

In the absence of any external stimulus (e.g. electron, photons, hadrons, etc.), as a reverse bias is applied across a p-n junction, leakage current (also called dark current) is flowing through the device. The total leakage current consists of surface and bulk currents. The leakage current curves are widely used in the detector community for sensor characterisation and testing [57]. Manufacturing issues and improper device handling (often resulting in scratches) strongly affect the shape of the IV curves and can increase the amount of leakage current.

The IV curves of a PiN diode and an LGAD are shown in Figure 3.22. A reverse biased PiN diode behaves according to the predictions of the diode law [70] - the leakage current reaches a plateau and remains roughly constant until the breakdown voltage V_{bd} is reached, at which point the current sharply increases (not visible in the plot, typically around 500-600 V). On the other hand, the leakage current of an LGAD features a rapid increase above the gain layer depletion voltage V_{gl} due to the presence of the gain layer.

3.2.3.1 Breakdown voltage extraction

One of the key parameters of LGADs is the breakdown voltage V_{bd}. As the bias voltage approaches breakdown, the electric field in the detector becomes so great that the structure can no longer withstand it, and the sensor shows a resistive behaviour [56]. This is apparent as the leakage current increases rapidly, where small changes in the bias voltage of a few volts change the leakage current by orders of magnitude. This regime should be avoided due to the potential damage to the sensor. The ATLAS HGTD collaboration defines V_{bd} as the bias voltage at which the leakage current between the top electrode (pad) and backside exceeds 200 nA [58].

The HGTD Technical Specifications states that the breakdown should be below 12 V/µm multiplied by the active epitaxial thickness, which in the case of 50 µm thick devices corresponds to the limit of the safety limit of 600 V. This condition is in place to prevent Single Event Burnout (SEB) [71]. SEB is a destructive event due to a large deposited charge in the active layer by a single traversing particle. Additionally, the requirements specify the maximum tolerable differences between the breakdown voltage of different sensors to be within 8% from the average V_{bd}.

IV uniformity across a wafer

The leakage current at a given bias voltage applied between the pad metallisation and the substrate was measured for several devices on the wafer. To assess the uniformity of the leakage current across wafers, IV measurements were performed on 1×1 mm^2 single LGAD devices from 5 fields across the wafer. The Needle-Bias configuration is used with the guard ring left floating. The tested devices are the same as those presented in Section 3.2.2. Within each field, two 1×1 mm^2 LGAD devices of variant D were measured for wafers W05, W07, W12, W14 and W17, resulting in 10 measurements per wafer. For wafers W02 and W10, only measurements from one LGAD device of variant D per field are available, with a total of 5 measurements per wafer. To illustrate the results, IV curves obtained for wafer W07 are shown in Figure 3.23.

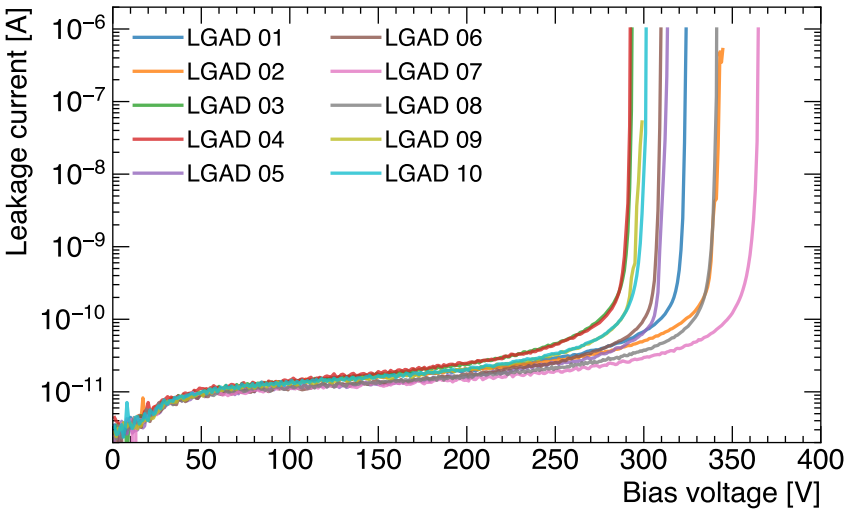


Figure 3.23: Leakage current of 1×1 mm^2 devices measured on wafer W07. Curves are measured using the Needle-Bias configuration, where the LGAD top side is biased via a probe needle, and the backside of the sensor is held at ground potential.

IV variation between wafers

As LGAD devices manufactured in the first production batch feature a range of gain layer implant energy and dose, a variation of the breakdown voltage is expected across the various structures. This V_{bd} variation is visualised in Figure 3.24. No tested LGADs exhibit breakdown voltage above the 600 V safety limit. Due to the variation of the implantation process, the breakdown voltage varies for devices produced on the same wafer. Figure 3.25 shows a spread of the values.

From Figures 3.24 and 3.25, the wafers with higher implant energy show a lower breakdown voltage. Samples with increased energy feature a gain layer implant buried deeper in the silicon. Comparing devices with different implant dose, higher doses correspond to lower breakdown voltages.

The breakdown voltage variation for the manufactured devices should be within $\pm$8% of the wafer average [58]. As shown in Figure 3.25, only devices from wafers W21 and W14 satisfy this fully (for all tested devices). These wafers, however, have the lowest implant dose and so do not satisfy the minimum V_{gl} condition (V_{gl} > 24 V). Encouragingly, wafer W07 shows 90% yield on passing the variation conditions (1 device did not pass) while demonstrating gain layer depletion voltage above 24 V.

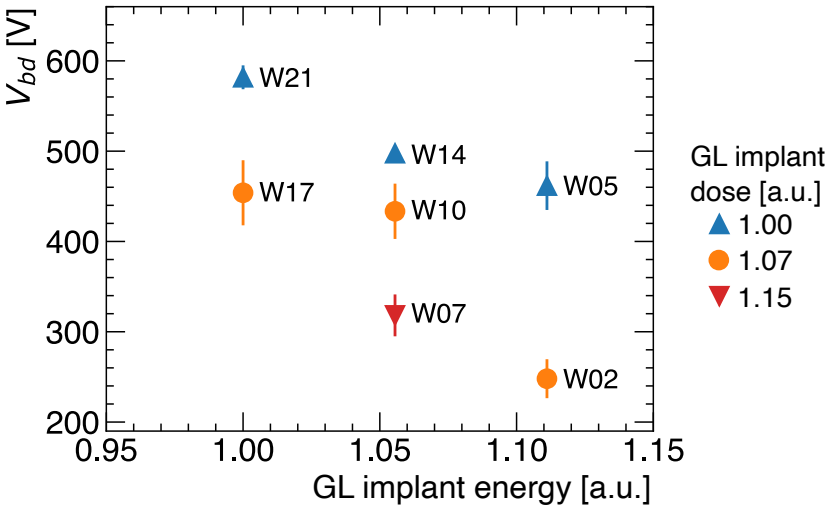


Figure 3.24: The average breakdown voltage V_{bd} for a given wafer as a function of the gain layer (GL) implant energy. Different markers are used for wafers with different gain layer (GL) implant dose. Both the GL implant energy and dose are normalised to wafer W21. The error bars represent the standard deviation of the wafer V_{bd} distribution.

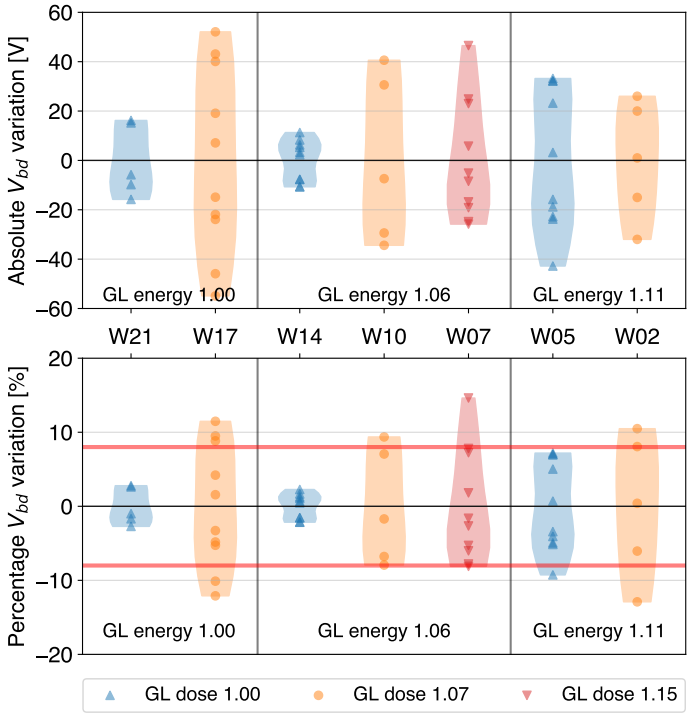


Figure 3.25: Absolute (top) and percentage (bottom) variation of extracted breakdown voltage V_{bd} for individual LGAD devices compared to the mean value for a given wafer. Wafers are grouped by gain layer implant energy into three groups - energy 1.00 (*Low*), 1.06 (*Medium*), 1.11 (*High*) - with the GL implant energy values normalised to that of W21. Colours represent the GL implant dose grouping of the wafers. The horizontal red lines shown in the bottom plot correspond to the maximum allowed variation of sensor V_{bd} ($\pm$8%) from the wafer average.

3.2.4 Summary

The results presented in this section demonstrate the importance of well-controlled gain layer implant parameters during the production of Low Gain Avalanche Detectors. The investigated LGAD wafers manufactured by Te2v vary in the gain layer implant dose (1.00, 1.07, and 1.15 relative to the reference W21) and gain layer implant energy (1.00, 1.06, and 1.11 relative to the reference). Within this range, average breakdown voltages vary from 248 V (W02) to 582 V (W21). None of the measured wafers exhibits LGAD breakdown voltage above the safety limit of 600 V. The observed in-wafer variation of breakdown voltage from the average value exceeds the required $\pm$8% for all wafers apart from W21 (reference wafer, *Low* dose 1.00, *Low* energy 1.00) and W14 (*High* dose 1.07, *Medium* energy 1.06).

With regards to the technical specifications related to the capacitance of the devices, a minimum gain layer depletion voltage of 24 V is demonstrated by all tested devices from W02 (*High* dose 1.07, *High* energy 1.11) and W07 (*Very High* dose 1.15, *Medium* energy 1.06), showing a clear preference for high implant energy and dose. In terms of the allowed maximum variation of the gain layer depletion voltage from the wafer mean for individual devices, only devices from wafer W21 deviate from the mean value by less than 1%. There were no observed problems with the requirements on the full depletion voltage for any investigated wafer.

For further investigations, LGAD devices from wafer W02 and W07 appear to be the best candidates, as they demonstrate gain layer depletion voltage $V_{gl} > 24$ V. However, the variance of V_{gl} and breakdown voltage V_{bd} is above the allowed levels, prompting more rigorous wafer evaluation. Working closely with Te2v as manufacturer, recommendations of implant properties guided the chosen implant parameters used in the second batch production (*Batch 2*), which is discussed further in Section 3.6.

3.3 Hadron beam measurements of Te2v-LGADs at the SPS

This section presents collected charge, hit efficiency, and timing resolution measurements from non-irradiated single-pixel 1×1 mm^2 LGAD sensors manufactured by Teledyne e2v. Three LGAD devices were tested, each from a different wafer of Batch 1 production – Wafer 2 (W02), Wafer 8 (W08) and Wafer 9 (W09). The three wafers differ in the gain layer implant energy and gain layer implant dose as stated in Table 3.2. Throughout this section, the devices will be referred to by their wafer number (e.g. the investigated device from Wafer 2 is referred to as LGAD W02). The investigation aims to demonstrate the capabilities of the LGAD sensors in the context of the HGTD requirements for sensors at the start of their operation - before radiation damage effects. Among other requirements, at the start of their operation, the LGAD sensors are required to achieve a timing resolution better than 40 ps per hit, a hit efficiency of 97%, and a collected charge >15 fC at their operation voltage (corresponding to a charge gain of $\sim$20) [58].

3.3.1 Experimental setup

The measurements were carried out with a 180 GeV mixed hadron beam at the Super Proton Synchrotron (SPS) facility at the North Area of CERN. The MALTA telescope [72], permanently installed at the H6 beamline, was used for beam tracking. With the incident particle track information, the precise hit location on the tested device can be investigated. The telescope consists of six MALTA tracking planes and a scintillator for timing (timing resolution $\sim$0.5 ns) located behind the telescope planes. The trigger system of the telescope is fully configurable, allowing for triggering on the coincidence between the individual planes and the scintillator. More information regarding the performance of the MALTA telescope is available in [72].

As the timing resolution of the telescope scintillator is over an order of magnitude worse compared to the expected timing resolution of the LGAD as the Device Under Test (DUT), a second LGAD device with a comparable timing resolution was added as a timing reference (referred to as Reference LGAD). The Reference LGAD was calibrated in beam tests to achieve a timing resolution of 54.8 ps at 180 V operating bias at room

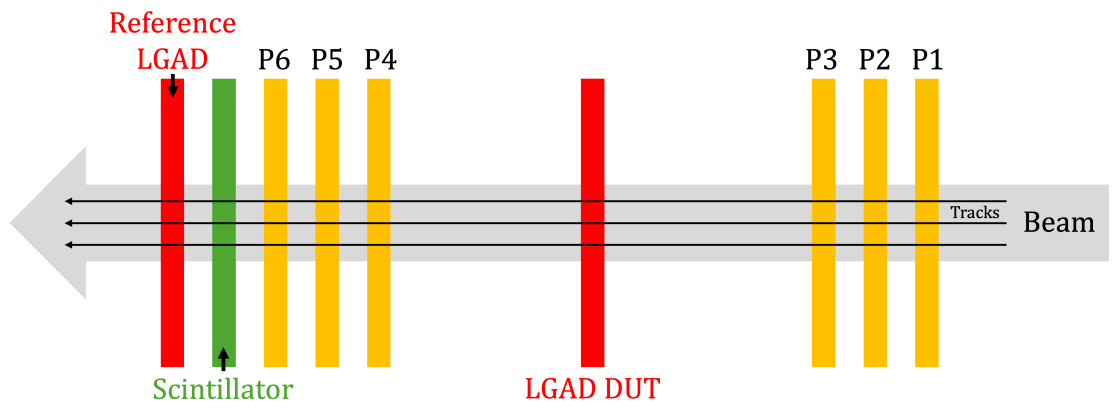


Figure 3.26: Experimental setup in the beamline showing the MALTA tracking planes (P1-P6, grouped into the Upstream and Downstream arms), the Scintillator for telescope timing, the LGAD device under test (DUT), and the Reference LGAD. The direction of the arrow indicates the path of the hadron beam.

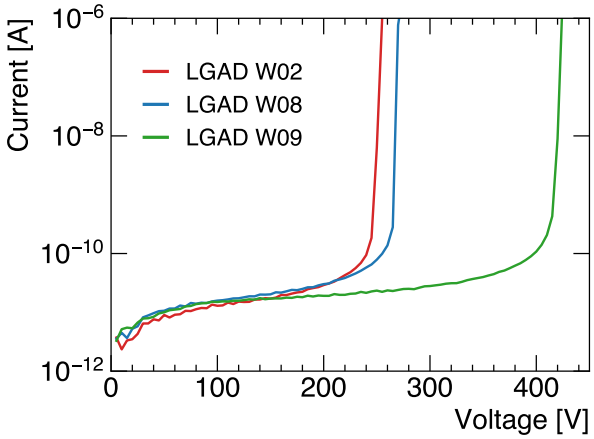


Figure 3.27: IV curves for the three investigated LGAD devices at room temperature

temperature [73]. The arrangement of the telescope planes, scintillator, DUT, and Reference are shown in Figure 3.26.

Prior to the testbeam measurements, the investigated LGAD devices underwent a current-voltage (IV) scan - shown in Figure 3.27. The breakdown voltages extracted from the IV curves guided the selection of the appropriate range of operating voltages for the devices. Table 3.5 shows the list of the bias voltages investigated for each LGAD device and the breakdown voltage as determined by the IV measurement. The reference LGAD device was biased at V_{bias} = 180 V throughout the investigation to maintain a constant timing resolution.

Table 3.5: The range of applied bias voltages to the investigated LGAD devices. Breakdown voltage V_{bd} is defined as the point at which the leakage current exceeds 200 nA.

Device	V_{bd}	**Range of applied bias voltages [V]**
W02	255 V	50, 75, 100, 125, 150, 175, 200, 225, 250
W08	275 V	50, 100, 125, 150, 175, 200, 225, 250, 260, 270
W09	425 V	50, 100, 150, 200, 250, 300, 325, 350, 375, 400, 420

3.3.1.1 Data Acquisition

The LGAD sensor is wirebonded to a COLA v1.4 custom readout board providing 316 V/A transimpedance signal amplification with 1.5 GHz bandwidth. Further amplification is achieved by an external TESEQ LNA 6901 amplifier with 28 dB voltage amplification gain [74], giving a combined gain of 7.94×10^3 V/A. This gain factor is used in the data analysis step to convert the area under the voltage waveform to the corresponding collected charge.

A Teledyne LeCroy WaveRunner 8104 oscilloscope (20 GSa/s, 1 GHz bandwidth) was used to sample the signal from the DUT and the Reference LGAD. A trigger signal from the telescope initiates the data acquisition on the oscilloscope. The modifiable telescope Trigger Logic Unit (TLU) system allowed for a custom Region of Interest (ROI) to be defined - a 2×2 mm^2 acceptance window which included the LGAD devices. Hence, whenever the MALTA telescope recorded a track within the defined ROI, the corresponding DUT and Reference signals were saved into the oscilloscope's internal memory, available for analysis later. The track reconstruction and extrapolation onto the plane of the DUT is performed with the software package Proteus [75]. The MALTA telescope has a tracking resolution of 4.8 ± 0.2 µm in the x-direction and 4.6 ± 0.2 µm in the y-direction [72].

At each telescope trigger, the oscilloscope recorded a 20 ns window of voltage signal for each of the LGAD sensors. With the North Area beam characteristics, it is expected that the 1×1 mm^2 LGAD sensor will be hit on average 1-5 times per 1 ms [76]. Hence, a 20 ns window is suitable to see individual hits. The first 4 ns of the recorded signal (*noise window*) allows for noise evaluation, with the remaining 16 ns constituting a *signal window*. The average voltage of the noise window defines the *baseline*. Internal delays were implemented in the data acquisition protocol to ensure that the noise

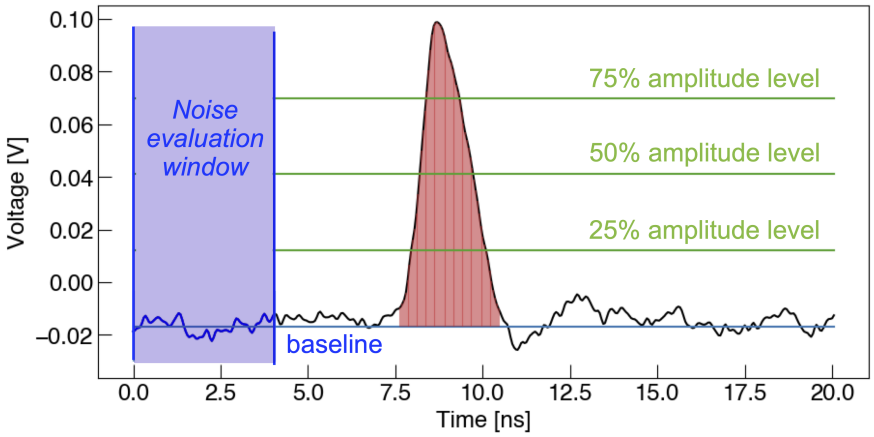


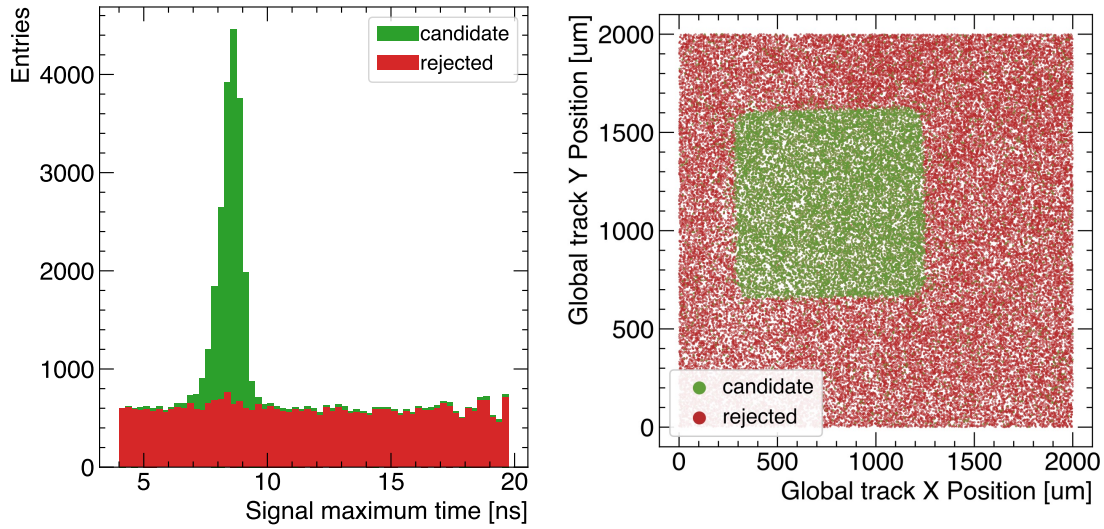
Figure 3.28: An LGAD signal as recorded by the oscilloscope within a 20 ns window. The first 4 ns are dedicated as a Noise evaluation window. The average voltage of the Noise window is considered as the baseline, and the standard deviation is the noise. The difference between the baseline and the maximum voltage recorded within the last 16 ns is the signal amplitude (25%, 50%, and 75% amplitude level shown).

window sufficiently proceeds the passing of the charged particle through the sensors. A sample waveform is shown in Figure 3.28, which shows the signal baselines evaluated within the noise window, followed by a signal appearing around the 8 ns time-stamp. The red shaded region defines the area under the signal.

3.3.1.2 Candidate selection and device alignment

To find a region corresponding to the physical location of the device, hit candidates are defined, which are associated with tracks likely to have passed through the DUT. The analysis algorithm classifies a signal as a hit candidate if the maximum recorded voltage within the signal window relative to the baseline is at least 5 times the standard deviation of the voltage within the noise window. Counting the entries by the time a signal maximum is reached, the effect of labelling hit candidates and rejected noise signals (the waveforms which do not meet the candidate criteria) can be seen in Figure 3.29a. The cumulative histogram shows that the candidate signals are temporally related, whereas the noise signals show a roughly uniform distribution of peaking times relative to the telescope trigger, as a noise distribution is expected to do. The noise signals are still retained for further analysis, particularly the efficiency calculation.

Investigating the telescope track position of candidate signals is an effective method for finding the physical location of the DUT and performing track alignment. Clusters



(a) **(b)**

Figure 3.29: Temporal and spatial profile of the hit candidates. In (a), a cumulative histogram of the data entries based on the time at which signal maximum was reached. The waveforms classified as candidates (green) form a distinct cluster on top of the constant rejected noise background (red). In (b), the scatter distribution of track position associated with a candidate waveform (green) forms a shape of the device's active region with the surrounding rejected noise (red).

of the candidate tracks form a region visually distinct from the noise tracks. This is illustrated in Figure 3.29b, where the green square shape of LGAD's active region formed by candidate tracks is visible on top of the red rejected noise background. The candidates are spatially and temporarily related, as would be expected from LGAD hits. To aid data analysis, a series of transformations (translations and rotations) is applied to convert the global track data to a device-centric frame, with the origin at the centre of the device and device edges parallel to the axes.

3.3.2 Data analysis

The data analysis process is briefly discussed, with results presented later in Section 3.3.3. To suppress edge effects, a central DUT region of 900×900 μm^2 is defined and used for further analysis. As the LGAD devices have a 1×1 mm^2 pitch, the region covers >80% of the total area. This approach is analogous to the fiducial region selection as used in [73], which however only accounted for 15% of the device area (0.5×0.5 mm^2 region selected on a 1.3×1.3 mm^2 LGAD device).

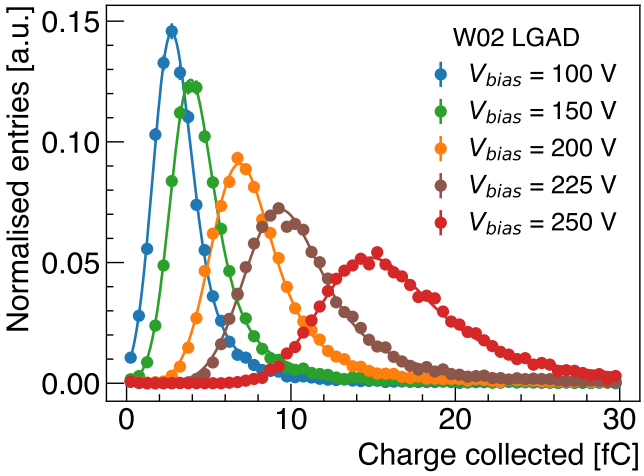


Figure 3.30: Histograms of the collected charge by W02 LGAD at different reverse bias voltages. The data is fitted with a Landau-Gaussian fits.

3.3.2.1 Collected charge

The amount of charge collected per incident particle is obtained by integrating the induced current. As the oscilloscope records voltage values rather than current, the appropriate transimpedance scaling factor 7.94×10^3 V/A is applied. Figure 3.28 shows a signal with the associated area highlighted. The charge gain of the LGAD device increases with increasing bias voltage, as shown in Figure 3.30 with charge histograms from device W02 for various operating bias voltages (100 V, 150 V, 200 V, 225 V, and 250 V). The data is fitted with a Landau function convoluted with a Gaussian distribution. The maximum of the fitted distribution gives the most probable value (MPV) of the collected charge.

3.3.2.2 Hit detection efficiency

Based on the target specifications of the ALTIROC readout chip for LGADs in the HGTD detector, as low as 1 fC discriminator threshold for the collected charge can be implemented [61]. Recent measurements from ALTIROC1 prototype ASIC show that the lowest detectable charge threshold increased when the ASIC is connected to an LGAD array [77]. To accommodate this increase and allow for a larger operation window, at least 2 fC of charge are considered as necessary to generate a digital signal that can be interpreted as a hit. Therefore, the efficiency is defined as the ratio of the

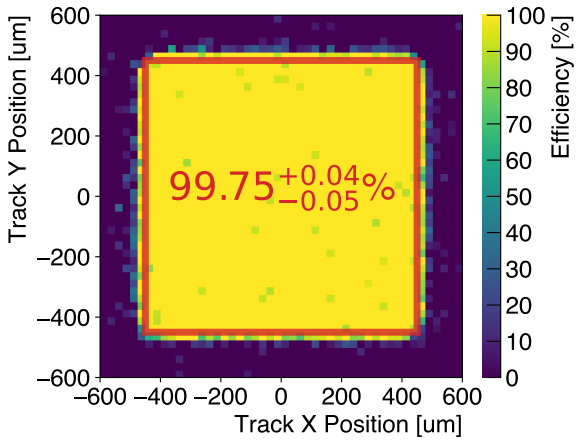


Figure 3.31: Efficiency map of W02 LGAD at 250 V bias voltage - bin size 25×25 µm. The red square shows the ± 450 µm extent of the central region. The efficiency within the central region is (99.75 + 0.04 - 0.05)%. The upper and lower confidence interval values are obtained using the Clopper–Pearson method.

number of tracks associated with a signal with a collected charge greater than 2 fC relative to all tracks passing through a given area

$$\epsilon = \frac{k}{n}, \tag{3.7}$$

where ϵ is the efficiency, k is the number of tracks considered a hit, and n is the total number of tracks. The uncertainty associated with the efficiency values is treated using the Clopper–Pearson interval method with a confidence level of 68% (equivalent to 1 standard deviation of a Gaussian distribution) [78]. The lower and upper bounds on the efficiency value ϵ_{lower} and ϵ_{upper}, respectively, are given implicitly by solving Equations 3.8 and 3.9,

$$\frac{1 - level}{2} = I_{\epsilon_{lower}}(k, n - k + 1), \tag{3.8}$$

$$\frac{1 + level}{2} = I_{\epsilon_{upper}}(k + 1, n - k), \tag{3.9}$$

where *level* gives the confidence level (0.68 in this case), $I_\epsilon(\alpha,\beta)$ is the regularised incomplete beta function, with k and n defined as before.

Applying the hit condition (>2 fC) to the LGAD W02 sensor at 250 V bias, a two-dimensional efficiency map of the LGAD is shown in Figure 3.31. This figure also shows the central region bounded by a red square, where the device efficiency is evaluated. The horizontal efficiency profile of the device for various bias voltages is shown in Figure

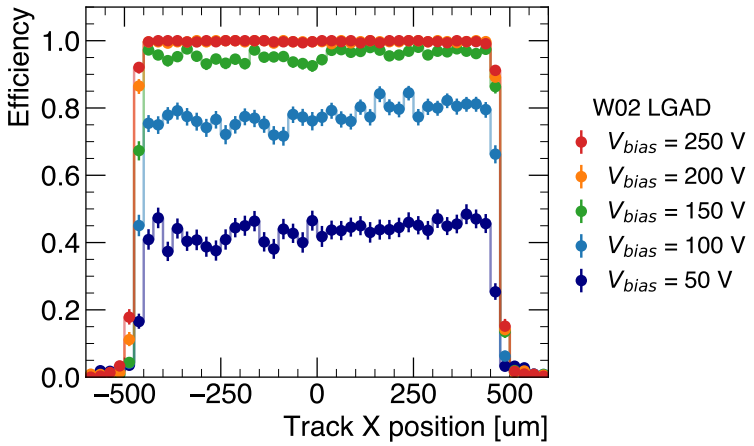
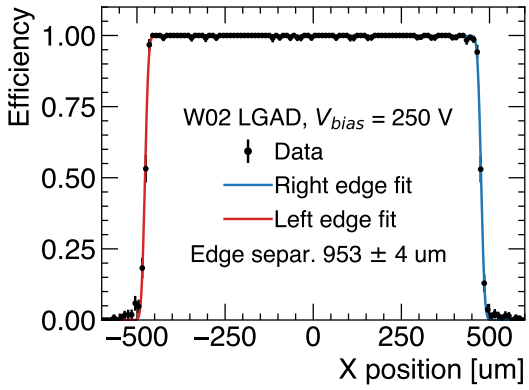


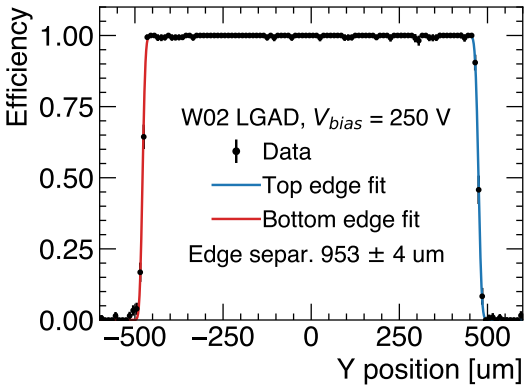
Figure 3.32: Horizontal efficiency profile variation of W02 LGAD. Along the x-direction, tracks are binned into 25 µm bins. The y-coordinate is required to lie within $\pm$ 450 µm from the pixel centre to ensure that the track's y-coordinate is within the extent of the pixel.

3.32. The profile is obtained by sorting tracks into 25 µm wide bins (in x-direction) while requiring the y-coordinate to be within $\pm$ 450 µm form the pixel centre (equivalent to the extent of the central region). The devices show a uniform efficiency across the pixel, with >90% efficiency for bias voltages above 150 V. Below 150 V, the efficiency falls off as the gain of the device is not sufficient to guarantee a 2 fC charge to be collected.

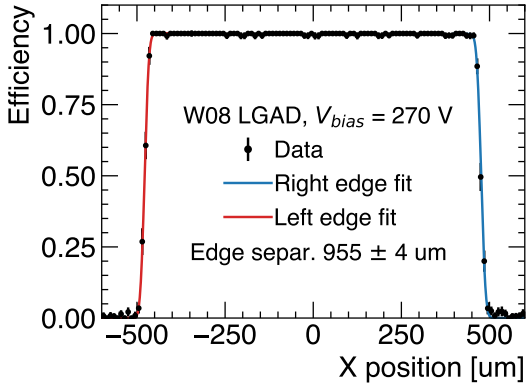
Considering an idealised sensor performance, neglecting edge-smearing effects, and assuming a perfect track resolution, the efficiency is 1 if the track passes through the gain layer, and 0 outside the device. A cross-section of the device efficiency profile would resemble a top-hat response function, the edges of which define the physical edges of the device. Using this principle, the dimensions of the pixel's active region can be obtained. To approach these conditions as much as possible, the configuration with the highest bias voltage is selected for each device, such that the efficiency of the LGAD is close to 1. The edge smearing and finite track resolution effects are introduced using an Error function fit on the device edges rather than a sharp step-function. The left and right device edges are fitted independently, with the extent of the active region given by the distance between the mid-point of the two edges. According to the device design, the width of the active region is 970 µm (for further discussion, see Section 3.3.3). The vertical and horizontal efficiency profiles of the devices at their maximum operating voltage with the extracted device size (edge separation) are shown in Figure 3.33.



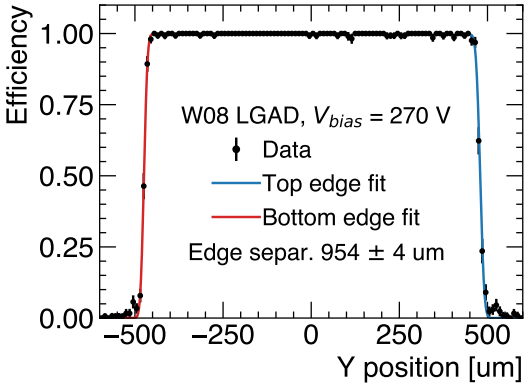
(a) W02 - horizontal



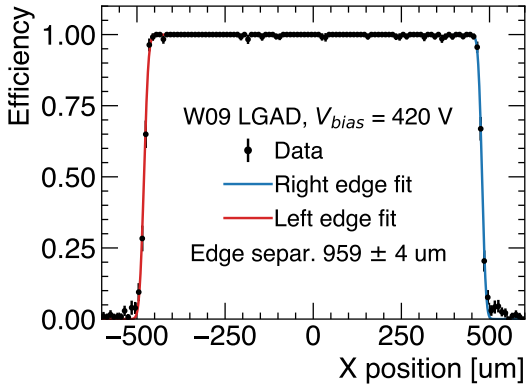
(b) W02 - vertical



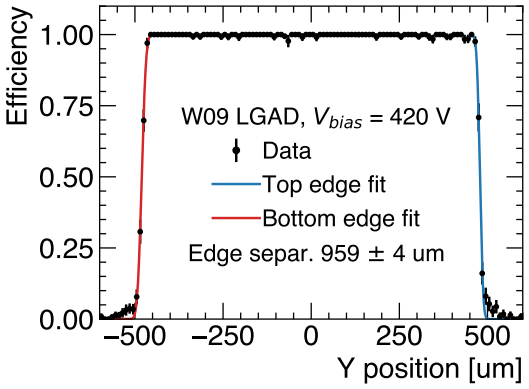
(c) W08 - horizontal



(d) W08 - vertical



(e) W09 - horizontal



(f) W09 - vertical

Figure 3.33: Efficiency profiles of the devices at maximum applied bias. Plots (a) and (b) show W02 LGAD biased at 250 V, plots (c) and (d) show W08 LGAD biased at 270 V, and plots (e) and (f) show W09 LGAD biased at 420 V. The data was sorted into bins of size 10 µm. The left-hand and the right-hand plots correspond to the horizontal profiles (along the X-axis) and vertical profiles (along the Y-axis), respectively. Each set of data points had both edges fitted with an Error function. The separation of the mid-points of the fitted Error functions gives the size of the device.

3.3.2.3 Timing resolution

Timing resolution is one of the key parameters when assessing the performance of LGAD sensors. The time delay between the DUT signal and the Reference LGAD varies according to the timing resolution of the respective devices. Assuming that the two devices are independent, the standard deviation of the delay between them σ_t is given by

$$\sigma_t^2 = \sigma_{DUT}^2 + \sigma_{REF}^2, \tag{3.10}$$

where σ_{DUT} and σ_{REF} are the timing resolutions of the DUT and the Reference LGAD, respectively. The resolution of the DUT was obtained by assuming that the Reference LGAD has a timing resolution σ_{REF} = 54.8 ps at an operating bias voltage of 180 V at room temperature.

A time reference point is selected when the signal reaches a given threshold. With a constant threshold, the delay between the signal start and the time reference is affected by time-walk, where signals with different amplitudes cross the constant threshold at different times. The constant fraction discriminator (CFD) method was used during the analysis to suppress the time-walk effect. Rather than using one fixed threshold value, the CFD method enhances the timing resolution by using a given fraction of the signal amplitude as the threshold. The fraction of the signal amplitude used to determine the threshold is known as the CFD value.

To calculate the timing resolution, the time delay between the DUT and the Reference LGAD was sorted into 20 ps bins, and the histogram was fitted with a Gaussian distribution. The fit is a convolution of two Gaussian profiles, one for the Reference LGAD (with a standard deviation of σ_{REF} = 54.8 ps and a negligible uncertainty) and the other one for the DUT with σ_{DUT} to be extracted. The convolution of two Gaussian distributions also follows a Gaussian distribution. An example histogram of a fit function with individual deconvolved Gaussian components is shown in Figure 3.34. The delay values are calculated using a 50% CFD value - the time reference point is evaluated when the signal reaches half its maximum value. The standard deviation of the combined Gaussian fit σ_t = 70.0 $\pm$ 0.5 ps gives the timing resolution of W02 LGAD at 250 V as σ_{DUT} = 43.6 $\pm$ 0.8 ps.

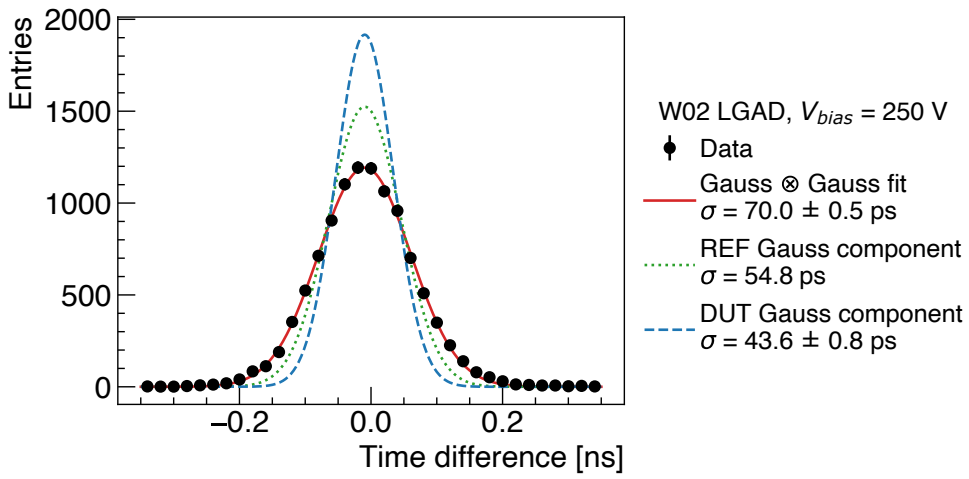


Figure 3.34: Time difference between the W02 LGAD at 250 V bias (DUT) and the Reference LGAD (REF). The solid red line shows the combined Gaussian fit to the data. The dotted green line represents the Reference LGAD contribution, and the blue dashed line represents the DUT LGAD contribution. The two contributions are assumed to be independent.

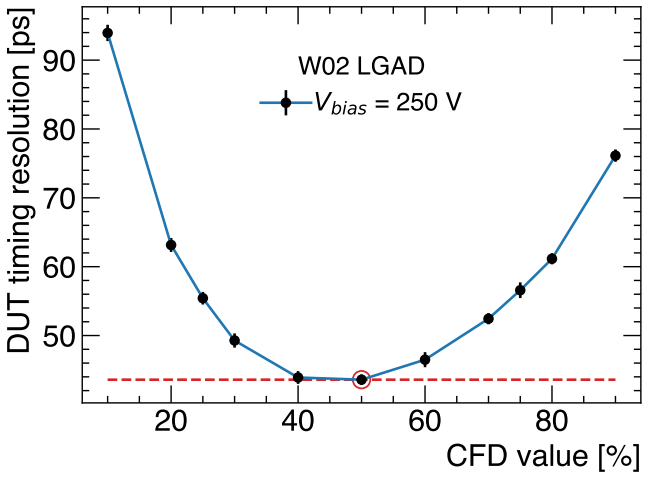


Figure 3.35: Timing resolution of W02 LGAD as a function of the CFD value. The minimum timing resolution extracted from the fit (dashed red line) is found to be around 50% CFD value (red circle).

Figure 3.35 shows the timing resolution of W02 at 250 V bias for different values of the CFD threshold. The combined timing resolution of the devices is minimised for 50% CFD, which was the value used for analysis. When finding the time at which the signal crossed a given threshold, linear interpolation between the data points was used to mimic a higher sampling rate - the oscilloscope records a sample every 50 ps. This treatment did not artificially enhance the performance of the LGAD but rather minimised the uncertainty associated with the oscilloscope acquisition process.

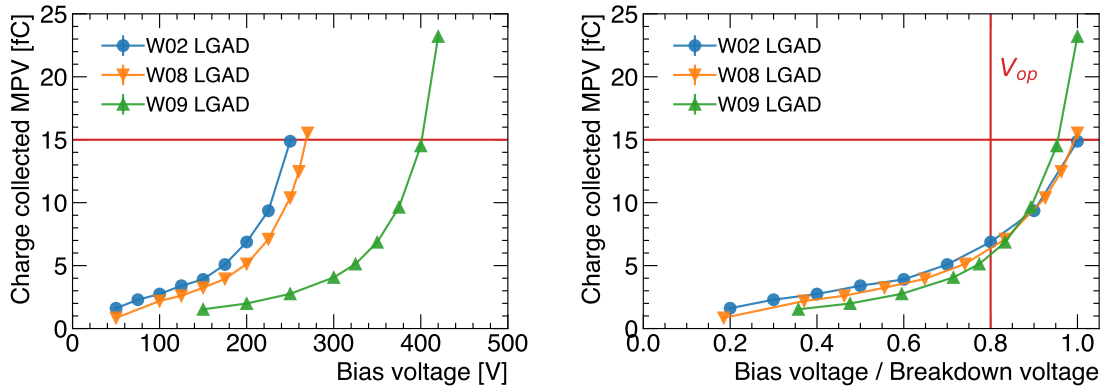
It is important to note that using a reference device with σ_{REF} = 54.8 ps is suboptimal for measuring timing resolutions smaller than this value. When resolutions are combined in quadrature, as shown in Equation 3.10, the total measured standard deviation of the delay is dominated by the larger resolution. For example, with DUT resolutions of 20 ps and 30 ps, the total measured standard deviation would be approximately 58.3 ps and 62.5 ps, respectively — a difference of only ∼4 ps. As the DUT resolution decreases, the measured standard deviation becomes increasingly insensitive to small variations. Consequently, this limits the accuracy of timing measurements.

3.3.3 Results

The charge, efficiency, and timing results are presented both as a function of the absolute bias voltage applied to the LGADs and as a function of the applied bias relative to the breakdown voltage V_{bd} for the particular device. The latter allows for better comparison, as the breakdown voltage varies almost by a factor of 2 between the individual devices, as shown in Figure 3.27. The breakdown voltage variation is expected, given the different gain layer implant parameters. In the context of HGTD, the operation voltage V_{op} of an LGAD sensor is defined as 80% of V_{bd}, which serves as a reference point to characterise the performance of the devices. The V_{op} value is chosen to ensure the sensors operate do not operate too close to the breakdown region, where high currents could potentially damage the device.

Collected charge

As shown in Figure 3.36, the LGAD sensors can collect a charge greater than 15 fC (most probable value). However, this is only achieved at bias voltages above V_{op}. The highest observed value was 23.2 fC for the W09 LGAD sample biased at 420 V. As the amount of the collected charge rises rapidly around 90% V_{bd}, further measurements are needed to confirm that W02 and W08 devices can also achieve comparable performance at bias voltages closer to the breakdown. Near V_{op}, the collected charge is greater than 5 fC. To achieve the desired gain, future productions aim to increase the gain layer doping.



(a) **(b)**

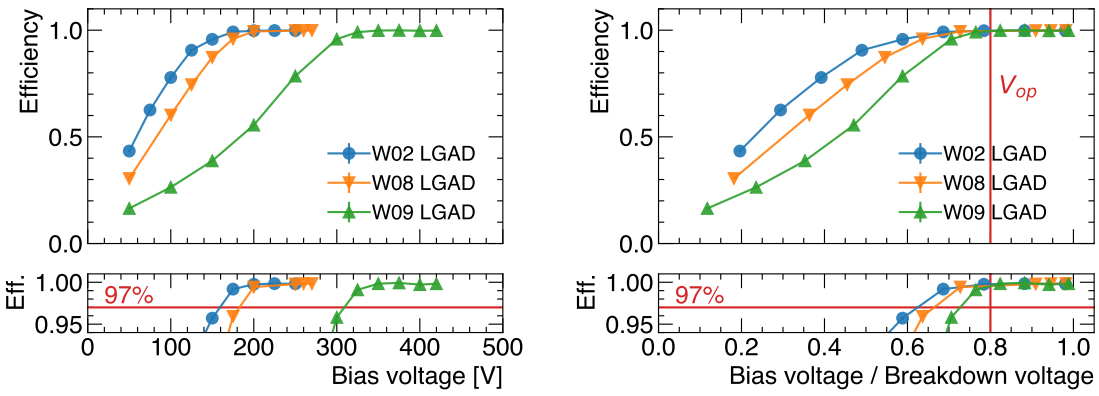
Figure 3.36: Most probable value of the collected charge. The results are shown as a function of the applied bias voltage in (a), and relative to the breakdown voltage of the given device in (b), with a vertical red line denoting the operational voltage V_{op} at 80% of breakdown. The horizontal red line denotes the 15 fC level.

Hit efficiency

The hit efficiency is shown in Figure 3.37 both as a function of bias voltage and the fraction of V_{bd} applied. The lower plots show the same data, but only with the 94%-100% efficiency range to allow for easier differentiation between the high efficiency data points. The devices exhibit efficiency >97% for bias voltages above V_{op}, with W02 LGAD achieving this efficiency threshold already at around 60% of the breakdown voltage. The results demonstrate good operation of the HGTD sensors in terms of hit efficiency.

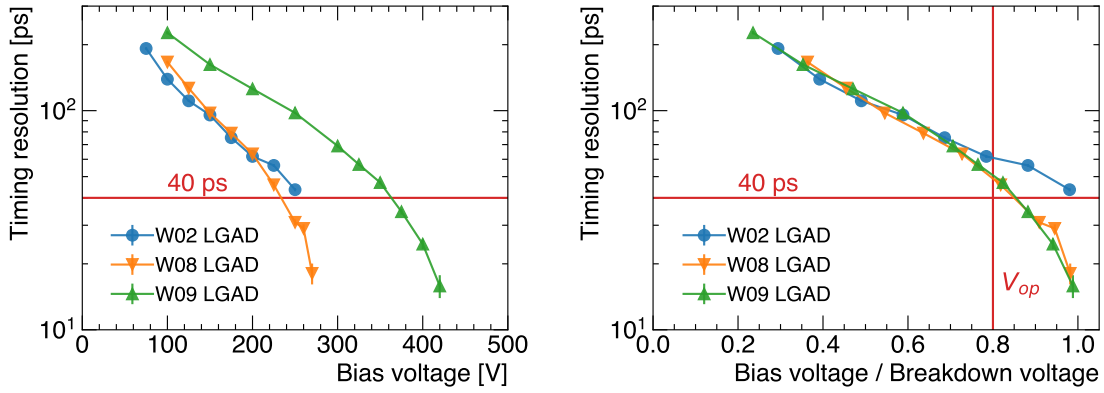
Timing resolution

From Figure 3.38, the W08 and W09 devices show timing resolution better than 50 ps at V_{op}. With increasing bias voltage, the timing resolution improves further, with the two devices achieving an excellent timing resolution below 20 ps. Whereas the LGAD from W02 could still achieve a very good timing resolution below 50 ps, this was only possible at a bias voltage of 250 V (above 95% of V_{bd}). When comparing devices relative to the V_{bd}, it is observed that the trend is similar up to ∼80% of V_{bd}, but after this point, while W08 and W09 devices improve significantly, the improvement of the W02 device is limited and does not follow the same trend. Further measurements are needed to establish if this behaviour applies to all devices from W02 or only to the measured sample.



(a) **(b)**

Figure 3.37: Hit efficiency of the LGAD devices. The results are shown as a function of the applied bias voltage in (a), and relative to the breakdown voltage of the given device in (b), with a vertical red line denoting the operational voltage V_{op} at 80% of breakdown. A signal is considered a hit if more than 2 fC of charge are collected. The bottom plots show the same data but with a focus on the >94% efficiency region. The red horizontal line represents the 97% efficiency level.



(a) **(b)**

Figure 3.38: Timing resolution of the LGAD devices. The results are shown as a function of the applied bias voltage in (a), and relative to the breakdown voltage of the given device in (b), with a vertical red line denoting the operational voltage V_{op} at 80% of breakdown. The horizontal red line denotes the 40 ps threshold.

Device profile

The efficiency profiles shown in Figure 3.33 give vertical and horizontal sizes of the devices, which are summarised in Table 3.6. Each device yielded a horizontal-vertical size ratio of 1.00 with a 1% relative error. This observation confirms that the devices were at normal incidence to the particle beam, with no significant tilt. Tilted devices would result in an elongation along one of the dimensions. All tested devices showed a comparable active region extent in the range of 953-959 µm, with good agreement

Table 3.6: Extracted extent of the active area of the devices. The extent is obtained from the width of a top-hat function fitted on the efficiency profile of a given device.

Device	**Vertical size** X	**Horizontal size** Y	X/Y **size ratio**
W02	954 ± 4 µm	953 ± 4 µm	1.00 ± 0.01
W08	955 ± 4 µm	954 ± 4 µm	1.00 ± 0.01
W09	959 ± 4 µm	959 ± 4 µm	1.00 ± 0.01

within the quoted uncertainty. This matched the design expectations, as the different LGAD samples differ in the gain layer depth profile but not its lateral extent.

As stated previously, the devices investigated in this section have a pixel pitch of 1×1 mm^2 measured between the outer edges of the pixel JTE. As these devices all feature a 15 µm JTE width, the maximum design extent of the active/gain area is 970 µm. The fact that the measured extent of $\sim$955 µm is smaller can be accounted for by noting that the 970 µm design estimate does not account for JTE diffusion, which can further shrink the extent of the active region.

3.3.4 Summary

The performance of three devices from the first production batch of LGADs manufactured at Teledyne e2v was measured in a hadron test beam at the SPS using the MALTA Telescope. To comply with the HGTD requirements, the LGADs must achieve charge gain greater than 15 fC at the expected operational voltage levels. All tested devices reached this gain value, however bias voltages higher than V_{op} were necessary. At sufficiently high voltage, the sample from W09 collected 24 fC at 420 V bias voltage.

The devices demonstrated excellent hit efficiency, surpassing the 97% threshold already below V_{op}. All measured LGADs achieved timing resolution better than 50 ps, with W08 and W09 devices improving further beyond the 40 ps requirement and reaching a superior timing resolution below 20 ps. To improve the accuracy of the timing measurements, future measurements should utilise an oscilloscope with a faster sampling rate and a higher bandwidth, and use a reference device with even better timing resolution, around 20-30 ps.

3.4 Characterisation of neutron-irradiated LGAD sensors

Irradiation characterisation of silicon sensors is necessary to understand the changes in the sensor's properties in a radiation environment. The LGAD sensors within the HGTD detector need to withstand fluence greater than 2.5×10^{15} 1 MeV $n_{eq}cm^{-2}$ [58]. Commonly, selected samples are exposed to proton and neutron radiation in dedicated facilities in a controlled manner. Afterwards, their performance is studied as a function of received radiation fluence. In the case of LGADs, the two most prominent consequences of radiation damage are the increase in the device leakage current and the reduction of the gain layer effective doping. This section discusses the techniques used to characterise neutron-irradiated LGAD sensors and presents the obtained results.

3.4.1 Neutron irradiation of LGAD samples

The 1×1 mm^2 LGAD samples selected for irradiation were taken from wafers W02, W08, and W09 from Batch 1 of LGAD production by Teledyne e2v. The devices were irradiated at the JSI TRIGA Mark II reactor at the Institute Jožef Stefan in Ljubljana, Slovenia [79, 80]. The reactor produces neutrons as its Uranium-235 fuel undergoes nuclear fission. As neutrons of different energies cause different defects in silicon, the NIEL hypothesis scaling is applied to normalise the received fluence to that of 1 MeV neutrons [81]. The NIEL scaling damage factor for the TRIGA reactor is 0.88 ± 0.05 [82]. The position of the samples relative to the fuel rods when inserted into the reactor and the total exposure time dictates the neutron fluence received. The equivalent flux is typically between 1.7-3.1$\times10^{12}$ 1 MeV $n_{eq}cm^{-2}s^{-1}$ [80]. At the quoted flux, the irradiation of a sample to the fluence of 10^{16} 1 MeV $n_{eq}cm^{-2}$ takes roughly 1.5 hours. The accuracy of the equivalent fluence is approximately $\pm10\%$ [82].

Two successive irradiation campaigns were carried out at the TRIGA reactor. The first irradiation campaign in 2022 targeted fluences of 1×10^{13}, 1×10^{14}, 1×10^{15}, and 1×10^{16} 1 MeV $n_{eq}cm^{-2}$, with up to eight 1×1 mm^2 LGAD devices from each wafer per fluence level. Guided by the preliminary results from the 2022 campaign, the target fluences of interest for the second campaign in 2023 were chosen as 2×10^{14}, 5×10^{14}, 2×10^{15}, and 3×10^{15} 1 MeV $n_{eq}cm^{-2}$.

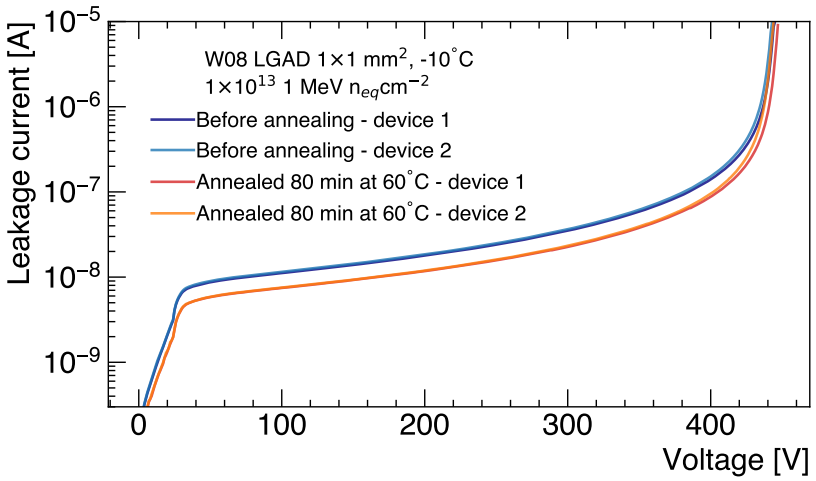


Figure 3.39: The effect of beneficial annealing at 60°C for 80 minutes on the leakage current. Two 1×1 mm^2 LGAD samples from W08 are shown – labelled 'device 1' and 'device 2', both before and after beneficial annealing. The samples were irradiated to the fluence of 1×10^{13} 1 MeV $n_{eq}cm^{-2}$. The measurements were taken at -10°C.

3.4.1.1 Device storage and annealing

To prevent annealing, irradiated samples are typically kept at low temperatures. Following irradiation, the LGAD samples were stored at -25°C until residual radiation activity dropped below safety limits and then transported in a cool box to the OPMD laboratory in Oxford. As the samples were not exposed to an elevated temperature and the total transportation time was limited (2-3 days), any annealing effects within this period are considered negligible. For long-term storage, the devices are kept in a freezer at -40°C.

Over a short period of time (order of weeks) at room temperature, the radiation damage effects have been shown to decrease [35]. This process is referred to as *beneficial annealing*, previously discussed in Section 2.4.3. Before electrical characterisation, the irradiated LGAD devices were subjected to beneficial annealing at a temperature of 60°C for 80 minutes. The rate of beneficial annealing increases with temperature. This is a common approach to ensure the best possible performance of irradiated sensor [83, 84]. As illustrated in Figure 3.39, the magnitude of the leakage current of the irradiated samples decreases after beneficial annealing, but the breakdown voltage does not change significantly. However, annealing over a long time period has detrimental effects on the detector performance as the space charge starts to increase [35]. Caution should be taken not to anneal the devices too much.

3.4.1.2 Leakage current scaling with neutron fluence

After irradiation, the leakage current of the LGAD devices increases. Therefore, samples irradiated to high fluence must be operated at low temperatures, otherwise thermal runaway may occur. Thermal runaway occurs when high leakage current causes significant heating of the device, which increases the number of thermally-generated charge carriers. A higher number of charge carriers increases the leakage current, further increasing the heat dissipation until the device cannot sustain the current, resulting in permanent damage [85].

While performing capacitance and leakage current measurements, the irradiated samples are placed on a metal chuck whose temperature can be controlled using the ATT Cooling Unit L60 chiller [86] with Galden HT 135 [87] used as a coolant liquid. The chiller control unit provides a reading of the chuck's temperature within 0.01°C. Given that the sample is in thermal contact with the chuck and is much smaller in size, the temperature of the sample is considered to be the same as that of the chuck. The humidity inside the probe station is kept low by a constant supply of dry air blown over the surface of the chuck. Increased humidity could lead to water droplets or ice crystals forming on the surface of the sensor. The current-voltage curves for the irradiated devices from wafer W08 are shown in Figure 3.40. For visual clarity, only one device per irradiation level is shown. The plot shows that both the magnitude of the leakage current and the breakdown voltage increase with radiation fluence. The non-irradiated sample is not included as its leakage before breakdown at -20°C is below the sensitivity of the measurement setup (< 1 pA).

3.4.2 Active gain fraction after irradiation

One of the main consequences of radiation damage on LGADs is the drop in the device gain. This is a crucial effect, as the charge gain directly influences the detector's timing resolution, hence heavily irradiated LGADs tend to show worse timing resolution. Usually, a greater bias voltage is required to achieve a comparable resolution as before the radiation damage, which, in combination with the increased device leakage current, leads to higher power dissipation of the device [88].

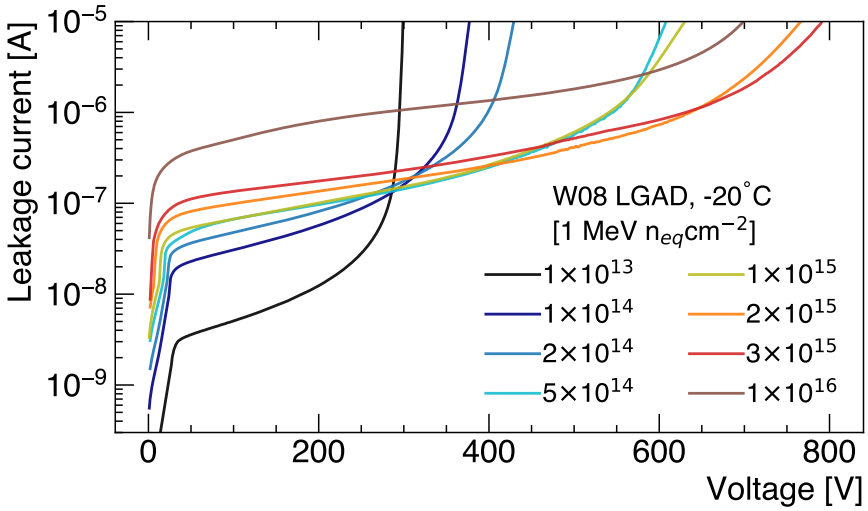


Figure 3.40: The leakage current as a function of bias voltage for neutron-irradiated 1×1 mm^2 LGAD samples from wafer W08. All samples underwent beneficial annealing at 60°C for 80 minutes. The measurements were taken at -20°C.

The gain decrease with radiation fluence can be parametrised with the acceptor removal coefficient c_n. At a given neutron fluence ϕ, the gain layer depletion voltage V_{gl} is related to the acceptor removal coefficient c_n as

$$\frac{V_{gl}(\phi)}{V_{gl}(\phi=0)} = e^{-c_n\phi}, \tag{3.11}$$

where $V_{gl}(\phi=0)$ denotes the gain layer depletion at zero fluence – before irradiation [57]. The ratio on the left-hand side of Equation 3.11 is also known as the *active gain fraction*. Note that despite c_n being referred to as the 'removal' coefficient, the boron dopants are not physically removed from the gain volume but only displaced due to the radiation damage [89]. It is the displacement within the lattice rather than complete removal which lowers the effective doping, reducing the charge gain.

For non-irradiated sensors, the gain layer depletion voltage $V_{gl}(\phi=0)$ can be extracted from the $1/C^2$-V curve (referred to as the *CV method*), using the principles presented in Section 3.2.2. The capacitance characteristic of a non-irradiated LGAD device does not show a strong frequency dependence up to the frequency of ~100 kHz. Above this value, the capacitance decreases due to the shunting of the AC signal frequency to the ground before the full sensor volume can be explored [57]. However, the capacitance-frequency characteristic of an irradiated LGAD sensor differs from that

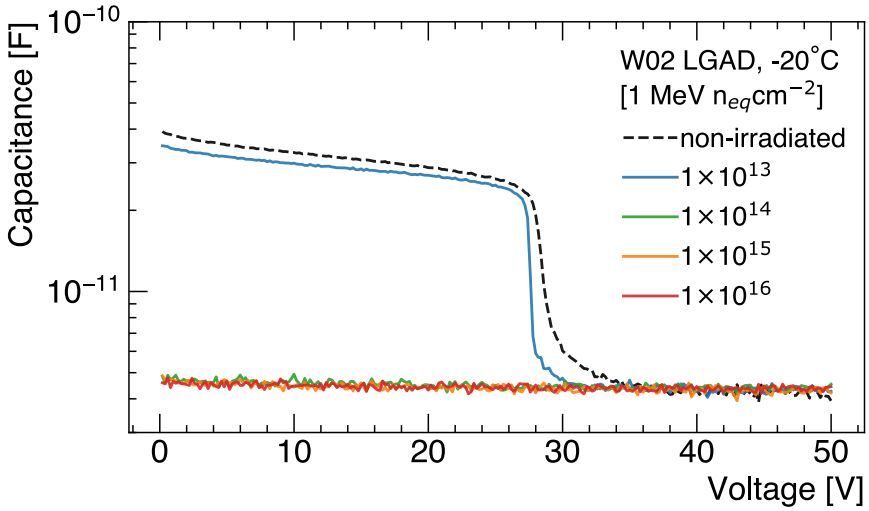


Figure 3.41: The pad capacitance as a function of bias voltage for neutron-irradiated 1×1 mm^2 LGAD samples from wafer W02. Measurements taken at AC signal frequency f = 100 kHz. All samples underwent beneficial annealing at 60°C for 80 minutes. The measurements were taken at -20°C.

of non-irradiated devices. In particular, the range of suitable AC signal frequencies to perform capacitance measurements is reduced, favouring frequencies only up to a few kHz [90]. One of the reasons for the frequency dependence is the introduction of radiation defects. The trapping and de-trapping time constants of the defects (the order of µs to ms) influence the time response to the applied AC voltage [91]. The effect of the suitable frequency range reduction can be seen in Figure 3.41, which compares the capacitance characteristic of a non-irradiated 1×1 mm^2 LGAD to the irradiated devices at the signal frequency f = 100 kHz. At this frequency, the curves for samples irradiated to the fluence of 1×10^{14} 1 MeV $n_{eq}cm^{-2}$ and above do not show any features which would allow for $V_{gl}(\phi)$ value extraction.

3.4.2.1 Leakage Current Transition (LCT) method

Instead of employing the CV method, $V_{gl}(\phi)$ can also be determined from the derivative of the leakage current-voltage (IV) curve. This method is sometimes referred to as the *leakage current transition* (LCT) method [89]. The LCT method relies on the sharp increase of the leakage current as the gain layer depletion voltage V_{gl} is reached, which results in a prominent peak in the current derivative dI/dV curve.

The following derivation serves to justify the presence of a leakage current transition at V_{gl}. For an idealised semiconductor junction under an applied bias voltage V, the width of the depletion region w is

$$w = \sqrt{\frac{2\varepsilon}{qN_{eff}}(V + V_{bi})}, \tag{3.12}$$

where ε is the permittivity, q is the elementary charge, N_{eff} is the effective doping density, and V_{bi} is the built-in potential [20]. Without the loss of generality, for the rest of the argument, it will be assumed that V_{bi} is small compared to the applied V. Considering an LGAD junction n^{++}-p^{+}-p^{-}, the effective doping of the n^{++}-layer is much greater than p^{+} (gain layer) or p^{-} (substrate) and therefore the width of the junction will grow from the n^{++}-p^{+} interface towards the p^{-} substrate. The substrate will be reached (by definition) at the gain layer depletion voltage V_{gl}. At bias voltages above V_{gl}, the expression for the width of the junction must be modified as the effective doping density N_{eff} and the permittivity ε are different between the p^{+} and p^{-} layers. Hence the full expression for the depletion width w in an idealised n^{++}-p^{+}-p^{-} junction is

$$w = \begin{cases} \sqrt{\frac{2\varepsilon^{+}}{qN^{+}_{eff}}V} & \text{for } V \leq V_{gl} \\ \sqrt{\frac{2\varepsilon^{+}}{qN^{+}_{eff}}V_{gl}} + \sqrt{\frac{2\varepsilon^{-}}{qN^{-}_{eff}}(V - V_{gl})} & \text{for } V \geq V_{gl} \end{cases}, \tag{3.13}$$

where the quantities have the same meaning as before, but a superscript $+$ or $-$ is used to identify those relating to p^{+} and p^{-} layers, respectively. Considering the relative doping of the layers, it is also true that $N^{+}_{eff} >> N^{-}_{eff}$.

As the leakage current flowing across the junction is primarily due to thermally generated electron-hole pairs generated within the depleted region, its magnitude is proportional to the volume of the depleted region [92]. For a sensor where the cross-sectional area A is constant and fully laterally depleted, the leakage current can be considered as proportional to the depletion width, given by the right-hand side of Equation 3.13. Then the derivative with respect to the voltage V is

$$\frac{dI}{dV} \propto \begin{cases} \sqrt{\frac{2\varepsilon^{+}}{qN^{+}_{eff}}\frac{1}{V}}, & \text{for } V < V_{gl} \\ \sqrt{\frac{2\varepsilon^{-}}{qN^{-}_{eff}}\frac{1}{(V-V_{gl})}}, & \text{for } V > V_{gl} \end{cases}, \tag{3.14}$$

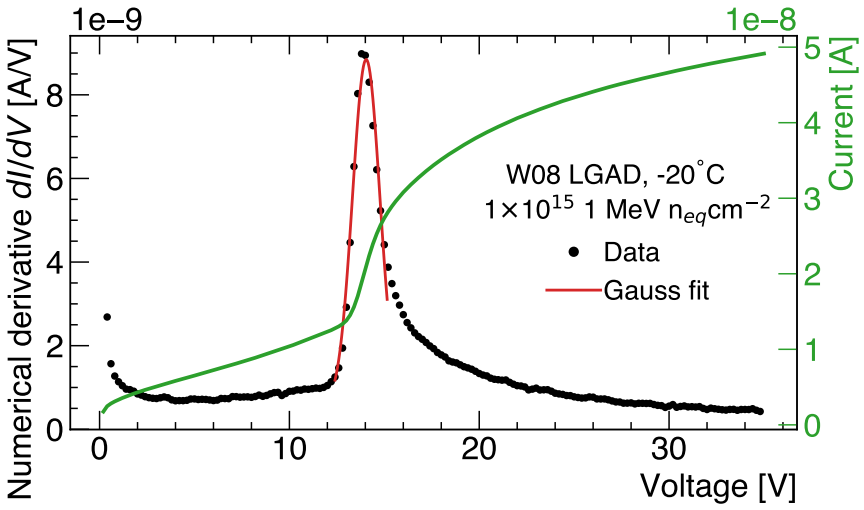


Figure 3.42: The numerical derivative of the leakage current with a Gaussian fit of the peak (left axis). The leakage current over the identical voltage range from which the derivative is extracted is shown in green (see right axis for scale). The sample is an LGAD from wafer W08 neutron-irradiated to a fluence of 1×10^{15} 1 MeV $n_{eq}cm^{-2}$. The data was taken at -20°C.

with the value at V_{gl} undefined. The derivative is finite when approached from below, but infinite when the limit from above is taken. In a non-ideal case without a sharp boundary between the p^+ and p^- layers and taking into account the resolution of the measurement devices, the undefined transition point at V_{gl} manifests as a peak of finite amplitude and width. By fitting this peak with a Gaussian function and associating the mean of the Gaussian distribution with the V_{gl} value, the gain layer depletion voltage is obtained.

An example data fit with the LCT method is shown in Figure 3.42, where the leakage current (in green - see right axis for scale), its derivative, and the Gaussian fit with the extracted V_{gl} value are shown for a 1×1 mm^2 LGAD sensor from wafer W08 irradiated to a fluence of 1×10^{15} 1 MeV $n_{eq}cm^{-2}$. All leakage current data presented in this section was measured using a Keithley SCS 4200 parameter analyser integrated with a probe station SemiProbe SA-12. The voltage was ramped from 0 V to 35 V with the voltage step of 0.2 V. The time between applying a voltage step and taking a current measurement (the *delay* setting) is set to 1.5 s.

To compute the numerical derivative, the *symmetric difference quotient* formula is used [93], where the derivative of a function f at a point x is given by

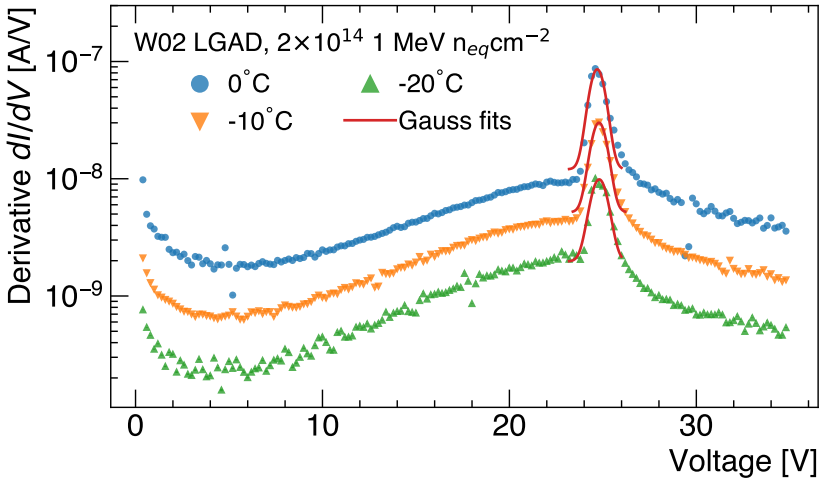


Figure 3.43: The current derivative dI/dV of an LGAD W02 irradiated to a fluence of 2×10^{14} 1 MeV $n_{eq}cm^{-2}$ taken at 0°C (blue), -10°C (orange), and -20°C (green). The peak of each dataset is fitted with a Gaussian distribution.

$$f'(x) = \frac{f(x+h) - f(x-h)}{2h}, \tag{3.15}$$

with h being the measurement step. Compared to the similar Newton's difference quotient (shown here in the *forward difference* form)

$$f'(x) = \frac{f(x+h) - f(x)}{h}, \tag{3.16}$$

where the error is proportional to h, the symmetric difference quotient formula's error is sensitive to the second order h^2, hence providing a more accurate approximation to the tangent line [93]. As mentioned above, the measurement step for the data presented in this section is h = 0.2 V. The fitting algorithm selects the maximum value of the numerical derivative and fits a Gaussian distribution within a 3 V window containing the selected maximum as shown in Figure 3.42. Since V_{gl} is the mean of the Gaussian, the error on the fit mean gives the V_{gl} uncertainty that is propagated further.

3.4.2.2 Temperature variation

Even though the magnitude of the leakage current and its derivative depend on the temperature at which the measurement is taken, V_{gl} should not exhibit a strong temperature dependence. The current derivative was calculated for data at three different temperature points (-20°C, -10°C, and 0°C) and is presented in Figure 3.43. In this

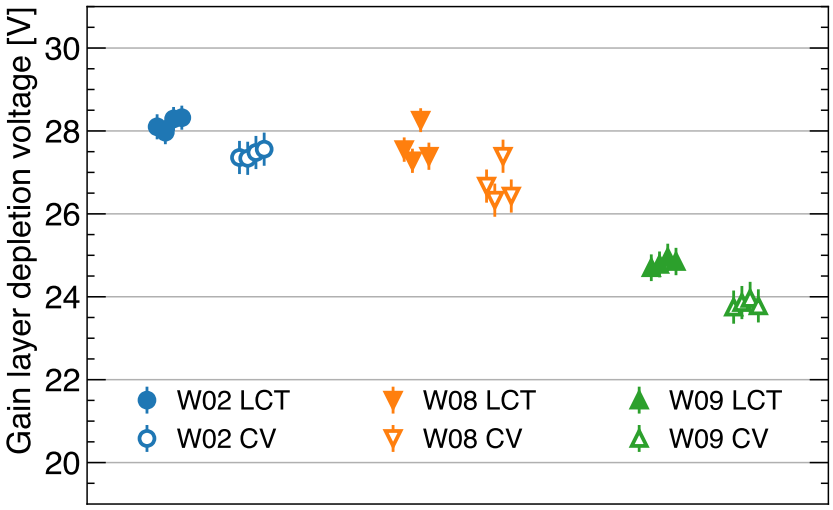


Figure 3.44: The comparison of the gain layer depletion voltage values extracted using the capacitance-voltage (CV, empty markers) and the leakage current transition (LCT, full markers) methods. The LGAD devices are from wafers W02 (blue), W08 (orange), and W09 (green). For each wafer, four devices irradiated to the fluence of 1×10^{13} 1 MeV $n_{eq}cm^{-2}$ are shown. Measurements taken at -20°C.

example, the device is a 1×1 mm^2 LGAD from wafer W02 that has been irradiated to a fluence of 1×10^{14} 1 MeV $n_{eq}cm^{-2}$. The figure shows that the Gaussian fit identifies the V_{gl} value with <0.1 V variation irrespective of the sample temperature. Given that the temperature does not play a significant role in the V_{gl} extraction, to prevent thermal runaway for highly irradiated sensors, measurements at -20°C were used for the following investigation.

3.4.2.3 LCT method validation

To validate the use of the LCT method for V_{gl} extractions, its predictions are compared to those obtained from the CV method. The comparison is performed on LGAD samples irradiated to the fluence of 1×10^{13} 1 MeV $n_{eq}cm^{-2}$ from wafers W02, W08, and W09 with four LGAD devices per wafer. The fluence is chosen such that both methods can give meaningful values for the V_{gl} parameter. The V_{gl} values are shown in Figure 3.44, with the corresponding devices displayed next to each other (LCT - filled markers, CV - empty markers). Both methods probe the same devices giving a direct comparison. The data shows a high degree of correlation between the two data sets, with a correlation coefficient of $R = 0.9986$. The LCT method tends to estimate the V_{gl} value on average

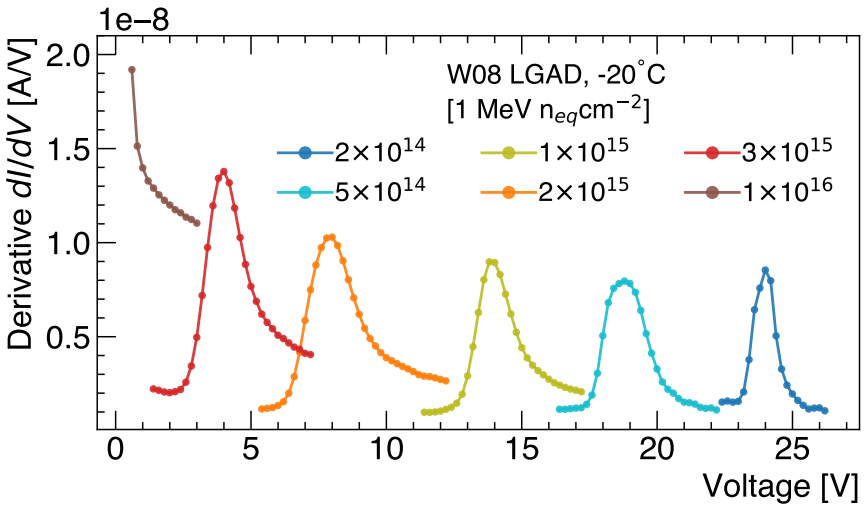


Figure 3.45: The current derivative dI/dV of LGAD W08 samples irradiated to a fluences between 2×10^{14} and 1×10^{16} 1 MeV $n_{eq}cm^{-2}$ taken at -20°C. For visual clarity, only a subset of data which features the derivative peak is shown for each device.

0.9 V $\pm$ 0.1 V higher than the CV method. This factor is accounted for in the uncertainty calculations in the following analysis when values from the two different methods are compared. A similar level of agreement (within 1 V) is also observed in other works [57].

3.4.3 Acceptor removal coefficient calculation

With the increased neutron fluence, the amount of active gain decreases, resulting in a lower gain layer depletion voltage. The shifting position of the peak of the dI/dV curve, which is caused by the decrease of V_{gl} is illustrated for samples from wafer W08 in Figure 3.45. The fitting algorithm cannot extract any gain layer depletion voltage from devices irradiated to 1×10^{16} 1 MeV $n_{eq}cm^{-2}$ neutron fluence as no peak is found.

When calculating the active gain ratio according to Equation 3.11, the value of the gain layer depletion voltage before irradiation is also required. For samples irradiated to 2×10^{14}, 5×10^{14}, 2×10^{15}, and 3×10^{15} 1 MeV $n_{eq}cm^{-2}$, the $V_{gl}(\phi = 0)$ values were obtained before irradiation using the CV method and these values are used in the calculations for each corresponding device. The pre-irradiation data is not available for the samples irradiated to other fluences. In these cases, the wafer average is used instead, and the average value's uncertainty is propagated through the calculation.

Table 3.7: The active gain fraction of LGAD samples from wafers W02, W08, and W09 for neutron fluences up to 5×10^{15} 1 MeV $n_{eq}cm^{-2}$. The values are an average of up to four devices per wafer irradiated to the given fluence.

Fluence ϕ	**Active gain fraction**		
[1 MeV $n_{eq}cm^{-2}$]	W02 LGAD	W08 LGAD	W09 LGAD
1×10^{13}	0.98 ± 0.07	0.99 ± 0.08	0.98 ± 0.08
1×10^{14}	0.88 ± 0.07	0.89 ± 0.07	0.88 ± 0.07
2×10^{14}	0.85 ± 0.08	0.84 ± 0.07	0.81 ± 0.08
5×10^{14}	0.70 ± 0.07	0.67 ± 0.07	0.68 ± 0.08
1×10^{15}	0.49 ± 0.06	0.47 ± 0.07	0.44 ± 0.08
2×10^{15}	0.27 ± 0.07	0.26 ± 0.07	0.23 ± 0.07
3×10^{15}	0.10 ± 0.07	0.12 ± 0.07	0.15 ± 0.10

The average active gain fraction values per neutron fluence are listed in Table 3.7. Each value is an error-weighted average of up to four devices measured per fluence per wafer. The uncertainty shown combines the uncertainties from the LCT-extracted $V_{gl}(\phi)$ and the CV-extracted $V_{gl}(\phi = 0)$ values in quadrature. The data is also shown in Figure 3.46 with the acceptor removal coefficient c_n values extracted from an exponential fit according to Equation 3.11. The extracted acceptor removal coefficient ranges from $(7.1 \pm 0.8)\times10^{16}$ cm^2 for wafer W02 to $(7.8 \pm 1.0)\times10^{16}$ cm^2 for wafer W09. It should be noted that the three extracted coefficients agree within the measurement uncertainty.

A lower c_n value implies a better radiation tolerance as the gain layer fraction decreases at a slower rate with respect to the radiation fluence received. Depending on the exact gain layer parameters, the acceptor removal coefficients found in the literature mostly fall within the range of 4-9$\times10^{16}$ cm^2 [57]. Values below 4×10^{16} cm^2 are only achievable for LGAD devices with additional fabrication improvements for radiation hardness, such as carbon implantation [84], which are not implemented in the devices investigated in this thesis. Carbon implantation in the gain layer can mitigate boron acceptor removal by replacing boron in defect formation. However, carbon implantation also has disadvantages, such as boron deactivation by carbon and increased leakage currents. Further details on carbon-enriched LGAD design can be found in [57].

For devices with c_n values of approximately 7×10^{16} cm^2, Equation 3.11 predicts an active gain fraction of only about 0.001 after irradiation to 1×10^{16} 1 MeV $n_{eq}cm^{-2}$. With

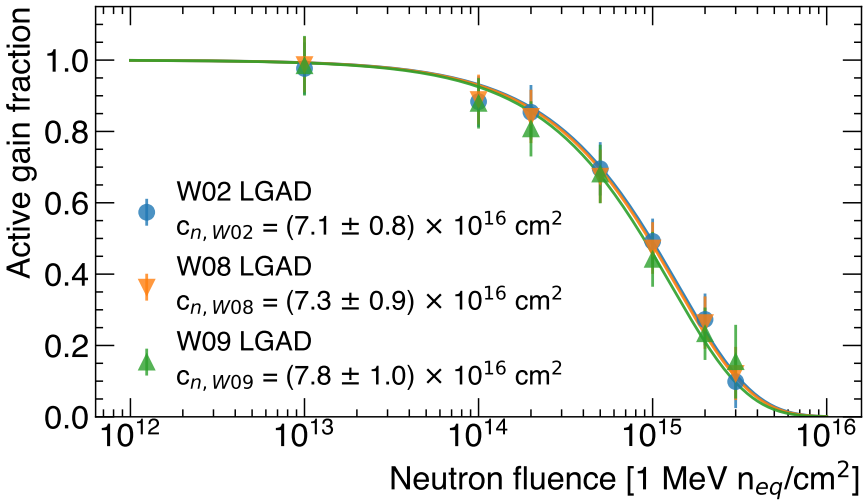


Figure 3.46: The active gain fraction of LGAD samples from wafers W02 (blue), W08 (orange), and W09 (green) as a function of the neutron fluence. Each data point represents an average of up to four devices per wafer irradiated to a given fluence. Each dataset is fitted with an exponential decay function, and the extracted value of the acceptor removal coefficient is shown.

pre-irradiation V_{gl} of about 25 V, this means that as little as 2.5 mV would be sufficient to deplete the gain layer if the model can be extrapolated to such fluence. The values of the extracted acceptor removal coefficient hence validate the absence of a characteristic peak associated with the V_{gl} value for devices irradiated to 1×10^{16} 1 MeV $n_{eq}cm^{-2}$.

3.4.4 Summary

In the studies presented, sets of 1×1 mm^2 LGAD devices from three wafers manufactured by Te2v were neutron irradiated up to the fluence of 1×10^{16} 1 MeV $n_{eq}cm^{-2}$. The leakage current transition (LCT) method was validated and successfully used to extract the gain layer depletion voltage V_{gl} for the irradiated sensors up to 3×10^{15} 1 MeV $n_{eq}cm^{-2}$. By applying a model assuming an exponential decrease of the active gain fraction with neutron fluence, the acceptor removal coefficient for the three investigated wafers was deduced to be between 7-8$\times10^{16}$ cm^2. These findings show that the radiation hardness of the Te2v-LGADs is comparable to non-carbon-enriched productions from other manufacturers. To lower the acceptor removal coefficient value, carbon implantation or other designs improving radiation hardness need to be implemented.

3.5 Laser injection measurements of irradiated LGAD devices

This section describes the use of the laser injection method to evaluate the charge gain and timing performance of LGADs before and after neutron irradiation up to the fluence of 2×10^{15} 1 MeV $n_{eq}cm^{-2}$. The investigated devices were 1×1 mm^2 LGADs manufactured by Te2v from wafer 2 (W02), wafer 8 (W08), and wafer 9 (W09). The neutron irradiation was carried out at the TRIGA reactor in Ljubljana, as discussed in Section 3.4.1. The radiation damage affects the effective doping of the gain layer, which directly influences the gain of the device and, hence, its timing performance. For the LGADs in the HGTD detector, in order to guarantee good timing performance, it is required that the most probable collected charge is larger than 4 fC and that the timing resolution is better than 50 ps, up to the fluence of 2.5×10^{15} 1 MeV $n_{eq}cm^{-2}$ [58]. For 50 µm thick sensors, this corresponds to a charge gain of $\sim$10. The collected charge requirement should be fulfilled at a bias voltage below 600 V, as Single Event Burnout (SEB) is likely at higher bias voltages [71].

The laser injection measurements are commonly used to characterise LGAD devices and other silicon particle detectors [94–96]. For device testing, a fast pulsed laser incident on a device can be used to mimic a high-energy particle crossing the detector [97]. A current is induced by the drift of the electron-hole pairs generated inside the sensor volume due to the laser beam [98]. The induced current signal can then be measured and used to infer the sensor behaviour. One of the major advantages of the laser injection method is the repeatability of the measurements, where the laser can be set to generate photon beams at a given intensity and fired at fixed time intervals. Without the need for large particle accelerators, a suitable laser system can be set up even in a small-sized laboratory.

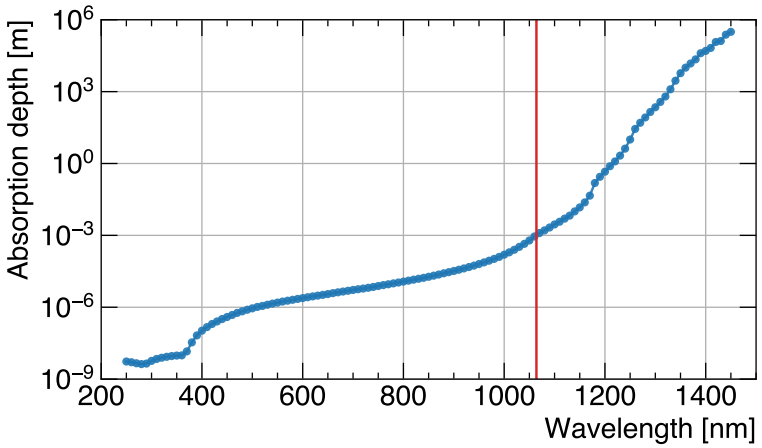


Figure 3.47: The absorption depth in silicon as a function of wavelength for visible and infrared photons. The red vertical line marks the wavelength of 1064 nm. Displayed values correspond to that of an intrinsic silicon at 300 K [100].

3.5.1 Principle of operation

The laser wavelength λ = 1064 nm is often chosen for laser injection measurements [95, 99]. This choice is motivated by the fact that silicon is more transparent for infrared light compared to photons in the visible region, as illustrated in Figure 3.47. The IR photons of ∼1000 nm wavelength with absorption depth of ∼1000 µm have an approximately uniform absorption probability in devices with a typical active depth of tens micrometres [100]. Therefore, the 1064 nm laser will generate a uniform distribution of electron-hole pairs along its path. In other studies, setups with laser wavelength λ = 404 nm or 660 nm [95] are also common, though for different applications. For λ > 1200 nm, silicon becomes fully transparent and laser injection is hence unsuitable.

To first order, the amount of charge generated inside the volume of the device is proportional to the intensity of the photon beam. As the beam propagates through the material, the photons interact with the material with a certain probability. If such interaction occurs, the photon can be considered to be 'removed' from the beam. As such, this process can be modelled as an exponential decay, hence the intensity I of the beam decreases according to

$$I(x) = I_0 e^{-\alpha x}, \tag{3.17}$$

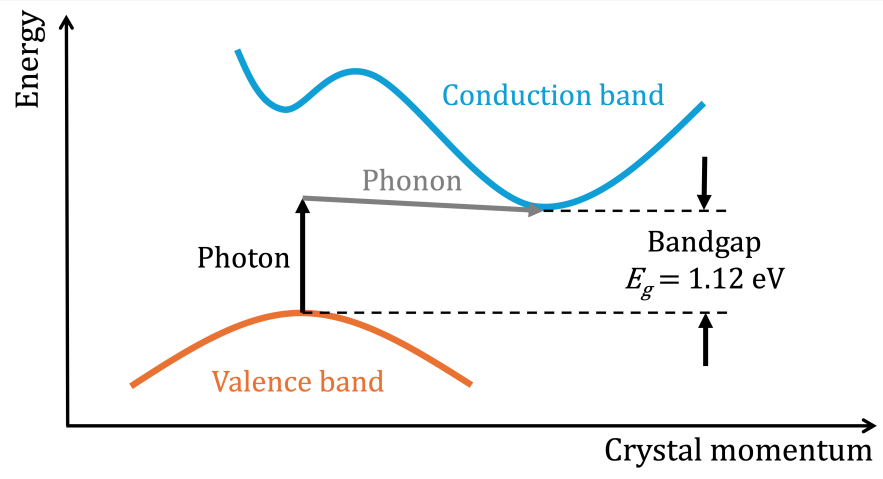


Figure 3.48: Energy as a function of crystal momentum for silicon, showing valence (red) and conduction (green) bands. To promote an electron from the highest-energy state in the valence band to the lowest-energy state in the conduction band, both photon (vertical arrow) and phonon (horizontal arrow) are necessary as a change in momentum is required.

where x is the distance travelled in the material, I_0 is the initial beam intensity (corresponding to x = 0 m) and α is the material-specific wavelength dependent absorption coefficient. The absorption depth, shown in Figure 3.47, is the reciprocal of the absorption coefficient α as it is defined as the distance after which the intensity is attenuated by a factor of $1/e$.

In addition to being wavelength dependent, the absorption coefficient α also varies with temperature. As the silicon bandgap is not direct (1.12 eV at room temperature), promoting an electron from the highest-energy state in the valence band to the lowest-energy state in the conduction band requires a change in crystal momentum [101]. Therefore, phonons must be involved in addition to the absorption of the infrared photon. This mechanism is illustrated in Figure 3.48. As the phonon density in a silicon lattice is temperature dependent, so does the absorption probability of an infra-red photon (leading to the electron excitation) vary with temperature [102]. *Svantesson and Nilsson* [103] showed that the silicon absorption coefficient α for 1064 nm photons has a temperature dependence that can be expressed as a power law

$$\alpha(T) = \left(\frac{T[K]}{172.3}\right)^{4.25} \text{cm}^{-1}, \tag{3.18}$$

where the temperature T is in the unit of Kelvin.

Assuming that the charge generated within the active silicon volume of thickness x is proportional to the reduction of laser beam intensity I, the generated charge Q follows

$$\begin{aligned} Q &\propto I(x=0) - I(x) \\ &\propto I_0(1 - e^{-\alpha(T)x}) \end{aligned}, \tag{3.19}$$

where Equation 3.17 is used to describe the exponential reduction of laser intensity $I(x)$ as the photons propagate through the material. For small temperature variations around 20°C of ±1°C only a small (±1.5%) charge variation is expected for λ = 1064 nm and x = 50 µm. However, if the temperature of the silicon is changed by tens of degrees, the temperature dependence causes a significant impact and cannot be ignored [103].

In an experiment, the incident intensity I_0 can be modified by tuning the operational parameters of the laser or by employing neutral-density (ND) filters. The advantage of ND filters is that they reduce the intensity of all wavelengths of light equally [104]. The transmitted intensity I through an ND filter of optical density d is given by

$$I = I_0 \times 10^{-d}, \tag{3.20}$$

where I_0 is the incident intensity [104].

3.5.1.1 Experimental laser setup

The setup at the OPMD laboratory uses a 1064 nm laser QCED106G-6410 by QD Laser [105] focused onto the device under test (DUT) as shown in Figure 3.49. According to the datasheet supplied by the manufacturer, the laser has a pulse width of 15.4 ps [106]. The laser spot has a size of ∼20×20 µm^2 positioned roughly in the centre of the DUT circular aperture. The laser focusing aperture Thorlabs GBE15-B [107] is mounted on a Standa linear stage [108], allowing for the adjustment of the distance between the aperture and the device (Z-axis). Additionally, the DUT is mounted on an XY stage (a pair of orthogonal Standa linear stages), allowing for a full 3D movement of the laser beam with respect to the device. All stepping motors on the linear stages have a step size of 1.25 µm. These components are enclosed in a thermally-insulated dark box together with a pair of temperature and humidity sensors Sensiron SHT35 [109] and a Meech Vortex Tube cooler [110]. The signals from the DUT and laser trigger

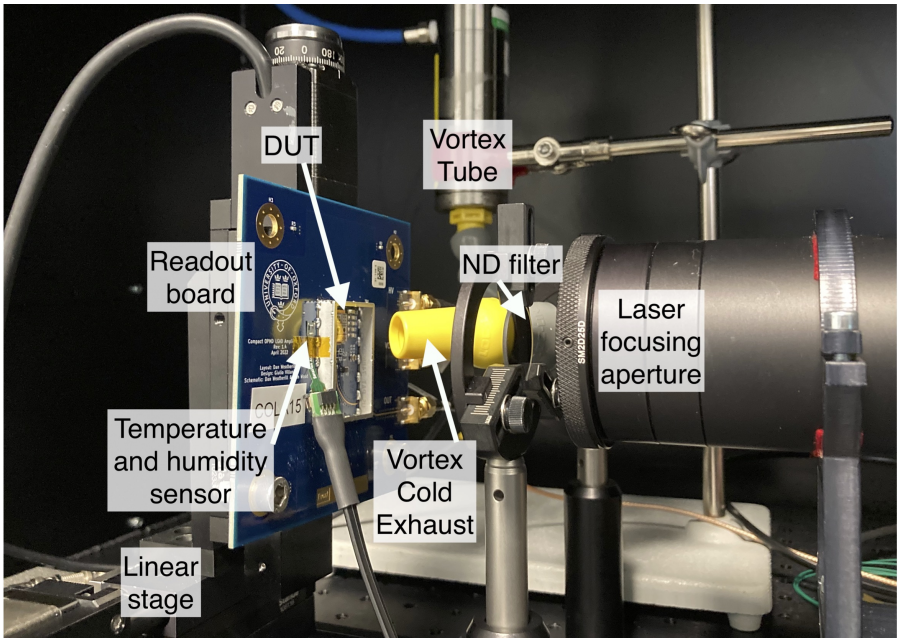


Figure 3.49: The experimental laser setup. The photon beam emerging from the laser focusing aperture is attenuated as it passes through an ND filter before hitting the DUT. The DUT signal is amplified by the readout board mounted on a linear stage used to move the device. Cooling is achieved by blowing cold dry air from the vortex cooler. To prevent condensation, temperature and humidity are monitored when data is taken. The whole setup is enclosed in a dark thermally insulated box.

are sampled using a Keysight UXR0134A oscilloscope (128 GSa/s, 13 GHz bandwidth) [111]. A Keithley 2410 [112] unit is used to supply high voltages (up to 800 V), while low voltage powering of the readout and laser electronics (up to 6 V) is provided by a pair of Aim-TTi QL355TP power supplies [113]. The data acquisition is coordinated using a PC which communicates with the oscilloscope, the HV power supply, the laser, and the motion stages via USB or Ethernet.

It was observed that when the laser is operated towards the low intensity end of its operational range, the pulse-to-pulse variation of the laser output intensity increases. To avoid this issue, the laser is operated at higher intensity mode, with the intensity subsequently attenuated using an ND 1.0 filter (optical density 1). This change corresponds to a reduction of the intensity by a factor of 10. This configuration is preferable when low laser intensities are desired for the measurements, though it should be noted that the ND filter affects the focal distance of the setup, hence device repositioning is necessary when the filter is inserted.

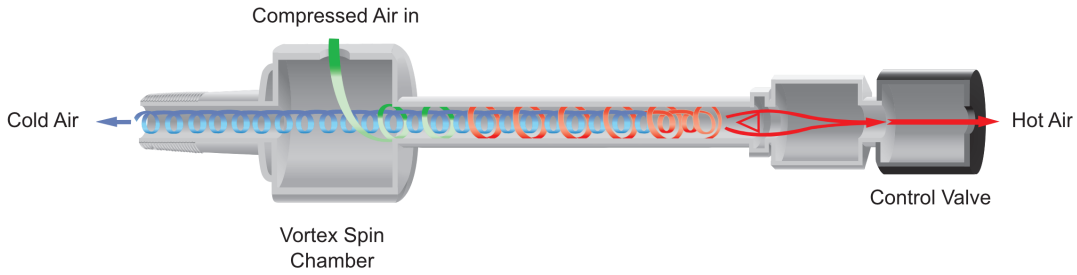


Figure 3.50: Diagram of the basic operation of a vortex cooler. Pressurised air enters tangentially into the *swirl chamber* through a *generator* where it starts to spin rapidly. The hot particles from the outer layer are allowed to escape through a nozzle, while the cold particles in the inner layer are forced in the opposite direction. The diagram is adapted from [110].

3.5.1.2 Vortex cooling

As discussed in Section 3.4.1, irradiated samples need to be kept at a cold temperature. When the devices are being tested, there are several possible methods for device cooling such as a Peltier chip, dry ice, or a chiller [114, 115]. The choice of a particular method heavily depends on the exact experimental configuration and technical constraints. Some methods, such as dry ice or liquid nitrogen, can be inconvenient due to the need for refills, especially when access to the test setup may be limited.

During the measurements, cooling of the sensor is achieved by a constant supply of cold air incident on the front side of the sensor supplied by a vortex cooler. The vortex cooler is a mechanical device that separates compressed air into separate hot and cold streams without any moving parts [116]. The basic principle of operation of a vortex cooler is illustrated in Figure 3.50. The use of a vortex cooler is suitable for small-scale experiments due to its small size and relative affordability [117]. This investigation uses the vortex cooler Meech Medium Vortex Tube with the Meech A21015 (white) generator [110].

The temperature of the cold air from the vortex cooler is controlled by the pressure of the dry air supply. The relation between the input pressure, controlled via a valve, and the air temperature at the vortex cold exhaust (measured using a Sensiron SHT35 sensor) is shown in Figure 3.51. The *cold operation* point for laser measurements is set at the dry air supply pressure of 6 bar, corresponding to an exhaust temperature of -16°C. The use of pressure above 6 bar is avoided due to the increased number of pressure

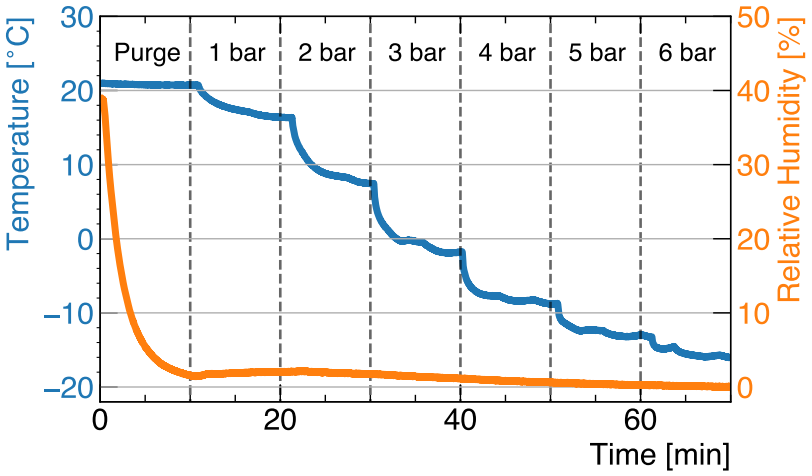


Figure 3.51: The temperature of the vortex tube cold exhaust and the relative humidity inside the dark box as the vortex dry air input pressure is increased up to 6 bar. The pressure is increased by 1 bar approximately every 10 minutes. The first 10 minutes are dedicated as the *Purge*, where dry air at room temperature is supplied into the box, causing a decrease in the relative humidity but not affecting the temperature.

drops observed, since the dry air supply cannot keep up with the high consumption rate. Before cooling, dry air at room temperature is supplied to the laser box until the humidity reading inside decreases below 2%. This process is referred to as the *Purge*.

3.5.1.3 Temperature calibration

Even though the temperature of the air supplied by the Vortex cooler is known, the temperature of the DUT itself can be higher, as it is still in thermal contact with the readout board. The leakage current I depends on temperature T according to

$$I(T) = I(T_0)\left(\frac{T}{T_0}\right)^2 \exp\left[-\frac{E_{eff}}{2k_B}\left(\frac{1}{T}-\frac{1}{T_0}\right)\right], \tag{3.21}$$

where $I(T_0)$ is the reference leakage current measured at temperature T_0, k_B is the Boltzmann constant, and E_{eff} = 1.214 eV [118].

The temperature scaling according to Equation 3.21 describes the leakage current change with temperature – the scaling itself is not applied to the data presented. The temperature of the DUT can be found by matching the leakage current recorded during the laser measurements to a reference leakage current taken at known temperatures. The reference leakage currents are recorded by the Keithley 2410 power supply used for reverse biasing while the DUT is being kept in a small dark thermally-insulated box

with known set temperatures between 0°C and -20°C (measurements taken with 1°C step). The devices are not exposed to any laser light during these measurements.

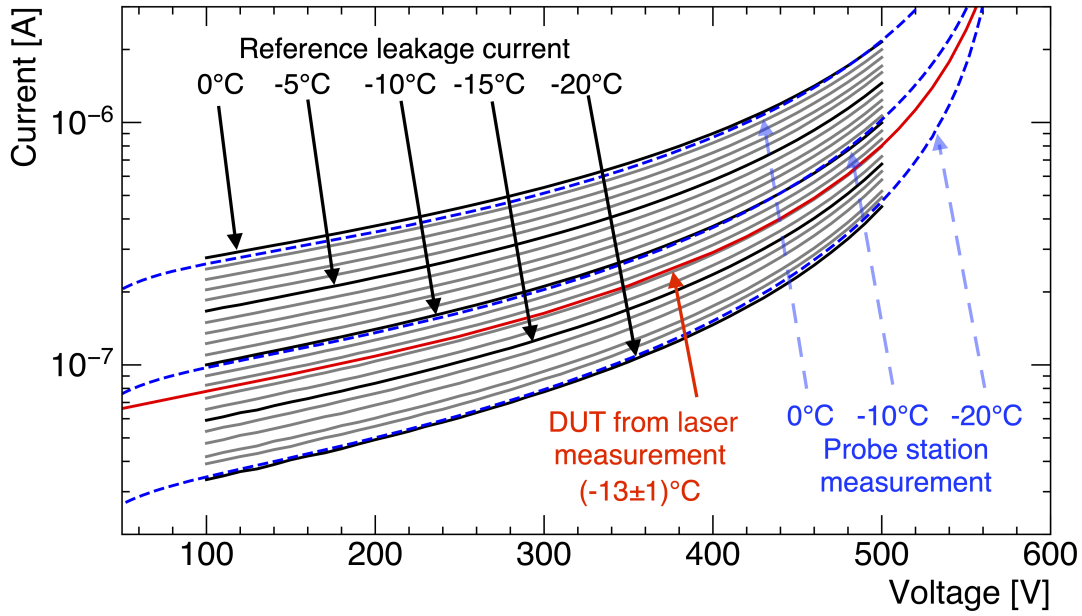
The reference leakage current measurements were taken for bias voltages in the range from 100 V to 500 V for W09 LGADs irradiated to 2×10^{14} (Figure 3.52a) and 5×10^{14} 1 MeV $n_{eq}cm^{-2}$ (Figure 3.52b). The reference data is shown as black and grey lines. The red line represents the leakage current curve obtained with vortex cooling. For both devices, the red line agrees well with the reference curve for -13°C measurement within a $\pm$1°C variation. As the position of the vortex cooler and the DUTs were kept fixed as much as possible, all investigated devices are considered to be at -13$\pm$1°C.

For validation and temperature cross-calibration, the device leakage current measured using a Keithley SCS 4200 during the characterisation of neutron-irradiated LGADs (see Section 3.4.1.2) is also compared to the reference temperatures in Figure 3.52 (plotted as dashed blue lines). The measurements at 0°C, -10°C, and -20°C are available. These agree with the corresponding reference leakage current curves within 1°C variation, hence demonstrating good calibration of the procedure. It should be noted that for the Keithley SCS 4200 measurements, the devices are measured as a bare die rather than bonded to a COLA readout board. However, as the leakage current increases significantly after irradiation, the contribution of the readout board is small compared to that of the DUT.

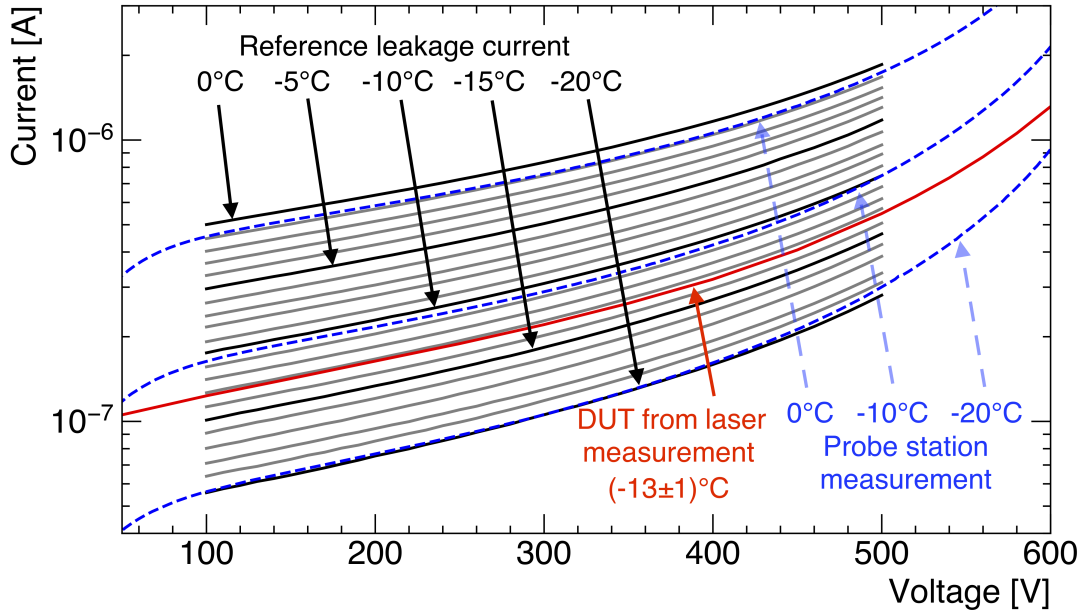
3.5.2 Data acquisition and processing

The current signal from the DUT is amplified by a COLA v1.4 readout board, which was discussed in Section 3.1.6. Following further signal amplification by a 28 dB TESEQ LNA 6901 voltage amplifier [74], the signal is recorded with the Keysight oscilloscope. To suppress high-frequency noise, a digital low-bandpass filter is applied at 1.5 GHz on the relevant oscilloscope channels. This setting was shown not to significantly deteriorate the sharpness of the LGAD signal while effectively eliminating high-frequency noise.

In addition to the signal from the DUT, the oscilloscope records the laser trigger signal, which is used to trigger the data acquisition. The trigger signal goes from low ($\sim$ -0.2 V) to high ($\sim$ 0.4 V) when the laser is fired, as shown in Figure 3.53. It should



(a) W09 LGAD 2×10^{14} 1 MeV $n_{eq}cm^{-2}$



(b) W09 LGAD 5×10^{14} 1 MeV $n_{eq}cm^{-2}$

Figure 3.52: The comparison of leakage current measurement at different temperatures for W09 LGAD 1×1 mm^2 devices neutron-irradiated to the fluence of 2×10^{14} (a) and 5×10^{14} 1 MeV $n_{eq}cm^{-2}$ (b). The grey and black solid lines show measurements between 0°C and -20°C (1°C step) where the device is in a dark cooled box at a known temperature. The red solid line represents the measurement with the Vortex cooling in the laser setup. The dashed-blue lines are validation measurements at 0°C, -10°C, and -20°C, obtained using a probe station. The calibration lines are used to determine DUT temperature with vortex cooling as -13°C ±1°C.

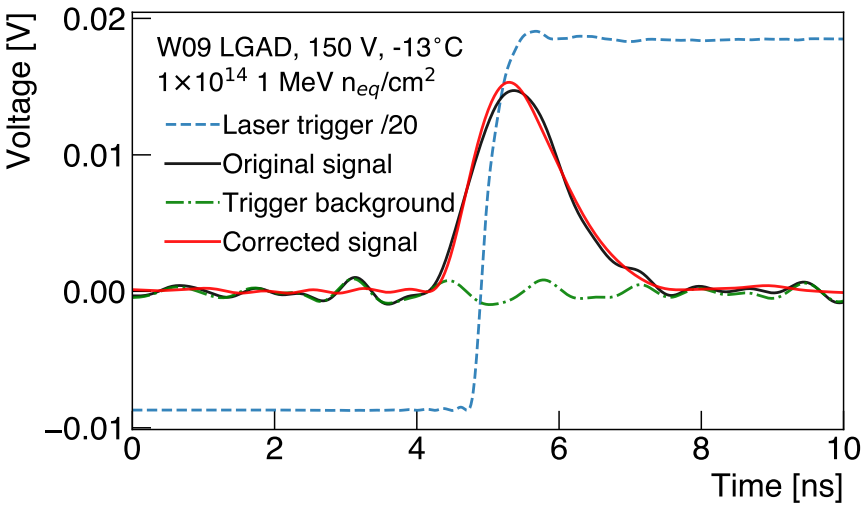


Figure 3.53: The effect of trigger background on the captured voltage signal from a W09 LGAD biased to 150 V while kept at -13°C. The *trigger background* is obtained when the device is not exposed to the photon beam, but the laser trigger is active. The corrected signal is calculated by subtracting the *trigger background* from the original voltage signal. The measured device was neutron irradiated to the fluence 1×10^{14} 1 MeV $n_{eq}cm^{-2}$. The shown curve represents the average over 1024 recorded signals.

be noted that the laser trigger signal has a small, but non-negligible effect on the DUT signal. Even when the laser shutter is completely closed and the DUT is not exposed to the photon beam, the DUT signal shows a small voltage fluctuation correlated with the laser trigger. The *trigger background* can be obtained by averaging the signal fluctuation over 1024 laser triggers to eliminate random electrical noise. During data analysis, the trigger background is subtracted from individual DUT waveforms. As the background is not influenced by the charge gain of the device, it is particularly important to perform this correction for small voltage signals, for example when measuring the response of a PiN device or a heavily irradiated LGAD. An example of this correction is shown in Figure 3.53.

Upon each trigger, the oscilloscope captured a 10 ns window of voltage signal from the DUT. Internal delays were configured to ensure that the initial 3 ns of the recorded window sufficiently preceded the laser beam's arrival, thus creating a *noise evaluation window*. The mean voltage within the noise window gives the *baseline* of the signal. The analysis algorithm identifies the maximum voltage as the peak of the signal, with the signal *amplitude* calculated as the difference between the baseline

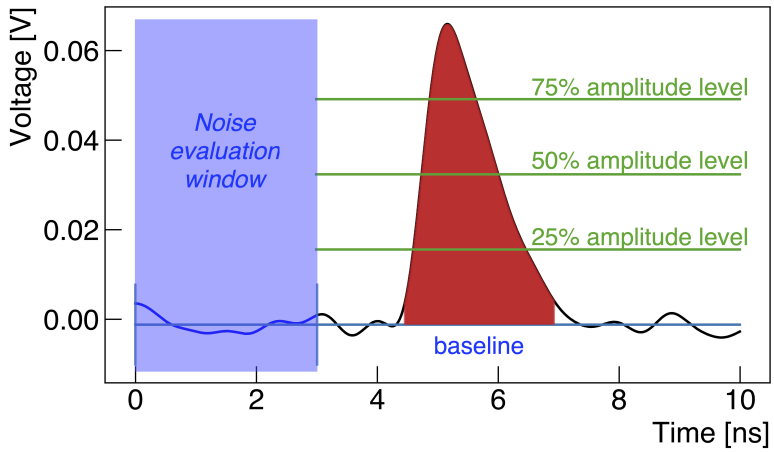


Figure 3.54: An LGAD signal as recorded by an oscilloscope within a 10 ns window. The first 3 ns are designated as the Noise evaluation window. The average voltage of the Noise widow is considered as the baseline, and the standard deviation as the noise. The difference between the baseline and the maximum voltage recorded within the last 7 ns is the signal amplitude (25%, 50%, and 75% amplitude level shown).

and the peak. The *extent of the signal* is found as the window around the maximum where the voltage relative to the *baseline* is at least 3 times greater than the standard deviation of the voltage within the *noise evaluation window*. A sample waveform with the analysis regions and parameters is shown in Figure 3.54. The red area between the baseline and the signal voltage within the *extent of the signal* is proportional to the charge collected by the DUT.

3.5.2.1 Charge gain

As the fabricated LGAD wafers also contain PiN devices which have the same device geometry but lack the charge multiplication layer, the LGAD charge gain can be obtained by directly comparing the electrical signals the devices produce. The charge gain $g(V)$ of an LGAD at a particular bias voltage V can be expressed as the ratio of the collected charge Q_{LGAD} compared to a PiN diode Q_{PiN}

$$g(V) = \frac{Q_{LGAD}(V)}{Q_{PiN}(V)}. \tag{3.22}$$

Given that all devices are exposed to the same photon beam and the same voltage signal readout chain is implemented, the ratio of the charge collected is approximately equal to the ratio of the area defined by the voltage signal (shown as the red region

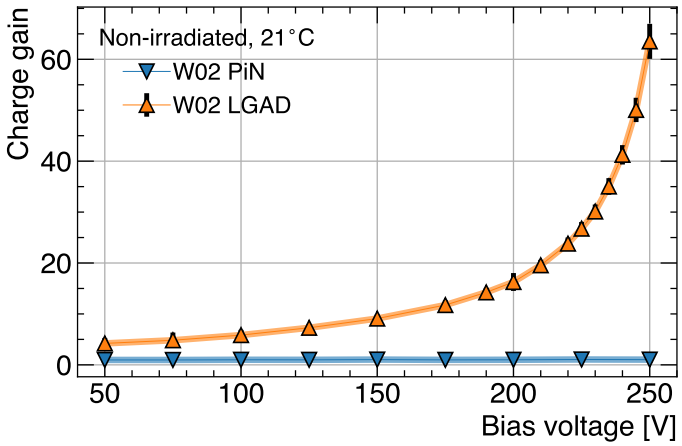


Figure 3.55: The charge gain of non-irradiated W02 LGAD and PiN for bias voltages from 50 V to 250 V. The W02 PiN has an average charge gain of 1 by definition, as it is the reference device. The measurements were taken at room temperature.

in Figure 3.54), giving

$$g(V) = \frac{Area_{LGAD}(V)}{Area_{PiN}(V)}. \tag{3.23}$$

Figure 3.55 demonstrates that, unlike the LGAD, the charge collected by the PiN does not increase significantly as the bias voltage is increased. The data is scaled such that the PiN device has an average charge gain of 1. In the bias voltage range from 50 V to 450 V, the average PiN signal area is $Area_{PiN}$ = 8.28 $\pm$ 0.44 pVs, which corresponds to a charge of 1.04 $\pm$ 0.05 fC using the combined transimpedance gain of the readout 7.94$\times 10^3$ V/A. The standard deviation of the signal area is propagated into the charge gain uncertainty in quadrature.

The response to a minimum-ionising particle (MIP) is an important parameter to quantify the detector's performance. A MIP produces an average of 80 electron-hole pairs per µm [119]. The investigated sensors have an active depth of 50 µm; hence, the expected charge corresponds to ~0.64 fC. The amount of charge deposited by the laser given above (~1 fC) was selected to roughly correspond to that of a MIP. Due to the indirect bandgap of silicon, the energy required to generate an electron-hole pair is greater than the bandgap energy (1.12 eV) and averages around 3.6 eV. The discrepancy arises because the electron excitation requires a change in crystal momentum, which is achieved via phonon interactions (see Section 3.5.1). Therefore, a fraction of the energy goes into exciting lattice vibrations [20].

3.5.2.2 Jitter

The timing resolution of a detector σ_t can be broken down into four main terms according to the expression

$$\sigma_t^2 = \sigma_{jitter}^2 + \sigma_{ionisation}^2 + \sigma_{distortion}^2 + \sigma_{TDC}^2, \tag{3.24}$$

where σ_{jitter} describes the electronic noise, $\sigma_{ionisation}$ is due to the non-uniform energy deposition by the impacting particle (Landau noise), $\sigma_{distortion}$ is the distortion term due to non-saturated drift velocity of charge carriers and non-uniform weighting field, and σ_{TDC} originates from the uncertainty due to the finite size of the time-to-digital converter bin (oscilloscope) [57]. Each of these contributions is briefly discussed. The time-walk effect is mitigated by using the CFD method rather than the constant threshold discriminator. This method was explained in Section 3.3.2.3.

Jitter

For a signal to be considered a hit, it needs to cross a given threshold. Regardless if this threshold is fixed or adjusted to the signal peak value, the presence of noise shifts the exact time the threshold is reached, hence affecting the timing resolution. The noise can either come from the sensor or be added by the amplifier electronics. The effect is directly proportional to the noise N and inversely proportional to the slope of the signal dV/dt when crossing the threshold. This can be written as

$$\sigma_{jitter} = \frac{N}{dV/dt} \approx \frac{t_r}{S/N}, \tag{3.25}$$

where the approximation assumes a constant slope equal to the ratio of the signal amplitude S to the signal rise time t_r. Equation 3.25 highlights the importance of fast rise time and large signal-to-noise ratio for devices with excellent timing resolution.

Ionisation

A charged particle generates charge carriers along its path with a density that varies on an event-by-event basis. The energy loss follows the Landau distribution, which is an asymmetric distribution with a not negligible high energy tail. Localised charge

clusters cause a non-uniform charge deposition, which leads to irregularities in the signal shape. The non-uniformity contributes to the timing resolution of the device. Whereas the 1064 nm photon beam completely penetrates the active depth, it produces a uniform charge deposition along its path. As such, the Landau fluctuations do not affect the timing resolution when the laser injection method is used.

Distortion

Distortion effects arise from the non-uniformity of the drift velocity and weighting field across the device. To address these points, sensors are produced using a parallel plate geometry with a pitch much larger than the sensor thickness. Even though these effects are important, the variations and the overall effect of the distortion term are negligible for laser measurements where the photon beam is repeatedly fired at the same spot.

TDC

The oscilloscope (or any other instrument used to read the signal) records the values into bins with a finite time width ΔT. This adds a contribution to the time uncertainty equal to $\Delta T/\sqrt{12}$. As the oscilloscope used in this investigation has a binning width of ΔT = 7.8125 ps (corresponding to 128 GSa/s), the resolution contribution σ_{TDC} = 2.3 ps is negligible.

From the considerations presented, the jitter is the most important contribution to the timing resolution of the devices measured with the laser injection method. To avoid possible confusion with the 'full' timing resolution as shown in Equation 3.24, the timing performance values from the laser measurements will be referred to as the *jitter*. To calculate the jitter, the time delay between the DUT and the laser trigger was sorted into 7.8 ps bins (width of the oscilloscope time bins) and the core of the histogram was fitted with a Gaussian distribution. The time reference point for both the DUT and the trigger is evaluated at 50% CDF value. The jitter of the laser trigger was measured to be $\approx$ 1.5 ps. An example histogram with a Gaussian fit function is shown in Figure 3.56. The standard deviation of the Gaussian fit σ_{jitter} = 8.1 $\pm$ 0.1 ps

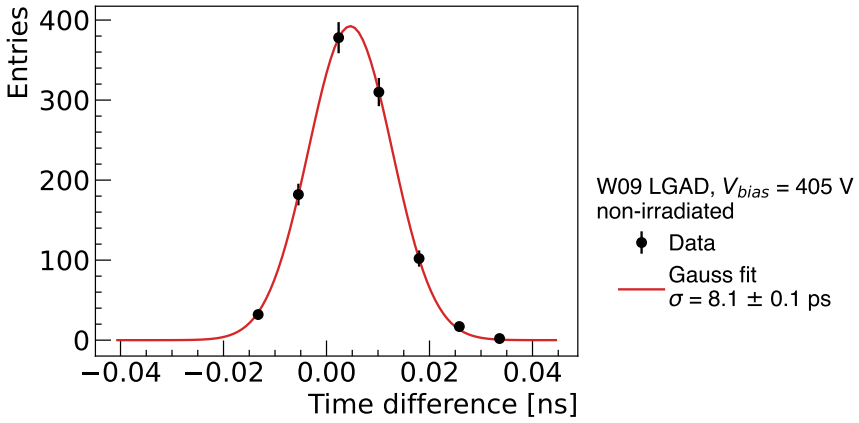


Figure 3.56: The time difference between the device trigger and the laser trigger timing for a non-irradiated W09 LGAD biased at 405 V. The data is sorted into 7.8 ps bins, with the histogram fitted with a Gaussian distribution. The standard deviation of the distribution gives the jitter of the device. The contributions of the trigger jitter and the TDC are not subtracted. The measurements were done at room temperature.

represents the upper limit of the jitter of the non-irradiated W09 LGAD at 405 V bias. The contributions of the trigger jitter and the TDC are not subtracted.

3.5.2.3 Laser calibration

The output power of the 1064 nm laser can be tuned by adjusting its operational parameters: the gate voltage and the bias current. Additionally, the intensity is attenuated using an ND filter. At room temperature, the output power was calibrated such that the average charge collected by a PiN diode is similar to the most probable value of the charge deposited by a MIP in silicon. This setting is referred to as *warm calibration*, and the used parameters are shown in Table 3.8.

The calibration was performed such that the jitter measurement would approximate that of a MIP traversing the sensor. As the jitter depends on the height of the signal S, high-intensity photon beams can artificially improve the jitter performance. Additionally, if the beam's intensity is too high, the charge gain of the LGAD can worsen due to a mechanism called the *gain suppression* [71]. A large number of charge carriers inside a small gain layer volume will produce a local reduction in the electric field by screening and will lead to a reduction of the charge multiplication [120].

Table 3.8: Laser parameters for the two power modes - *warm* and *cold calibrations*.

Laser parameter	**Warm calibration**	**Cold calibration**
Firing frequency	100 kHz	100 kHz
Gate voltage	875 mV	660 mV
Bias current	9 mA	9 mA
ND filter	ND 1.0	ND 1.0

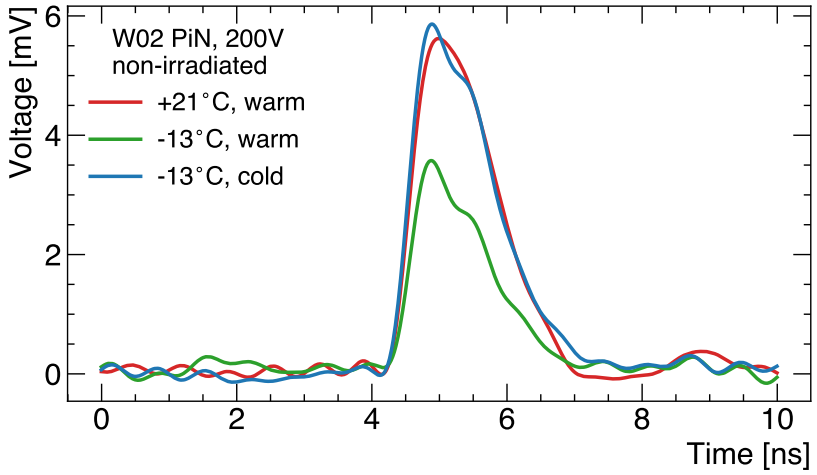


Figure 3.57: The average signal produced by a non-irradiated W02 PiN device biased at 200 V at two temperature points: 21°C and -13°C. The description of *warm* and *cold* refer to the laser power calibration. The *cold* calibration is adjusted such that the signal produced at -13°C is roughly equivalent to that produced at 21°C with the *warm* calibration.

When the devices are cooled down, a recalibration of the laser power is necessary as the absorption length of 1064 nm photons in silicon has a temperature dependence – see Section 3.5.1. Equation 3.19 predicts a (34±1)% reduction of the charge collected when the temperature is decreased from 21°C to (-13±1)°C. This prediction agrees with the observed reduction of the amplitude by 37% as shown in Figure 3.57. At -13°C, the laser parameters are adjusted such that the PiN signal area is equivalent within 5% to that produced by the *warm calibration* at room temperature – see blue curve in Figure 3.57. The new setting is referred to as *cold calibration*, with parameters shown in Table 3.8.

No significant variation of the charge collected as a function of the irradiation fluence was observed for the PiN devices. The observed differences within ±8% are consistent with the expected device-to-device variations.

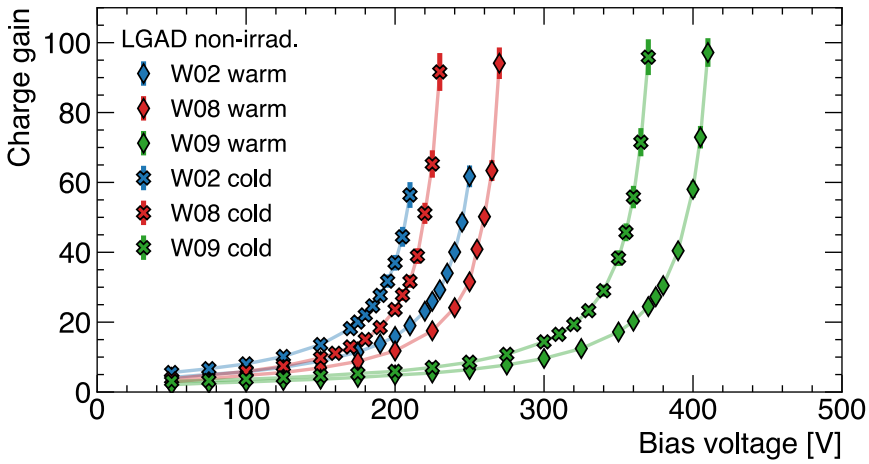


Figure 3.58: The charge gain of non-irradiated 1×1 mm^2 LGAD samples from W02, W08, and W09 measured using laser injection. The *warm* and *cold* conditions correspond to 21°C and -13°C, respectively. The laser power is adjusted according to the temperature such that the charge generated in a reference PiN diode is approximately equal.

3.5.3 Performance before irradiation

The charge gain of the non-irradiated 1×1 mm^2 LGAD samples from W02, W08, and W09 was measured at room temperature and while cooled by the vortex tube. The laser settings were adjusted to the temperature of the sensor. The results are summarised in Figure 3.58, showing the averages from 1024 laser pulses. The variation of the response contributes to the measurement uncertainty together with the reference PiN variation, as outlined before.

All samples reach a high gain above 50, both in warm and cold conditions. The W02 LGAD sample reaches a charge gain of only ∼60, whereas the samples from W08 and W09 approach a charge gain of 100. However, the difference can be attributed to device-to-device variations and the rapid increase of signal amplitude near breakdown. It is possible that a suitable fine-tuned bias voltage could have achieved a higher gain for the W02 LGAD sample as well. The results are not sufficient to indicate a clear difference between wafers in terms of maximum possible gain. Further investigation with multiple devices is needed. The observed breakdown voltages at room temperature (∼250 V for W02, ∼280 V for W08, ∼420 V for W09) agree within 10% with the previous measurements presented in Section 3.2.3.

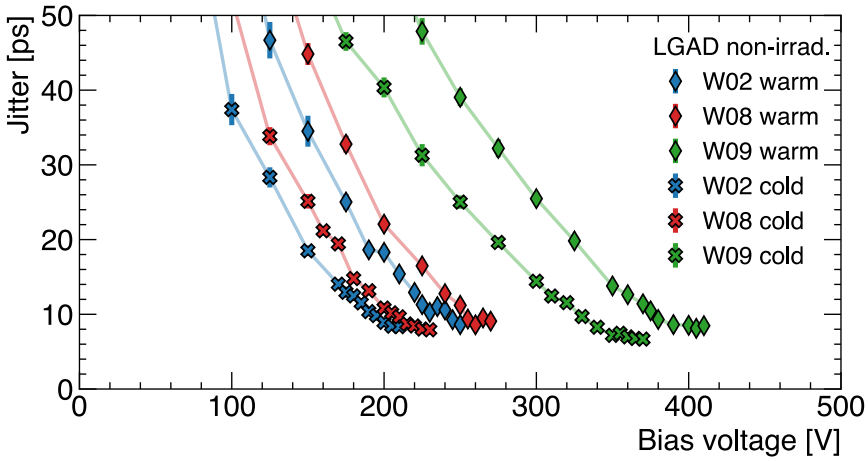


Figure 3.59: The jitter of non-irradiated 1×1 mm^2 LGAD samples from W02, W08, and W09 measured using laser injection as a function of the bias voltage. The *warm* and *cold* conditions correspond to 21°C and -13°C, respectively. The laser power is adjusted according to the temperature such that the charge generated in a reference PiN diode is approximately equal. The contributions of the laser trigger jitter or the TDC are not subtracted from the data.

The breakdown voltages shift towards lower values as the devices are cooled down. The temperature variation of the breakdown voltage has also been observed in other works [120, 121]. This behaviour can be explained by the increased charge carrier mean free path at lower temperatures due to reduced phonon scattering [122]. With a greater mean free path, the avalanche process in the LGAD gain layer produces more charge per seed electron-hole pair. Due to the greater number of generated charge carriers, breakdown is reached at a lower bias voltage.

The jitter of the LGAD devices is shown in Figure 3.59 for both the *warm* and *cold* conditions. The devices achieve comparable performance, reaching jitter better than 10 ps close to the breakdown when the charge gain is the highest. The best performance is observed for the W09 LGAD at -13°C, reaching 6.7 ± 0.1 ps jitter. The contributions of the laser trigger jitter or the TDC are not subtracted from the values.

As per Equation 3.25, the jitter term depends inversely on the signal-to-noise ratio S/N. This is illustrated using Figure 3.60 where the gain results from Figure 3.58 are combined with the jitter values from Figure 3.59. Irrespective of the temperature, the data follows the same pattern observed in other works [40].

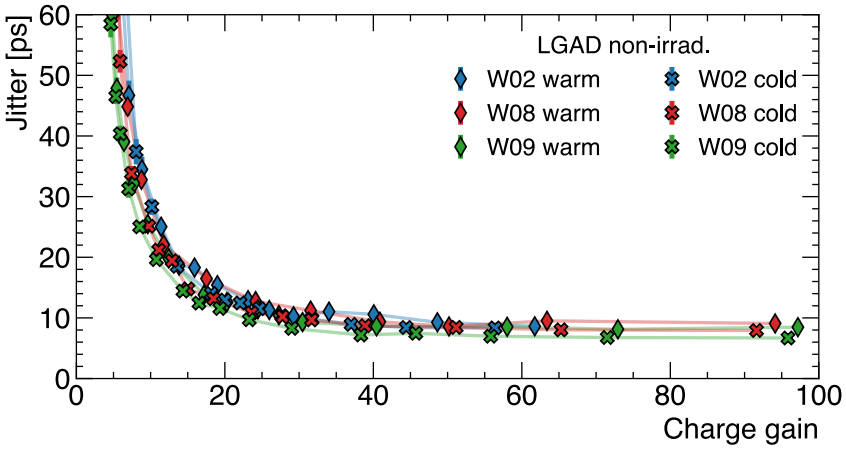
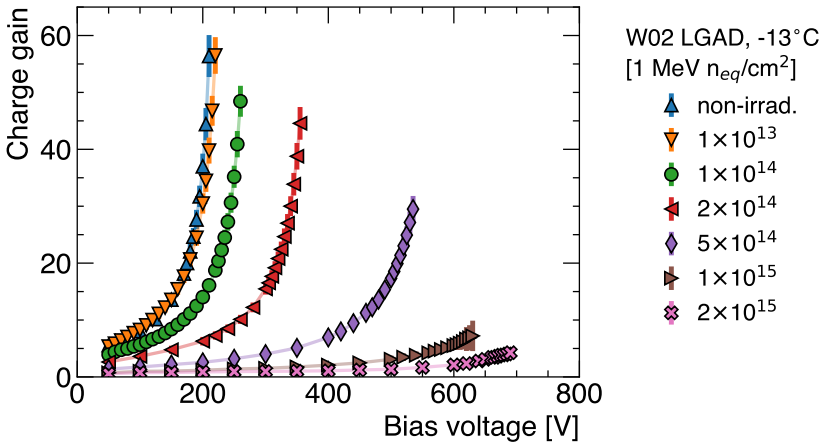


Figure 3.60: The jitter of non-irradiated 1×1 mm^2 LGAD samples from W02, W08, and W09 measured using laser injection as a function of the charge gain of the device. The *warm* and *cold* conditions correspond to 21°C and -13°C, respectively.

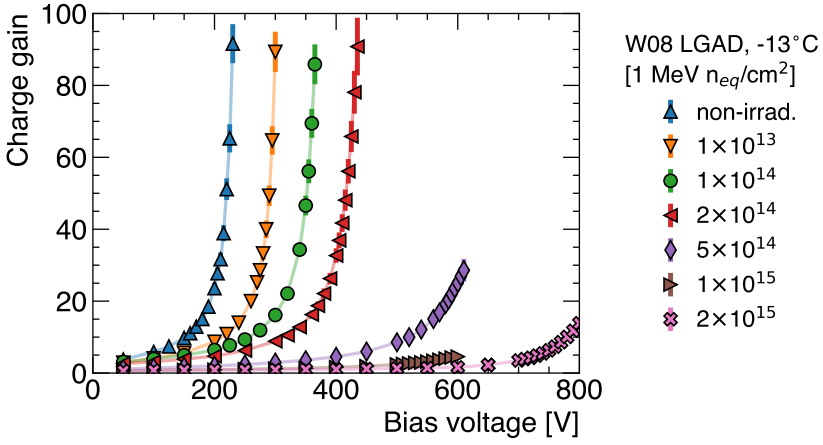
3.5.4 Results for irradiated samples

The charge gain of the neutron-irradiated LGAD sensors compared to that of the non-irradiated samples is shown in Figure 3.61. The performance is plotted separately for W02 in (a), W08 in (b), and W09 in (c). The samples were cooled to -13°C via a vortex cooler. Due to the lower active fraction of the gain layer doping, the devices require a higher bias voltage to reach comparable charge gain as the non-irradiated device. For devices irradiated up to the fluence of 2×10^{14} 1 MeV $n_{eq}cm^{-2}$ it is still possible to recover the pre-irradiation charge gain levels if the bias voltage is increased. Furthermore, high charge gain >40 can be reached below the critical voltage of 600 V beyond which SEB events can occur.

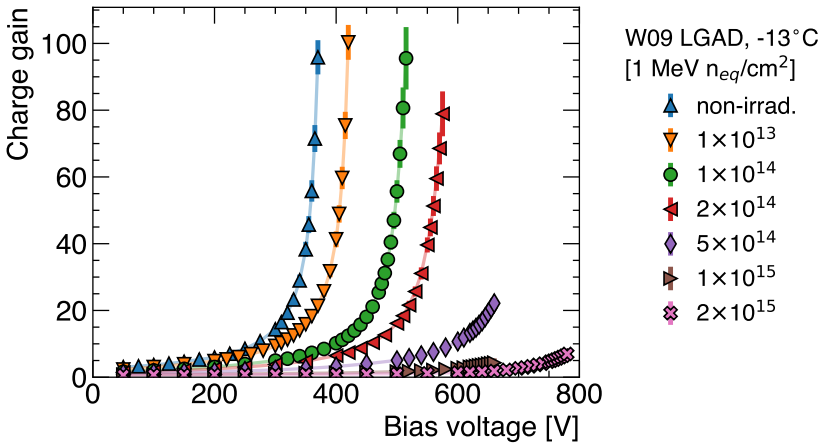
A more substantial decrease of the maximum charge gain is observed for the devices irradiated to and above the fluence of 5×10^{14} 1 MeV $n_{eq}cm^{-2}$. It appears that the 2×10^{15} samples from W08 and W09 can eventually reach a higher gain compared to the less irradiated 1×10^{15} samples. However, this effect is attributed to an earlier than expected breakdown of the 1×10^{15} samples. Investigation of a larger number of irradiated devices is warranted to address potential device-to-device variation causing this apparent effect. Out of the most irradiated samples, the W08 LGAD irradiated to 2×10^{15} 1 MeV $n_{eq}cm^{-2}$ still shows a charge gain of $\sim$15, albeit when bias at 800 V – far above the safety bias threshold.



(a) W02 - Charge gain



(b) W08 - Charge gain



(c) W09 - Charge gain

Figure 3.61: The charge gain of neutron-irradiated 1×1 mm^2 LGAD samples from W02, W08, and W09 measured using laser injection as a function of bias voltage. The measurements were done at -13°C. Each data point shows an average value from 1024 analysed signals.

The jitter measurements obtained for the irradiated sensors from the three LGAD wafers are plotted in Figure 3.62. The jitter improves significantly as the bias voltage is increased. It should be noted that there is a trend that the jitter worsens close to the maximum bias voltage, just before breakdown is reached. This behaviour is explained by the increase in noise as the leakage current grows rapidly close to breakdown.

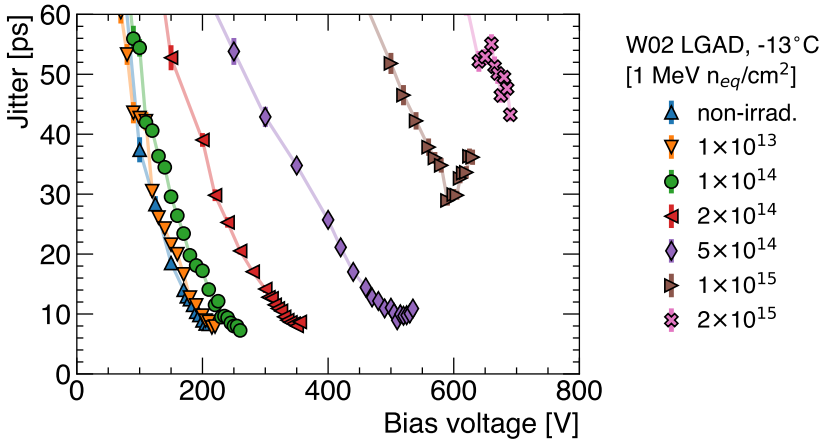
Following the approach used in Figure 3.60, which plots jitter as a function of charge gain, this relationship is illustrated for irradiated devices from W08 in Figure 3.63. Except near the breakdown region where jitter begins to increase, the curves show a high degree of overlap, irrespective of the received fluence. This pattern is similarly observed for devices from W02 and W09.

An excellent jitter performance of below 10 ps can be achieved for sensors irradiated up to 5×10^{14} 1 MeV $n_{eq}cm^{-2}$. For more irradiated sensors, the best jitter performance is ~40 ps, though the 2×10^{15} LGAD sensor from W08 demonstrated jitter <25 ps at 800 V, owing to its charge gain greater than 10.

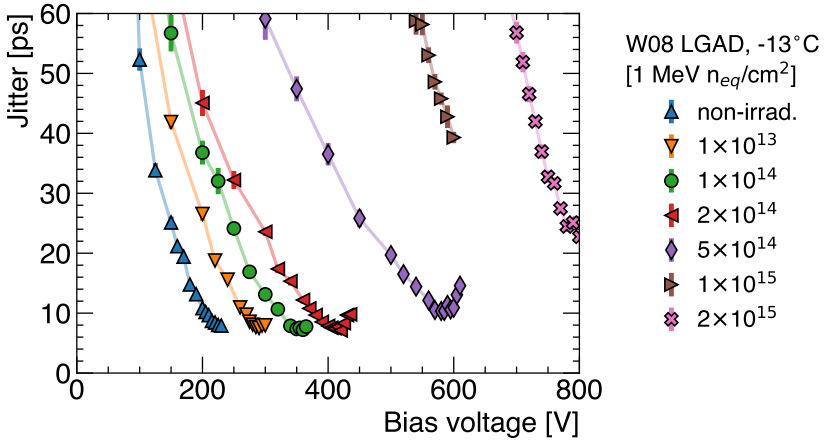
3.5.5 Summary

This section summarised the laser measurements of the irradiated 1×1 mm^2 LGAD sensors produced by Te2v. With their intrinsic gain, the LGAD sensors are an excellent choice for providing accurate track timing information in future particle detector systems. To produce timing resolution better than 50 ps as part of the HGTD, the detectors need to maintain high charge gain up to the fluence of 2.5×10^{15} 1 MeV $n_{eq}cm^{-2}$. The investigated devices were taken from wafer 2 (*High* GL implant energy, *High* GL implant dose), wafer 8 (*Medium* GL implant energy, *Very High* GL implant dose), and wafer 9 (*Medium* GL implant energy, *High* GL implant dose). For a more detailed wafer description, see Section 3.1.5.

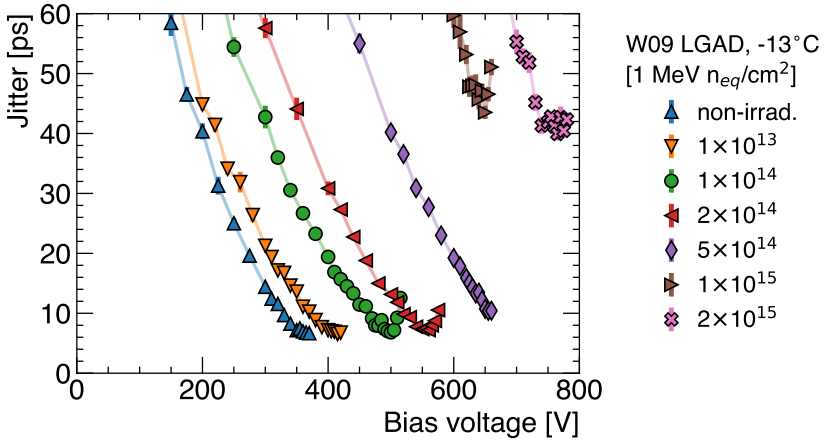
A 1064 nm laser beam generating a charge similar to that produced by a MIP is used in these studies. As the photon beam cannot simulate the Landau fluctuations of the charged particle passing through the sensor, the measurements only probe the jitter of the devices rather than the full-timing resolution. Nevertheless, the investigated devices demonstrated jitter better than 10 ps for irradiation fluences up to



(a) W02 - Jitter



(b) W08 - Jitter



(c) W09 - Jitter

Figure 3.62: The jitter of neutron-irradiated 1×1 mm^2 LGAD samples from W02, W08, and W09 measured using laser injection as a function of bias voltage. The measurements were done at -13°C. Each datapoint shows an average value from 1024 analysed signals. The contribution of the laser trigger jitter and the TDC are not subtracted from the data.

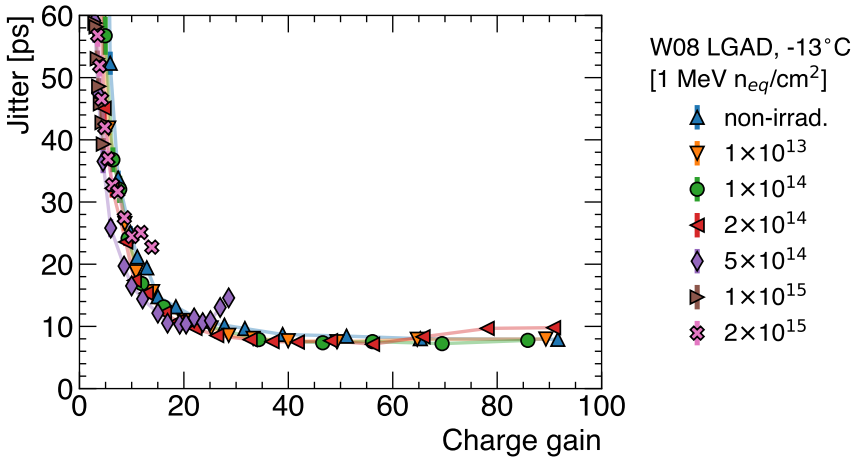


Figure 3.63: The jitter of neutron irradiated 1×1 mm^2 LGAD samples from W08 measured using laser injection as a function of the charge gain of the device. The measurements were done at -13°C. Each datapoint shows an average value from 1024 analysed signals.

5×10^{14} 1 MeV $n_{eq}cm^{-2}$. Similarly, charge gain comparable to that of non-irradiated devices (>50) was reached for devices irradiated to 2×10^{14} 1 MeV $n_{eq}cm^{-2}$ when the bias voltage was sufficiently increased. Promisingly, an LGAD from W08 was able to achieve a charge gain of ∼15 and jitter <25 ps after being exposed to the fluence of 2×10^{15} 1 MeV $n_{eq}cm^{-2}$.

The results indicate that the devices exhibit good radiation-hardness up to the fluence of 5×10^{14} 1 MeV $n_{eq}cm^{-2}$. The biggest drawback of the investigation was the lack of duplicate devices irradiated to the same fluence. As such, the results can be susceptible to device-to-device variation and premature device breakdowns caused by structural defects.

3.6 Characterisation of LGAD pixel arrays

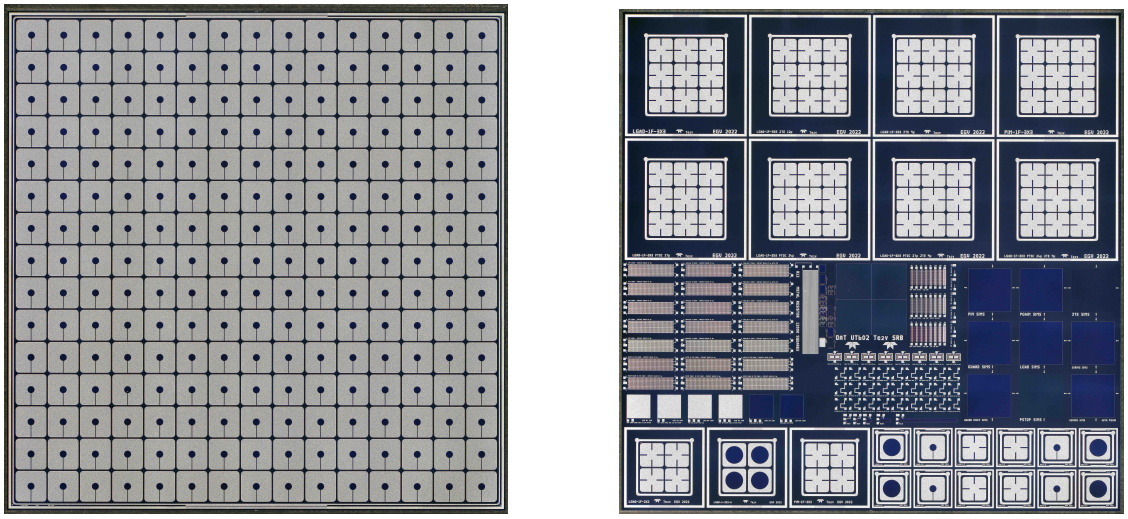
Until now, this chapter has been exclusively concerned with testing and parametrising single-pixel LGAD devices that were electrically isolated from other devices with a guard ring. In practice, particle detectors want to maximise the area covered by active sensors, and so individual pixels are grouped into arrays [123, 124]. As mentioned in Section 3.1.4, the HGTD detector will use LGAD devices arranged into arrays of 15×15 pixels, each pixel 1.3×1.3 mm^2 in size [41].

When pixels are arranged into arrays, there is still space between adjacent pads which does not belong to either pixel, referred to as the *inter-pad gap*. The terms *pixel* and *pad* are used interchangeably. If a charged particle passes through this area, the generated charge is collected and shared between the two (or more) pixels, hence lowering the probability that any one pixel will register enough charge to trigger the electronics readout. Furthermore, in the case of LGADs, there is no charge multiplication layer in the gap, so the charge generated in this region will not get enough amplification to guarantee good timing. Due to these effects, the sensor design aims to minimise the gap extent – referred to as the *inter-pad distance* or *IP*. The ratio of the sensitive area to the total area of the sensor is defined as the *fill factor*.

This section discusses the measurement of the inter-pad distance of the LGAD array of 3×3 pads with 1×1 mm^2 pad size with different pixel geometries. The distance is extracted using laser injection measurements by scanning along the edge of two adjacent devices with a 1064 nm laser and monitoring the drop of the recorded signal amplitude.

3.6.1 LGAD array description

The investigated 3×3 LGAD arrays are taken from the second batch of LGAD wafers produced by Te2v - referred to as the *Batch 2*. The second batch focused more on multi-pad devices, offering HGTD compatible 15×15 arrays of pad size 1.3×1.3 mm^2 (see Figure 3.64a) in addition to smaller test arrays of 3×3 and 2×2 arrays with 1×1 mm^2 pad size as shown in Figure 3.64b. In total, 24 6-inch wafers were produced on high resistivity silicon substrate (> 1500 Ωcm) – two of the wafers contained PiN devices with no gain implant (split P). The thickness of the active layer was kept at 50 µm, as



(a) **(b)**

Figure 3.64: LGAD devices produced in the second batch 15×15 LGAD array in (a), and smaller test structures including 3×3 and 2×2 arrays, and single LGADs in (b).

Table 3.9: The four splits of LGAD wafers from Te2v Batch 2 and a PiN-only split P. Each split features a unique combination of gain layer (GL) implant energy and dose. Values are normalised to that of the reference wafer W21 from Batch 1. Retaining the naming system from Batch 1, the GL implant energies are grouped into *Medium*, and *High*. The GL implant doses are grouped into *Low*, *High*, and *Very High*.

Split	Wafers	GL implant energy	GL implant dose
A	1-5, 7	1.11 / *High*	1.07 / *High*
E	6, 8-12	1.05 / *Medium*	1.15 / *Very High*
X	13-18, 23, 24	1.11 / *High*	1.15 / *Very High*
H	19, 20	1.11 / *High*	1.00 / *Low*
P	21, 22	none	none

was the case in *Batch 1*. Splits A, H, and E were retained from the first batch, and an additional split X was introduced, combining *High* gain layer implant energy and *Very High* gain layer implant dose. The wafers are listed in Table 3.9 with gain layer parameters scaled to that of split F from *Batch 1*.

In order to explore the methods of decreasing the inter-pad distance while maintaining suitable electrical properties, wafers from *Batch 2* feature 3×3 LGAD arrays with slightly different geometries, which affect the IP distance. Namely, these are the width of the JTE and the distance between the P-stop and the central cathode pad (PTOC distance). Further details about these structures can be found in Section 3.1.2. The standard geometry from *Batch 1* uses 15 µm JTE width and 30 µm PTOC distance. Two variants have the JTE width reduced to 9 µm, and one of them also features a reduced

Table 3.10: The width of the Junction Termination Extension (JTE), the distance of the P-stop to the pad cathode (PTOC) and the expected geometrical inder-pad distance (IP) of three LGAD 3×3 array variants.

Device	PTOC distance	JTE width	Expected IP
LGAD_P30J15	30 µm	15 µm	97 µm
LGAD_P30J09	30 µm	9 µm	84 µm
LGAD_P24J09	24 µm	9 µm	72 µm

PTOC distance down to 24 µm. The array properties and the expected IP (based on device geometry) are listed in Table 3.10. All investigated arrays are from wafer 20, which is referred to as W20B2, to distinguish it from W20 from *Batch 1*. Throughout the section, the device names listed in Table 3.10 are used when referring to a given device.

The HGTD Technical Specification [58] requires the low gain region between the pads to be narrower than 100 µm in order to maximise the sensor fill factor and overall efficiency. Additionally, the IP distance should be more than 45 µm to prevent early breakdown between the pads. The expected IP distance (derived from the design geometry) satisfies these requirements. It is important to stress that the 3×3 array has a pad size of 1×1 mm^2 rather than 1.3×1.3 mm^2 used for the HGTD devices, which affects the predicted fill factor for a given inter-pixel distance. Despite a non-negligible gap relative to the size of the pads, staggering multiple LGAD layers will achieve hermetic coverage and reduce the probability of a particle not being detected.

3.6.2 IV measurements of LGAD arrays

Before the inter-pad distance measurements, the devices were subjected to static electrical characterisation, measuring the leakage current as a function of the bias voltage (IV). The main purpose of this investigation was to establish a working range of bias voltages for the IP measurements and verify that the device geometry modifications do not adversely affect the electrical characteristics of the arrays.

The measurements were performed, and data was analysed according to the procedures outlined in Section 3.2.3. The backside of the LGAD array is in electrical contact with the chuck held at 0 V while bias is applied to the metallisation on the top of a given pad under test while all the other pads and the guard ring are left floating. Individual electrode pads are referred to using the [X, Y] system, where X is the column number

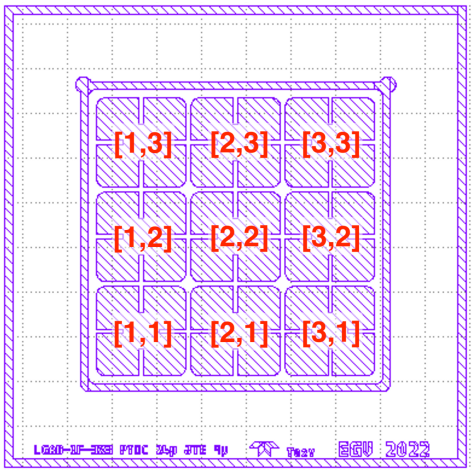


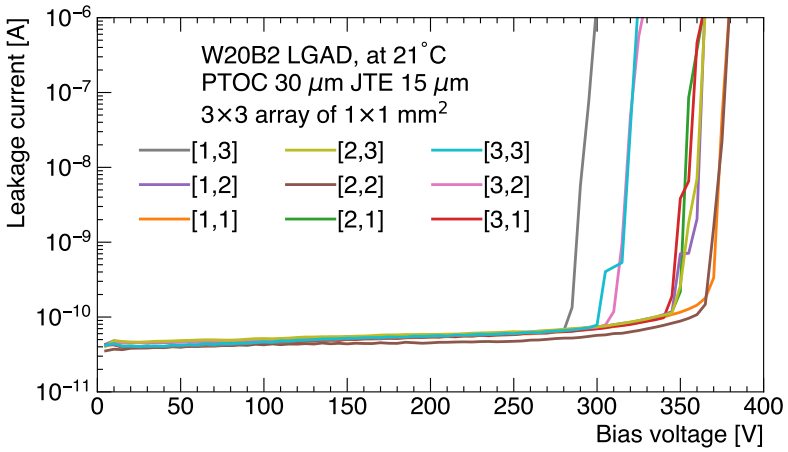
Figure 3.65: A diagram of the 3×3 LGAD array with pad size of 1×1 mm^2. Individual pads are labelled as [X, Y], where X is the column number and Y is the row number.

starting with 1 on the left, and Y is the row number beginning with 1 on the bottom, as shown in Figure 3.65. The writing on the bottom gives the orientation of the array.

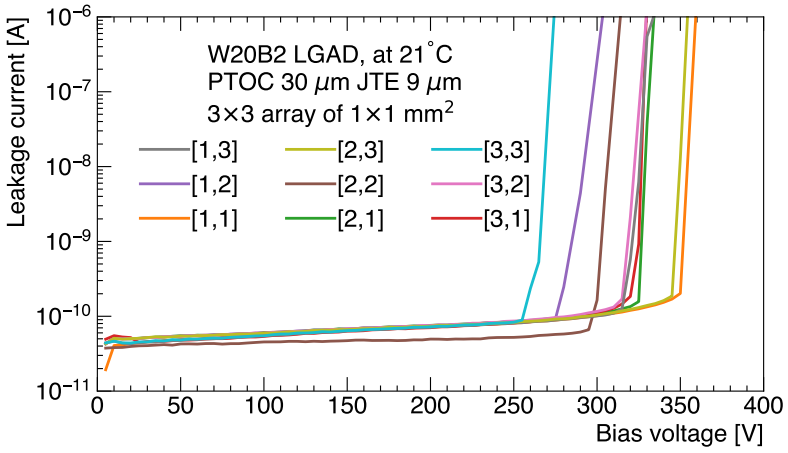
The leakage current of the individual pads was measured until it reached 1 µA, where the measurement was terminated to prevent damage to the sensor. Figure 3.66 shows the individual current-voltage curves. The breakdown voltage is defined as the voltage at which the current exceeds 200 nA. The weighted average, the lowest, and the highest breakdown voltages, together with the standard deviation of the range, are summarised in Table 3.11. The uncertainty on the standard deviation of the pad population is given by the uncertainty on an individual breakdown voltage measurement 5 V/$\sqrt{12}$ $\sim$ 1.44 V (with a 5 V bias step).

The weighted arithmetic mean of the 9 pads $< V_{bd} >$ decrease slightly from 352 V (for LGAD_P30J15) to 326 V (for LGAD_P30J09) and 331 V (for LGAD_P24J09), however due to high variation between the individual pads (standard deviation 24-26 V), the shift is not significant enough to draw conclusive evidence. Overall, no significant differences in the breakdown voltage are observed as the JTE width is decreased from 15 µm to 9 µm and the PTOC distance is lowered from 30 µm to 24 µm.

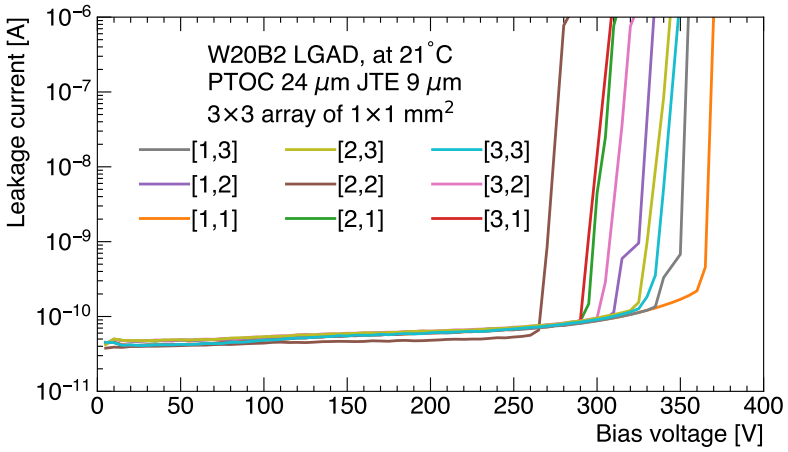
In order to avoid one pad going into breakdown much before the rest, the HGTD requires that the ratio of the standard deviation of the breakdown voltages to the average breakdown voltage does not exceed 0.05. The ratio of all the measured samples exceeds this value (0.075 $\pm$ 0.004 for LGAD_P30J15, 0.074 $\pm$ 0.004 for LGAD_P30J09,



(a) LGAD_P30J15 - Leakage current



(b) LGAD_P30J09 - Leakage current



(c) LGAD_P24J09 - Leakage current

Figure 3.66: The leakage current of the individual LGAD pads within 3×3 arrays of various geometries. The array with JTE width 15 μm and PTOC 30 μm is shown in (a), JTE width 9 μm and PTOC 30 μm in (b), and JTE width 9 μm and PTOC 24 μm in (c).

Table 3.11: The minimum and the maximum breakdown voltage of the LGAD pads within a given array, together with the weighted average $< V_{bd} >$ and the standard deviation of the values.

Device	**Min** V_{bd}	**Max** V_{bd}	$< V_{bd} >$	**st dev** V_{bd}
LGAD_P30J15	300 ± 1 V	380 ± 1 V	352 ± 1 V	26 ± 1 V
LGAD_P30J09	275 ± 1 V	360 ± 1 V	326 ± 1 V	24 ± 1 V
LGAD_P24J09	280 ± 1 V	370 ± 1 V	331 ± 1 V	26 ± 1 V

and 0.080 ± 0.004 for LGAD_P24J09), hence improving the breakdown homogeneity between the LGAD pixels needs to be addressed in the future iterations of the production.

3.6.3 Inter-pad distance

Laser measurements are commonly used to determine the inter-pad distance between pixels in an array [125, 126]. The laser is focused into a small spot (typically a few up to tens of μm), which is scanned across the surface of the sensor. As the laser spot moves from the sensitive region into the inter-pixel gap, the signal generated within the sensor decreases. By fitting the falling or rising signal with an appropriate fitting curve, the position of the edge separating the two regions is established. Alternatively, some investigations use test beam data, where the inter-pixel distance is determined from the drop of the pixel efficiency [127]. The results presented in this section were obtained with the 1064 nm fast laser setup at the OPMD laboratory as outlined in Section 3.5.1.1.

3.6.3.1 Measurement procedure

As the 1064 nm photons cannot penetrate the metal layer on top of the silicon, the metallisation pattern of the 3×3 LGAD arrays differs from that of the LGADs from Te2v Batch 1. The devices from the first batch had a metal aperture that did not extend to the edge of the pixel, and hence, the device's edge could not be located using a laser. As shown in Figure 3.65, rather than having a circular aperture, the devices in the array have rectangular openings in the metallisation along each edge of the size 300×50 μm^2. These are aligned such that the apertures of two adjacent pads face each other, and a laser spot can be scanned from one pad to the other without hitting a metallised surface.

As the laser spot moves across an edge of the pixel, the collected charge increases from a small (theoretically zero) value to a maximum once the beam spot is fully within

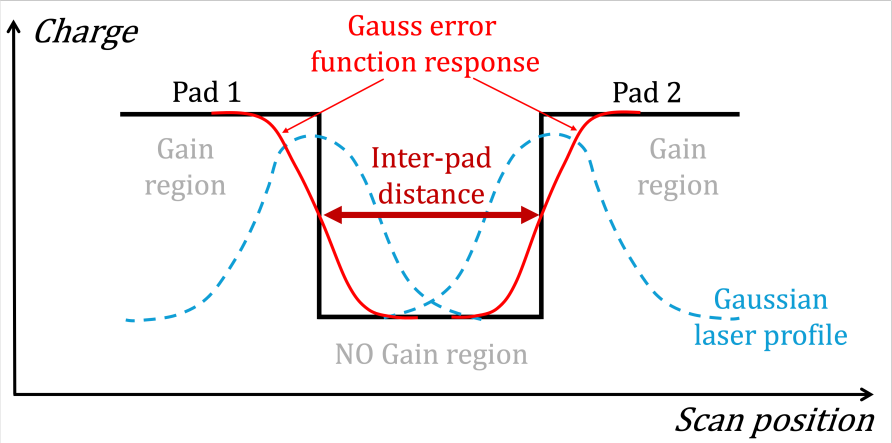


Figure 3.67: A schematic view of the charge profile as a function of the laser scan position. The profile can be modelled as a convolution of the geometrical/idealised box shape of the pads and a Gaussian laser profile. The inter-pad distance is the separation of the error function midpoints.

the active area of the pixel. A diagram showing the collected charge as a function of the scan position is shown in Figure 3.67. The profile of a pixel edge convoluted with the Gaussian profile of the laser spot can be modelled with an S-shaped function

$$f(x) = \frac{h}{2}\left[\text{erf}\left(\frac{x - x_0}{\sqrt{2}\sigma}\right) + 1\right], \tag{3.26}$$

where h is the maximum height, x_0 is the position of the edge, σ is related to the width of the function, and erf(x) denotes the Gauss error function [128]. The error function can be written as

$$\text{erf}(z) = \frac{2}{\sqrt{\pi}} \int_0^z e^{-t^2}\, dt. \tag{3.27}$$

The 3×3 array is mounted on an XY Stanza stage as described in Section 3.5.1.1. Whereas the stages can be moved to position the device such that the laser spot passes along the slit from one pad to the other, the stages cannot correct for small rotations that can affect the measured distance between the two edges. To account for a possible rotation angle θ, two laser scans (referred to as *cuts*) perpendicular to the line connecting adjacent pads are performed as shown in Figure 3.68 (referred to as the *left* and the *right* perpendicular cut). Using the x-y axes of the stages as the principal directions, the perpendicular cuts are done along the y-axis (each cut of

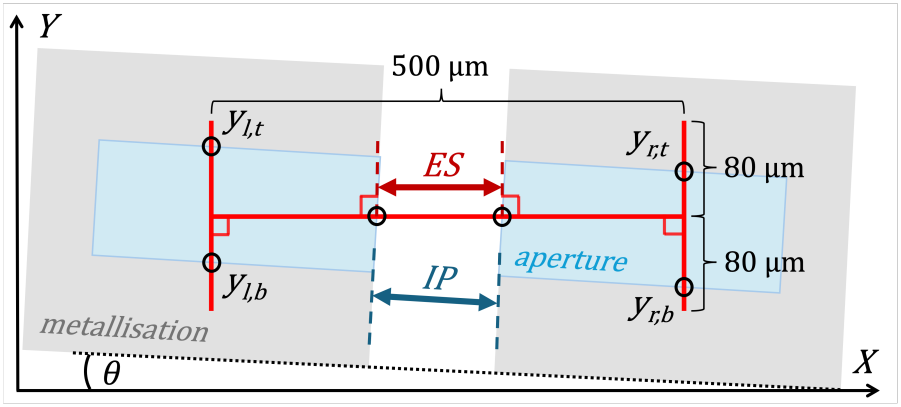


Figure 3.68: A diagram of the laser cuts in red. The main horizontal cut along the X-axis starts in the rectangular aperture of one pixel, crosses the inter-pad gap and enters the aperture of the adjacent pixel. The measured array is rotated by a small angle θ in the XY plane. The black circles show the position where the laser crosses an edge. ES denotes the edge separation between the pixel edges, and IP corresponds to the true inter-pad distance.

160 µm). The main cut to find the IP distance is done along the x-axis (total length of 500 µm), starting and ending at the mid-point of the perpendicular cut.

Along each of the perpendicular cuts, two edges are encountered at the boundaries of the rectangular aperture – where the metallisation layer stops and then starts (referred to as the *bottom* and *top* edge). The y-position of each edge is found as the x_0 parameter of the fit - see Equation 3.26. Using the y-positions of the edges, the angle θ is found according to

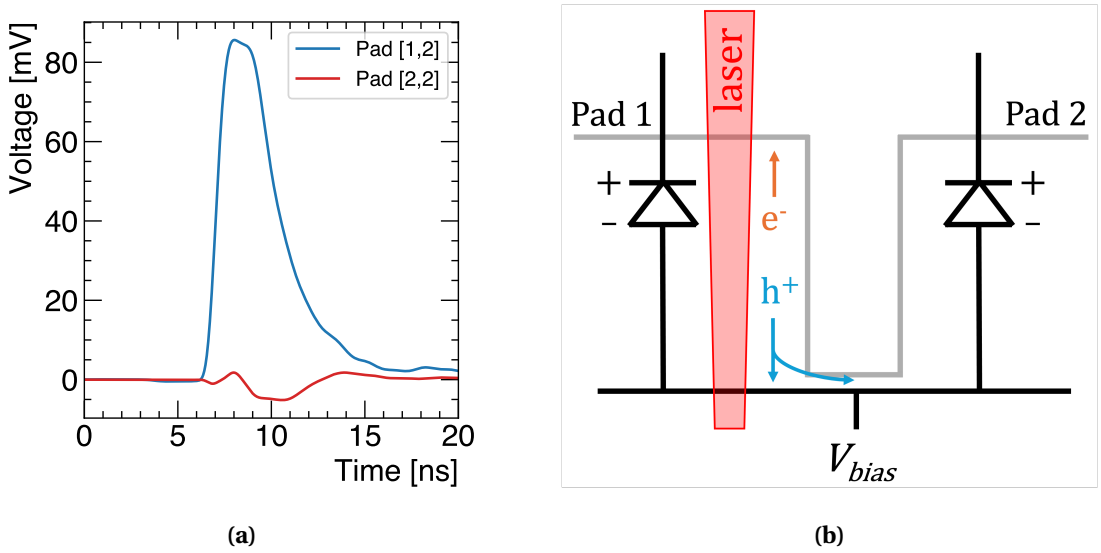
$$tan(\theta) = \frac{(y_{l,t} + y_{l,b})/2 - (y_{r,t} + y_{r,b})/2}{d} = \frac{y_{l,t} + y_{l,b} - y_{r,t} - y_{r,b}}{2d}, \tag{3.28}$$

where d = 500 µm is the length of the main cut and the *l, r, t, b* sub-scripts of the y-positions denote *left, right, top,* and *bottom* - see Figure 3.68.

The edge separation ES of the pad edges along the main cut is related to the inter-pad distance *IP* via θ as

$$IP = ES \times \cos(\theta). \tag{3.29}$$

The focused laser spot has an FWHM width of approximately σ = 30 µm. To resolve the two neighbouring pixels, it is necessary for the width of the laser spot to be below the expected inter-pixel distance. As the minimum expected distance is more than twice the spot width, this condition is satisfied.



(a) **(b)**

Figure 3.69: (a) The voltage signal when the laser beam is striking near the edge of pad [1,2] produces a large positive signal (blue) in the given pad but also a small negative signal (red) in the adjacent pad [2,2]. (b) A diagram showing the common Ohmic contact of the adjacent pads via the bias plane causing the appearance of the negative signal.

3.6.3.2 Signal readout

The IP distance measurement requires simultaneous readout from at least two adjacent pixels. As such, the COLA v1.4 readout board is unsuitable for the measurements as it only provides readout for one of the channels. For multi-channel readout, the COLA v2.1 amplifier board was used instead, allowing for the signal from up to three pads to be recorded simultaneously. See Section 3.1.6 for further details on the COLA v2.1 readout board.

For all the investigated arrays, pads [1,2] and [2,2] are connected to the readout channels 1 and 3 of the COLA v2.1 readout board. The laser scan is performed perpendicular to the edges of the two pads. The remaining pads are grounded. Upon each laser trigger, a 20 ns signal window is recorded from both pixels. An analysis analogous to that outlined in Section 3.5.2 is applied to the average signal over 1024 recorded triggers to obtain the average signal area at a given laser position for each pixel. As the fitting function mainly searches for the position of the edge x_0, the signal areas presented in this section are normalised to the maximum signal area of the given LGAD pixel within each cut and referred to as *normalised collected charge*. This normalisation does not affect the results.

Table 3.12: The extracted edge separation (ES) and calculated inter-pad distance (IP) for the three LGAD arrays.

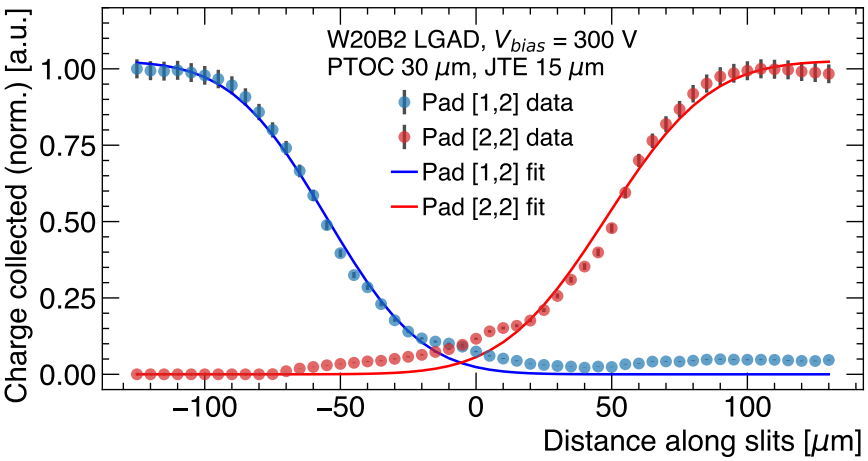
Device	ES [µm]	θ [°]	IP [µm]	IP_{geo} [µm]	IP/IP_{geo}
LGAD_P30J15	103 ± 2	4.0 ± 0.2	103 ± 2	97	1.06 ± 0.02
LGAD_P30J09	86 ± 1	3.1 ± 0.2	86 ± 1	84	1.02 ± 0.01
LGAD_P24J09	70 ± 1	3.7 ± 0.2	70 ± 1	72	0.97 ± 0.02

It was observed that when a positive signal is recorded by the pixel exposed to the laser beam, a small negative signal is detected by the adjacent pixel, as shown in Figure 3.69a. This effect may be explained by the fact that the pads share the same HV bias plane. The negative signal could arise from the charging and discharging of the adjacent pad as the holes are collected by the common bias contact - see Figure 3.69b. The effect was noted in other works as well [129]. When performing the analysis, only positive areas are considered to counteract the effect of the negative signal.

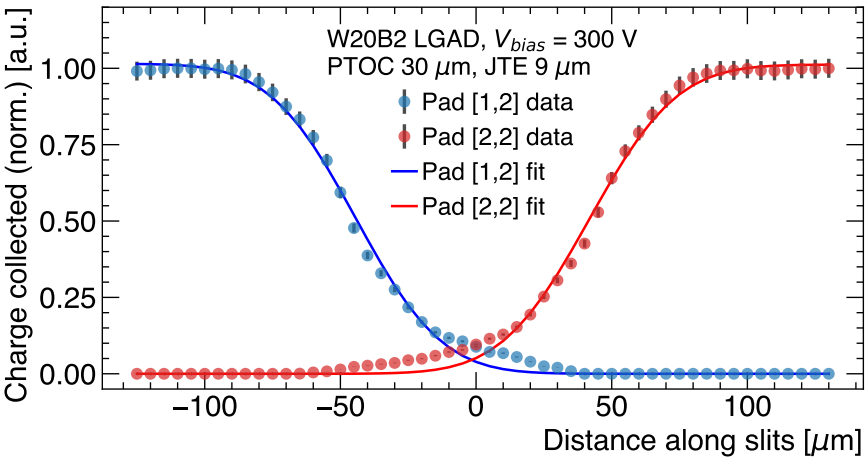
3.6.3.3 Results

The average charge collected from the two adjacent pads as a function of the laser position is shown in Figure 3.70. The figures show the middle 300 µm section of the 500 µm *main cut* as shown in Figure 3.68. The value of the laser position was shifted such that the centre of the gap between the two pixels roughly corresponds to 0 µm. The distance between the mid-points of the Gauss error function fit to the charge data gives the ES value (edge separation). The bias voltage V_{bias} of the devices is set sufficiently high such that the active volume is fully depleted – 300 V for LGAD_P30J15 (a), 300 V for LGAD_P30J09 (b), and 250 V for LGAD_P24J09 (c).

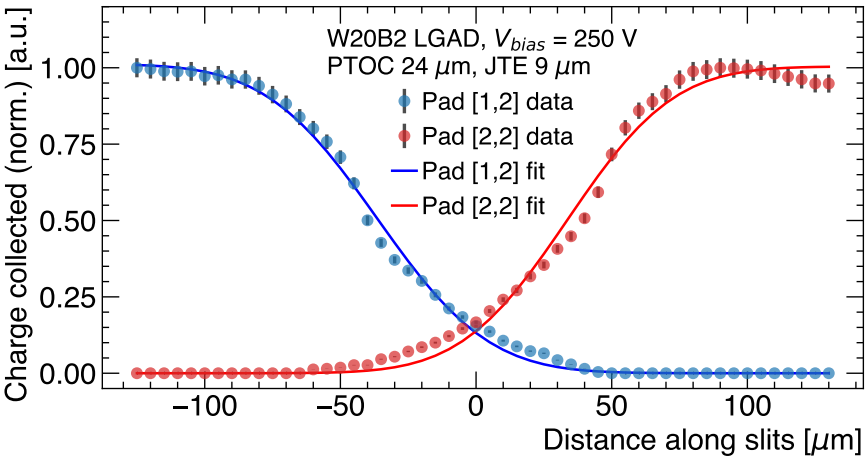
These extracted values are summarised in Table 3.12 together with the obtained θ angle values and the calculated IP. The ratios of the calculated IP values to those predicted from array geometry IP_{geo} are also included. The results show good agreement between the inter-pad distance from geometrical considerations and the obtained IP values from the laser measurements – maximum deviation is 6% in the case of the LGAD array with JTE width of 15 µm and PTOC 30 µm. The table also shows that the rotation angle θ was small and did not have a significant effect on the results.



(a) LGAD_P30J15 - Edge fit



(b) LGAD_P30J09 - Edge fit



(c) LGAD_P24J09 - Edge fit

Figure 3.70: The average normalised collected change from pads [1,2] and [2,2] of the 3×3 LGAD arrays of type LGAD_P30J15 (a), LGAD_P30J09 (b) and LGAD_P24J09 (c).

The error function fits show a good agreement as the collected charge starts decreasing from its maximum value. However, the charge tends to be higher than the predicted from the fit as it approaches zero. This can be explained by the generated charge diffusing from the gap region into the pad region, increasing the total collected charge. To confirm this hypothesis, a simulation of the process is needed.

3.6.4 Summary

This section outlined the importance of maximising the detector fill factor and provided direct measurements of the inter-pad distance using a 1064 nm laser setup. Three 3×3 LGAD arrays with different geometries were investigated to determine if the implemented modifications resulted in the reduction of the inter-pad distance between pixels within the arrays. The reduction of the JTE width from 15 µm to 9 µm and the PTOC distance from 30 µm to 24 µm proved to be effective ways of reducing the inter-pad distance between LGAD pixels while not compromising the electrical properties of the device.

The obtained inter-pad distances agreed with the geometrical predictions within 6%. The HGTD requirement for an inter-pad distance smaller than 100 µm is met by the designs featuring a 9 µm wide JTE. In terms of the electrical properties, no significant reduction of the breakdown voltage or early breakdowns were observed for the modified array geometries. The absence of detected electrical issues motivates future investigation of devices with even smaller PTOC distance and JTE width, which could achieve a higher fill factor if they maintain good electrical performance. In future LGAD productions, greater attention should be devoted to enhancing the uniformity of breakdown voltages across pixels.

4

The MALTA2 Monolithic Active Pixel Sensor

This chapter presents the MALTA2 Depleted Monolithic Active Pixel Sensor (DMAPS) produced in Tower 180 nm CMOS technology targeting radiation hard applications for the HL-LHC and other high-energy physics experiments. The MALTA (Monolithic ALICE To ATLAS) sensor family was developed as an option for the outermost layer of the ATLAS ITk - see Section 1.2.1. As such, the detector is required to meet certain performance criteria, a selection of which is summarized in Table 4.1 [17].

Section 4.1 provides an introduction to the MALTA2 sensor and its predecessors. The rest of the chapter presents experimental results obtained from test beam measurements, focusing on the radiation hardness of MALTA2 (Section 4.2) and the improvement of position and timing resolution of the sensor (Section 4.3).

Table 4.1: The main requirements of MALTA in terms of efficiency, radiation hardness, hit rate, timing resolution, and power consumption.

Parameter	**Value**
Hit detection efficiency	>97%
Radiation tolerance (NIEL)	1×10^{15} 1 MeV $n_{eq}cm^{-2}$
Radiation tolerance (TID)	80 Mrad
Particle rate capability	100 MHz/cm^2
Timing resolution	25 ns
Power consumption	<500 mW/cm^2

4.1 Introduction

4.1.1 The MALTA family

Before delving into the specifications of the MALTA2 sensor [130], this section briefly introduces the development of DMAPS that preceded the MALTA2 sensor and significantly shaped its design features. The MALTA sensor family is still under active research and development, constantly improving based on the understanding gained from laboratory and test beam measurements, and sensor simulations.

4.1.1.1 The ALPIDE sensor

The MALTA sensor is based on the ALPIDE sensor developed for the ALICE Inner Tracking System (ITS) upgrade [131]. The ALPIDE sensor was produced in the 180 nm Tower Semiconductor (formerly TowerJazz) [132] standard process on a high-resistivity p-type 25-30 µm epitaxial layer, featuring a small collection electrode. Due to the small collection electrode geometry of the sensor, the depletion region of the pixel volume is limited to the vicinity of the n-well electrode, with no depletion near the pixel edges, as shown in Figure 4.1. As a result, charges generated in the undepleted area move by diffusion and hence take longer to be collected, increasing the risk of recombination and worsening the timing resolution, with a collection time of ∼100 ns [130]. Furthermore, if the sensor has received non-ionising energy loss (NIEL) fluence above 10^{13} 1 MeV $n_{eq}cm^{-2}$, the charge generated in the pixel edges is not collected, resulting in deterioration of sensor performance [133]. Whereas this fluence is within the tolerance accepted for ITS of the ALICE experiment, implementations in the outermost layer of the ATLAS ITk require radiation tolerance a few orders of magnitude higher, up to 10^{15} 1 MeV $n_{eq}cm^{-2}$ [134]. To extend the depletion region and prevent charge loss in the pixel corners at high radiation doses, the standard Tower process was modified in the pixel design for the MALTA sensor.

4.1.1.2 MALTA

Starting with the ALPIDE design, in the MALTA pixel, an additional low-dose n-type implant was introduced below the collection electrode and deep p-wells to achieve full

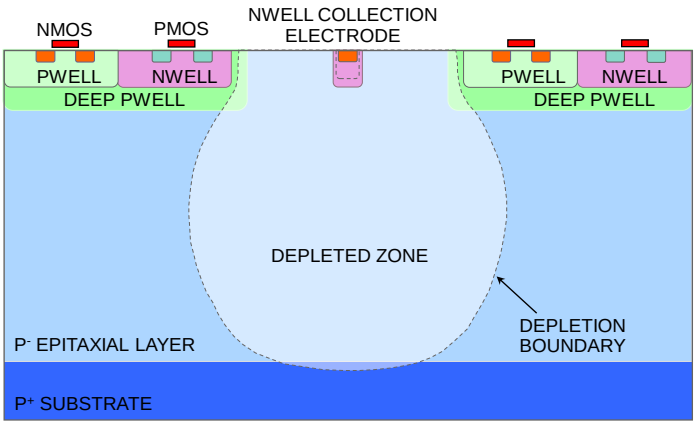


Figure 4.1: The cross-section of the ALPIDE pixel shows the limited extent of the depleted zone around the collection electrode. Figure adapted from [133].

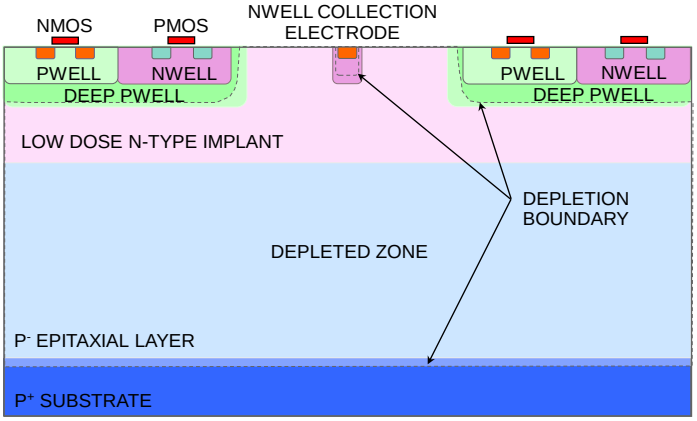


Figure 4.2: The cross-section of the MALTA pixel with the standard modified process (STD) design, introducing a low dose blanket n-type implant. Figure adapted from [133].

lateral depletion as shown in Figure 4.2 [133]. The unmodified process only allowed operating the ALPIDE chip at 6 V substrate bias, as the current flowing between the substrate and the PWELL (the punch-through current) was observed to increase rapidly above 8 V substrate bias. The modification (referred to as the standard modified process - STD) allowed for the bias voltage applied to the substrate voltage to be increased up to 20-30 V without causing punch-through. Higher reverse bias ensures full depletion and faster charge carrier collection via charge drift.

The MALTA sensors were fabricated in Tower 180 nm technology on wafers with a 25-30 µm epitaxial layer [135, 136]. An epitaxial layer is grown on top of a support wafer through a process called epitaxy. Epitaxy is a type of thin-film deposition where the new layer forms with a well-defined crystal orientation that matches the underlying

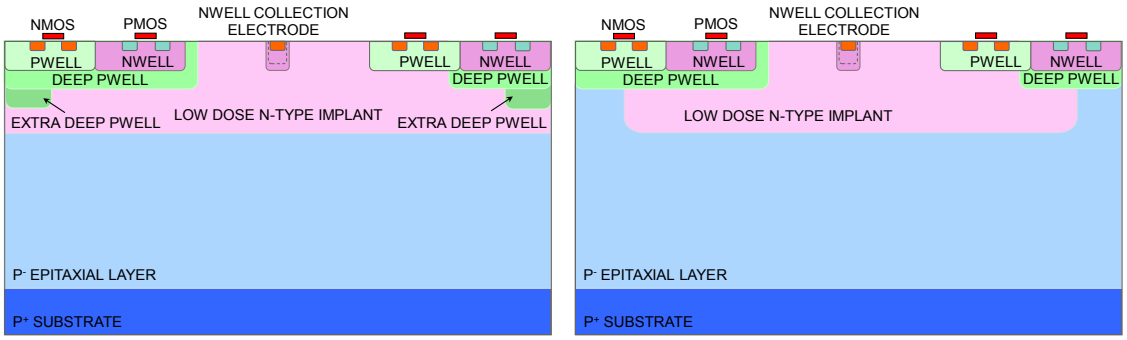
substrate. The sensor features a matrix of 512×512 square pixels, each with a size of 36.4×36.4 μm^2. The MALTA sensor is divided into eight sectors (S0-S7), which use different sensor and front-end pre-amplifier designs. The variations include the changes in the shape and size of the collection electrode and the reset mechanism for the voltage of the collection electrode. Digital-to-analogue converters (DACs) set the bias currents and voltages needed by the front-end pre-amplifiers. The readout logic and the function control registers are part of the sensor's digital periphery. Further information specific to the design and operation of the MALTA sensor can be found in [137].

The MALTA sensor was extensively tested in the laboratory and test beams, demonstrating good performance [138], however it suffers from efficiency losses in the pixel corners after irradiation [139]. Dedicated simulations were conducted to address the performance issues, which ultimately resulted in additional pixel design modifications and the fabrication of a small-scale demonstrator Mini-MALTA [140, 141].

4.1.1.3 Mini-MALTA

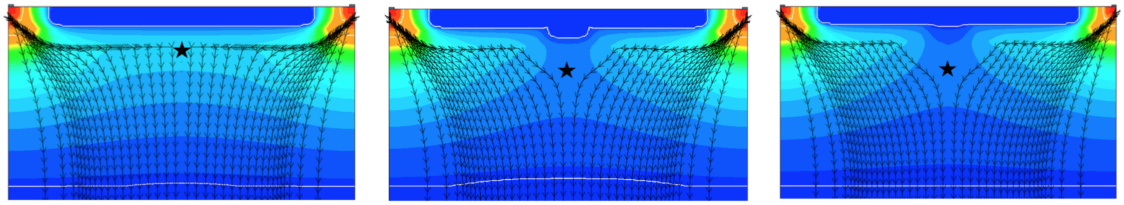
The Mini-MALTA chip contains a pixel matrix with 64×16 pixels of the same pitch as the original MALTA, 36.4×36.4 μm^2. The matrix is divided into eight sectors, each containing pixels of different flavours, with variations in the front-end, reset mechanism, and collection electrode geometries. Front-end electronics modifications with increased gain and lower noise allow operation at a lower charge threshold, aiming to improve the detection of signals in the pixel corners [142].

One of the most important modifications introduced in the Mini-MALTA sensor are the mask variations which modify the doping of the pixel corners. The electric-field simulations identified that after irradiation, the lateral electric field at the corner is too low, preventing efficient charge collection [140]. These observations motivated the modification of the design to introduce an additional deep p-type implant under the deep p-well (XDPW) or an n-well gap (NGAP). The two modifications generate a stronger lateral field in the pixel corners, hence improving the charge collection efficiency [140]. Figures 4.3a and 4.3b illustrate the pixel cross-section diagrams of the two new designs.



(a) XDPW **(b)** NGAP

Figure 4.3: The cross-section of the MALTA pixel – (a) with an extra deep p-well (XDPW) added at the edge of the pixel, (b) a gap in the low dose n^- implant (NGAP). Figure adapted from [133].



(a) STD **(b)** XDPW **(c)** NGAP

Figure 4.4: Electrostatic potential simulations of the different process variations of the MALTA pixel – standard modified STD (a), extra deep p-well XDPW (b), and an n-well gap NGAP (c). The black arrows show the electric field lines, with the star symbol placed at the location of the electric field minimum. The figures are centred at the pixel edges, with the collection electrodes of two neighbouring pixels visible on the left and right sides of the diagrams. Figure from [140].

The simulation of the electrostatic potential and electric field lines for the original standard modified process (STD) and the two process variations (XDPW and NGAP) are shown in Figure 4.4. Compared to the original STD pixel, the XDPW and NGAD designs bend the charges' drift path away from the electric field minimum (marked with a star symbol), preventing charge trapping in the minimum point and speeding up the charge collection process. Therefore, these modifications improve the radiation hardness of the sensor [115, 143]. On the other hand, the process modifications lowered the maximum bias that can be applied before punch-through back to 6-8 V [140].

4.1.1.4 MALTA Czochralski

To further improve the performance of the sensors and increase the amount of the collected charge, the original MALTA sensor was also produced on Czochralski silicon wafers, now introducing wafers with the XDPW and NGAP modifications as well. The Czochralski method is a standard method for growing single crystalline silicon,

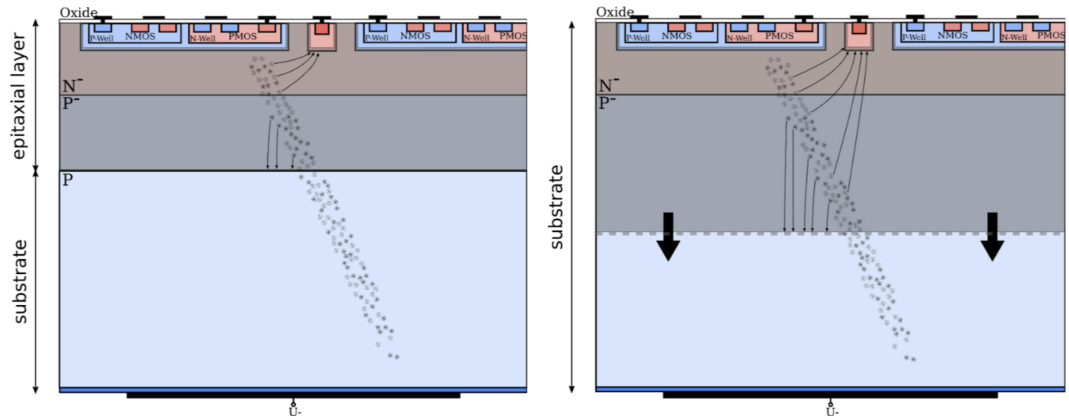


Figure 4.5: Comparison between the cross-section of the original MALTA pixel on epitaxial silicon (left) and the Czochralski substrate (right). The charge carriers created as a result of a passing particle are shown together with their paths. In the case of the Czochralski substrate, the extent of the depletion region can be expanded by increasing the reverse bias voltage – indicated by the black arrows. Figure from [146].

which can reach a high resistivity of 3-4 kΩcm [144, 145]. Previously, the MALTA and Mini-MALTA sensors were fabricated on high-resistivity epitaxial silicon of 25-30 µm thickness, which can be fully depleted at 6 V reverse bias. Moving to the Czochralski substrate, the thickness of the sensitive volume can be further increased by increasing the reverse bias as shown in Figure 4.5. The modification showed great improvements in sensor efficiency at high bias voltages after irradiation [144].

4.1.2 MALTA2

The MALTA2 sensor is the continuation of the MALTA family of monolithic active pixel sensors built in Tower 180 nm technology. Using the knowledge obtained from the previous generations of the MALTA family, the MALTA2 sensor was manufactured on both epitaxial and Czochralski substrates with a modified pixel corner design - XDPW and NGAP. In addition to these improvements, the sensor has a new front-end design with a higher gain and reduced noise [130]. As shown in Figure 4.6, the pixel matrix contains 224 rows and 512 columns of 36.4×36.4 µm^2 pixels, roughly half the matrix size of the original MALTA. Unlike the previous versions, the matrix is not divided into sectors and all pixels have the same front-end design [147]. The octagon-shaped n-well collection electrode has a diameter of 2 µm and is separated from the rest of the electronics by 4 µm. The small electrode design results in a small capacitance,

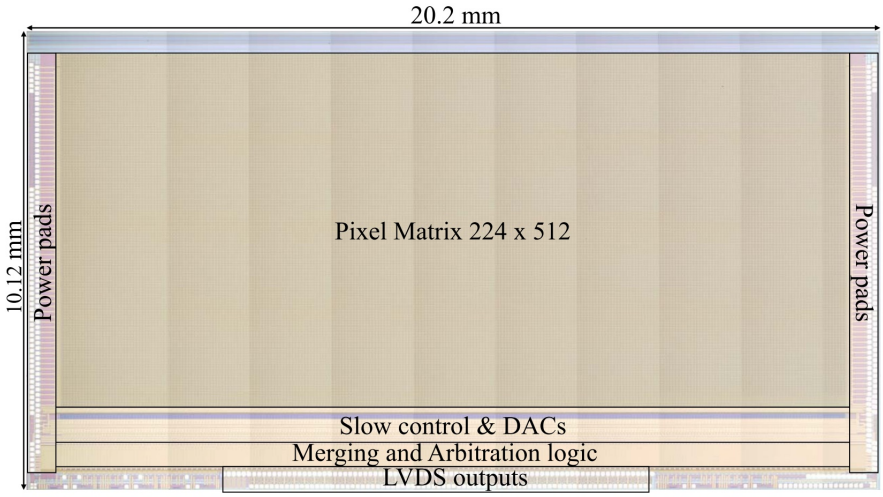


Figure 4.6: The micrograph of the MALTA2 sensor. Figure from [130].

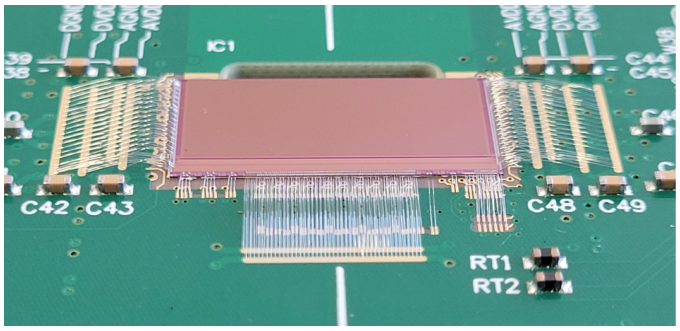


Figure 4.7: The MALTA2 sensor wire-bonded to a custom read-out carrier board.

minimising the noise and lowering power dissipation (10 mW/cm^2 digital and 70 mW/cm^2 analogue power) [148]. Figure 4.7 shows the MALTA2 sensor wire-bonded to a custom read-out carrier board.

4.1.2.1 Analogue Front-End

The MALTA2 front-end design builds on top of that implemented in the Mini-MALTA sensor with further improvements. The front-end features a continuously active circuit that performs the reset of the collection electrode, the amplification of the generated charge, the shaping of the analog signal, and the digitisation of this signal through a discrimination stage. *Piro, et al.* [130] provide a detailed description of the front-end electronics and a comprehensive summary of characterisation measurements.

4.1.2.2 Asynchronous Digital Matrix Readout

The digital matrix readout in MALTA2 is retained from its predecessor, the Mini-MALTA. The readout is asynchronous, which means that no global clock is distributed across the whole pixel matrix, which decreases the chip's power consumption. The reference signal inside a 2×8 pixel group (2 columns and 8 rows) collects the signals from any pixel within a 2 ns window, which is then transmitted via a 22-bit wide bus to the matrix periphery where they are stored in the end-of-column logic memory [149]. The matrix features two buses such that no two adjacent groups share a bus, avoiding signal overlap at the periphery.

4.1.3 Sensor characterisation with the MALTA telescope

The MALTA telescope at the Super Proton Synchrotron (SPS) North Area was briefly introduced in Chapter 3.3, but a more detailed description and performance is presented here as the telescope both uses the MALTA sensor and was used to characterise many MALTA2 samples whose performance is reported in this chapter.

Beam telescopes enable measurements not otherwise possible in a laboratory setting, mimicking the operation of a real tracking detector. Using the information from the telescope planes, the path of a charged particle passing through the telescope can be reconstructed and used to characterise the Device Under Test (DUT). The MALTA telescope, permanently installed at the H6 beamline in the SPS North Area at CERN, consists of six MALTA planes and a scintillator for timing reference (see Figure 4.8). The H6 beamline offers a high-energy hadron beam (mixed proton and pion) with energies in the range of 10-205 GeV/c with up to 4.5×10^6 particles per spill of ∼5 s duration [72]. Unless stated otherwise, the MALTA2 samples presented in this chapter have been investigated with a 180 GeV hadron beam. At such high energies, the multiple scattering of the particles is minimal, therefore the particle trajectories can be approximated to be straight lines.

Compared to the other members of the MALTA family, the original MALTA sensors have the largest pixel matrix, which allows them to cover the largest possible beam area. Due to its large pixel matrix, small pixel pitch and high hit efficiency, the MALTA

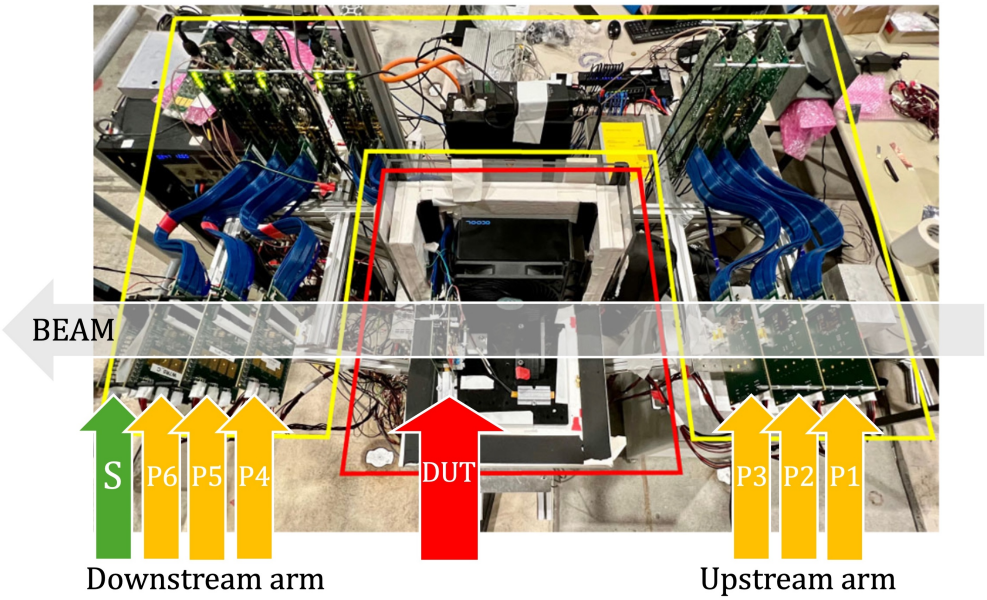


Figure 4.8: Top view of the MALTA telescope. The scintillator (S) and the telescope planes (P1-P6) with the readout are located within the yellow lines. The red lines define the space for the cold box where DUTs are mounted. The motion stages supporting the cold box can move independently from the rest of the telescope. The direction of the particle beam is indicated with an arrow. Figure adapted from [72].

sensor is an excellent choice as the basis for a beam telescope. Whereas the original MALTA does not benefit from the enhanced radiation tolerance design of Mini-MALTA and MALTA2 design, the telescope does not operate in a harsh radiation environment compared to that inside the ATLAS experiment. Therefore, the radiation hardness of the sensors is not a priority for this application. As shown in Figure 4.8, the downstream and upstream arms of the telescope (each consisting of three MALTA planes) are separated by 78 cm, allowing for an insulated polystyrene box to be placed in between, housing several DUTs at the same time. If the DUT has been irradiated and requires active cooling, an air chiller can supply cold dry air to the insulated box to lower the sensor temperature down to -30°C.

Trigger Logic

The telescope planes are connected to either a Xilinx Kintex [150] or Virtex [151] FPGAs, which are then connected to the Trigger Logic Unit (TLU) based on a Kintex FPGA evaluation board. The FPGAs can be used to build highly adjustable TLU systems, which do not require manual configuration. When a particle is detected and the TLU

interprets a coincidence in the tracking planes, the signal is sent from the telescope planes and the DUTs to the FPGAs to be recorded [152]. The fast signal from the scintillator is used as a timing reference with a timing resolution of approximately 0.5 ns. It should be noted that the recorded timing resolution of the DUT is not only due to the inherent timing resolution of the MALTA2 sensor, but also has a contribution from the FPGA. As the FPGA readout latches the trigger with the 320 MHz clock, the uncertainty corresponds to $1/(320\ \text{MHz}\times\sqrt{12}) \sim 0.9$ ns [72].

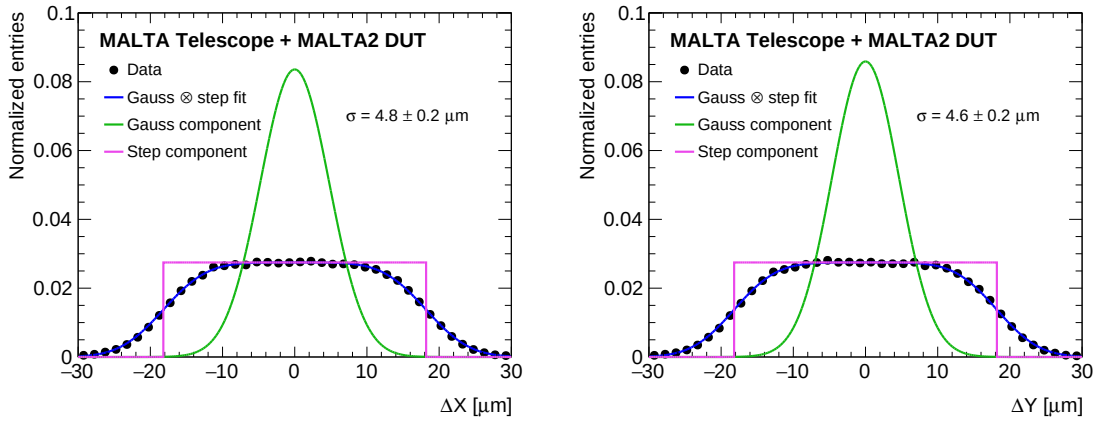
Track Reconstruction

Telescope track reconstruction and projection onto the DUT planes is handled by the software package Proteus [75]. For both the telescope planes and the DUT, Proteus identifies time-compatible hits in adjacent pixels (occurring within an adjustable 500 ns time window) and groups them into clusters. The hit clusters of the DUT are associated with a telescope track extrapolated to the DUT. The results presented in this chapter consider a track to be matched to a cluster if the distance between them is less than 80 µm (approximately 2.2 times the MALTA pixel pitch). By examining the proportion of the telescope tracks which are matched to a DUT hit cluster, sensor efficiency can be established.

Spatial resolution of the MALTA telescope

The spatial resolution of the telescope was evaluated by considering the track residuals – the distance between the reconstructed track and the fastest pixel in the associated DUT cluster. A MALTA2 sample with high efficiency (>99%) is used as the DUT. Using only the fastest pixel allows for the probability of a hit along the DUT pixel to be approximated as a uniform distribution (modelled by a two-sided step function of a width of 36.4 µm), whereas the telescope resolution can be described by a Gaussian distribution.

The distribution of the residuals along the X and Y axes takes the shape of a convolution of the two components, as shown in Figure 4.9. The spatial resolution of the telescope is extracted from the standard deviation of the Gaussian component, giving 4.8 ± 0.2 µm in the X-direction and 4.6 ± 0.2 µm in the Y-direction. These



(a) x-axis residuals

(b) y-axis residuals

Figure 4.9: The distribution of the distance between the extrapolated track position and the centre of the fastest hit within a MALTA2 cluster along the X (a) and Y (b) axes. The data is fitted with a convolution (blue) of a two-sided step function (magenta) with a Gaussian function (green). The quoted resolution is the standard deviation of the Gaussian component of the fit. Figure from [72].

values provide the upper bound of the estimated spatial resolution as they neglect any inhomogeneity and pixel edge effects of the DUT (the model uses an idealised two-sided step function response), which may inflate the width of the Gaussian function.

4.2 Radiation hardness of MALTA2

As discussed in Section 4.1.1, significant improvements in the MALTA sensor radiation hardness were achieved by modifying the process technology and adding an extra deep p-type implant (XDPW) or by introducing a gap in the low dose n^- layer (NGAP) [142]. No significant differences between the radiation hardness of the two process variations have been observed [141, 144]. This section presents data on samples with both modifications but does not directly compare the two. It focuses primarily on the performance of the chip at progressively higher neutron fluence and discusses the effect of the continuous n^- layer blanket doping on the sensor's radiation hardness – two different doping concentrations are presented, referred to as high (H-dop) and very high (VH-dop). The naming convention refers to the relative difference in the implantation dose of the n^- blanket layer, which changes by approximately 70% between H-dop and VH-dop. Results for irradiated MALTA2 produced on high-resistivity p-type epitaxial substrate (Epi) are presented first, with the rest of the section dedicated to samples produced on high-resistivity p-type Czochralski (Cz) substrate.

4.2.1 Test beam set-up and sample characterisation

Between 2021 and 2023, a dedicated set of measurements was performed to assess the radiation hardness of MALTA2 at the SPS North Area with a 180 GeV hadron beam. The MALTA telescope described in the previous section was used for beam monitoring and track reconstruction. During the data-taking process, the non-irradiated samples were kept at room temperature 20°C, while an air chiller was used to keep the irradiated samples at -20°C. The fabrication parameters and fluence levels of the MALTA2 samples studied in this thesis are listed in Table 4.2.

Neutron irradiation of the samples was carried out at the JSI TRIGA Mark II reactor at the Institute Jožef Stefan in Ljubljana, Slovenia [79, 80]. Further details on the irradiation facility are included in Section 3.4.1. The target fluences for the samples were 1, 2, 3, and 5×10^{15} 1 MeV $n_{eq}cm^{-2}$. Following irradiation, the samples were stored in a freezer at -20°C. The samples did not undergo any long-term reverse annealing at elevated temperatures.

Table 4.2: Overview of the main specification of the MALTA2 samples. For each sample, the substrate type, the fluence level, the sensor flavour, and the total thickness are specified. The doping level of the n^- blanket layer is given as high or very high. The last column indicates if the backside of the sample underwent metallisation (metal) or not (regular).

Substrate Type	**Irrad. fluence** [1 MeV $n_{eq}cm^{-2}$]	**Pixel Flavour**	**Total Thickness**	**n^- doping level**	**Backside Type**
Epi	2×10^{15}	NGAP	300 µm	high	regular
Cz	0	XDPW	100 µm	high	metal
Cz	1×10^{15}	XDPW	100 µm	high	metal
Cz	2×10^{15}	XDPW	100 µm	high	metal
Cz	3×10^{15}	XDPW	100 µm	high	metal
Cz	3×10^{15}	XDPW	100 µm	very high	regular
Cz	3×10^{15}	XDPW	100 µm	very high	metal
Cz	5×10^{15}	NGAP	100 µm	high	regular
Cz	5×10^{15}	XDPW	100 µm	very high	regular

For the standard operation of the MALTA2 chip, the p-well bias V_{PWELL} is set at -6 V, and the collection electrode's reset voltage is fixed at 0.8 V. The samples are depleted by increasing the magnitude of the reverse substrate bias referred to as V_{SUB} or SUB. For visual clarity, results presented in this thesis often show only the magnitude of the substrate voltage, which is a positive quantity. However, it should be noted that the applied bias voltage is always negative. To protect the electronics from high currents, the operational limit of the substrate voltage is set by the supply current compliance level of 2 mA. In the MALTA2 sensor, a global operating threshold is applied across the pixel matrix. The threshold is the minimum incident charge at which the pixel readout discriminator registers a hit, so its value is quoted in the unit of equivalent electron charge. The exact threshold of a pixel tends to vary with respect to the global threshold (known as *threshold dispersion*) – this variation is measured to be <10% for the MALTA2 samples. Sensor performance can be parameterised using several figures of merit. In this thesis, the focus is on cluster size, efficiency, and timing resolution of MALTA2 samples. More details on pixel noise and detection threshold can be found in [146].

Cluster size

When a particle passes through a pixelated sensor, enough charge can be deposited to trigger the electronics in multiple neighbouring pixels. A cluster is created by grouping adjacent pixels (those sharing an edge) that fired within a defined time window. The

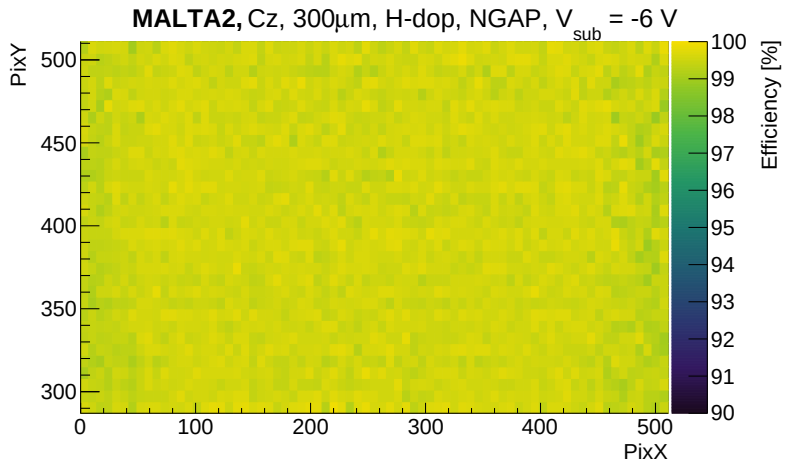
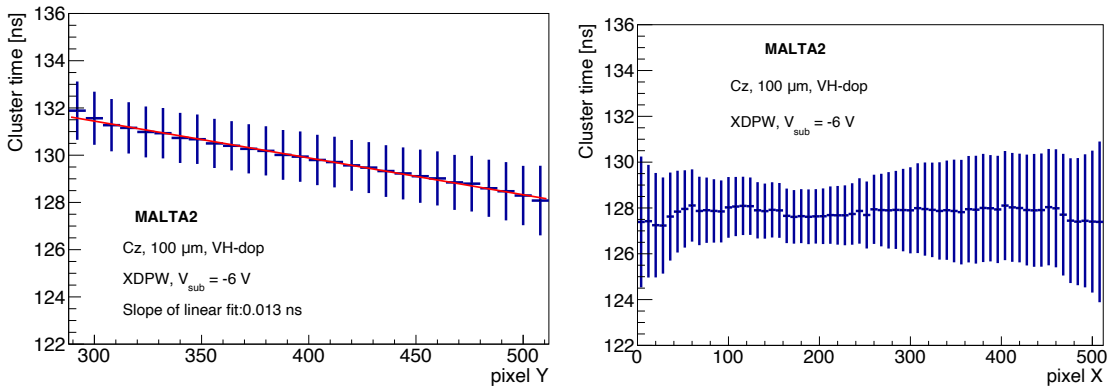


Figure 4.10: An example 2D efficiency map of a non-irradiated MALTA2 on Czochralski substrate. The sample is operated at V_{SUB} = -6 V bias, V_{PWELL} = -6 V bias, and a threshold of 150 electrons. The noise per pixel was found to be negligible $<1\times10^{-3}$ Hz.

number of pixels that can be grouped like this is called the *cluster size*. The cluster size depends on the pixel pitch, operating threshold, bias voltage, thickness, and other factors. It is an important quantity as it relates to the spatial resolution of the sensor. The position of the cluster is calculated by assigning equal weight to all neighbouring pixels that registered a hit and finding the average position along the *row* and *column* direction of the matrix. More information on this clusterisation method and possible alternatives can be found in the following Section 4.3.

Efficiency

The hit detection efficiency is calculated as the ratio of the matched clusters to the total number of reconstructed tracks. A matched cluster is one whose centre is found within 80 µm of a telescope track projected onto the surface of the DUT. Additionally, the track and the cluster must occur within a 500 ns acquisition window [72]. Narrowing the window will improve the timing resolution of the sensor but would also result in lower efficiency. During data acquisition, several noisy pixels are masked. The effect of masking on total efficiency is taken into account. A 2D efficiency plot of a non-irradiated MALTA2 sample is shown in Figure 4.10, showing a uniform efficiency of 99.6% across the whole matrix. The operating threshold of the electronics strongly influences the efficiency. Lowering the threshold increases the detector's efficiency, but



(a) Row correction **(b)** Column correction

Figure 4.11: Time of arrival of the leading hit in the cluster with respect to the scintillator as a function of the row (a) and column (b) number of the pixel matrix. The error bars represent the corresponding standard deviation of the binned data. Both measurements were performed on a MALTA2 Cz sample at V_{SUB} = -6 V and an operating threshold of 170 e^-.

the noise also increases. Understanding the trade-offs between the different figures of merit is critical when finding the optimal configuration for a given sensor.

Timing resolution

To assess the timing performance of the investigated MALTA2 samples during the test beam campaigns, a scintillator is used as a reference with jitter contribution $\sigma_{scintillator} \approx 0.5$ ns. The time delay between the fastest recorded hit in a matched cluster, and the scintillator reference signal is referred to as L1A. Before the performance can be characterised, some intrinsic effects of the MALTA2 sample must be considered. First is the time required for the hit signal to reach the matrix periphery as it travels over an asynchronous parallel bus along the matrix columns [153]. As shown in Figure 4.11a, the effect has a linear trend with a slope of 0.013 ns per row pixel. Secondly, a correction is applied for different columns of the matrix as shown in Figure 4.11b. The column variation is attributed to the non-uniformities in the chip response [3].

Figure 4.12 shows the corrected distribution of the time of arrival of the fastest hit in a pixel cluster with respect to the scintillator. The data was obtained for a non-irradiated MALTA2 Czochralski sample, and its core is fitted with a Gaussian distribution (plotted in red) whose standard deviation parametrises the timing resolution of the sample as σ_t = 1.7 ns. The distribution contains the jitter contribution from the scintillator and from

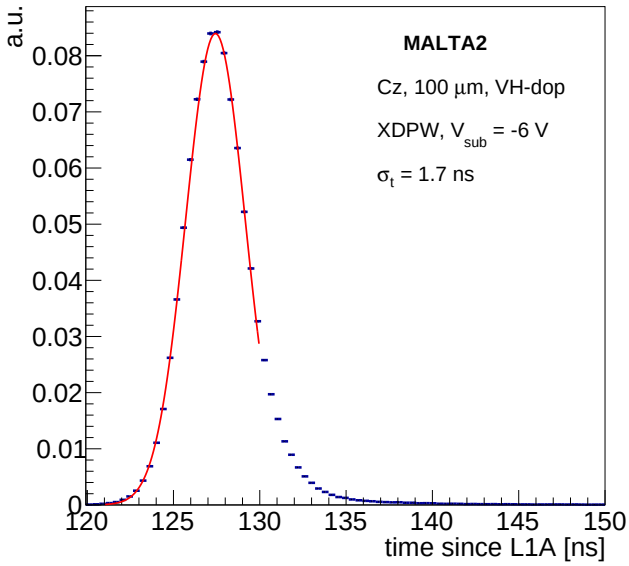


Figure 4.12: Time of arrival of the leading hit in the cluster with respect to a scintillator reference. The y-axis showing the number of events in each bit is normalised to an arbitrary unit. The quoted σ_t corresponds to the Gaussian fit to the core of the distribution. The measurement was performed on a MALTA2 Cz sample with very high n^- blanket layer doping at V_{SUB} = -6 V and operating threshold of 170 e^-.

oversampling within the FPGA used for readout (σ_{FPGA} = 3.125 ns/$\sqrt{12}$ = 0.9 ns). After radiation damage, the core of the distribution can no longer be approximated using a Gaussian function; hence, for the irradiated sample, the numerical standard deviation of the full distribution is used as a measure of the timing performance. In order to avoid confusion with the standard deviation of the Gaussian fit, the numerical value is referred to as the Root Mean Square (RMS). Due to the long tail of the distribution, the RMS value is larger than the standard deviation of the Gaussian fit to the core.

4.2.2 Irradiated MALTA2 on Czochralski substrate

The following section focuses on the performance of MALTA2 samples on the Czochralski substrate. Compared to MALTA2 sensors on epitaxial substrates which are presented later in Section 4.2.4, MALTA2 Cz sensors can generate a larger depletion volume, leading to a significantly larger signal [144].

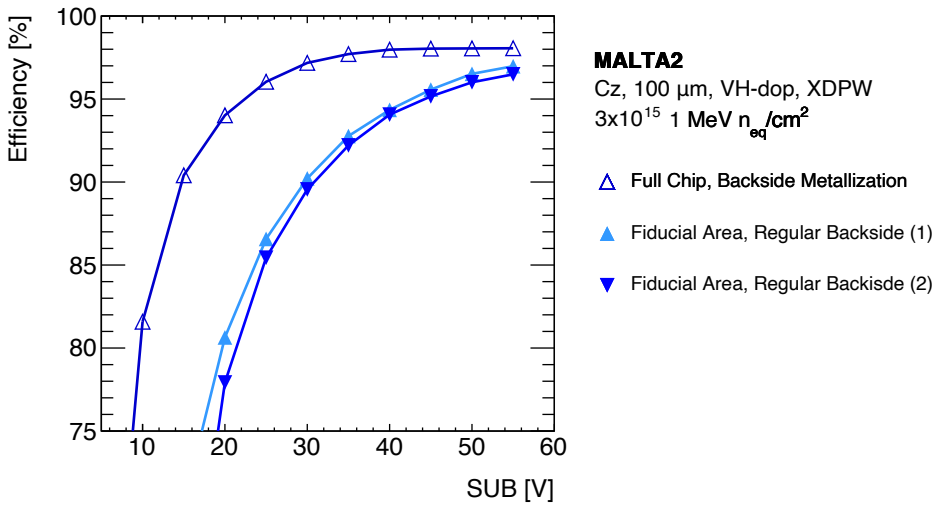


Figure 4.13: The average efficiency of 3×10^{15} 1 MeV $n_{eq}cm^{-2}$ irradiated MALTA2 on Cz substrate (XDPW, very high doping n-layer, 100 µm) as a function of substrate bias voltage. The samples differ in the processing step of the backside to enhance the contact with the substrate – regular backside (two samples shown) or backside metallisation. All samples were operated at the best performing operating threshold ($\sim$100 e^-) and -6 V PWELL bias. The efficiency of the backside metallised sample corresponds to the performance of the full chip. For the other samples, the efficiency refers to the performance in fiducial regions, where good contact is achieved.

4.2.2.1 Backside treatment

The bias voltage is applied to the sensor from the carrier PCB via electronically conductive Staystik® 571 film [154] in contact with the right and left edge of the backside of the MALTA2 matrix. It was observed that after irradiation, this approach can no longer guarantee sufficient backside voltage propagation, resulting in a non-uniform efficiency distribution across the chip. In this case, the sensor's performance is quantified using only the regions where good contact can be guaranteed (referred to as *fiducial areas*) - along the right and left edges where the conductive film is applied. An alternative approach using *backside metallisation* was studied to improve bias voltage propagation for the irradiated Czochralski samples. Samples without this treatment are referred to as *regular backside*. The backside metallised samples have a 1.0 ± 0.1 µm thick aluminium layer deposited on their backside, which assists biasing the sensors from the periphery. As shown for the 3×10^{15} 1 MeV $n_{eq}cm^{-2}$ samples in Figure 4.13, backside metallisation increases the efficiency of the samples and allows for the full chip to be used. Whereas the regular samples can reach an efficiency comparable to the backside metallised samples, the substrate bias voltage must be approximately twice as high to

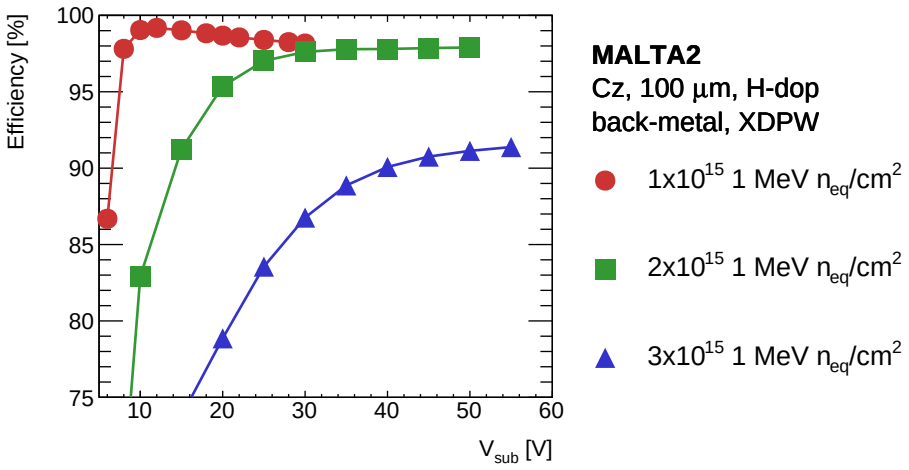


Figure 4.14: The average efficiency as a function of substrate voltage for three MALTA2 samples (XDPW, high doping of n^- layer, 100 µm, backside metallisation) irradiated to 1, 2, and 3×10^{15} 1 MeV $n_{eq}cm^{-2}$. The operating threshold corresponds to 240, 260, and 120 e^-, respectively.

achieve the same performance. More information about the thinning, implantation, annealing, and aluminium deposition is included in [3].

4.2.2.2 Performance of irradiated back-metallised samples

The three backside metallised irradiated MALTA2 Cz samples with high doping of the n^- blanket layer listed in Table 4.2 are considered further. As shown in Figure 4.14, the 1×10^{15} 1 MeV $n_{eq}cm^{-2}$ sample achieves high efficiency (∼99%) at relatively low substrate voltage (V_{SUB} = -10 V). However, a higher substrate voltage is required to obtain high efficiency for the samples with elevated radiation damage. A general trend is observed, where the efficiency increases with applied substrate bias voltage and then levels off as the bias is increased further. For the high-doped 3×10^{15} 1 MeV $n_{eq}cm^{-2}$ sample, only an efficiency of ∼90% is recovered.

By monitoring the current flowing between the substrate and the PWELL, it was observed that with increased fluence levels, the punch-through threshold voltage increases. This increase allows the MALTA2 Cz to be operated at a higher substrate voltage compared to the non-irradiated samples - usually only up to ∼12 V. A similar behaviour was also observed for the MALTA Cz sensors [144]. A possible explanation for this behaviour was attributed to the so-called double junction model [155], where irradiation causes the creation of deep-level donors, which introduce a region of

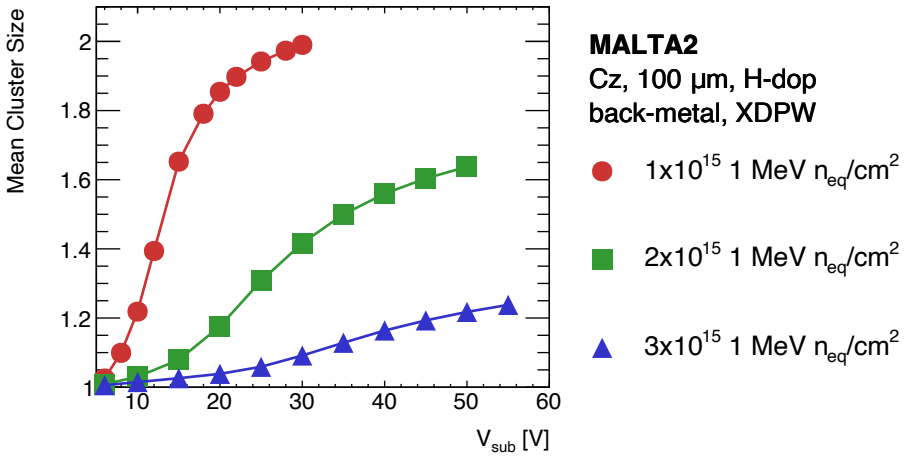


Figure 4.15: The cluster size as a function of substrate voltage for three MALTA2 samples (XDPW, high doping of n^- layer, 100 µm, backside metallisation) irradiated to 1, 2, and 3×10^{15} 1 MeV $n_{eq}cm^{-2}$. The operating threshold corresponds to 240, 260, and 120 e^-, respectively.

effective n-doping near the p-well. This effect increases the potential barrier between p-well and p-type substrate.

The average cluster size also evolves with the radiation fluence and bias voltage, as shown in Figure 4.15. As the bias voltage increases, the cluster size grows due to the enhanced effect of charge sharing between pixels and larger active depths in the Czochralski substrate. For the 1×10^{15} 1 MeV $n_{eq}cm^{-2}$ sample, the average cluster size reaches up to 2 pixels at V_{SUB} = -30 V. At higher radiation fluences, the cluster size decreases. The decrease is attributed to the reduced charge collection due to increased charge trapping and overall reduction in hit efficiency. The smaller signals fall below the threshold and therefore are not included in the cluster.

4.2.2.3 The effect of n^- layer doping on efficiency

In order to test the effect of n-layer blanket doping on the sensor performance, a back-metallised MALTA2 Cz sample with very high doping of the n^- layer was irradiated to the fluence of 3×10^{15} 1 MeV $n_{eq}cm^{-2}$. As shown in Figure 4.16, the sample with the very high doping of the n^- layer achieves a much higher efficiency (>97%) compared to the sample with high doping. The difference is even more significant at lower bias voltages. With radiation damage, the lateral depletion of the n^- layer diminishes, but the results suggest that this effect is less pronounced in the sample with very high

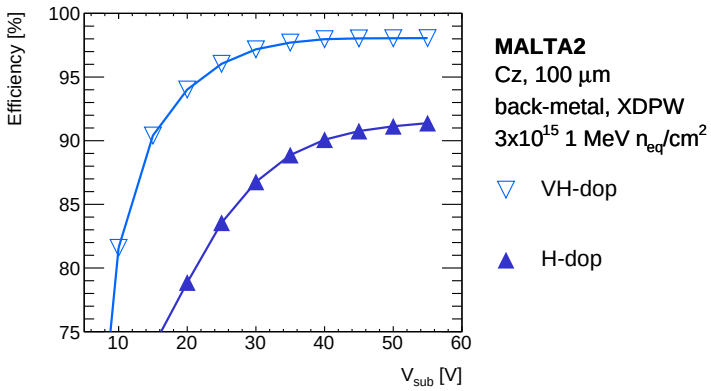


Figure 4.16: The average efficiency as a function of substrate voltage for two MALTA2 samples (XDPW, 100 µm thick, backside metallisation) irradiated to 3×10^{15} 1 MeV $n_{eq}cm^{-2}$. The samples differ in the doping level of the n^- layer – high (H-dop) and very high (VH-dop). Their operating threshold corresponds to 120 and 110 e^-, respectively.

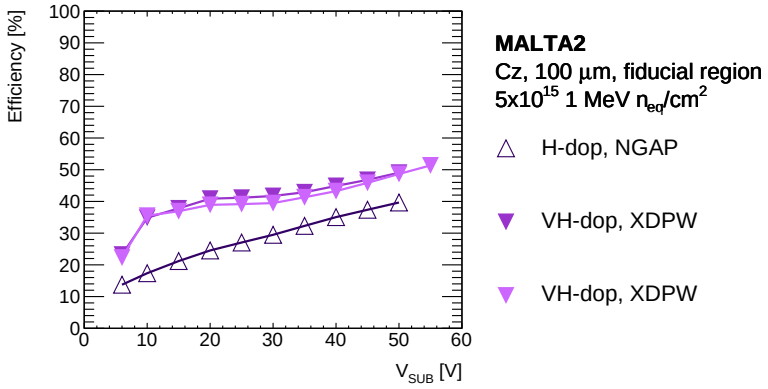
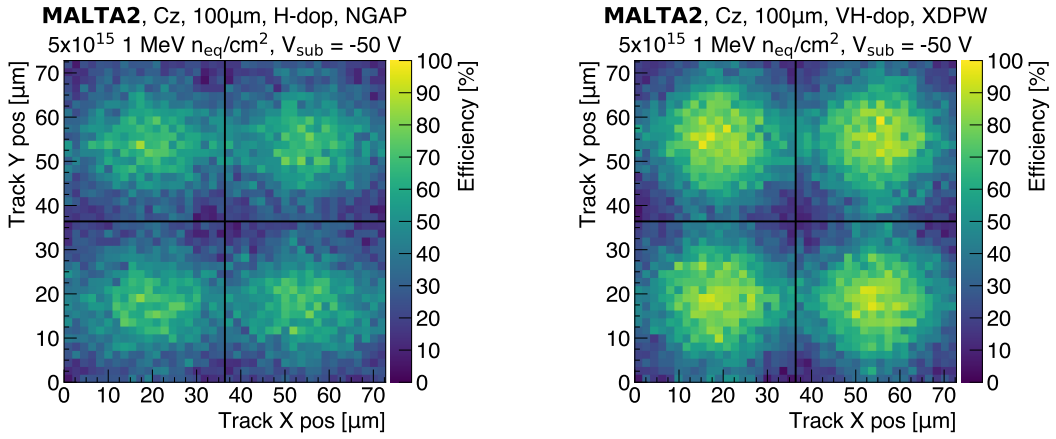


Figure 4.17: The average efficiency as a function of substrate voltage for the MALTA2 samples (100 µm thick, regular backside) irradiated to 5×10^{15} 1 MeV $n_{eq}cm^{-2}$. The efficiency is evaluated within a selected fiducial region where good electrical contact is achieved. The samples differ in the doping level of the n^- layer – high (H-dop) and very high (VH-dop), and in the process modification (NGAP or XDPW). Their operating threshold corresponds to ~100 e^-. Measurements were performed at -15°C.

doping. Further analysis showed that the efficiency uniformity within the MALTA2 pixel is greatly improved in the case of the very high doping sample [3].

The comparison between the samples with various doping layers was also explored for samples irradiated to the fluence of 5×10^{15} 1 MeV $n_{eq}cm^{-2}$, with the efficiency shown in Figure 4.17. Results for one sample with high doping and two samples with very high doping of the n^- layer are available. None of the samples were back-metallised, so only selected fiducial regions with good electrical contact with the backside were analysed. The increased radiation fluence greatly diminishes the hit efficiency. Nevertheless, the very high doping of the n-layer improves the performance.



(a) H-dop **(b)** VH-dop

Figure 4.18: The 2D sample efficiency projected onto a 2×2 pixel matrix. Shown are the MALTA2 samples on the Czochralski substrate, XDPW, 100 µm thick, with high (a) and very high (b) doping of n-implant. The samples were irradiated to a fluence of 5×10^{15} 1 MeV $n_{eq}cm^{-2}$ and are operated at -6 V PWELL bias and -50 V SUB bias. The operating threshold corresponds to ∼100 e^-. Measurements were performed at -15°C.

As mentioned, the relative difference in the implantation dose between the two doping levels is approximately a factor of 1.7.

To better understand the impact of irradiation on the samples' efficiency, the telescope tracks projected onto the DUT were analysed further. The position of the hit track from the whole chip was projected onto a 2×2 pixel matrix using a modulo operation to get the remainder as

$$X_{IP} = X_{track} \bmod 72.8, \tag{4.1}$$

$$Y_{IP} = Y_{track} \bmod 72.8, \tag{4.2}$$

where X/Y_{IP} correspond to the position on the reduced 2×2 pixel grid, and X/Y_{track} are the global position coordinates of the telescope track projected onto the MALTA2 matrix. All quantities are in the unit of µm. The value of 72.8 is used as this is the height and width of two MALTA2 pixels in µm. This approach allows for the exploration of the in-pixel efficiency after irradiation. Figure 4.18 shows the in-pixel efficiency after 5×10^{15} 1 MeV $n_{eq}cm^{-2}$ irradiation for two samples with different n^- layer doping concentrations. The plots suggest that the samples' efficiency loss originates from the pixel corners, where the diminished electric field degrades the charge collection. An improvement in the efficiency near the pixel centre is observed for the very high doping sample.

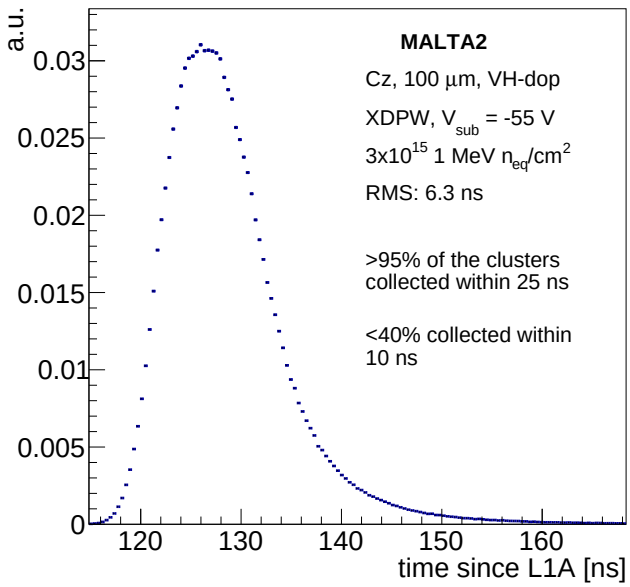


Figure 4.19: The time of arrival of leading hit in the cluster with respect to a scintillator for a MALTA2 sample on Cz substrate (XDPW, very high doping of the n^- blanket layer, 100 µm, backside metallisation), irradiated to 3×10^{15} 1 MeV $n_{eq}cm^{-2}$. The sample is operated at V_{SUB} = -55 V and an operating threshold of 110 e^-.

4.2.3 Timing performance of the irradiated MALTA2-Cz samples

As mentioned above, the timing performance of MALTA2 samples after irradiation is quantified using the RMS value of the measured delay distribution between the leading hit in a cluster and the scintillator reference (referred to as L1A). To illustrate this approach, the timing difference distribution of a MALTA2 Cz sample irradiated to 3×10^{15} 1 MeV $n_{eq}cm^{-2}$ with very high doping of the n^- layer is shown in Figure 4.19. The RMS value of the distribution corresponds to 6.3 ns. Analysing the data further, it is possible to extract that more than 95% of the clusters are collected within a 25 ns window and nearly 40% within a 10 ns window. For the non-irradiated sample shown previously in Figure 4.12, the fraction of clusters collected within a 25 ns and 10 ns window is 99% and 96%, respectively.

Comparing MALTA2 Cz samples irradiated up to a fluence of 3×10^{15} 1 MeV $n_{eq}cm^{-2}$, Figure 4.20 shows the evolution of the timing performance as a function of bias voltage. Only instances where the efficiency is greater than 85% are considered (compare with Figure 4.14). As the substrate bias voltage and the extent of the depletion area increase,

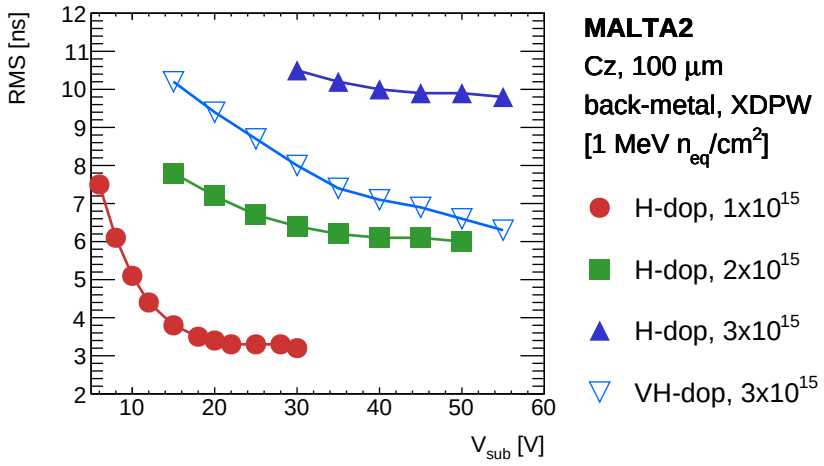
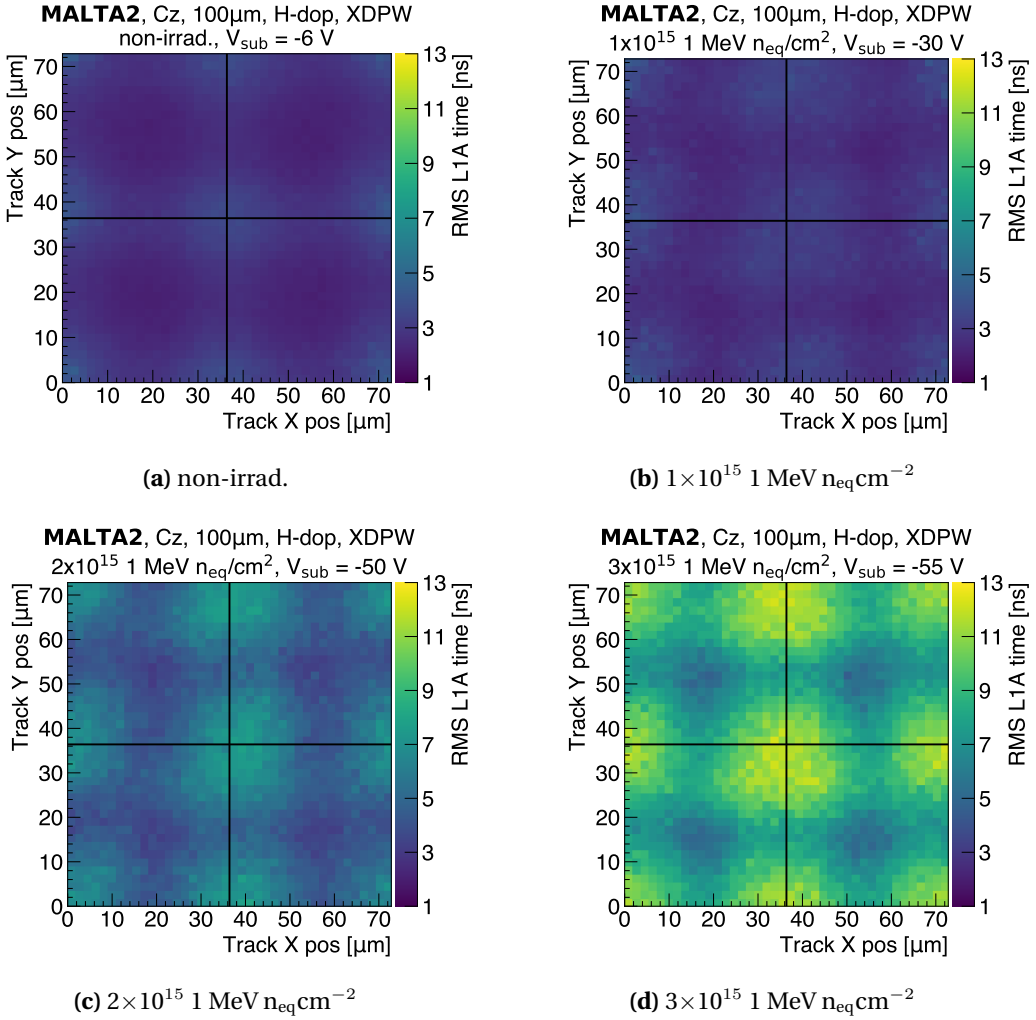


Figure 4.20: The root-mean-square (RMS) of timing difference distribution as a function of the substrate bias voltage. Shown here are four MALTA2 samples (XDPW, 100 µm thick and backside metallisation). Three samples feature a high doping of the n^- blanket layer. These are irradiated to 1, 2, and 3×10^{15} 1 MeV $n_{eq}cm^{-2}$, and the threshold corresponds to 240, 260, and 120 e^-, respectively. One sample features a very high doping of the n^- blanket layer. It is irradiated to 3×10^{15} 1 MeV $n_{eq}cm^{-2}$ and operated at the threshold of 110 e^-.

faster signals with greater amplitude decrease the spread of the timing distribution and lower the extracted RMS value. On the other hand, as displacement damage creates deep traps and modifies the effective doping of the n^- blanket layer, the timing resolution worsens. The sample with very high n^- blanket layer doping achieves a better timing performance than the one irradiated to the same neutron fluence but with high doping. This observation is discussed later in Section 4.2.3.2.

4.2.3.1 In-pixel projections

The impact of irradiation on the samples' timing performance is further studied by using the in-pixel projections as outlined in Equations 4.1 and 4.2. The leading hit time data are sorted into 1.82×1.82 µm^2 bins based on their associated track position within the pixel (X_{IP} and Y_{IP}). The projection of the RMS value of the time distribution within each bin is shown for the four different irradiation levels (non-irradiated, 1, 2, and 3×10^{15} 1 MeV $n_{eq}cm^{-2}$) in Figure 4.21. For this comparison, only the samples with high doping of the n^- layer are considered. For each bin, data points that deviate by more than seven times the RMS value from the bin mean value are excluded from the calculation. The operating condition of the four samples corresponds to the data



(a) non-irrad.

(b) 1×10^{15} 1 MeV $n_{eq}cm^{-2}$

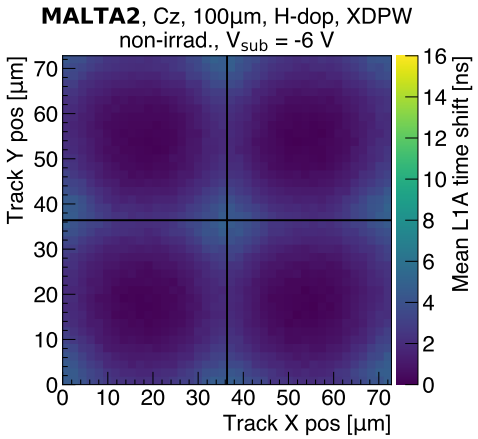
(c) 2×10^{15} 1 MeV $n_{eq}cm^{-2}$

(d) 3×10^{15} 1 MeV $n_{eq}cm^{-2}$

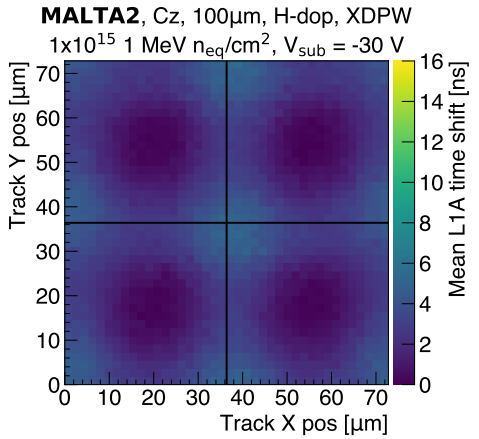
Figure 4.21: Projection of the RMS value of the leading hit time within a cluster with respect to a scintillator reference for four MALTA2 samples (Cz, XDPW, high doping of n^- layer, 100 µm thick, and back metallised). The samples were irradiated to four different irradiation levels (non-irradiated, 1, 2, and 3×10^{15} 1 MeV $n_{eq}cm^{-2}$) and the threshold corresponds to 250, 240, 250, and 120 e^-, at V_{SUB} = -6, -30, -50, -55 V bias voltage, respectively.

point where the timing RMS is minimised while the efficiency is above 90%. The results show that the RMS value is the smallest if the pixel is hit near the centre, whereas the value increases for corner hits, particularly at large fluences. One of the proposed effects which contribute to the degraded timing performance in the pixel corners is the increased charge trapping probability due to the longer drift path of the charge carriers compared to those from the pixel centre.

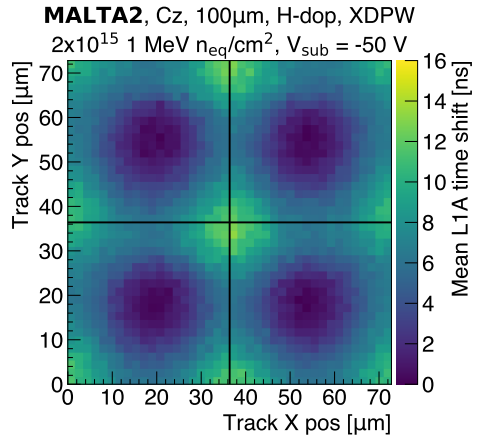
The mean timing of the leading hit within a cluster with respect to the scintillator also varies depending on the track position. Using the same binning strategy as before,



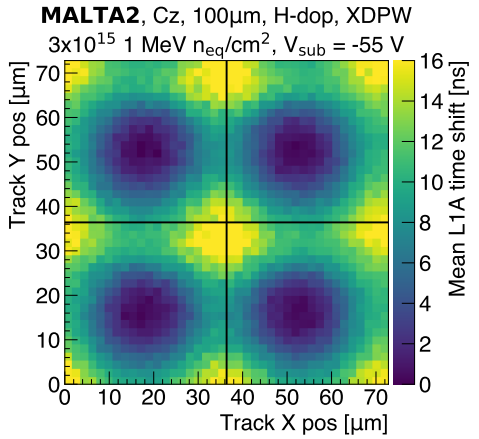
(a) non-irrad.



(b) 1×10^{15} 1 MeV $n_{eq}cm^{-2}$



(c) 2×10^{15} 1 MeV $n_{eq}cm^{-2}$



(d) 3×10^{15} 1 MeV $n_{eq}cm^{-2}$

Figure 4.22: Projection of the variation of the mean timing of the leading hit within a cluster with respect to a scintillator reference for four MALTA2 samples (Cz, XDPW, high doping of n^- layer, 100 µm thick, and back metallised). The samples were irradiated to four different irradiation levels (non-irradiated, 1, 2, and 3×10^{15} 1 MeV $n_{eq}cm^{-2}$) and the threshold corresponds to 250, 240, 250, and 120 e^-, at V_{SUB} = -6, -30, -50, -55 V bias voltage, respectively. The quoted mean time value is extracted from a Gaussian fit to the core of the timing distribution for each bin relative to the bin with the smallest value.

Figure 4.22 shows the difference between the mean time delay across the MALTA2 pixel. The time shift values are scaled such that the pixel centre corresponds to a zero time shift. Comparing the individual figures for the samples with different irradiation levels qualitatively shows that the uniformity of the mean time of arrival of the leading hit deteriorates as the fluence increases. Although this is not the only effect impacting the timing performance, the loss of uniformity further increases the RMS values shown in Figure 4.20.

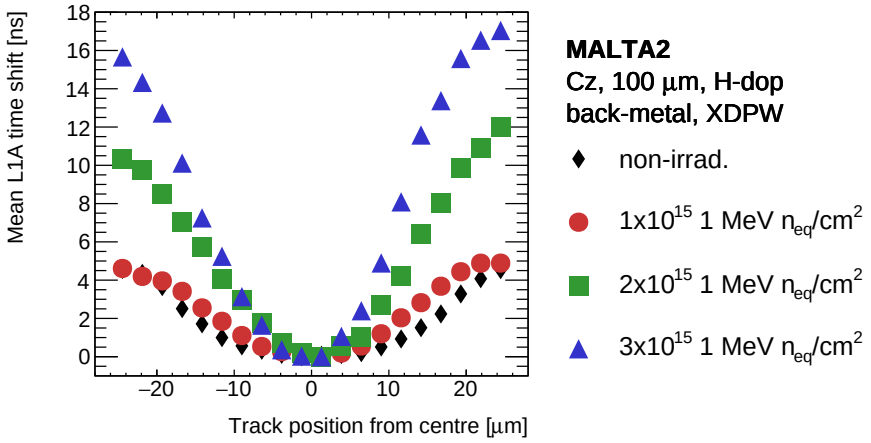


Figure 4.23: The relative shift of the mean time of arrival of the leading hit within the cluster with respect to the scintillator as a function of the distance of the associated telescope track from the pixel centre. Results are shown for four MALTA2 samples (Cz, XDPW, high doping of n^- layer, 100 µm thick, and back metallised). The samples were irradiated to four different irradiation levels (non-irradiated, 1, 2, and 3×10^{15} 1 MeV $n_{eq}cm^{-2}$) and the threshold corresponds to 250, 240, 250, and 120 e^-, at V_{SUB} = -6, -30, -50, -55 V bias voltage, respectively. The quoted mean time value is extracted from a Gaussian fit to the core of the timing distribution for each bin relative to the bin with the smallest value.

To evaluate this effect quantitatively, the bins along the diagonal of the MALTA2 pixel are considered for the samples shown in Figure 4.22. Only selecting the bins along the MALTA2 pixel diagonal, Figure 4.23 shows the relative shift of the mean time of hit as a function of the associated telescope track distance from the pixel centre. The quoted mean is extracted from a Gaussian fit to the core of the distribution for each bin along the pixel's diagonal. The data show only a small difference in the shift in the mean hit time between the non-irradiated sample and the sample irradiated to 1×10^{15} 1 MeV $n_{eq}cm^{-2}$. In both instances, the difference between the pixel centre and the pixel corner is less than 5 ns. The shift grows with the fluence to more than three times the original value, reaching close to 17 ns in the case of the 3×10^{15} 1 MeV $n_{eq}cm^{-2}$.

Further investigation indicates that the operating threshold does not have a substantial impact on the mean time shift, which suggests that the variation between the samples is not due to time walk. The slight ($\sim$2 ns) asymmetry between the arbitrarily defined positive and negative distance from the pixel centre may stem from the non-exact symmetry of the MALTA2 pixel as the p-well shape is diagonally asymmetric. Furthermore, there are additional readout effects, such as the data merging of the MALTA2 readout – these are discussed in Section 4.3.

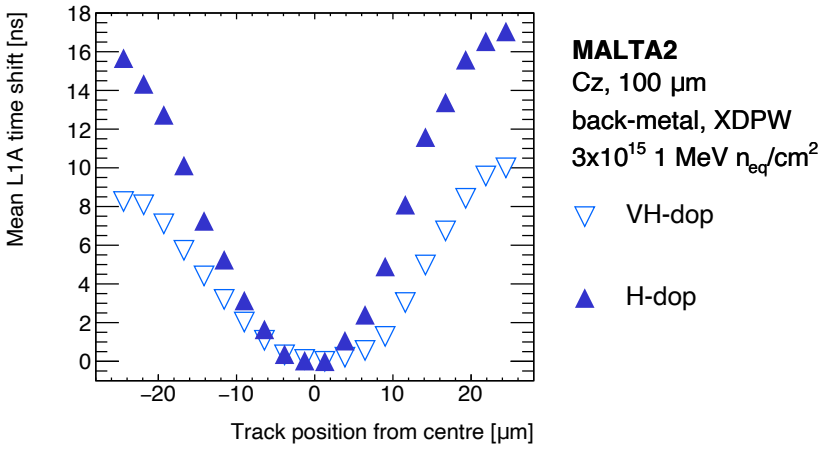


Figure 4.24: The relative shift of the mean L1A time with respect to the scintillator as a function of the distance of the associated telescope track from the pixel centre. Results are shown for two MALTA2 samples (Cz, XDPW, 100 µm thick, and back metallised) irradiated to 3×10^{15} 1 MeV $n_{eq}cm^{-2}$) and operated at V_{SUB} = -55 V. The samples differ in the doping level of the n^- layer – high and very high, and the threshold corresponds to 120 and 110 e^-, respectively.

4.2.3.2 The effect of n^- layer doping on timing performance

Further consideration is given to the two samples irradiated to the fluence of 3×10^{15} 1 MeV $n_{eq}cm^{-2}$ which differ in the doping concentration of the n^- blanket layer. It was already demonstrated in Figure 4.16 that the sample with very high doping of the n^- layer shows higher efficiency (∼98%) compared to that with high doping (∼91%). The comparison between the mean time shift along the diagonal of the two samples in Figure 4.24 indicates that the sample with very high doping of the n^- layer displays better uniformity of the mean time of hit across the pixel. As the samples otherwise share identical design parameters (XDPW, back-metal, Czochralski substrate, etc.), this observation suggests that the VH-dop sample exhibits better radiation tolerance compared to the sample with high doping. Despite being subject to a higher radiation fluence, the VH-dop 3×10^{15} 1 MeV $n_{eq}cm^{-2}$ sample shows comparable or marginally better (∼2 ns) time shift in the pixel corners compared to the H-dop 2×10^{15} 1 MeV $n_{eq}cm^{-2}$ sample shown in Figure 4.23. However, the RMS value of the VH-dop 3×10^{15} sample is still slightly higher than that of the H-dop 2×10^{15} sample (see Figure 4.20), highlighting that even though the uniformity of the timing response across the pixel is an important factor, other effects need to be considered when evaluating the evolution of the timing performance with increasing radiation fluence.

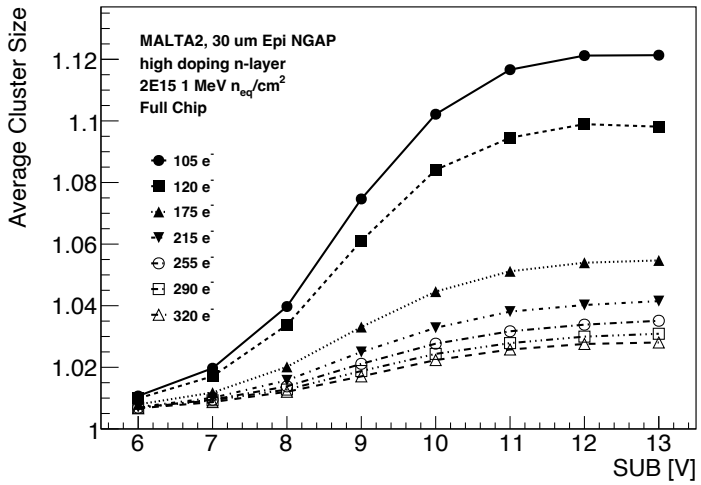


Figure 4.25: Average cluster size of irradiated MALTA2 (30 µm thick Epi, NGAP, high doping of n-blanket) versus bias voltage at various operating thresholds and -6 V PWELL bias. The sample was neutron-irradiated to the fluence of 2×10^{15} 1 MeV $n_{eq}cm^{-2}$. The average cluster size corresponds to the performance across the whole chip.

4.2.4 Irradiated MALTA2 on epitaxial substrate

Following the discussion of Czochralski MALTA2 samples, this section presents the results obtained from a sample produced on an epitaxial substrate. The investigated MALTA2 sample (NGAP, H-dop) has a total thickness of 300 µm, of which the top 30 µm active layer is grown using the epitaxial process. The sample was neutron-irradiated to the fluence 2×10^{15} 1 MeV $n_{eq}cm^{-2}$. The average cluster size as a function of substrate voltage at various operating threshold points is shown in Figure 4.25. For comparison, an equivalent non-irradiated Epi MALTA2 sample reached a cluster size of 1.45 ± 0.01 at 155 e^- threshold [156]. The data shows that the average cluster size increases as the operating threshold is lowered. Irrespective of the operating threshold, the average cluster size grows between 6 V and 10 V and consequently plateaus for voltages above 11 V. Similar trends have also been observed on other irradiated Epi MALTA2 samples.

In Figure 4.26, the efficiency of the sample is plotted as a function of the substrate voltage. As the threshold is lowered, the efficiency increases. For all thresholds, the number of masked noisy pixels was below 50. Irrespective of the operating threshold, the maximum efficiency rises with bias voltage until about 10 V, but decreases if the bias voltage is further increased. The pattern of the efficiency levelling off and then

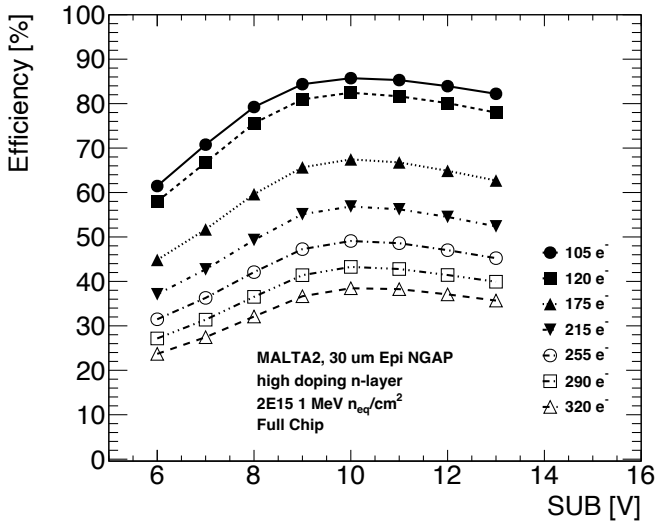


Figure 4.26: Average efficiency of irradiated MALTA2 (30 µm thick Epi, NGAP, high doping of n-blanket) versus bias voltage at various operating threshold points and -6 V PWELL bias. The sample was neutron-irradiated to the fluence of 2×10^{15} 1 MeV $n_{eq}cm^{-2}$. Quoted efficiency corresponds to the performance across the whole chip.

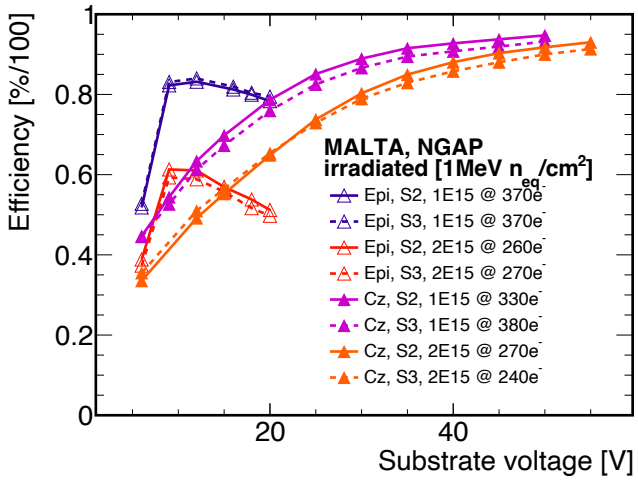


Figure 4.27: Efficiency of MALTA samples irradiated to 1×10^{15} and 2×10^{15} 1 MeV $n_{eq}cm^{-2}$ on epitaxial and Czochralski silicon with the NGAP modification to the planar n-layer versus substrate bias. Measurements were done with a 4 GeV electron beam at the DESY test beam facility in 2019 on the second and third sectors of the MALTA matrix. Figure from [157].

declining was previously observed for the MALTA epitaxial samples, which are shown in Figure 4.27 together with Cz samples. To understand the reasons behind the decline in sample efficiency, a full simulation of the electric field inside the irradiated Epi samples is needed. As the irradiated Czochralski samples exhibit efficiency that surpasses the epitaxial samples and do not show the levelling effect, more attention was focused on studying their performance after irradiation.

4.2.5 Summary

Monolithic pixel detectors provide an exciting opportunity to reduce the material and lower production costs. The MALTA2 sensor is the latest DMAPS prototype of the MALTA family, targeting the radiation tolerance requirements of the outermost layer of the upgraded ATLAS ITk Pixel Detector at the HL-LHC (detector efficiency >97% and timing resolution better than 25 ns up to NIEL fluence of 10^{15} 1 MeV $n_{eq}cm^{-2}$). Results presented in this section are part of an effort to improve the radiation tolerance of MALTA sensors, which requires testing different substrates, pixel designs, and post-manufacture treatments.

As part of the endeavour, MALTA2 samples irradiated up to the fluence of 5×10^{15} 1 MeV $n_{eq}cm^{-2}$ were tested at the SPS with a 180 GeV hadron beam. At a sufficiently low operating threshold (105 e^-), the samples produced on epitaxial substrate reach efficiency of $\sim$90% after being irradiated to 2×10^{15} 1 MeV $n_{eq}cm^{-2}$. Compared to a MALTA2 sample on a Czochralski, the Cz sample performs much better at the same neutron fluence levels, achieving an efficiency of $\sim$98% at sufficiently high substrate bias. Increasing the doping of the n^- blanket layer enabled the sensor to maintain maximum efficiency of $\sim$98% and achieve an average cluster size of 1.7 at the irradiation fluence of 3×10^{15} 1 MeV $n_{eq}cm^{-2}$. At this fluence, the RMS of the VH-dop MALTA2 equals 6.3 ns, with 95% of the cluster collected within a 25 ns window. It was demonstrated that the 3×10^{15} irradiated MALTA2 sample with very high doping of the n^- layer exhibits a more uniform timing response across its pixel compared to a sample with high n^- layer doping.

When testing the MALTA2 samples irradiated to the highest available fluence of 5×10^{15} 1 MeV $n_{eq}cm^{-2}$ a noticeable decrease of efficiency was observed. As the sample with very high n^- doping did show an improvement, exploring even higher doping levels was suggested to verify if this could lead to a more radiation-hard design. However, if the n^- blanket doping is too high, the extent of the depletion region diminishes. Alternatively, backside metallisation of the 5×10^{15} sample is to be tested, as this treatment was already demonstrated to improve sensor efficiency. In any case, the radiation hardness limit of MALTA2 is yet to be reached.

4.3 Improving position and timing resolution with clusters

This section outlines how the MALTA2 sensor assigns hit positions when a cluster of pixels registers a hit. A proposed time-weighted clustering method for MALTA2 is presented, improving the sensor's spatial resolution. The effect of the method is demonstrated on a selected non-irradiated MALTA2 sample on a Czochralski substrate. Towards the end of the section, the possibility of further improvements to the timing resolution is discussed.

The data used in the analysis was obtained at the SPS North Area with a 180 GeV hadron beam at normal incidence to the sensor. The particle tracks were reconstructed using the MALTA telescope previously described in Section 4.1.3. A MALTA2 Cz sensor with a total thickness of 300 µm was used as the DUT. The sample has not been irradiated, has a high doping of the n-type blanket layer, and features the NGAP pixel flavour. The substrate and p-well operational bias voltages were both set to -6 V. The sample was operated at 20°C.

The ITHR DAC value sets the operating threshold, with the investigated DAC values listed in Table 4.3 together with the corresponding electron threshold, measured detection efficiency, and the average cluster size for a given configuration. As shown in the table, the sample's efficiency was consistently high irrespective of the operating threshold - greater than 98% and reaching up to 99.5% for the configuration with the lowest threshold of 145 e^-. The average cluster size increases with the operating threshold, as visualised in Figure 4.28. As the threshold is lowered, the neighbouring pixels with smaller collected charge due to charge sharing are registered as hit pixels, increasing the cluster size.

A cluster is defined as a collection of neighbouring pixels recording a hit within a specified time window. Each cluster consists of different pixels, so a single cluster position must be determined to represent the DUT hit position. This position is referred to as the cluster *centroid*. The X (column number) and Y (row number) centroid position is denoted as X_{CL} and Y_{CL}. Similarly, a single time tag is assigned to a cluster - the cluster retains the timing information from the pixel which fired first.

Table 4.3: The MALTA2 Cz sample operating threshold, detection efficiency, and average cluster size obtained at a given ITHR DAC value configuration.

ITHR [DAC value]	**Threshold** [e$^-$]	**Efficiency** [%]	**Cluster size**
15	145 ± 10	99.5	2.06
20	175 ± 10	99.4	1.83
30	215 ± 15	99.4	1.59
40	255 ± 20	99.4	1.49
60	315 ± 20	99.3	1.31
80	370 ± 25	99.3	1.23
100	435 ± 25	99.1	1.17
120	490 ± 25	98.5	1.13

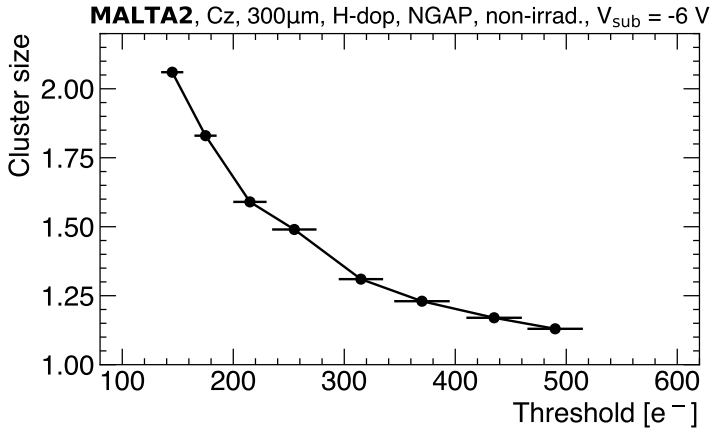


Figure 4.28: Average cluster size of a non-irradiated MALTA2 sensor (Cz, NGAP, 300 µm thick, high doping of the n-blanket) as a function of the threshold in electrons. The variation in threshold was achieved by varying the ITHR discriminator DAC value. The sample was operated at V_{SUB} = -6 V and V_{PWELL} = -6 V bias.

If the centroid is assigned based only on one of the cluster pixels or the cluster only consists of one pixel, the number of possible assigned X_{CL} and Y_{CL} positions is equal to the number of pixels in the pixel matrix. When information from multiple pixels from a cluster is included, the number of possible centroid positions increases, and the position resolution capabilities of the chip improve. For a collection of n pixels, the centroid is defined as

$$X_{CL} = \frac{\sum_{i=1}^{n} X_i w_i}{\sum_{i=1}^{n} w_i}, \tag{4.3}$$

$$Y_{CL} = \frac{\sum_{i=1}^{n} Y_i w_i}{\sum_{i=1}^{n} w_i}, \tag{4.4}$$

where X_i and Y_i are the position of the centre of pixel i, which is assigned a weight w_i. The denominator in the expression normalises the weights. The process of assigning

the weights to the given pixels within a cluster is referred to as *clustering*.

The default clustering method employed by the MALTA2 readout assigns equal weights to all pixels within the cluster. This approach is known as the *binary clustering*, as it assigns a weight of $w_i = 1$ to the pixels within the cluster and disregards all pixels not in the cluster (equivalent to $w_i = 0$). Using binary clustering, the centroid for a collection of n pixels can be expressed as

$$X_{CL} = \frac{\sum_{i=1}^{n} X_i}{n}, \tag{4.5}$$

$$Y_{CL} = \frac{\sum_{i=1}^{n} Y_i}{n}, \tag{4.6}$$

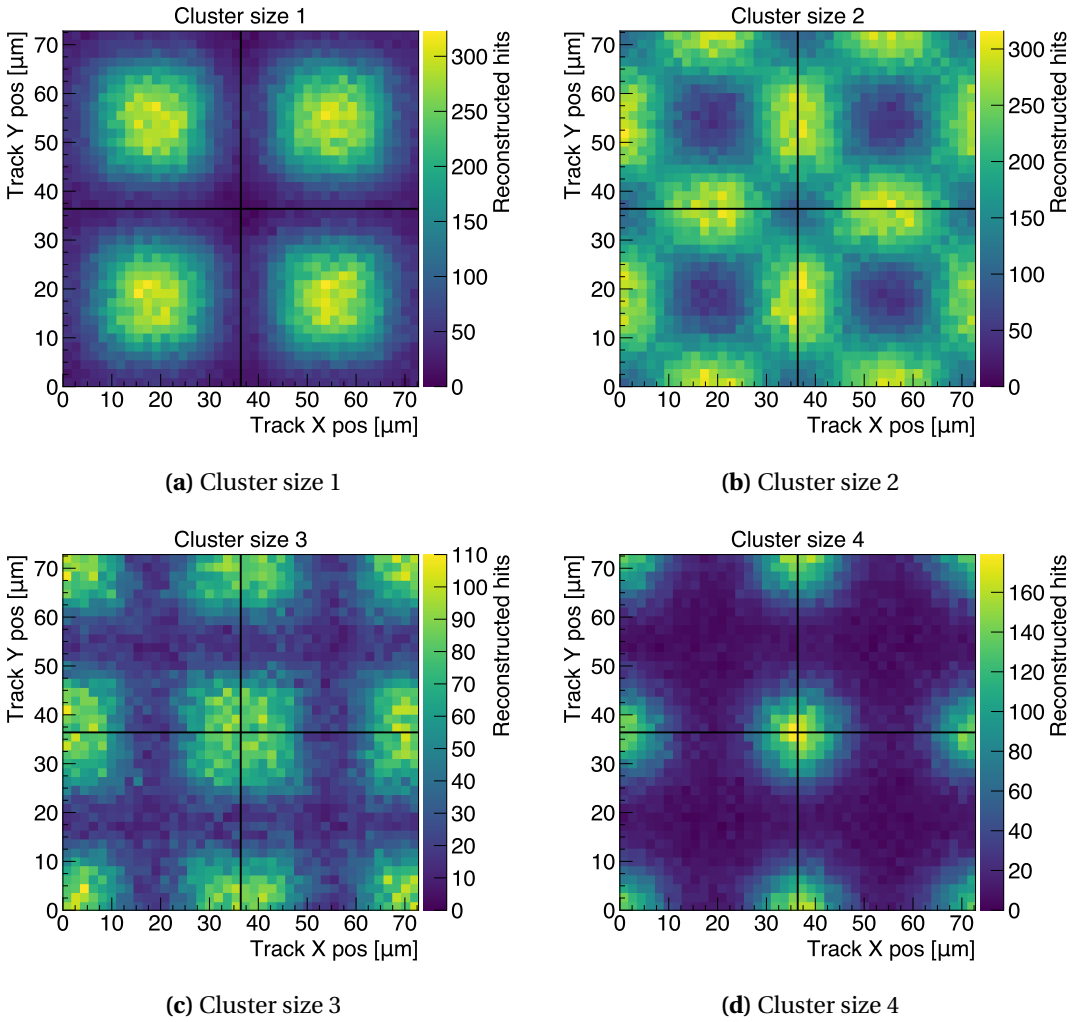
where X_i and Y_i are defined as before. The y-axis formulas are omitted from the rest of the chapter to avoid redundancy. Whenever an equation is presented for the x-axis, the y-axis expression is defined analogously.

Figure 4.29 visualises where the telescope tracks associated with clusters of a particular size appear within the MALTA2 pixel. The track position is projected onto a 2×2 pixel matrix. The data suggests that the region of the pixel being hit (i.e. centre, edge or corner) strongly influences the cluster size. As expected, a particle passing through the centre produces mainly clusters of size 1, those passing near the edges produce clusters of size 2, and those striking near the pixel corners produce greater clusters of size 3 and above.

The position resolution of a sensor is quantified by considering the distance between the centroid and the matched telescope track. This distance is referred to as the *residual*. The residuals in the X (row) direction X_{res} are defined as

$$X_{res} = X_{track} - X_{CL}, \tag{4.7}$$

where X_{track} is the track X position when projected onto the DUT. The resolution value is extracted as the standard deviation of a Gaussian fit to the distribution of the residuals in the respective principal direction. The uncertainty of the telescope tracks is also taken into consideration. When the track is projected onto the plane of the DUT, the telescope has a position resolution of 4.8 ± 0.2 µm in the x-direction and 4.6 ± 0.2 µm in the y-direction – see Section 4.1.3.



(a) Cluster size 1

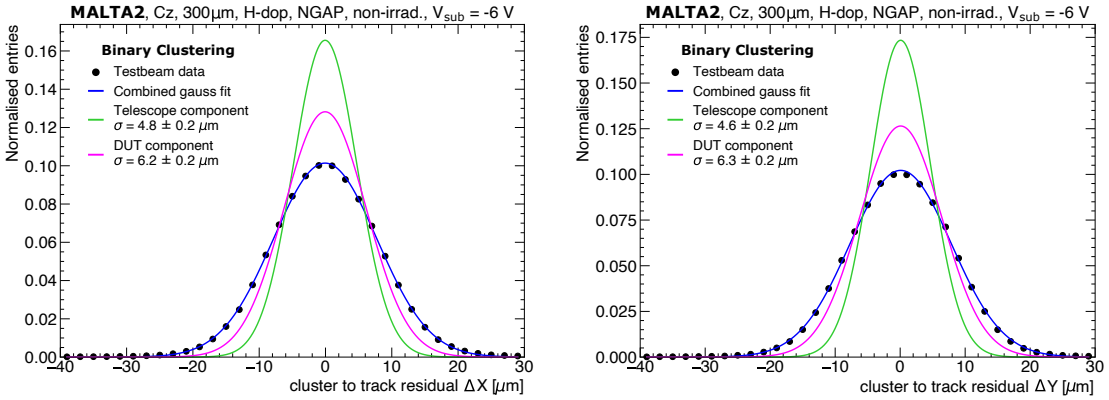
(b) Cluster size 2

(c) Cluster size 3

(d) Cluster size 4

Figure 4.29: MALTA2 2D colour histogram of telescope track positions sorted by the size of the associated cluster. Shown are the tracks matched to clusters of size 1 (a), 2 (b), 3 (c), and 4 (d). The track coordinates are projected onto a 2×2 pixel matrix. The sample is operated at the threshold of 145 e^-.

Figure 4.30 illustrates how the test beam residual data from the MALTA2 sensor is fitted with a Gaussian fit (dark blue curve). The sensor is operated at the threshold of 145 e^-. As a Gaussian distribution convoluted with another Gaussian distribution is also Gaussian, the fit is deconvoluted into the DUT component and the telescope component with a known standard deviation. The standard deviation of the DUT component gives the position resolution of the sensor – 6.2 µm and 6.3 µm in the x and y-direction, respectively.



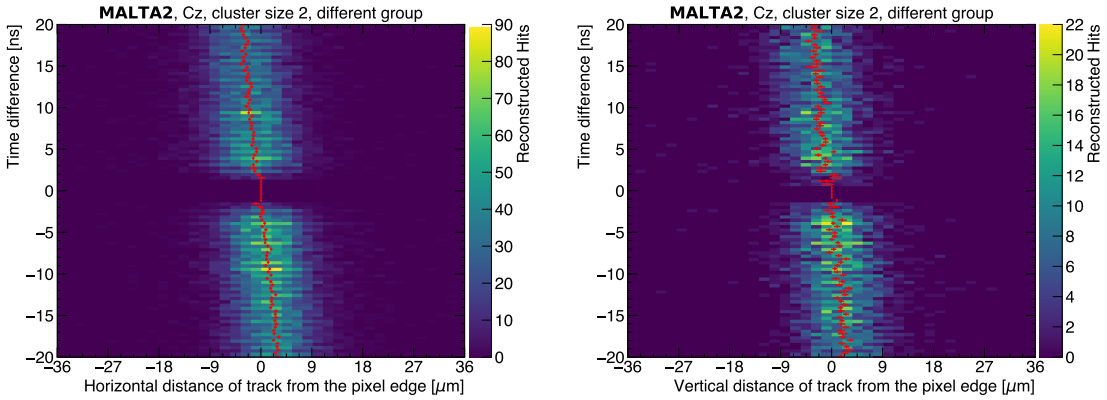
(a) x-axis residuals **(b)** y-axis residuals

Figure 4.30: The distribution of the residuals between the cluster centres and the associated telescope track along the x (a) and y-axis (b). The MALTA2 Cz sample is operated at the threshold of 145 e^-. The cluster centroids are assigned using the binary clustering method. The data is fitted with a Gaussian distribution deconvoluted into the DUT and telescope components.

4.3.1 Introduction of timing

As an alternative to the binary clustering approach, the Time-over-Threshold (ToT) information from the pixels is commonly used when assigning the centroid position [158, 159]. This approach assumes that the pixel closest to the particle hit will register the greatest amount of deposited charge. The large amount of charge will, in turn, cause the signal to stay above the discriminator threshold longer and lead to a large ToT value [160]. The pixel with a large ToT value is assigned a greater weight w_i than those with lower ToT values. As the MALTA2 sensor does not provide ToT information, the ToT-weighted approach is not directly employable. However, the chip offers information about the Time-of-Arrival (ToA) for individual pixels within a cluster. The potential of the ToA information being used when assigning weights to pixels is outlined below.

Firstly, it is necessary to establish that the ToA information within a cluster correlates with the position information. The least complex clusters containing multiple pixels are of size 2. As there are also the most prevalent clusters for the investigated MALTA2 chip when operated at the 145 e^- threshold, the timing structure of size 2 clusters is studied in greater detail. The cluster is described as *vertical* if the two hit pixels share the same pixel column but a different row. Similarly, the two pixels in a *horizontal* cluster are located on the same row but in different columns. Due to the readout architecture of



(a) Horizontal Clusters

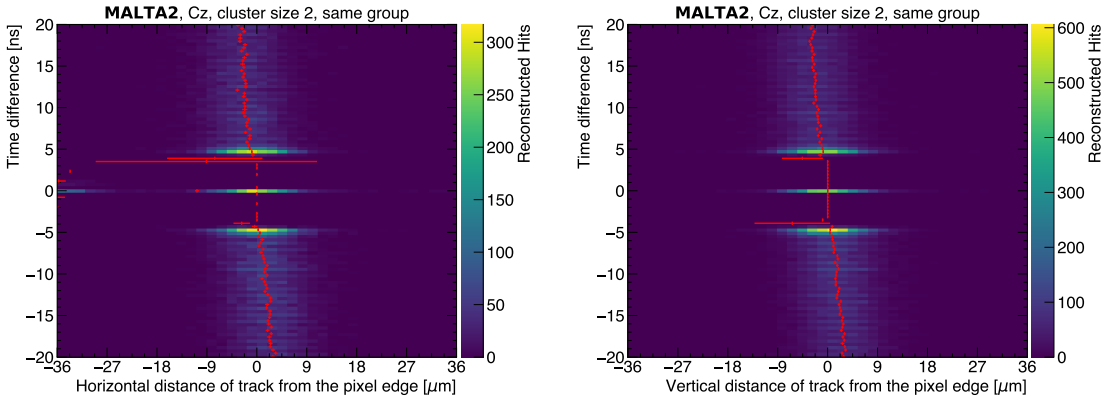
(b) Vertical Clusters

Figure 4.31: The 2D colour histogram showing the distribution of MALTA2 clusters based on the time difference between the pixel ToA and the horizontal (vertical) distance of the telescope track to the pixel edge for the horizontal (vertical) cluster. Only clusters of size 2 with the two pixels in a different group are considered. The sample is operated at the threshold of 145 e^-.

MALTA2, an important distinction arises between clusters of size 2 where the two pixels are in the same or different groups. A *group* is a collection of 2×8 pixels (2 columns, 8 rows). If the pixels are in the same group, the signal is transferred along the matrix columns on the same asynchronous bus. However, if the pixels belong to different groups, two separate buses are used for the data transfer as neighbouring groups do not share a bus. In the latter case, the signals from the two hit pixels are merged at the periphery rather than in the group.

Clusters formed in different groups

Figure 4.31 shows a 2D colour histogram for vertical (a) and horizontal (b) clusters formed in different pixel groups. The data is binned according to the time difference between the two pixels and the perpendicular distance of the matched track to the edge between the pixels. The calculation is performed such that if the bottom/left pixel fires first, the time difference is positive. The perpendicular distance is negative if the associated track is within the bottom/left pixel. The red points show the average distance from the edge for a given time difference between the pixels, with the error bars visualising the standard deviation of the distribution. This specific method of visualising the data highlights the correlation between the track lying within the bottom/left pixel



(a) Horizontal Clusters **(b)** Vertical Clusters

Figure 4.32: The 2D colour histogram showing the distribution of MALTA2 clusters based on the time difference between the pixel ToA and the horizontal (vertical) distance of the telescope track to the pixel edge for the horizontal (vertical) cluster. Only clusters of size 2 with the two pixels in the same group are considered. The sample is operated at the threshold of 145 e^-.

(negative distance) and positive ToA difference values. The telescope's finite resolution enhances the smearing of the distribution along the distance axis.

A prominent feature of the distribution shown in Figure 4.31 is the apparent absence of clusters with a time difference of less than ∼2 ns. This observation is understood as the result of signal merging from two different buses at the matrix periphery. If two signals on different buses reach the periphery closely spaced in time, there is a higher probability that one of these signals will be lost. In that case, only a cluster of size 1 is registered by the readout.

Clusters formed within the same group

The 2D histograms for the clusters formed within the same group are shown in Figure 4.32. These plots demonstrate that the pixel where the track position was assigned tends to, on average, have a lower ToA value (firing first). However, in the case of the pixels being in the same group, the shape of the distribution features prominent peaks at the 0 ns and ±5 ns time difference mark. These observations are understood in the context of the signal generation within the same group. If the two pixels register a hit within ±2 ns, the signals are merged in the group and sent to the periphery together. The pixels will share the same ToA information, producing a 0 ns time difference. When the pixel hit delay is greater than ±2 ns, the signal from the second pixel is delayed due to a non-zero

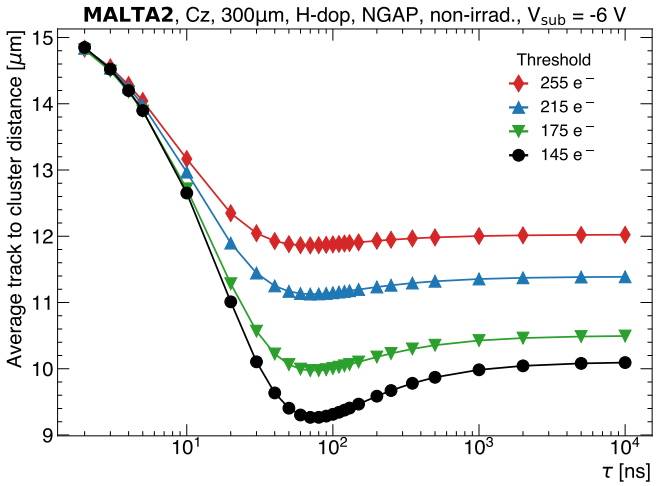


Figure 4.33: The average distance between the telescope track and the centroid as a function of the exponential clustering parameter τ. The plot shows the data for four configurations with different operating thresholds.

dead time before another signal from the group can be generated. These readout effects cause an apparent abundance of clusters with 0 ns and ± 5 ns time difference.

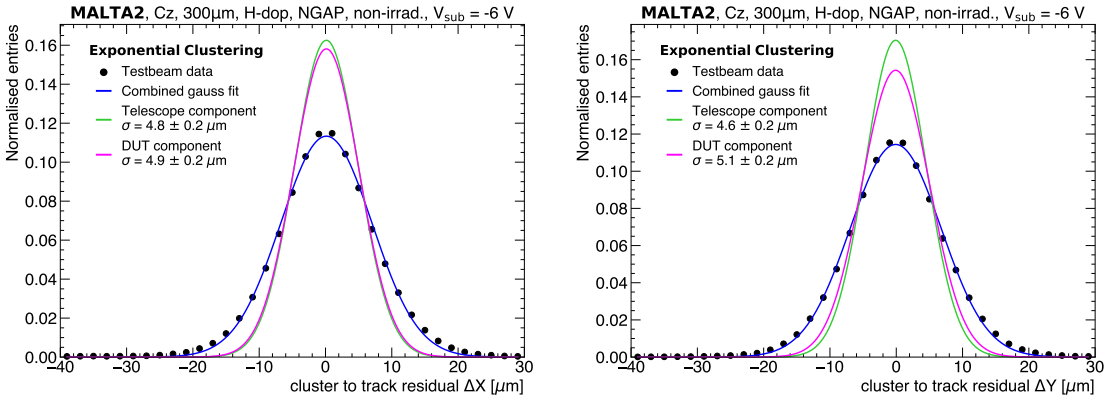
4.3.2 Exponential clustering

The correlation between the ToA difference and the position of the track within the MALTA2 pixel, as displayed in Figure 4.31 and 4.32, motivated further investigation of the ToA implementation into the clustering method. The ToA-weighted clustering assumes that the pixels closest to the true hit position should register the hit before pixels which are further away. A lower ToA value will result in a higher weight w_i. This thesis focuses on the exponential form of the w_i weights such that a pixel i within a cluster is assigned a weight

$$w_i = e^{-t_i/\tau}, \tag{4.8}$$

where t_i is the ToA value and τ is a scale factor common to all clusters. Note that constant shifts applied to all t_i values in a cluster do not affect the centroid. Hence, there is no need to define a global reference time. This clustering method is referred to as the *exponential clustering*.

The average distance between the track and the centroid as a function of the parameter τ is shown in Figure 4.33. The data suggests that for the investigated



(a) x-axis residuals **(b)** y-axis residuals

Figure 4.34: The distribution of the residuals between the centroid and the associated telescope track along the x (a) and y-axis (b). The MALTA2 Cz sample is operated at the threshold of 145 e^-. The exponential clustering method assigns the cluster centres with τ = 70 ns. The data is fitted with a Gaussian distribution deconvoluted into the DUT and telescope components.

threshold configurations, the best performance (the smallest average distance) is achieved with $\tau \approx 70$ ns. For $\tau \to \infty$, the weights approach the limit of binary clustering. The opposite limit of $\tau \to 0$ corresponds to the clustering method, where only the pixel with the lowest ToA value is included. It is also observed that a greater improvement is achieved with a lower operating threshold. This observation is understood in terms of the lower operating thresholds leading to an increase in the average cluster size.

The configuration with the lowest threshold was selected for further investigation as it produces, on average, the largest clusters. Using exponential clustering, the residual distribution with τ = 70 ns scale factor is shown in Figure 4.34. The Gaussian fit is deconvoluted to the DUT and telescope component using an analogous fitting to the data previously performed for the binary clustering. The fitted standard deviation of the DUT component is 4.9 µm and 5.1 µm in the x and y-direction, respectively. Compared to the binary weights shown in Figure 4.30, the reduction corresponds to a 21% (19%) improvement in the DUT spatial resolution along the x-axis (y-axis).

By comparing the performance across the different threshold configurations, it was observed that the main factor affecting the degree of improvement was the average cluster size. A similar trend was also observed with other non-irradiated MALTA2 sensors. As the average cluster size decreases, the proportion of clusters of size 1 increases. Therefore, large clusters are necessary to obtain an improvement in position resolution.

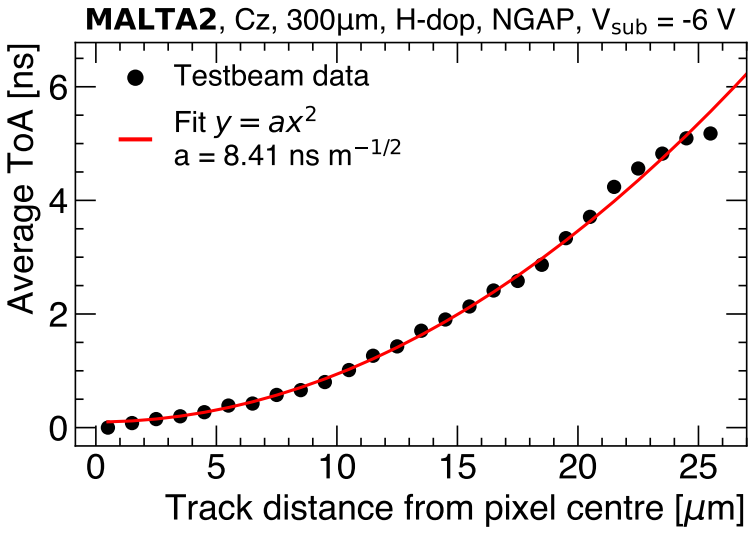


Figure 4.35: The average ToA with respect to the pixel centre as a function of the distance between the pixel centre and the track position. The data was obtained from the MALTA2 Cz sample operated at the threshold of 145 e^- and was fitted with a quadratic fit $y = ax^2$.

4.3.3 Improving timing with position information

The distribution of the average cluster time presented in Section 4.2 is non-uniform along the pixel diagonal - see Figure 4.23. The time shift between the pixel centre and the edge is ∼5 ns for the non-irradiated MALTA2 sample. The non-uniformity worsens the timing resolution of the sensor. The rest of this section discusses a novel method of minimising the non-uniformity to improve timing. If the position of the hit can be reliably identified using the available cluster information, the cluster ToA can be corrected. The initial investigations into this correction approach are presented below.

Starting with a simple parametrisation, a quadratic correction to the cluster timing is explored. The ToA time reference assigned to a cluster t_{CL} is given by

$$t_{CL} = t_{first} - \lambda d^2, \tag{4.9}$$

where t_{first} is the ToA time reference of the pixel that fired first, λ is a scale parameter, and d is the distance between the cluster centroid and the pixel centre. The cluster centroid is calculated using exponential clustering to enhance position resolution. The default MALTA2 readout is equivalent to $\lambda = 0$.

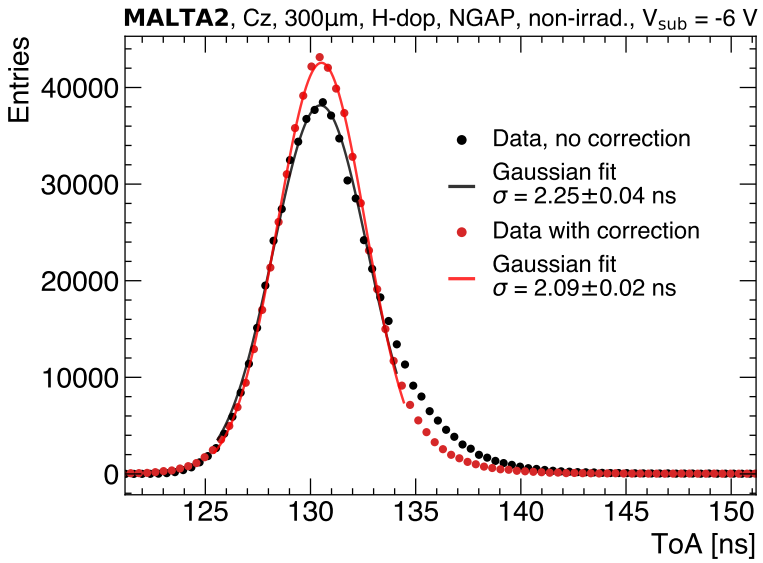


Figure 4.36: The timing distribution of MALTA2 Cz sample (Cz, NGAP, 300 µm thick, high doping of the n-blanket) operated at the threshold of 145 e^-. The ToA data points with no additional correction are shown in black, and those where the quadratic correction with parameter λ = 8.41 ns $m^{-1/2}$ was applied are plotted in red. The correction uses centroid values calculated with the exponential clustering. The standard deviation of the Gaussian fits applied to the core of the distributions parametrise the timing resolution of the sensor.

The λ value is obtained from the quadratic fit to the distribution of the mean cluster time relative to the pixel centre as a function of the distance between a particle track and the pixel centre – see Figure 4.35. Note that the track information is obtained from the telescope. It is not equivalent to d in Equation 4.9, which is calculated using the cluster centroid. The track distance can be considered the idealised d value for a sensor with infinite spatial precision. The quadratic fit to the data yields a value of λ = 8.41 ns $m^{-1/2}$.

Figure 4.36 shows the change in the distribution of the assigned cluster time t_{CL} value relative to the scintillator reference when the correction from Equation 4.9 is introduced. The cluster centroids are calculated using the exponential clustering method presented earlier. The timing resolution of the sensor is quoted as the standard deviation of the Gaussian fit to the core of the distribution. Without the correction, the sample achieves a timing resolution of 2.25 $\pm$ 0.04 ns. When the quadratic correction with λ = 8.41 ns $m^{-1/2}$ is applied, the timing resolution improved by ~7% to 2.09 $\pm$ 0.02 ns. The contributions from the resolution of the scintillator and the FPGA sampling are not subtracted from the distributions.

4.3.4 Summary

This section discussed a possible method for improving the spatial and timing resolutions of a non-irradiated MATLA2 Cz sensor using an alternative clustering method and an in-pixel timing correction. The sensor operated at a threshold of 145 e^- achieves a spatial resolution of 6.2 µm and 6.3 µm in the x and y-direction, with the binary clustering algorithm. By exploiting the ToA information assigned to individual pixels within each cluster, the position resolution can be improved by up to 21%. With the exponential clustering method, the spatial resolution of the MALTA2 sensor was measured to be 4.9 µm and 5.1 µm in the x and y-direction, respectively.

The preliminary timing correction method successfully demonstrated that MALTA2 timing performance can be improved. Instead of using only the ToA of the fastest hit, the quadratic parametrisation based on the centroid position within the MALTA2 pixel achieved up to 7% improvement in the timing resolution. Further investigation is necessary to optimise the parametric form of the correction and demonstrate the generalisation of the approach to a broader range of samples. The correction method must also be tested for tilted tracks, as this chapter only considered particles at normal incidence. The parametric form will likely have to be expanded, and some form of dependence on the track angle will be included.

5 Conclusions and Outlook

In this thesis, I have presented the characterisation techniques and the performance results of novel particle detectors. The ATLAS experiment and its future upgrade were discussed in Chapter 1. The basic principles of semiconductor particle detectors were outlined in Chapter 2. Chapter 3 was dedicated to the Low Gain Avalanche Detectors (LGADs) fabricated by Teledyne e2v (Te2v) and their characterisation before and after neutron irradiation using hadron test beam and infra-red laser measurements. Finally, Chapter 4 was focused on the radiation hardness and clustering methods of the MALTA2 sensor, the latest prototype of the MALTA family of DMAPS in 180 nm Tower Semiconductor CMOS imaging technology.

With the High-Luminosity LHC upgrade, modifications to the LHC experiments are needed to enable them to collect a total integrated luminosity of 3,000 fb^{-1}. The ATLAS Inner Detector will be replaced by the Inner Tracker (ITk), which will have a significantly improved radiation tolerance and better spatial resolution to cope with the higher instantaneous luminosity. Additionally, a High-Granularity Timing Detector (HGTD) will be installed adjacent to the ITk endcap detector. Employing the LGAD technology, the HGTD will mitigate against the effect of increased pile-up and improve vertex separation in the forward region by providing timing information with 30 ps resolution per track.

The electrical characterisation of the LGAD wafers from the first Te2v batch presented in this thesis highlighted the importance of a well-controlled gain layer implant

dose and energy during device production. The tested wafers satisfy the minimum gain layer depletion voltage of 24 V set by the HGTD Technical Specification but exceed the maximum allowed device-to-device variation from the mean. The 1×1 mm^2 devices with the best electrical performance (from wafers W02, W08, and W09) were tested at the CERN North Area test beam with 180 GeV hadrons. The test beam investigation yielded several significant results, such as demonstrating excellent hit efficiency of the tested devices (>99%) and charge collection above 15 fC. Furthermore, the W08 and W09 LGAD devices achieved a superior timing resolution below 20 ps.

LGAD samples from the three best-performing wafers were selected for neutron irradiation up to the fluence of 1×10^{16} 1 MeV $n_{eq}cm^{-2}$. The leakage current transition method was used to extract the gain layer depletion voltage for the irradiated sensors and to derive the acceptor removal coefficient in the range of 7-8$\times10^{16}$ cm^2. These findings demonstrated that the Te2v-LGAD sensors achieve a comparable radiation hardness to non-carbon-enriched LGAD devices fabricated by other vendors. The irradiated devices were tested in a laser injection setup with a fast infra-red laser, showing jitter better than 10 ps up to the fluence of 5×10^{14} 1 MeV $n_{eq}cm^{-2}$. An LGAD from W08 irradiated to 2×10^{15} 1 MeV $n_{eq}cm^{-2}$ reached charge gain of $\sim$15 and jitter <25 ps. Multi-pad LGAD devices were discussed towards the end of Chapter 3. The reduction of the inter-pad distance between LGAD pixels was achieved by reducing the Junction Termination Extension (JTE) width from 15 µm to 9 µm and the P-stop to cathode distance from 30 µm to 24 µm. The laser injection measurements verified that the inter-pad distance was effectively reduced without compromising the devices' electrical properties.

After successful test beam measurements of the non-irradiated Te2v-LGAD sensors presented in this thesis, future campaigns with irradiated devices are planned. Following these, non-irradiated and irradiated multi-pad devices will be characterised with the custom-design COLA v2.1 readout board. These measurements will be crucial to establish the particle detection efficiency, fill factor, and timing resolution of the devices as a function of the received radiation fluence. The new thinner LGADs currently under investigation by the ALICE Collaboration [161] are of particular interest. The initial

results show that the thinner devices can maintain a comparable timing resolution to the standard LGADs while reducing the total material budget.

The MALTA collaboration undertook an extensive test beam characterisation campaign of the MALTA2 sensor. The results presented in this thesis indicate that after neutron irradiation, the samples produced on the Czochralski (Cz) substrate show better radiation hardness than those on an epitaxial layer. Additionally, the efficiency of the irradiated Cz samples was enhanced by backside metallisation post-processing. At the fluence of 3×10^{15} 1 MeV $n_{eq}cm^{-2}$, the MALTA2 Cz sample with very high doping of the n^- layer exhibits an excellent efficiency of 98% and 6.3 ns timing RMS value at an operating threshold of 110 e^-. A decrease in efficiency was observed when exploring samples with regular backside irradiated to a fluence of 5×10^{15} 1 MeV $n_{eq}cm^{-2}$. Based on the observations from other irradiated samples, the performance can still be improved by backside metallisation, but the effect of this treatment on 5×10^{15} MALTA2 samples is yet to be verified.

It was demonstrated that non-irradiated MALTA2 samples produced on the Czochralski substrate achieve efficiencies of >99% and an average cluster size of 2.06 pixels at a low operational threshold (145 ± 10 e^-). The increased cluster size motivated the exploration of alternative clustering methods outlined in this thesis. By including the Time-of-Arrival information available from MALTA2, the position resolution of the sensor can be improved from 6.2 ± 0.2 µm (6.3 ± 0.2 µm) to 4.9 ± 0.2 µm (5.1 ± 0.2 µm) along the x-axis (y-axis). The proposed spatial and timing improvement methods must be further optimised and generalised on a wider range of samples. Nevertheless, the preliminary results show a promising improvement in the sensor performance and highlight the importance of large cluster size.

Whereas the MALTA family was developed to explore its suitability for the ATLAS Phase-II upgrade, the ATLAS ITk has opted for the hybrid ITk Pixel module instead. This decision was made because of the limited MALTA design readiness given the anticipated production timeline. Nevertheless, the ongoing advancements of the MALTA family have led to greater radiation tolerance and enhanced sensor performance. As high-energy physics continues to evolve, the insights and lessons gained from MALTA

will significantly influence the development of future detectors, further expanding the boundaries of scientific discovery. MALTA is being considered as a potential candidate for the upgrade of the Upstream Tracker (UT Upgrade II) of LHCb [162], and also for the Electron-Ion Collider (EIC) to be constructed at Brookhaven National Laboratory (BNL) [163, 164].

The most recent member of the MALTA family, the MiniMALTA3 demonstrator, was produced towards the end of 2023 and has been under active investigation and testing since. The synchronisation memory was upgraded to achieve a sub-nanosecond timing resolution, enabling clock speeds of up to 1.28 GHz. The readout architecture of the demonstrator will be a baseline for the future full-scale prototype, MALTA3 [165].

Bibliography

[1] M. Gazi, et al. “Low Gain Avalanche Detector development for the LHC’s High-Luminosity upgrade at Teledyne e2v”. In: *Nucl. Instrum. Meth. A* 1037 (2022), p. 166876. ISSN: 0168-9002. DOI: 10.1016/j.nima.2022.166876.

[2] M. Gazi, et al. “Characterization of neutron- and proton-irradiated LGADs from Teledyne e2v”. In: *41st RD50 Workshop on Radiation Hard Semiconductor Devices for Very High Luminosity Colliders, Sevilla, Spain* (Dec. 2022). [Conference session].

[3] M. van Rijnbach, D.V. Berlea, V. Dao, M. Gazi, et al. “Radiation hardness of MALTA2 monolithic CMOS imaging sensors on Czochralski substrates”. In: *Eur. Phys. J. C* 84.251 (2024). DOI: 10.1140/epjc/s10052-024-12601-3.

[4] M. Gazi, et al. “Performance and radiation hardness of Tower 180 nm MALTA monolithic pixel sensors”. In: *18th Trento Workshop on Advanced Silicon Radiation Detectors, Trento, Italy* (Mar. 2023). [Conference session].

[5] G. Apollinari, et al. “High-Luminosity Large Hadron Collider (HL-LHC): Preliminary Design Report”. In: *CERN Yellow Reports: Monographs, CERN-2015-005* (2015). DOI: 10.5170/CERN-2015-005.

[6] M. Wu, et al. *A High-Granularity Timing Detector for the ATLAS Phase-II Upgrade*. ATLAS ATL-HGTD-PROC-2023-002, CERN, Geneva, 2023. URL: https://cds.cern.ch/record/2846406.

[7] O.S. Bruning, et al. “LHC Design Report”. In: *CERN Yellow Reports: Monographs, CERN-2004-003* (2004). DOI: 10.5170/CERN-2004-003-V-1.

[8] CERN. *The CERN accelerator complex, layout in 2022*. URL: https://cds.cern.ch/images/CERN-GRAPHICS-2022-001-1 (visited on 05/25/2024).

[9] The ATLAS Collaboration. “The ATLAS Experiment at the CERN Large Hadron Collider”. In: *JINST* 3.08 (2008), S08003. DOI: 10.1088/1748-0221/3/08/S08003.

[10] CMS collaboration. “The CMS experiment at the CERN LHC. The Compact Muon Solenoid experiment”. In: *JINST* 3.08 (2008), S08004. DOI: 10.1088/1748-0221/3/08/S08004.

[11] LHCb collaboration. “The LHCb Detector at the LHC”. In: *JINST* 3.08 (2008), S08005. DOI: 10.1088/1748-0221/3/08/S08005.

[12] The ALICE Collaboration. “The ALICE experiment at the CERN LHC”. In: *JINST* 3.08 (2008), S08002. DOI: 10.1088/1748-0221/3/08/S08002.

[13] ATLAS experiment. *Public ATLAS Luminosity Results for Run-3 of the LHC*. URL: https://twiki.cern.ch/twiki/bin/view/AtlasPublic/LuminosityPublicResultsRun3 (visited on 05/25/2024).

[14] CERN. *High Luminosity LHC Project*. URL: https://hilumilhc.web.cern.ch/content/hl-lhc-project (visited on 05/25/2024).

[15] CERN. *ATLAS Feature: A new ATLAS for the high-luminosity era*. URL: https://cds.cern.ch/images/ATLAS-PHOTO-2023-002-4 (visited on 05/25/2024).

[16] The ATLAS Collaboration. *ATLAS inner detector: Technical Design Report, 1*. CERN-LHCC-97-16, ATLAS-TDR-4, CERN, Geneva, 1997. URL: https://cds.cern.ch/record/331063.

[17] The ATLAS Collaboration. *Technical Design Report for the ATLAS Inner Tracker Pixel Detector*. CERN-LHCC-2017-021, ATLAS-TDR-030, CERN, Geneva, 2017. DOI: 10.17181/CERN.FOZZ.ZP3Q.

[18] The ATLAS Collaboration. *Technical Design Report for the ATLAS Inner Tracker Strip Detector*. CERN-LHCC-2017-005, ATLAS-TDR-025, CERN, Geneva, 2017. URL: https://cds.cern.ch/record/2257755.

[19] ATLAS experiment. *Public Upgrade Inner Tracker ITk Public Results*. URL: https://twiki.cern.ch/twiki/bin/view/AtlasPublic/ITkPublicResults (visited on 05/25/2024).

[20] W.R. Leo. *Techniques for nuclear and particle physics experiments*. 2nd. Springer Berlin, Heidelberg, 1994. DOI: 10.1007/978-3-642-57920-2.

[21] P.A. Zyla on behalf of the Particle Data Group. "Review of Particle Physics". In: *Prog. Theor. Exp.* 2020.8 (2020), p. 083C01. DOI: 10.1093/ptep/ptaa104.

[22] M. Mironova. "Search for Higgs Boson Decays to Charm Quarks with the ATLAS Experiment and Development of Novel Silicon Pixel Detectors". DPhil thesis. University of Oxford, 2022. URL: https://ora.ox.ac.uk/objects/uuid:03373b84-4eca-41d3-87f3-a5ca7a1cb2e7.

[23] J.R. Schwank. "Basic mechanisms of radiation effects in the natural space radiation environment". In: *IEEE Nuclear and Space Radiation Effects Conference (Tucson, Arizona)* (June 1994). URL: https://www.osti.gov/biblio/10158182.

[24] E. Bossini, N. Minafra. "Diamond Detectors for Timing Measurements in High Energy Physics". In: *Front. Phys* 8 (2020), p. 248. DOI: 10.3389/fphy.2020.00248.

[25] J.F. Amann, et al. "Use of high-purity germanium detectors for intermediate energy physics experiments". In: *Nucl. Instrum. Methods* 126.2 (1975), pp. 193–198. ISSN: 0029-554X. DOI: 10.1016/0029-554X(75)90631-X.

[26] S.P. Beaumont, et al. "GaAs solid state detectors for particle physics". In: *Nucl. Instrum. Meth. A* 322.3 (1992), pp. 472–482. ISSN: 0168-9002. DOI: 10.1016/0168-9002(92)91217-W.

[27] N.D. Arora, J.R. Hauser, and D.J. Roulston. "Electron and hole mobilities in silicon as a function of concentration and temperature". In: *IEEE Trans. Electron Devices*. 29.2 (1982), pp. 292–295. DOI: 10.1109/T-ED.1982.20698.

[28] S. Ramo. "Currents induced by electron motion". In: *Proc. Ire.* 27 (1939), pp. 584–585. DOI: 10.1109/JRPROC.1939.228757.

[29] J. Schwandt and R. Klanner. "On the weighting field of irradiated silicon detectors". In: *Nucl. Instrum. Meth. A* 942 (2019), p. 162418. ISSN: 0168-9002. DOI: 10.1016/j.nima.2019.162418.

[30] L. Rossi, P. Fischer, T. Rohe, and N. Wermes. *Pixel detectors: From fundamentals to applications*. Springer, Heidelberg, 2006. DOI: 10.1007/3-540-28333-1.

[31] M. Garcia-Sciveres and N. Wermes. "A review of advances in pixel detectors for experiments with high rate and radiation". In: *Rep. Prog. Phys.* 81.6 (2018), p. 066101. DOI: 10.1088/1361-6633/aab064.

[32] M. Munker. "Test beam and simulation studies on High Resistivity CMOS pixel sensors". PhD thesis. University of Bonn, 2018.

[33] B. Abelev on behalf of the ALICE Collaboration. *Technical Design Report for the Upgrade of the ALICE Inner Tracking System*. CERN-LHCC-2013-024, ALICE-TDR-017, CERN, Geneva, 2014. DOI: 10.1088/0954-3899/41/8/087002.

[34] G. Anelli, et al. "Radiation tolerant VLSI circuits in standard deep submicron CMOS technologies for the LHC experiments: practical design aspects". In: *IEEE Trans. Nucl. Sci.* 46.6 (1999), pp. 1690–1696. DOI: 10.1109/23.819140.

[35] M. Moll. "Displacement Damage in Silicon Detectors for High Energy Physics". In: *IEEE Trans. Nucl. Sci.* 65.8 (2018), pp. 1561–1582. DOI: 10.1109/TNS.2018.2819506.

[36] M. Moll. "Radiation Damage in Silicon Particle Detectors: Microscopic Defects and Macroscopic Properties". PhD thesis. University of Hamburg, 1999. URL: https://bib-pubdb1.desy.de/record/300958.

[37] M. Ferrero, et al. "Radiation resistant LGAD design". In: *Nucl. Instrum. Meth. A* 919 (2019), pp. 16–26. ISSN: 0168-9002. DOI: 10.1016/j.nima.2018.11.121.

[38] R. Wunstorf. "Systematische untersuchungen zur strahlenresistenz von silizium-detektoren für die verwendung in hochenergiephysikexperimenten". PhD thesis. University of Hamburg, 1992. URL: https://bib-pubdb1.desy.de/record/153817.

[39] G. Lutz. *Semiconductor Radiation Detectors: Device Physics*. Springer Berlin, Heidelberg, 2007. DOI: 10.1007/978-3-540-71679-2.

[40] H.F.W. Sadrozinski, A. Seiden, and N. Cartiglia. "4D tracking with ultra-fast silicon detectors". In: *Rept. Prog. Phys.* 81.2 (2018), p. 026101. DOI: 10.1088/1361-6633/aa94d3.

[41] The ATLAS HGTD Project. *Technical Proposal: A High-Granularity Timing Detector for the ATLAS Phase-II Upgrade*. CERN-LHCC-2018-023, LHCC-P-012, CERN, Geneva, 2018. DOI: 10.17181/CERN.CIUJ.KS4H.

[42] F. Yunyun on behalf of the ATLAS Collaboration. "IHEP-NDL prototype LGAD sensors for HGTD". In: *12th international "Hiroshima" Symposium on the Development and Application of Semiconductor Tracking Detectors, Hiroshima, Japan* (Dec. 2019). [Conference session]. URL: https://cds.cern.ch/record/2705714.

[43] S.M. Mazza, et al. "A High-Granularity Timing Detector (HGTD) for the Phase-II upgrade of the ATLAS detector". In: *JINST* 14.10 (2019), p. C10028. DOI: 10.1088/1748-0221/14/10/C10028.

[44] W. Maes, K. De Meyer, and R. Van Overstraeten. "Impact ionization in silicon: A review and update". In: *Solid-State Electron.* 33.6 (1990), pp. 705–718. DOI: 10.1016/0038-1101(90)90183-F.

[45] P.P. Webb and R.J. McIntyre. "Large Area Reach-Through Avalanche Diodes for X-Ray Spectroscopy". In: *IEEE Trans. Nucl. Sci.* 23.1 (1976), pp. 138–144. DOI: 10.1109/TNS.1976.4328228.

[46] A.V. Akindinov, et al. "New results on MRS APDs". In: *Nucl. Instrum. Meth. A* 387.1 (1997), pp. 231–234. ISSN: 0168-9002. DOI: 10.1016/S0168-9002(96)01201-6.

[47] G. Pellegrini, et al. "Technology developments and first measurements of Low Gain Avalanche Detectors (LGAD) for high energy physics applications". In: *Nucl. Instrum. Meth. A* 765 (2014), pp. 12–16. ISSN: 0168-9002. DOI: 10.1016/j.nima.2014.06.008.

[48] N. Moffat, et al. "Low gain avalanche detectors (LGAD) for particle physics and synchrotron applications". In: *JINST* 13.03 (2018), p. C03014. DOI: 10.1088/1748-0221/13/03/C03014.

[49] O.A. Marti Villarreal, et al. "Characterization of thin LGAD sensors designed for beam monitoring in proton therapy". In: *Nucl. Instrum. Meth. A* 1046 (2023), p. 167622. ISSN: 0168-9002. DOI: 10.1016/j.nima.2022.167622.

[50] K. Wu, et al. "Design of Low Gain Avalanche Detectors (LGAD) with 400 keV ion implantation energy for multiplication layer fabrication". In: *Nucl. Instrum. Meth. A* 984 (2020), p. 164558. ISSN: 0168-9002. DOI: 10.1016/j.nima.2020.164558.

[51] I. Cortés, et al. "Gain estimation of RT-APD devices by means of TCAD numerical simulations". In: *Proceedings of the 8th Spanish Conference on Electron Devices, CDE'2011*. 2011, pp. 1–4. DOI: 10.1109/SCED.2011.5744152.

[52] B.J. Baliga. *Fundamentals of Power Semiconductor Devices*. Springer, New York, 2008. DOI: 10.1007/978-0-387-47314-7.

[53] N. Cartiglia, et al. "Design optimization of ultra-fast silicon detectors". In: *Nucl. Instrum. Meth. A* 796 (2015), pp. 141–148. DOI: 10.1016/j.nima.2015.04.025.

[54] P. Fernández-Martínez, et al. "Design and fabrication of an optimum peripheral region for low gain avalanche detectors". In: *Nucl. Instrum. Meth. A* 821 (2016), pp. 93–100. DOI: 10.1016/j.nima.2016.03.049.

[55] V.A.K. Temple. "Increased avalanche breakdown voltage and controlled surface electric fields using a junction termination extension (JTE) technique". In: *IEEE Trans. Nucl. Sci.* 30.8 (1983), pp. 954–957. DOI: 10.1109/T-ED.1983.21243.

[56] N. Moffat. "Low gain avalanche detectors for particle physics and synchrotron applications". PhD thesis. University of Glasgow, 2020. URL: https://theses.gla.ac.uk/81281/.

[57] M. Ferrero, et al. *An Introduction to Ultra-Fast Silicon Detectors*. CRC Press, 2021. DOI: 10.1201/9781003131946.

[58] The ATLAS HGTD Project. *Invitation to Tender for Production of LGAD Sensors for the ATLAS High Granularity Timing Detector (HGTD)*. IT-4705/EP/ATLAS, CERN, Geneva, 2023.

[59] The ATLAS HGTD Project. *Market Survey for Production of LGAD Sensors for the ATLAS High Granularity Timing Detector (HGTD)*. MS-4705/EP/ATLAS, CERN, Geneva, 2021.

[60] Teledyne e2v. URL: https://www.teledyne-e2v.com/ (visited on 04/13/2023).

[61] N. Seguin-Moreau, et al. "ALTIROC1, a 25 pico-second time resolution ASIC for the ATLAS High Granularity Timing Detector (HGTD)". In: *PoS* TWEPP2019 (2019), p. 042. DOI: 10.22323/1.370.0042.

[62] N. Cartiglia, et al. "Beam test results of a 16 ps timing system based on ultra-fast silicon detectors". In: *Nucl. Instrum. Meth. A* 850 (2017), pp. 83–88. DOI: 10.1016/j.nima.2017.01.021.

[63] K. Nakamura, et al. "First prototype of finely segmented HPK AC-LGAD detectors". In: *JPS Conf. Proc.* 34.010016 (2021). DOI: 10.7566/JPSCP.34.010016.

[64] S. Xie, et al. "Design and performance of the Fermilab Constant Fraction Discriminator ASIC". In: *Nucl. Instrum. Meth. A* 1056 (2023), p. 168655. ISSN: 0168-9002. DOI: 10.1016/j.nima.2023.168655.

[65] Infineon. *BFR840L3RHESD*. URL: https://www.infineon.com/cms/en/product/rf/rf-transistor/low-noise-rf-transistors/bfr840l3rhesd/ (visited on 04/13/2024).

[66] Analog Devices. *LTC6269*. URL: https://www.analog.com/en/products/ltc6269.html (visited on 04/13/2024).

[67] Tektronix. *Keithley 4200A-SCS Parameter Analyzer*. URL: https://www.tek.com/en/products/keithley/4200a-scs-parameter-analyzer (visited on 05/07/2024).

[68] Inseto. *Semiautomatic Wafer Probe Equipment*. URL: https://www.inseto.co.uk/equipment/wafer-probers-by-semiprobe/ (visited on 05/07/2024).

[69] Tektronix. *Keithley SMU 2650 Series High Power SourceMeter*. URL: https://www.tek.com/en/products/keithley/source-measure-units/2650-series-high-power-sourcemeter (visited on 07/11/2024).

[70] W. Shockley. "The theory of p-n junctions in semiconductors and p-n junction transistors". In: *BSTJ* 28.3 (1949), pp. 435–489. DOI: 10.1002/j.1538-7305.1949.tb03645.x.

[71] G. Laštovička-Medin, M. Rebarz, G. Kramberger, et al. "Studies of LGAD performance limitations, Single Event Burnout and Gain Suppression, with Femtosecond-Laser and Ion Beams". In: *Nucl. Instrum. Meth. A* 1041 (2022), p. 167388. ISSN: 0168-9002. DOI: 10.1016/j.nima.2022.167388.

[72] M. van Rijnbach, G. Gustavino, et al. "Performance of the MALTA telescope". In: *Eur. Phys. J. C* 581 (2023), p. 83. DOI: 10.1140/epjc/s10052-023-11760-z.

[73] S. Ali, et al. "Performance in beam tests of carbon-enriched irradiated Low Gain Avalanche Detectors for the ATLAS High Granularity Timing Detector". In: *JINST* 18 (2023), P05005. DOI: 10.1088/1748-0221/18/05/P05005.

[74] AMETEK. *TESEQ LNA 6901*. URL: https://www.ametek-cts.com/products/brands/teseq/lna-6901 (visited on 04/13/2024).

[75] M. Kiehn. "Proteus beam telescope reconstruction". In: *Zenodo* (2019). DOI: 10.5281/zenodo.2586736.

[76] B Rae, et al. "Overview over CERN test beam facilities and LS2 modifications". In: *8th Beam Telescopes and Test Beam Workshop, Tbilisi, Georgia* (Jan. 2020). [Conference session].

[77] C. Agapopoulou, et al. "Performance of a front-end prototype ASIC for the ATLAS High Granularity timing detector". In: *JINST* 18 (2023), P08019. DOI: 10.1088/1748-0221/18/08/P08019.

[78] C.J. Clooper, E.S. Pearson. "Proteus beam telescope reconstruction". In: *Biometrika* 26.4 (1934), pp. 404–413. DOI: 10.1093/biomet/26.4.404.

[79] P. Filliatre, et al. "Experimental assessment of the kinetic parameters of the JSI TRIGA reactor". In: *Ann. Nucl. Energy* 83 (2015), pp. 236–245. ISSN: 0306-4549. DOI: 10.1016/j.anucene.2015.03.054.

[80] K. Ambrožič, et al. "Computational analysis of the dose rates at JSI TRIGA reactor irradiation facilities". In: *Appl. Radiat. Isot.* 130 (2017), pp. 140–152. DOI: 10.1016/j.apradiso.2017.09.022.

[81] J.R. Srour, C.J. Marshall, and P.W. Marshall. "Review of displacement damage effects in silicon devices". In: *IEEE Trans. Nucl. Sci.* 50.3 (2003), pp. 653–670. DOI: 10.1109/TNS.2003.813197.

[82] M. Mikuž, et al. "Transnational acces to TRIGA Mark II reactor". In: *4th Annual AIDA Meeting, Oxford, UK* (Apr. 2019). [Conference session].

[83] L. Diehl, et al. "Comparison of the time resolution of unirradiated and irradiated LGADs and 3D sensors". In: *Nucl. Instrum. Meth. A* 1046 (2023), p. 167691. ISSN: 0168-9002. DOI: 10.1016/j.nima.2022.167691.

[84] K. Wu, et al. "Design and testing of LGAD sensor with shallow carbon implantation". In: *Nucl. Instrum. Meth. A* 1046 (2023), p. 167697. ISSN: 0168-9002. DOI: 10.1016/j.nima.2022.167697.

[85] G. Beck and G. Viehhauser. "Analytic model of thermal runaway in silicon detectors". In: *Nucl. Instrum. Meth. A* 618.1 (2010), pp. 131–138. ISSN: 0168-9002. DOI: 10.1016/j.nima.2010.02.264.

[86] Systems ATT. URL: https://www.att-systems.com/ (visited on 04/17/2024).

[87] Syensqo. *Galden HT 135*. URL: https://www.syensqo.com/en/product/galden-ht-135 (visited on 04/17/2024).

[88] L. Castillo García, et al. "Characterization of Irradiated Boron, Carbon-Enriched and Gallium Si-on-Si Wafer Low Gain Avalanche Detectors". In: *Instruments* 6.1 (2022). DOI: 10.3390/instruments6010002.

[89] E.L. Gkougkousis, L. Castillo Garcia, S. Grinstein, and V. Coco. "Comprehensive technology study of radiation hard LGADs". In: *JPCS* 2374.1 (2022), p. 012175. DOI: 10.1088/1742-6596/2374/1/012175.

[90] M.K. Petterson, et al. "Charge collection and capacitance–voltage analysis in irradiated n-type magnetic Czochralski silicon detectors". In: *Nucl. Instrum. Meth. A* 583.1 (2007), pp. 189–194. ISSN: 0168-9002. DOI: 10.1016/j.nima.2007.08.222.

[91] S. Mägdefessel, et al. "Understanding the Frequency Dependence of Capacitance Measurements of Irradiated Silicon Detectors". In: (2023). [Preprint]. DOI: 10.48550/arXiv.2301.09371.

[92] B. Grob. *Basic electronics*. Glencoe/McGraw-Hill, New York, 2000. ISBN: 9780073510859.

[93] P.R. Mercer. *More Calculus of a Single Variable*. Undergraduate Texts in Mathematics. Springer, New York, 2014. ISBN: 9781493919260.

[94] E.G. Villani, et al. "Design and development of Low Gain Avalanche Detectors using Teledyne e2v process". In: *JINST* 19.01 (2024), p. C01038. DOI: 10.1088/1748-0221/19/01/C01038.

[95] J. Villegas, et al. "Gain measurements on NLGAD detectors". In: *Nucl. Instrum. Meth. A* 1055 (2023), p. 168377. ISSN: 0168-9002. DOI: 10.1016/j.nima.2023.168377.

[96] C. Gallrapp, et al. "Study of gain homogeneity and radiation effects of Low Gain Avalanche Pad Detectors". In: *Nucl. Instrum. Meth. A* 875 (2017), pp. 27–34. DOI: https://doi.org/10.1016/j.nima.2017.07.038.

[97] K. Metodiev. "Characterization of depleted monolithic active pixel sensors". DPhil thesis. University of Oxford, 2021. URL: https://ora.ox.ac.uk/objects/uuid:d4cc0a00-ddca-4352-a48c-35c47cf2fdeb.

[98] J. Bronuzzi, et al. "Principle and modelling of Transient Current Technique for interface traps characterization in monolithic pixel detectors obtained by CMOS-compatible wafer bonding". In: *JINST* 11.08 (2016), P08016. DOI: 10.1088/1748-0221/11/08/P08016.

[99] M. Senger, et al. "A Comprehensive Characterization of the TI-LGAD Technology". In: *Sensors* 23.13 (2023), p. 6225. DOI: 10.3390/s23136225.

[100] M.A. Green. "Self-consistent optical parameters of intrinsic silicon at 300K including temperature coefficients". In: *Sol. Energy Mater. Sol. Cells* 92.11 (2008), pp. 1305–1310. ISSN: 0927-0248. DOI: 10.1016/j.solmat.2008.06.009.

[101] H. Kolanoski and N. Wermes. *Particle Detectors fundamentals and applications*. Oxford University Press, 2020. ISBN: 9780198858362.

[102] D.S. Kim, et al. "Temperature-dependent phonon lifetimes and thermal conductivity of silicon by inelastic neutron scattering and ab initio calculations". In: *Phys. Rev. B* 102 (17 2020), p. 174311. DOI: 10.1103/PhysRevB.102.174311.

[103] K.G. Svantesson and N.G. Nilsson. "Determination of the temperature dependence of the free carrier and interband absorption in silicon at 1.06μm". In: *J. Phys. C: Solid State Phys.* 12.18 (1979), p. 3837. DOI: 10.1088/0022-3719/12/18/029.

[104] R. Hanke. *Filter-Faszination (in German)*. Monheim/Bayern, 1979. ISBN: 3-88324-991-2.

[105] QD Laser. URL: https://www.qdlaser.com (visited on 05/07/2024).

[106] QD Laser. *QLD106G-6410 Series*. URL: https://www.qdlaser.com/assets/pdf/product/1064nm%2015ps%20DFB-LD%20Butterfly%20with%20SMPM%20connector%20QLD106G-6410%20series%20C00167-04.pdf (visited on 05/07/2024).

[107] Thorlabs. *GBE15-B*. URL: https://www.thorlabs.com/thorproduct.cfm?partnumber=GBE15-B (visited on 05/07/2024).

[108] Standa Ltd. URL: https://www.standa.lt/ (visited on 05/07/2024).

[109] Sensiron. *SHT35-DIS-B*. URL: https://sensirion.com/products/catalog/SHT35-DIS-B/ (visited on 05/07/2024).

[110] Meech Static Eliminators Ltd. *Meech Vortex Experimental Kit*. URL: https://meech.com/product/experimental-kit/ (visited on 05/07/2024).

[111] Keysight. *UXR0134A Infiniium UXR-Series Oscilloscope: 13 GHz, 4 Channels*. URL: https://www.keysight.com/us/en/support/UXR0134A/infiniium-uxr-series-oscilloscope-13-ghz-4-channels.html (visited on 05/07/2024).

[112] Tektronix. *Keithley 2400 Standard Series SMU*. URL: https://www.tek.com/en/products/keithley/source-measure-units/2400-standard-series-sourcemeter (visited on 05/07/2024).

[113] Aim TTi. *QL Series II*. URL: https://www.aimtti.com/product-category/dc-power-supplies/aim-qlseries (visited on 05/07/2024).

[114] M. Boscardin, et al. "Performance of new radiation-tolerant thin planar and 3D columnar n+ on p silicon pixel sensors up to a maximum fluence of 5×1015 neq/cm2". In: *Nucl. Instrum. Meth. A* 953 (2020), p. 163222. ISSN: 0168-9002. DOI: 10.1016/j.nima.2019.163222.

[115] M. Mironova, et al. "X-Ray measurements of radiation hard monolithic CMOS sensors at Diamond Light Source". In: *PoS* VERTEX2019 (2019), p. 054. DOI: 10.22323/1.373.0054.

[116] A. Sarifudin, D.S. Wijayanto, and I. Widiastuti. "Parameters optimization of tube type, pressure, and mass fraction on vortex tube performance using the Taguchi method." In: *IJHT* 37.2 (2019), pp. 597–604. DOI: 10.18280/ijht.370230.

[117] K. Metodiev, et al. "A compact air cooling system for testing silicon detectors based on a vortex chiller". In: *Nucl. Instrum. Meth. A* 940 (2019), pp. 405–409. ISSN: 0168-9002. DOI: 10.1016/j.nima.2019.06.066.

[118] A. Chilingarov. "Temperature dependence of the current generated in Si bulk". In: *JINST* 8.10 (2013), P10003. DOI: 10.1088/1748-0221/8/10/P10003.

[119] C.J.S. Damerell. *Vertex detectors: The State of the art and future prospects*. RAL-P-95-008, Rutherford Appleton Laboratory, 1995.

[120] E. Currás, M. Fernández, and M. Moll. "Gain reduction mechanism observed in Low Gain Avalanche Diodes". In: *Nucl. Instrum. Meth. A* 1031 (2022), p. 166530. ISSN: 0168-9002. DOI: 10.1016/j.nima.2022.166530.

[121] R. Mulargia, et al. "Temperature dependence of the response of ultra fast silicon detectors". In: *JINST* 11.12 (2016), p. C12013. DOI: 10.1088/1748-0221/11/12/C12013.

[122] C.R. Crowell and S.M. Sze. "Temperature dependence of avalanche multiplication in semiconductors," in: *Appl. Phys. Lett.* 9.6 (1966), p. 242. DOI: 10.1063/1.1754731.

[123] E.H.M. Heijne. "Semiconductor micropattern pixel detectors: a review of the beginnings". In: *Nucl. Instrum. Meth. A* 465.1 (2001), pp. 1–26. ISSN: 0168-9002. DOI: 10.1016/S0168-9002(01)00340-0.

[124] X. Llopart, et al. "Timepix4, a large area pixel detector readout chip which can be tiled on 4 sides providing sub-200 ps timestamp binning". In: *JINST* 17.01 (2022), p. C01044. DOI: 10.1088/1748-0221/17/01/C01044.

[125] P. Skomina, et al. "Studies of inter-pad distance in Low Gain Avalanche Detectors". In: *Nucl. Instrum. Meth. A* 1027 (2022), p. 166158. ISSN: 0168-9002. DOI: 10.1016/j.nima.2021.166158.

[126] M. Senger, et al. "Characterization of timing and spacial resolution of novel TI-LGAD structures before and after irradiation". In: *Nucl. Instrum. Meth. A* 1039 (2022), p. 167030. ISSN: 0168-9002. DOI: 10.1016/j.nima.2022.167030.

[127] K. Ma. "Low Gain Avalanche Detectors for the ATLAS High Granularity Timing Detector: Laboratory and test beam campaigns". In: *Nucl. Instrum. Meth. A* 1063 (2024), p. 169237. ISSN: 0168-9002. DOI: 10.1016/j.nima.2024.169237.

[128] L. Andrews. *Special functions of mathematics for engineers*. SPIE Press, 1998. ISBN: 9780819426161.

[129] S. Bharthuar, et al. "Study of interpad-gap of HPK 3.1 production LGADs with Transient Current Technique". In: *Nucl. Instrum. Meth. A* 979 (2020), p. 164494. ISSN: 0168-9002. DOI: 10.1016/j.nima.2020.164494.

[130] F. Piro, et al. "A 1-uW Radiation-Hard Front-End in a 0.18-um CMOS Process for the MALTA2 Monolithic Sensor". In: *IEEE Trans. Nucl. Sci.* 69.6 (2022), pp. 1299–1309. DOI: 10.1109/TNS.2022.3170729.

[131] G.A. Rinella, et al. "The ALPIDE pixel sensor chip for the upgrade of the ALICE Inner Tracking System". In: *Nucl. Instrum. Meth. A* 845 (2017), pp. 583–587. ISSN: 0168-9002. DOI: 10.1016/j.nima.2016.05.016.

[132] Tower Semiconductor. URL: https://towersemi.com (visited on 02/23/2024).

[133] W. Snoeys, et al. "A process modification for CMOS monolithic active pixel sensors for enhanced depletion, timing performance and radiation tolerance". In: *Nucl. Instrum. Meth. A* 871 (2017), pp. 90–96. ISSN: 0168-9002. DOI: 10.1016/j.nima.2017.07.046.

[134] ATLAS collaboration. *ATLAS phase-II upgrade scoping document*. CERN-LHCC-2015-020, CERN, Geneva, 2015. DOI: 10.17181/CERN.7CRX.AJHP.

[135] R. Cardella, et al. "MALTA: an asynchronous readout CMOS monolithic pixel detector for the ATLAS High-Luminosity upgrade". In: *JINST* 14.06 (2019), p. C06019. DOI: 10.1088/1748-0221/14/06/C06019.

[136] I. Berdalovic, et al. "MALTA: an asynchronous readout CMOS monolithic pixel detector for the ATLAS High-Luminosity upgrade". In: *Proceedings of the 2018 IEEE Nuclear Science Symposium and Medical Imaging* (2019), p. 8824349. DOI: 10.1109/NSSMIC.2018.8824349.

[137] R.C. Cardella. "CMOS Detector and System Developments for LHC Detector Upgrades". PhD thesis. University of Oslo, 2019. URL: https://cds.cern.ch/record/2702969.

[138] A. Sharma, et al. "The Malta CMOS pixel detector prototype for the ATLAS Pixel ITK". In: *PoS* VERTEX2018 (2019), p. 014. DOI: 10.22323/1.348.0014.

[139] B. Hiti, et al. "Development of the monolithic "MALTA" CMOS sensor for the ATLAS ITK outer pixel layer". In: *PoS* TWEPP2018 (2019), p. 155. DOI: 10.22323/1.343.0155.

[140] M. Munker, et al. "Simulations of CMOS pixel sensors with a small collection electrode, improved for a faster charge collection and increased radiation tolerance". In: *JINST* 14.05 (2019), p. C05013. DOI: 10.1088/1748-0221/14/05/C05013.

[141] M. Dyndal, et al. "Mini-MALTA: radiation hard pixel designs for small-electrode monolithic CMOS sensors for the High Luminosity LHC". In: *JINST* 15.02 (2020), P02005. DOI: 10.1088/1748-0221/15/02/P02005.

[142] P.M. Freeman, et al. "Recent measurements on MiniMALTA, a radiationhard CMOS sensor with small collection electrodesfor ATLAS". In: *PoS* VERTEX2019 (2020), p. 020. DOI: 10.22323/1.373.0020.

[143] K. Metodiev, et al. "New method for estimating detector efficiency for charged particles with Diamond Light Source". In: *Nucl. Instrum. Meth. A* 982 (2020), p. 164573. DOI: 10.1016/j.nima.2020.164573.

[144] H. Pernegger, et al. "MALTA-Cz: a radiation hard full-size monolithic CMOS sensor with small electrodes on high-resistivity Czochralski substrate". In: *JINST* 18.09 (2023), P09018. DOI: 10.1088/1748-0221/18/09/P09018.

[145] Y. Neria and R. Neugebauer. "Bulk Crystal Growth: Basic Techniques, and Growth Mechanisms and Dynamics". In: *Public Health* 121 (2007), pp. 572–575.

[146] L. Flores Sanz de Acedo. "Design and characterisation of monolithic CMOS detectors for high energy particle physics and SEU radiation tests for ATLAS Inner Tracker Upgrade readout chip". PhD thesis. University of Glasgow, 2023. URL: https://theses.gla.ac.uk/id/eprint/83781.

[147] C. Solans Sánchez, et al. "MALTA monolithic pixel sensors in TowerJazz 180 nm technology". In: *Nucl. Instrum. Meth. A* 1057 (2023), p. 168787. DOI: 10.1016/j.nima.2023.168787.

[148] M. van Rijnbach. "Radiation Hard Multi-chip Sensor to Module Integration for Monolithic and Hybrid Pixel Detectors". PhD thesis. University of Oslo, 2023. URL: https://www.duo.uio.no/handle/10852/106537.

[149] K.Y. Oyulmaz. "Design and Development of Safety and Control Systems in ATLAS". PhD thesis. Abant Izzet Baysal University, 2022. URL: https://cds.cern.ch/record/2833974.

[150] Xilinx. *AMD Kintex7 FPGA KC705 Evaluation Kit*. URL: https://www.xilinx.com/products/boards-and-kits/ek-k7-kc705-g.html (visited on 07/11/2024).

[151] Xilinx. *AMD Virtex 7 FPGA VC707 Evaluation Kit*. URL: https://www.xilinx.com/products/boards-and-kits/ek-v7-vc707-g.html (visited on 07/11/2024).

[152] I. Asensi Tortajada. "Design and Development of Safety and Control Systems in ATLAS". PhD thesis. University of Valencia, 2021. URL: https://cds.cern.ch/record/2791748.

[153] G. Gustavino. "Timing performance of radiation hard MALTA monolithic pixel sensors". In: *JINST* 18.03 (2023), p. C03011. DOI: 10.1088/1748-0221/18/03/C03011.

[154] Staystik. *Silver-filled Electrically Conductive Film*. URL: https://www.macdermidalpha.com/semiconductor-solutions/products/adhesives/staystik%C2%AE-571 (visited on 06/05/2024).

[155] V. Eremin, E. Verbitskaya, and Z. Li. "The origin of double peak electric field distribution in heavily irradiated silicon detectors". In: *Nucl. Instrum. Meth. A* 476.3 (2002), pp. 556–564. DOI: 10.1016/S0168-9002(01)01642-4.

[156] D.V. Berlea, et al. "Tower Jazz 180 nm MALTA monolithic active pixel sensor Test Beam results". In: *17th Trento Workshop on Advanced Silicon Radiation Detectors (Virtual)* (Mar. 2022). [Conference session].

[157] M. van Rijnbach, et al. "Radiation hardness and timing performance in MALTA monolithic pixel sensors in TowerJazz 180 nm". In: *JINST* 17.04 (2022), p. C04034. DOI: 10.1088/1748-0221/17/04/C04034.

[158] J. Lange, et al. "Beam tests of an integrated prototype of the ATLAS Forward Proton detector". In: *JINST* 11.09 (2016), P09005. DOI: 10.1088/1748-0221/11/09/P09005.

[159] K. Akiba, et al. "LHCb VELO Timepix3 telescope". In: *JINST* 14.05 (2019), P05026. DOI: 10.1088/1748-0221/14/05/P05026.

[160] S. Gkaitatzis, et al. "Performance of a real-time multipurpose 2-dimensional clustering algorithm developed for the ATLAS experiment". In: *Proceedings of 5th International Conference on Modern Circuits and Systems Technologies (MOCAST)* (2016), pp. 1–4. DOI: 10.1109/MOCAST.2016.7495166.

[161] S. Strazzi, et al. "Study of innovative LGAD silicon detectors for the ALICE 3 experiment in LHC Run 5 and 6". In: *Nuovo Cim. C* 47.3 (2024), p. 103. DOI: 10.1393/ncc/i2024-24103-3.

[162] Y. Li on behalf of the LHCb UT Upgrade II team. "MAPS for the Upstream Tracker in LHCb Upgrade II". In: *Nucl. Instrum. Meth. A* 1032 (2022), p. 166629. DOI: 10.1016/j.nima.2022.166629.

[163] R. Abdul Khalek, et al. "Snowmass 2021 White Paper: Electron Ion Collider for High Energy Physics". In: (2022). DOI: doi.org/10.48550/arXiv.2203.13199.

[164] X. Li, et al. "Forward silicon vertex/tracking detector design and R&D for the future Electron-Ion Collider". In: *PoS* PANIC2021 (2022), p. 084. DOI: 10.22323/1.380.0084.

[165] D. Dobrijevic, et al. "Future developments of radiation tolerant sensors based on the MALTA architecture". In: *JINST* 18.03 (2023), p. C03013. DOI: 10.1088/1748-0221/18/03/C03013.